Thèse n° 9252

Damage Assessment of Stone Masonry Piers Using Imaged Surface Cracks

Présentée le 30 septembre 2021

Faculté de l'environnement naturel, architectural et construit
Laboratoire du génie parasismique et dynamique des structures
Programme doctoral en génie civil et environnement

pour l'obtention du grade de Docteur ès Sciences

par

Amir REZAIE

Acceptée sur proposition du jury

Prof. A. Nussbaumer, président du jury
Prof. K. Beyer, directrice de thèse
Prof. P. Roca, rapporteur
Prof. V. Sarhosis, rapporteur
Prof. A. Alahi, rapporteur

École polytechnique fédérale de Lausanne

2021

Acknowledgements

First and foremost, I would like to express my gratitude to my parents, sister, and girlfriend for their unending love and support.

A big thank you goes to my supervisor, Professor Katrin Beyer, whose enthusiasm and helpful advice were invaluable. She was always there when I needed help. She allowed and trusted me to pursue novel research directions, for which I am grateful.

I would also like to thank the members of my thesis jury, Prof. Alain Nussbaumer (president), Prof. Pere Roca, Prof. Vasilis Sarhosis, and Prof. Alexandre Alahi, for their interest in my work and constructive comments.

Michele, a friend, mentor, and knowledgeable advisor deserves my heartfelt thanks. Without his assistance and backing, I would not have been able to finish this Ph.D. journey.

At EESD, we are all fortunate to have Yvonne's support. I am and will always be thankful to her for her kindness and help.

Bastian and Bryan have been two of the best officemates I have had during my time at EESD. Their upbeat, easygoing, and carefree demeanor makes them enjoyable company. Thank you for all of the wonderful memories. A big thank you to Igor and Maria Pia; for all those coffee break talks. I had very enjoyable times with you. I also thank all other EESD members with whom I have had the chance to spend time.

A huge thank you to the amazing technicians of the structural engineering laboratory of EPFL: Sylvain Demierre, Gérald Rouge, Gilles Guignet, Armin Krkic, Serge Despont, François Perrin, and Léa Frédérique Dubugnon. Without their invaluable and kind help, I could not perform my experimental campaign.

Last but not least, I would like to thank Dr. Radhakrishna Achanta, a principal data scientist at Swiss Data Science Center, with whom I had the pleasure to collaborate and learn from his vast experience and knowledge in Computer Vision and Machine Learning.

... they say that the "DARK AGE" began when Bastian and Michele left. But, with the arrival of newcomers Savvas, Ketson, Mathias, Ernesto, Qianqing, and Hnat, I can see the sun rising once more. I wish I had the chance to enjoy this sun with you, but that's life. Wish you all the best.

Lausanne, August 17, 2021 Amir Rezaie

Abstract

After an earthquake, the structural safety of all buildings in the affected region needs to be assessed. This is currently done by a visual inspection of each building. This approach is very time-consuming and requires a significant amount of expertise from the inspectors. A lack of the latter can lead to inaccurate assessments, which are often overly conservative. This is, of course, on the safe side but negatively affects the resilience of societies.

In the future, the post-earthquake assessment process will be accelerated and objectified by replacing the visual inspection with an automated image-based evaluation of the buildings. One research line of the Earthquake Engineering and Structural Dynamics Laboratory is to develop such a process for stone masonry buildings, which are among the most vulnerable buildings during earthquake loading. The objective of this thesis is to contribute to this vision.

Earthquake damage to stone masonry structures manifests itself mainly in cracks. Surface cracks have been shown to contain important information to build empirical and physics-based models to understand the activated mechanisms and estimate the level of damage to a structure.

This Ph.D. thesis aims at developing methods for detecting, segmenting, quantifying, and interpreting surface cracks using optical measurement and machine learning techniques. The methods are applied to a set of six large-scale quasi-static cyclic shear-compression tests on plastered rubble stone masonry piers, which have been conducted as part of the thesis and provide a unique data set of high-resolution images and displacement-field measurements.

Two methods for detecting cracks in laboratory images were implemented and compared: the threshold method, based on the digital image correlation technique, and the deep learning method. It was discovered that the deep learning method could better preserve the geometry of cracks and had a higher detection precision than the standard threshold method. The detected crack patterns were then quantified in terms of width, length density, complexity, and fractal dimension.

It was demonstrated that the axial load ratio has little influence on the maximum crack width at the peak force and ultimate drift limit states; however, at the ultimate drift limit state, the maximum crack width computed for walls with a shear span ratio of 1.0 was significantly greater than those computed for walls with a shear span ratio of 0.5. Furthermore, it was shown that crack width increases with the number of cycles with the same level of drift demand.

Regarding the fractal dimension of crack patterns estimated by the box-counting method, the sensitivity analysis showed that fractal dimension depends on the grid position and orientation, the scale factor, the break-point location, and the global cut-off and can change

up to 0.5. Due to the dependency of the fractal dimension on these parameters and the fact that a regression step is required to estimate it, another dimension called complexity dimension was used to quantify space-filling characteristics of crack patterns.
To quantify the degradation of stiffness, strength, and displacement capacity of tested stone masonry piers, three ratios were introduced: the stiffness ratio, the force ratio, and the drift ratio. Using linear and ridge regression with polynomial augmented features, a vector of features containing crack pattern characteristics, axial load, and shear span ratio was mapped to the degradation ratios.
It was discovered that including the axial load and shear span ratio could significantly reduce the error in predicting stiffness and force ratio but had less influence on drift ratio estimation. Moreover, it was found that both KNN and logistic regression could accurately predict whether the wall has been loaded beyond the drift at which the peak force is reached or not based on crack features.
The research presented in this Ph.D. thesis has important implications for the design of new automated pipelines for performing rapid post-earthquake assessments of stone masonry buildings. It focused on how to quantify crack patterns and map them to a reduction in stiffness, strength, and displacement capacity of a damaged stone masonry pier.
Keywords: Rubble stone masonry, Digital image correlation, Shear compression test, Machine learning, Crack detection, Damage assessment, Crack quantification.

Résumé

La sécurité des structures post-séisme est un aspect très important à vérifier dans les régions frappées par les tremblements de terre. Toutefois, à ce jour, l'inspection des fissures présentes dans chaque bâtiment se fait encore à l'œil nu. Ce type d'inspection comporte une procédure longue et qui demande beaucoup d'expertise. De plus, une observation inexacte peut comporter un jugement incorrect, ou qui s'avère excessivement en faveur de la sécurité, ce qui, enfin, a un impact négatif sur la société.

Dans l'avenir, l'évaluation post-sismique des bâtiments va s'accroitre rapidement et devenir plus objective, à travers l'introduction de méthodes de détection automatique utilisant des images du bâtiment. Le développement de telles procédées pour les bâtiments en pierre naturelle, étant parmi les structures les plus vulnérables aux séismes, est une des lignes de recherche principales au laboratoire de Génie Parasismique et Dynamique des Structures de l'EPF de Lausanne. Cette thèse veut contribuer à cette vision.

Les dégâts engendrés par les séismes se manifestent à la surface des structures á travers des fissures. L'observation de ces fissures constitue une source importante pour la construction de modèles empiriques et mécaniques, à travers lesquels il devient possible d'expliquer les mécanismes activés et estimer les dommages.

Cette thèse a pour but de développer des méthodes pour la détection, segmentation, évaluation et interprétation des fissures par l'utilisation de mesures optiques et de techniques d'apprentissage automatique. Ces méthodes sont appliquées sur un ensemble de six murs en pierre naturelle, construits à échelle réelle et recouverts d'enduit, soumis à des essais cycliques quasi-statiques de cisaillement-compression. Ces essais ont été effectués dans le cadre de cette thèse, et fournissent un ensemble de données unique, comprenant des images à haute résolution ainsi que des mesures de champ de déplacement.

Deux méthodes pour la détection des fissures á partir d'images de laboratoire ont été implémentées et comparées : une méthode basée sur le seuil de déformation, obtenu par corrélation d'image, et une méthode d'apprentissage automatique. Nous montrons que la méthode d'apprentissage automatique permet de mieux préserver la géométrie des fissures et qu'elle admet un niveau de précision plus élevé dans la phase de détection des fissures par rapport à la méthode basée sur le seuil de déformation.

Les réseaux de fissures ainsi détectés ont été ensuite évalués en termes d'ouverture, longueur densité, complexité, et dimension fractale. Nous montrons que le rapport de charge axiale exercé sur les murs lors des essais a peu d'influence sur l'ouverture maximale des fissures observées à l'état limite correspondant à la résistance des murs ainsi qu'à celui de drift ultime.

Or, à l'état limite de drift ultime, l'ouverture maximale des fissures observées sur des murs cantilevers (ayant une hauteur caractéristique de 1) est de loin plus importante que celle obtenue sur des murs doublement encastrés (ayant une hauteur caractéristique de 0.5). En outre, à chaque niveau de drift, l'ouverture des fissures augmente avec le nombre de cycles effectués pendant les essais.

La dimension fractale des fissures a été estimée par la méthode 'box-counting'. Les analyses de sensitivité ont montré que la dimension fractale dépend de la position ainsi que de l'orientation du maillage utilisé, mais aussi du facteur d'échelle, de la position du 'break-point', et du 'cut-off' globale. Tous ces facteurs peuvent changer la dimension fractale jusqu'à 0.5. En raison de la dépendance de la dimension fractale de ces paramètres, et en vue du fait qu'un incrément de régression est demandé par cette méthode, on fait appel à une autre mesure, nommée mesure de complexité, afin de d'évaluer les propriétés d'organisation spatiale des fissures.

Trois rapports caractéristiques ont été introduits afin de pouvoir évaluer le niveau de dégradation de la rigidité, résistance, et capacité en déplacement des murs par rapport aux valeurs initiales mesurées en début d'essais. En faisant appel à la régression linéaire et la régression Ridge ayant des termes polynomiaux augmentées, un vecteur des caractéristiques comprenant les propriétés du réseau de fissures, le rapport de charge axiale et la hauteur caractéristique, a été lié à ces trois rapports.

Nous avons pu constater que l'utilisation du rapport de charge axiale et de la hauteur caractéristique dans le vecteur des caractéristiques améliore sensiblement la prédiction de la dégradation de la rigidité ainsi que celle de la résistance des murs, mais cela affecte moins l'estimation de la dégradation de leur capacité en déplacement. En outre, l'utilisation d'une régression de type KNN et d'une régression logistique permet de prédire de façon précise si le mur se trouve dans un état pré- ou post-pic à partir des propriétés des réseaux de fissures.

Les résultats obtenus dans cette thèse ont des répercussions importantes sur la conception de nouvelles procédées pour la vérification post-sismique automatique des bâtiments en pierre naturelle. Nous nous sommes concentrés sur l'évaluation des réseaux de fissures et leur lien avec le niveau de dégradation de la rigidité, résistance, et capacité en déplacement des murs endommagés.

Mots-clés : : Maçonnerie en pierre naturelle, Corrélation d'image, Essais de cisaillement-compression, Apprentissage automatique, Détection des fissures, Évaluation des dommages, Quantification des fissures

Sommario

Dopo un terremoto, è necessario valutare la sicurezza strutturale di tutti gli edifici della regione colpita. Ad oggi, la valutazione si svolge attraverso un'ispezione visiva dell'edificio. Questo approccio richiede molto tempo e una notevole esperienza da parte dell'ispettore. Inoltre, un'osservazione inesatta può portare a una valutazione imprecisa, o troppo conservativa, con un impatto negativo sulla società.
In futuro, l'attività di valutazione post-sisma degli edifici sarà accelerata e oggettivata sostituendo l'ispezione visiva con un processo di valutazione automatizzata basato sull'analisi delle immagini dell'edificio. Una linea di ricerca del Laboratorio di Ingegneria Sismica e Dinamica delle Strutture dell'EPFL di Losanna è quella di sviluppare un tale processo per edifici edifici in muratura di pietra, un materiale da costruzione che è molto vulnerabile ai terremoti. Il presente lavoro di tesi vuole contribuire a questa visione.
I danni da terremoto alle strutture in pietra si manifestano principalmente sotto forma di fessure. È stato dimostrato che le fessure superficiali contengono informazioni importanti per costruire modelli empirici e basati sulla fisica volti a comprendere i meccanismi attivati e stimare il livello di danno di una struttura.
Questa tesi di dottorato ha come obiettivo lo sviluppo di metodi per rilevare, segmentare, quantificare e interpretare le fessure superficiali utilizzando tecniche di misurazione ottica e di apprendimento automatico (machine learning). Tali metodi sono stati applicati a una serie di sei prove cicliche quasi statiche di compressione e taglio, svolte su pareti murarie in pietra, intonacate ed in scala reale. Queste prove sono state condotte all'interno del progetto di tesi e forniscono una batteria di dati unica, con immagini ad alta risoluzione e misurazioni del campo di spostamento.
Sono stati implementati e confrontati due metodi per rilevare le fessure a partire da immagini di laboratorio: un metodo basato sulla soglia di deformazione, ottenuta attraverso il metodo di correlazione dell'immagine, e un metodo deep learning. Si è potuto osservare che il metodo deep learning preserva meglio la geometria delle fessure e ha una precisione maggiore nel rilevamento di quest'ultime rispetto al metodo basato sulla soglia di deformazione. I quadri fessurativi rilevati sono stati in seguito quantificati in termini di apertura, densità, lunghezza, complessità e dimensione frattale.
È stato dimostrato che il rapporto di carico assiale ha poca influenza sull'apertura massima di fessura allo stato limite corrispondente alla forza di picco e a quello corrispondente al drift ultimo. Tuttavia, allo stato limite di drift ultimo, l'apertura massima di fessura calcolata per le pareti con un'altezza caratteristica pari a 1.0 (muro con incastro alla base) è significativamente

maggiore di quella calcolata per le pareti con un'altezza pari a 0.5 (muro con incastro alla base e in testa). Inoltre, è stato dimostrato che l'apertura di fessura aumenta ad ogni livello di drift con il numero di cicli effettuati durante le prove.
La dimensione frattale delle fessure è stata stimata attraverso il metodo box counting. Le analisi di sensibilità hanno mostrato che la dimensione frattale dipende dalla posizione e dall'orientamento della griglia utilizzata, dal fattore di scala, dalla posizione del break-point e dal cut-off globale. Tutti questi fattori possono cambiare la dimensione frattale fino a 0.5. A causa della dipendenza della dimensione frattale da questi parametri, e del fatto che è necessariao un'analisi di regressione per stimarla, un'altra dimensione chiamata dimensione di complessità è stata utilizzata per quantificare le caratteristiche di organizzazione spaziale del quadro fessurativo.
Tre rapporti caratteristici sono stati introdotti al fine di quantificare il degrado della rigidezza, resistenza e capacità di spostamento dei muri in pietra testati rispetto ai loro valori iniziali. Usando la regressione lineare e la regressione ridge con valori polinomiali migliorati, un vettore delle caratteristiche contenente le proprietà del quadro fessurativo, il rapporto di carico assiale e l'altezza caratteristica, è stato collegato ai tre rapporti di degrado.
Si è visto che l'inclusione del rapporto di carico assiale e dell'altezza caratteristica nel vettore delle caratteristiche può ridurre significativamente l'errore nel prevedere il degrado della rigidità e della forza, ma che questo influenza meno la stima del degrado della capacità di spostamento. Inoltre, si è potuto osservare che una regressione di tipo KNN e una regressione logistica permettono di prevedere in maniera accurata se la parete è nella fase di pre- o post-picco, sulla base delle proprietà delle fessure.
La ricerca svolta in questa tesi ha delle implicazioni dirette nella concezione di nuove procedure per l'esecuzione automatizzata di valutazioni post-sisma di edifici in pietra. In particolare, Ci si è concentrati sulla valutazione del quadro fessurativo e sul suo legame con il degrado della rigidezza, della resistenza, e della capacità di spostamento di pareti murarie in pietra danneggiate.
Parole chiave: muratura in pietra, digital image correlation, test di compressione e taglio, machine learning, rilevamento delle fessure, valutazione dei danni, quantificazione delle fessure

Contents

1 Introduction

1.1 Background and problem statement

Stone masonry buildings are highly vulnerable against seismic actions due to low mortar tensile strength, poor interlocking between units, high self-weight, and, in many cases, the lack of proper connections between wall leaves (Kržan et al., 2015). When these structures are not retrofitted, they frequently fail in one of three ways: a) out-of-plane, b) in-plane, or c) a combination of out-of-plane and in-plane failure modes (Tomaževič, 1999). However, by improving connections between perpendicular walls, between walls and slabs, and by increasing slab stiffness, the building behavior will tend to a "box-behavior", and the failure modes will be primarily in-plane. Examples of in-plane and out-of-plane failure modes observed in unreinforced masonry buildings following an earthquake are shown in Figure 1.1.

(a) (b)

Figure 1.1 – Examples of failure modes of unreinforced masonry buildings after the 2016 earthquake in central Italy. (a) in-plane; (b) out-of-plane. (photo credit: EESD, EPFL)

Assessing the extent of damage caused by an earthquake and estimating the safety of damaged buildings is a difficult task that necessitates specialized knowledge and training. In the current rapid post-earthquake assessment practice, a group of experts visits the earthquake-affected region and visually inspects the damaged buildings. The experts assess the level of damage and decide whether the building is safe to use, following post-earthquake guidelines, for example, ATC-20-1 (Applied Technology Council, 2005), AeDES (Baggio et al., 2007), and EPPO (Anagnostopoulos et al., 2004). These guidelines include explanations as well as photos or sketches of damage patterns to assist engineers in classifying the severity of the damage, which often ranges from negligible to very heavy structural damage (Applied Technology Council, 2005; Anagnostopoulos et al., 2004). As an illustration, the sketch of common damage to masonry buildings and the description of damage, presented in AeDES (Baggio et al., 2007), plus an example image of a damaged masonry building are shown in Figure 1.2 and Table 1.1. In Figure 1.2b, widespread vertical (type 1), diagonal cracks (type 3) and almost horizontal cracks (type 11) at the level of the attic are present (Baggio et al., 2007). Based on the cracking pattern in this figure, AeDES (Baggio et al., 2007) suggests assigning the damage grade medium-heavy to the entire wall. Similarly, FEMA 306 (1998) and EPPO (Anagnostopoulos et al., 2004) classify the damage level to masonry elements based on the crack type and width.

There are, however, a couple of problematic issues with the current practices in rapid post-earthquake assessment. I mention several of them below:

- The current method is subjective. In other words, the decision-making process about a building's remaining capacity and safety is influenced by the inspectors' experience and level of expertise.
- The proposed rapid post-earthquake assessment, i.e., visual inspection, is not based on physics. In other words, no numerical analysis of stone masonry damaged buildings is required.
- In the literature, criteria for determining the level of damage to a structural component, such as crack width, are fitted against experimental data on brick masonry, and there is a scarcity of data on stone masonry.
- The criteria to designate damage severity mentioned in recommendations for post-earthquake assessment are not always quantitative.
- There are no end-to-end continuous functions that relate the damage variables to the degradation of physical properties of damaged structural components.

1.2 Objectives and scope of the study

In the last two decades, the advancements in artificial intelligence and its tremendous effect on computer vision have been a wake-up call for many engineering fields such as civil and construction engineering to look for more effective and objective pipelines. The EESD group has envisioned and conducted research studies toward a fully automated post-earthquake assessment pipeline that uses image data as the primary input. This Ph.D. thesis is the first step toward the realization of this goal for stone masonry buildings.

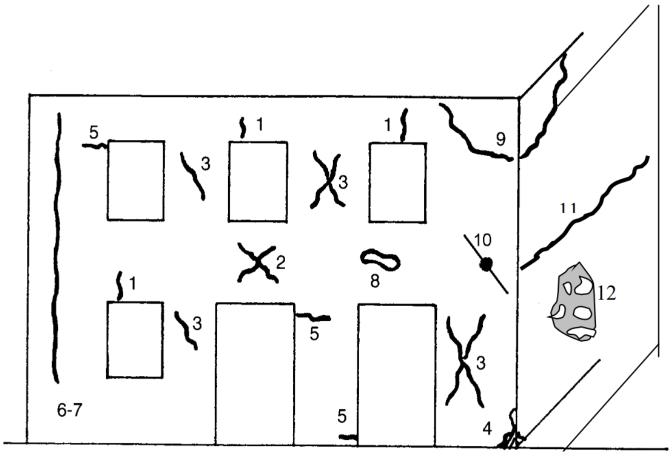

(a)

(b)

Figure 1.2 – (a) Sketch of damage pattern in masonry (taken from (Baggio et al., 2007)); (b) an example image of a damaged masonry building shown in AeDES (Baggio et al., 2007).

Damage number	Description
1	nearly vertical cracks on the opening lintels
2	diagonal cracks in the spandrel beams (window parapets, lintels)
3	diagonal cracks in vertical elements (masonry piers)
4	local crushing of masonry with or without material expulsion
5	nearly horizontal cracks at the top and/or at the foot of masonry piers
6	nearly vertical cracks at walls intersections
7	same as 6 but with through cracks
8	material expulsion at the beam supports due to pounding
9	formation of a displaced wedge at the intersection of two orthogonal walls
10	failure of tie rods or bond slippage
11	horizontal cracks at the floor level or at the attic level
12	separation of one of the wythes of a double-wythe wall

Table 1.1 – Description of the damage sketch shown in Figure 1.2.

To understand how this thesis fits into this vision, I first briefly discuss a widely used modeling strategy of regular (in plan and height) stone masonry buildings, equivalent frame modeling (EFM). EFM is one of the commonly used methods both in practice and academic research community to analyze seismic behavior of unreinforced masonry buildings (Vanin et al., 2020; Lagomarsino et al., 2013). In this approach, load-bearing walls are divided into three elements called piers, spandrels and rigid nodes. Within this discretization, piers are the most critical elements as they carry both vertical and horizontal loads caused by an earthquake. As an illustration, Figure 1.3c shows the EFM discretization of the building Holsteiner Hof shown in Figure 1.3a, which is an old stone masonry building located in the city of Basel, Switzerland.

After an earthquake, structural elements, such as piers and spandrels, will be damaged. This

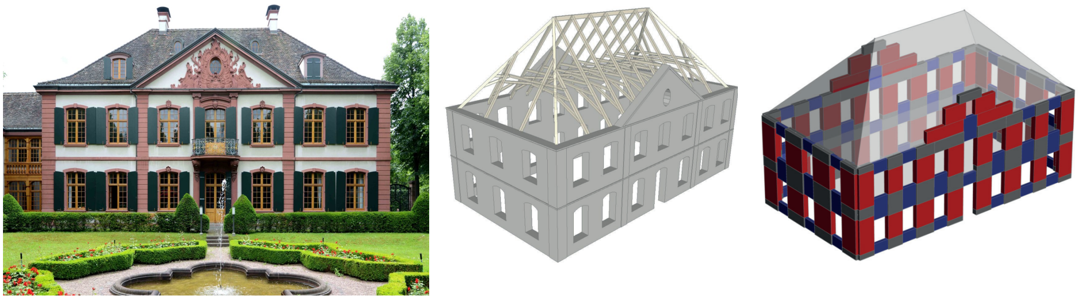

(a) (b) (c)

Figure 1.3 – Illustration of EFM discretization. (a) an image of the Holsteiner Hof building (photo credit: EESD, EPFL); (b) geometry and (c) macro-element model. Piers, spandrels and rigid nodes are shown in red, blue, and grey, respectively. This figure is taken from Vanin (2019).

damage appears in a variety of forms, including cracking, crushing, detachment/collapse of plaster layers, and collapse of a portion or entire wall. Once the damage is detected, we can use a predictive model to estimate the reduction in structural properties such as stiffness, strength and displacement capacity of damaged piers and spandrels as a function of the damage features. Thereafter, these damaged piers and spandrels can be modeled numerically within the EFM approach using the degraded properties. This approach is superior over the visual inspection and engineering judgment that is the current practice for rapid post-earthquake assessment as it includes physics-based modeling.

To achieve such a goal, we must address several research questions:

- Which damage features should we choose for building predictive models?
- In what context should these features be chosen? In the context of machine learning/-pattern recognition, or within the realm of physics, or a combination of the two?
- What are the effects of kinematic and static boundary conditions on damage features?

In this Ph.D. thesis, I address mainly the first and the third question, focusing solely on the in-plane damage to rubble stone masonry piers, with cracking serving as the primary indicator of damage. I studied various ways of quantifying damage and its robustness. Additionally, I propose simple machine learning models to estimate the damaged properties of rubble stone masonry piers, including stiffness, strength and displacement capacity. The main source of data used in this thesis to tackle the above-mentioned questions was the data obtained from an experimental campaign on plastered rubble stone masonry walls conducted as a part of the Ph.D. studies.

To summarize, the main objectives of this Ph.D. work were:

1. Provide a unique dataset of crack images from shear-compression tests on rubble stone masonry walls
2. Develop a framework to segment crack pixels in laboratory images
3. Develop methods to quantify crack patterns
4. Investigate parameters affecting crack features
5. Connect damage features to mechanical properties of damaged stone masonry piers using machine learning models

1.3 Organization of the thesis

The thesis is written in a paper-based format, with each chapter consisting of a paper that has been published or submitted for publication. Each author's contributions are listed at the beginning of each paper-based chapter. Below is the summary of each chapter:

- Chapter 2: In this chapter, the results of experimental tests on plastered rubble stone masonry walls are presented. The results include the data from quasi-static cyclic shear-compression tests on six large-scale rubble stone masonry piers, simple compression tests and diagonal compression tests on wallettes and material tests on mortar samples. The effect of axial load and shear span ratio on the stiffness, strength, and drift capacity of the walls is discussed. In addition, I assess how well existing mechanical and empirical models predict the strength and drift limit states. The data acquired from this experimental campaign is then used as input for the methods presented in chapter 3, chapter 4, and chapter 6 to detect and quantify damage (cracks).
- Chapter 3: This chapter discusses the problem of crack detection on gray-scale images taken for the digital image correlation (DIC) method. I address this task with two methods, namely the threshold method and deep learning. In the threshold method, I use the displacement field outputted by the DIC, while in the deep learning method, the gray-scale images are used to train a deep convolutional neural network to detect cracks. These approaches are compared in terms of segmentation metrics. I show that the deep learning approach is more precise in crack detection than the threshold method and the geometry of crack patterns is better preserved.
- Chapter 4: One common way to quantify damage is through measuring the crack width (often maximum crack width). In this chapter, I discuss how crack width is influenced by a variety of factors. I focus on the effect of axial load, shear span ratio, and loading protocol on crack width distribution.
- Chapter 5: Fractal dimension is a feature encoding the complexity and space-filling characteristics of crack patterns. In this chapter, I show that the estimation of fractal dimension is greatly influenced by the selection of parameter settings of the box-counting

method, i.e., the method to compute fractal dimension. Therefore, when correlating fractal dimension of crack patterns with a physical damage index, it is important to take into account the sensitivity of fractal dimension to those methodological parameters.

- Chapter 6: In this chapter, I use machine learning models for two purposes: 1) to classify pre-peak vs. post-peak regime of the wall based on crack features; 2) to estimate three ratios encoding the degradation of stiffness, strength and displacement capacity of the walls. I explore how adding axial load and shear span ratio to the crack feature vector affects the error of predictions.

- Chapter 7: This chapter summarizes the main findings of the research study in the following topics: a) stiffness, strength and displacement capacity of rubble stone masonry piers, b) damage detection and quantification, and c) machine learning for damage assessment of stone masonry walls.

- Appendix A: This chapter includes the data paper that explains the organisation of the data from the experimental campaign on plastered rubble stone masonry walls.

2 Experimental campaign on rubble stone masonry walls

This chapter represents the slightly modified post-print version of the article:

Rezaie, A., Godio, M. and Beyer, K. (2020). "Experimental investigation of strength, stiffness and drift capacity of rubble stone masonry walls". *Construction and Building Materials*, 251, p.118972.

The formatting and numbering of equations, tables and figures have been adapted to this document. The contributions of the first author are: designing and conducting the experimental campaign, analysis of the acquired data, writing the article. The contributions of the second author are: help the first author to conduct the experimental campaign, co-writing the article. The contributions of the third author are: supervision of the first author, co-writing the article.

Abstract

There is limited available research on rubble stone masonry walls, which are vulnerable under seismic loading. This paper presents an experimental campaign of cyclic shear compression tests on six large-scale walls of this topology. The effect of the axial load and shear span ratio on wall behaviour, notably on the wall stiffness, strength, and drift capacity, was investigated. It was found that the drift at crack onset was only half of that in previous campaigns on stone masonry walls, likely because one face of each wall was plastered, making the damage more visible. Additionally, splitting cracks opening between the wall leaves appears to play a key role in the collapse mechanism. Finally, testing the walls up to the loss of their axial-load-bearing capacity provides new input for the collapse risk analysis of stone masonry buildings.

Keywords: Rubble stone masonry; Plaster; Shear compression test; Diagonal compression test; Simple compression test; Digital image correlation.

2.1 Introduction

Stone blocks were often used in historical buildings due to their aesthetic beauty, low cost, durability, and the availability of natural stone (Siegesmund and Snethlage, 2011; Hendry and Khalaf, 2001). Stone masonry elements are typically composite structures consisting of units (stone), mortar, and in-fill material between the wall leaves (Kržan et al., 2015; Tomaževič, 1999). Due to variability in the stone shape and the pattern that is created by the stones, a large diversity in stone masonry typologies can be found throughout the world (Kržan et al., 2015).

Previous earthquakes highlighted the high vulnerability of stone masonry works (Rovero et al., 2016; D'Ayala and Paganoni, 2011; Carocci, 2012). During an earthquake, horizontal actions cause in-plane and out-of-plane deformations in the load-bearing masonry walls (Tomaževič, 1999). If there are proper connections between adjacent walls and between walls and slabs, local out-of-plane failures can be prevented, leaving the global behaviour of the structures to be governed by the in-plane capacity of the load-bearing walls (Rovero et al., 2016). Experimental investigations, mechanical models, and numerical analyses have shown that various parameters influence the horizontal stiffness, strength, and deformation capacity of masonry walls. Besides the properties of the stones and mortar themselves, other important factors include the texture created by the units, the wall geometry, the static and kinematic boundary conditions applied to the wall, and also the testing type (Kržan et al., 2015; Vanin et al., 2017; Zhang and Beyer, 2019; Vasconcelos and Lourenço, 2009; Silva et al., 2014; Milosevic et al., 2013; Zhang et al., 2018; Borri et al., 2015a; Corradi et al., 2003). One other important parameter that can affect especially the determination of the shear strength of masonry is whether tests are conducted on specimens built at the laboratory or on the panels taken from an existing building (Borri et al., 2015a; Corradi, 2018).

Performance-based assessment methods for masonry buildings require the drift capacity of the walls at one or several limit states, where "drift" is the relative horizontal displacement between the top and bottom of a wall divided by its height. Drift capacity models for masonry walls in general and stone masonry walls, in particular, are still under development. Available models in current codes have not been tailored for stone masonry walls, and the effect of this wall typology has not yet been included (Vanin et al., 2017). To address this issue, Vanin et al. (2017) gathered data from monotonic and cyclic shear compression tests on stone masonry walls with various textures and morphologies. Based on the collected data, empirical drift capacity models for various limit states were proposed, including the drift at the onset of cracking, at yield, at significant damage, at maximum force and at ultimate and collapse state. Additionally, reference values for the mechanical properties of the walls were derived (Vanin et al., 2017).

An analysis of the stone masonry database (Vanin et al., 2017) showed that there is little data for rubble stone masonry walls, i.e., stone masonry containing pebbles and irregular stones (Ministry of Infrastructures and Transportation (MIT), 2009), which is often referred to as masonry of typology A (Kržan et al., 2015). Masonry walls of this typology are at the highest risk of in-plane or out-of-plane damage due to a number of factors such as the lack of proper transversal connections, poor mortar characteristics, and improper characteristics of the vertical and bed joints (Corradi, 2018; Borri et al., 2015b). Thus, it implies the necessity to understand better the parameters affecting the cyclic performance of such masonry typology and also to investigate adequate retrofitting methods. This study focuses on unretrofitted stone masonry walls; it does not address the performance of retrofitted walls. Research studies investigating retrofitting methodologies can, for example, be found in Corradi et al. (2008); Borri et al. (2011, 2014); Corradi et al. (2014, 2016, 2002); Uranjek et al. (2012).

Figure 2.1 shows the tests available in the database published in Vanin et al. (2017) plus the data from four additional test series (Godio et al., 2019; Tomaževič et al., 2012; Milosevic et al., 2015; Wang et al., 2018). Two of these series were conducted since the database was published (Godio et al., 2019; Wang et al., 2018) while the other two had been overlooked when assembling the original database (Tomaževič et al., 2012; Milosevic et al., 2015). Out of the available 17 tests on stone masonry walls of typology A, only 8 are cyclic tests that are therefore usable for determining an unbiased estimation of the drift capacity of the walls (Wilding et al., 2017). Moreover, as illustrated in Figure 2.1, limited data is available on walls of typology A that are tested at a low axial load ratio (i.e., the ratio of the applied vertical stress to the compression strength of masonry).

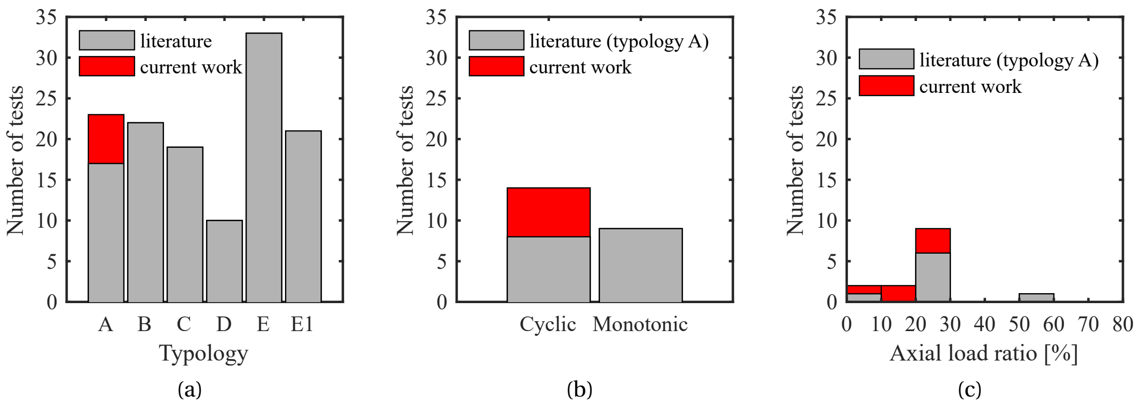

Figure 2.1 – Database of laboratory shear compression tests on stone masonry walls: Number of conducted tests in terms of a) typology; b) monotonic/cyclic and c) axial load ratio. The plots contain the database gathered by Vanin et al. (2017) plus additional wall tests available in the literature (Godio et al., 2019; Tomaževič et al., 2012; Milosevic et al., 2015; Wang et al., 2018).

In this study, the influence of the axial load ratio and the shear span ratio on the in-plane stiffness, strength, and drift capacity of walls of typology A is investigated. To do this, six quasi-static cyclic shear compression tests on large-scale rubble stone masonry walls and six material tests on rubble stone masonry wallettes were carried out at the École Polytechnique Fédérale de Lausanne (EPFL). The primary aim of this study is to generate new experimental data on the cyclic behaviour of rubble stone masonry walls to contribute to the available database and to assess to what extent the available models for stiffness, strength, and drift capacity can predict this new data. In addition, this test series investigated the drift capacity at axial load failure, i.e., the point where the walls were no longer able to support the constant axial load that was applied during the test, putting this among few campaigns on rubble stone masonry walls where the walls are tested to this point. This is a much-needed input parameter for the seismic risk estimation of stone masonry buildings.

This paper is organized as follows: Section 2.2 describes the experimental approach, construction material and instrumentation; Section 2.3 discusses the main findings, such as the influence of the axial load ratio and shear span ratio on the failure mode, stiffness, strength and drift capacity, including the drift at axial load failure. The final section summarizes the key findings of the study.

2.2 Experimental Program

This section describes the test units, test set-up, loading protocol and instrumentation for the shear-compression tests. In addition, it presents the results of the material tests on mortar, plaster, and masonry.

2.2.1 Test units and construction materials

The experimental campaign involved shear compression tests on six large-scale walls (specimen label: RS) of the dimensions 1600 mm x 1600 mm x 400 mm (H x L x t). In addition, diagonal compression tests on three wallettes (RSD) and simple compression tests on three wallettes (RSC) were carried out. The size of the wallettes used for the diagonal compression tests was 900 mm x 900 mm x 400 mm. Two wallettes with the dimensions of 900 mm x 900 mm and 400 mm and one with the dimensions of 900 mm x 800 mm and 400 mm were used for the simple compression tests. The walls were constructed by two experienced masons using uncut limestone blocks with dimensions between 10–30 cm and pebbles with a maximum size of around 10 cm. At each layer, the stones of the two outer layers were placed first, and then the area between the leaves was filled with stone chips and pebbles (Figure 2.2). To represent old building material characteristics (Moropoulou et al., 2005), a lime-based mortar with an aggregate/binder volume ratio of 3/1 with approximately one portion of water was used. As a binder, the commercial product ‘OTTERBEIN natural hydraulic lime (NHL5)’ was used. On one side of each wall, two layers of plaster were applied in two steps, i.e., the inner layer was firstly applied, then after 24 hours, the outer layer was added. The inner layer of the plaster was around 4–6 cm thick and was applied to smooth the surface of the wall. The outer layer was 1 cm thick. For both plaster layers, the product ‘GeoCalce® Intonaco’ (CSII class, according to EN 998-1) was used. It consists of pure NHL3.5 natural-lime-based mortar, geo-binder, siliceous washed natural river sand, dolomitic limestone, and pure fine white Carrara marble. For the first plaster layer, fine sand with a maximum aggregate size of approximately 2 mm was added; the binder to sand weight ratio was 2/1 mixed with 12 l of water. For the second layer, 25 kg of the binder with no extra sand was mixed with 5.1 l of water. Figure 2.2a and b show the constructed large-scale walls and a section of one of the walls during construction. Figure 2.2c shows a wall with the applied plaster. A strip of around 1–2 cm in height at the top and bottom of the wall was left unplastered to avoid direct loading onto the plaster layer during testing.

(a) (b) (c)

Figure 2.2 – (a) Construction of the walls; (b) six large-scale walls; (c) wall section and the applied plaster.

During construction, material samples were taken from each batch of mortar and plaster, and prisms measuring 16 cm x 16 cm x 4 cm were cast. To characterize the mortar and plaster, three-point bending tests on the mortar prisms and compression tests on the halves resulting from the three-point bending tests were performed according to EN 1015-Part 11 (2000). In Table 2.1, the results of material tests on the mortar and plaster samples are given. The terms f_{tmo}, f_{cmo} and f_{tp}, f_{cp} are the tensile and compression strength of the mortar and plaster, respectively.

To determine the mechanical properties of masonry as a composite, simple compression tests (i.e., with no confinements at the top and bottom of the specimens) and diagonal compression tests were conducted on stone masonry wallettes according to the described procedures in EN 1015-Part 1 (1999) and RILEM (1991), respectively. In the compression tests, three loading/unloading cycles were applied before the peak force. The Young's modulus (E) was derived by fitting a line to each of the three stress-strain cycles and taking the average value of the three slopes (Godio et al., 2019) as shown in Figure 2.3. Table 2.2 summarizes the Young's modulus and compression strength (f_c) of the masonry. The obtained compression strength (0.76 MPa) was smaller than the lower bound of the range (1–1.8 MPa) suggested by the Italian code (Ministry of Infrastructures and Transportation (MIT), 2009) for masonry of typology A. The Young's modulus is almost 37% higher than the suggested mean value (870 MPa) in the Italian code (Ministry of Infrastructures and Transportation (MIT), 2009). However, the obtained Young's modulus is quite close (around 7% difference) to the Young's modulus that

Table 2.1 – Results of material tests on mortar and plaster samples.

Wall name	Building Mortar			Plaster – inner layer			Plaster – outer layer		
	f_{tmo} (MPa)	f_{cmo} (MPa)	E^* (MPa)	f_{tp} (MPa)	f_{cp} (MPa)	E^* (MPa)	f_{tp} (MPa)	f_{cp} (MPa)	E^* (MPa)
RSC1	1.28 ± 0.32 (25%, 26)	5.57 ± 1.06 (19%, 51)	352 ± 87 (25%, 51)	0.47 ± 0.05 (11%, 6)	1.40 ± 0.15 (11%, 12)	166 ± 43 (26%, 12)	1.69 ± 0.27 (16%, 6)	4.83 ± 0.56 (12%, 12)	325 ± 55 (17%, 12)
RSC2	1.29 ± 0.33 (26%, 23)	5.68 ± 1.07 (19%, 45)	358 ± 89 (25%, 45)						
RSC3	1.32 ± 0.32 (24%, 23)	5.77 ± 0.95 (16%, 45)	364 ± 85 (23%, 45)						
RSD1	1.41 ± 0.40 (28%, 21)	5.57 ± 1.45 (26%, 34)	431 ± 91 (21%, 34)						
RSD2	1.40 ± 0.45 (32%, 15)	5.25 ± 1.67 (32%, 22)	428 ± 82 (19%, 22)						
RSD3	1.39 ± 0.44 (32%, 18)	5.51 ± 1.56 (28%, 29)	413 ± 110 (27%, 29)						
RS1	0.70 ± 0.23 (32%, 22)	3.83 ± 0.66 (17%, 46)	317 ± 85 (27%, 46)	0.57 ± 0.07 (12%, 9)	1.45 ± 0.23 (16%, 18)	152 ± 52 (34%, 18)			
RS2	0.90 ± 0.25 (27%, 24)	4.28 ± 0.81 (19%, 45)	337 ± 82 (24%, 45)						
RS3	1.11 ± 0.16 (14%, 21)	5.17 ± 0.90 (17%, 38)	407 ± 64 (16%, 38)	0.48 ± 0.08 (16%, 6)	1.23 ± 0.33 (27%, 12)	153 ± 52 (34%, 12)			
RS4	1.07 ± 0.14 (13%, 21)	4.79 ± 0.56 (12%, 38)	390 ± 62 (16%, 38)						
RS5	1.02 ± 0.21 (20%, 18)	4.11 ± 0.76 (18%, 36)	386 ± 69 (18%, 36)	0.78 ± 0.21 (26%, 11)	2.25 ± 0.76 (34%, 22)	241 ± 54 (23%, 22)			
RS6	1.13 ± 0.17 (15%, 24)	5.05 ± 0.81 (16%, 40)	413 ± 76 (18%, 40)						
Total	1.09 ± 0.32 (29%, 165)	4.80 ± 1.09 (23%, 306)	378 ± 86 (22%, 306)	0.61 ± 0.19 (31%, 32)	1.68 ± 0.64 (38%, 64)	185 ± 65 (35%, 64)	1.69 ± 0.27 (16%, 6)	4.83 ± 0.56 (12%, 12)	325 ± 55 (17%, 12)

Notation: mean ± standard deviation (CoV: Coefficient of Variation, number of samples)
* E-modulus of mortar and plaster samples were computed as the slope between 1/3 and 2/3 of the compression strength.

was back-calculated from the shear compression test database (1110 MPa) in Vanin et al. (2017).

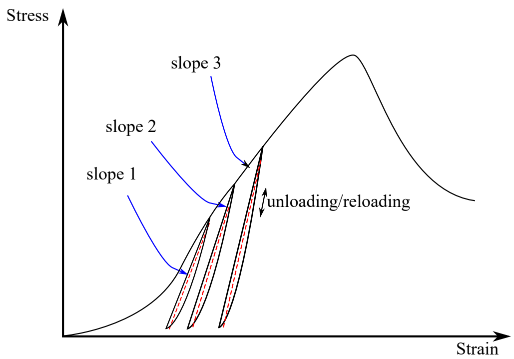

Figure 2.3 – Scheme of the determination of E-modulus in a compression test (Godio et al., 2019).

To obtain the tensile strength of masonry, diagonal-compression tests were performed on square wallettes. The test setup for diagonal compression tests (Figure 2.4) consisted of two V-shape steel shoes placed at the two corners of wallettes. The wallettes were rotated by 45 degrees and placed on the top of a steel beam. The force was applied vertically using a hydraulic actuator connected to the bottom steel beam, while the top beam was fixed. The

Table 2.2 – Results of simple compression tests on wallettes.

Wall name	E (MPa)	f_c (MPa)
RSC1	1604*	0.66
RSC2	1177	0.63
RSC3	792	1.00
	1191 ± 406 (34%)	0.76 ± 0.21 (27%)

Note: * based on only two cycles.
Notation: mean ± standard deviation (CoV)

deformation of wallettes was measured by taking images with two sets of a stereo camera at both sides of specimens and using the DIC method. In this test series, the applied load was increased monotonically. The tensile strength of the masonry was calculated as follows:

$$f_t = \alpha \frac{P_{max}}{A} \tag{2.1}$$

where P_{max} is the maximum applied vertical force, $A = (L + H)t/2$ is the net area of the specimen and α is the coefficient correcting for the stress state. Note that the interpretation of the diagonal compression test depends on the assumed stress state (Calderini et al., 2010; Brignola et al., 2008). Table 2.3 summarizes the computed tensile strength using various values for α that were suggested in the literature. For stone masonry walls of typology A, the tensile strengths included in the Italian code (Ministry of Infrastructures and Transportation (MIT), 2009) and Vanin et al. (2017) are 0.039 MPa and 0.045 MPa, respectively. According to Table 2.3, the coefficients suggested by ASTM (2002), RILEM (1991) and Frocht (1931) give tensile strength values for the herein-tested masonry that are larger than these reference values. However, the tensile strength is closer to the reference values when $\alpha = 0.35$, which is the value suggested by Brignola et al. (2008) for rubble stone masonry walls. This tensile strength is correspondingly 33% and 16% higher than the values suggested by the Italian code (Ministry of Infrastructures and Transportation (MIT), 2009) and Vanin et al. (2017), respectively. Additionally, the tensile strength is back-calculated using the Turnšek–Čačovič criterion in the next section; it will be shown that applying $\alpha = 0.35$ in the diagonal compression tests results in a better prediction of the tensile strength of the rubble stone masonry walls tested here. It must be pointed out that the testing method to obtain the tensile strength of masonry (Borri et al., 2015a) is a controversial topic as in previous studies, discrepancies were observed between tensile strengths obtained from in-situ tests and laboratory tests (Corradi, 2018). There are also some contradicting conclusions regarding the adequacy of using the reference shear parameters (based on which the tensile strength is calculated) in the Italian code (Ministry of Infrastructures and Transportation (MIT), 2009). Corradi (2018), by analyzing a database of in-situ tests on stone masonry wall panels, observed that the shear strength of masonry walls is overestimated by the Italian code (Ministry of Infrastructures and Transportation (MIT), 2009). On the other hand, Boschi et al. (2019) using the same methodology but a different database concluded that the reference shear strength of typology A proposed by the Italian code is smaller than the value obtained by the analysis of the in-situ experimental data. Therefore, the reported tensile strength should be treated with some caution. For a detailed discussion about the use of diagonal compression test to determine the tensile strength of masonry, refer to Segura et al. (2021) and Calderini et al. (2010).

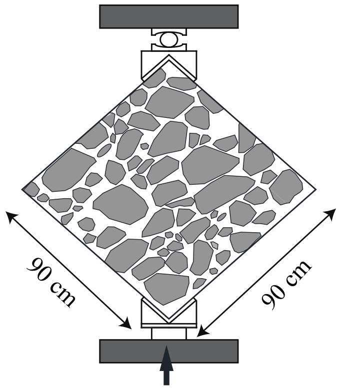

Figure 2.4 – Scheme of the test set-up of a diagonal compression test.

Table 2.3 – Results of diagonal compression tests on wallettes.

Wall name	f_t (MPa)		
	ASTM and RILEM (α=0.707)	Frocht (1931) (α=0.5)	Brignola et al. (2008) (α=0.35)
RSD1	0.088	0.063	0.044
RSD2	0.085	0.060	0.042
RSD3	0.142	0.100	0.070
	0.105 ± 0.032 (31%)	0.074 ± 0.022 (30%)	0.052 ± 0.016 (30%)

2.2.2 Test set-up and procedure

Figure 2.5 depicts the set-up for the shear compression tests. To apply the pre-compression load and the boundary condition, three servo-hydraulic actuators with a force capacity of ±1000 kN and a displacement capacity of ±500 mm were used. The forces were measured by load cells. The tests were performed in two phases. In the first phase, the axial load was applied through three loading/reloading cycles using two vertical actuators. In the second phase, horizontal displacements were applied following a loading protocol (Figure 2.6) in which two cycles were performed for each drift target level while the axial load was kept constant. To keep the height of the zero-moment constant along the moment profile, the two vertical actuators were force-controlled and were coupled to the force applied by the horizontal actuator, as described by Godio et al. (2019).The horizontal actuator was displacement controlled and the cyclic displacement loading protocol was applied. The target drift levels of the loading protocol were 0.025%, 0.05%, 0.10%, 0.15%, 0.20%, 0.25%, 0.30%, 0.40%, 0.50%, 0.60%, 0.80%, 1.00%, 1.50% and 2.00%. Testing was continued until axial load failure, i.e., until the wall could no longer carry the constant vertical load that was applied.

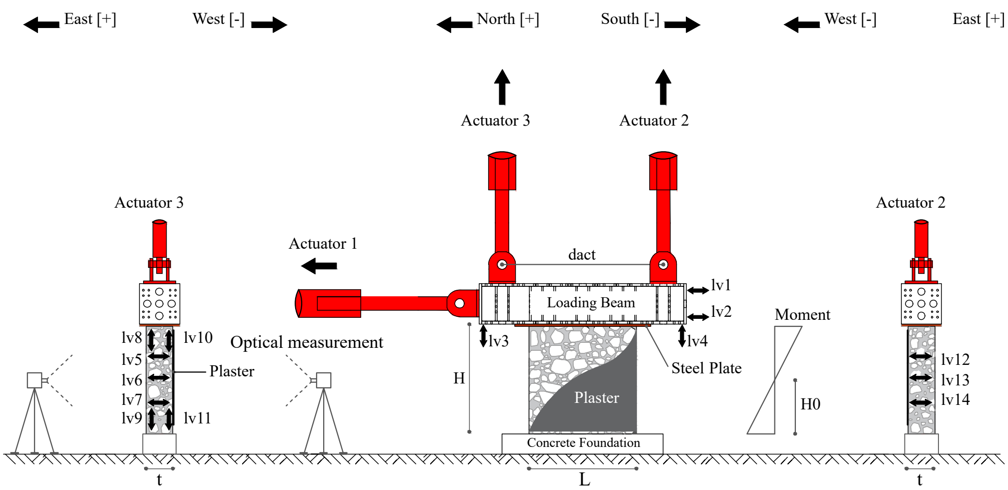

Figure 2.5 – Scheme of the test set-up of shear compression test and instrumentation.

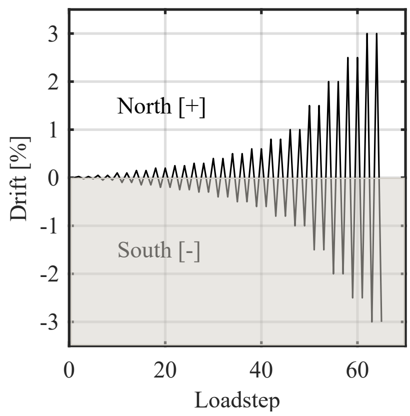

Figure 2.6 – Loading protocol.

In this study, the axial load ratio applied at the top of the wall ($\sigma_{v,top}/f_c$, where $\sigma_{v,top}$ is the vertical stress applied at the top of the wall) and accordingly at the bottom of the wall ($\sigma_{v,bot}/f_c$, where $\sigma_{v,bot}$ is the vertical stress at the bottom of the wall), and the height of zero-moment to height of the wall ratio (H_0/H) were varied for different tests as indicated in Table 2.4. The three axial load ratios correspond to average axial stresses between 0.06 and 0.19 MPa. This range was selected to increase the number of specimens tested under low and moderate levels of axial load ratios in the current database (see Figure 2.2c). For the H_0/H ratio, a value of 0.5 corresponds to a double-bending boundary condition. For a value of 1, the height of zero moment is at the top of the wall (i.e. lower edge of the steel plate, see Figure 2.5). For a value of 1.5, the height of zero moment is above the wall, i.e., the top and bottom moment have the same sign. A similar test design was used by Petry and Beyer (2015a) for tests on modern brick masonry walls.

Table 2.4 – Test matrix: Applied axial load and shear span ratio.

Wall name	H_0/H	N^*_{top}, $\sigma_{v,top}$, $\sigma_{v,top}/f_c$	N^*_{bot}, $\sigma_{v,bot}$, $\sigma_{v,bot}/f_c$
RS1	0.5	41 kN, 0.06 MPa, 8%	65 kN, 0.10 MPa, 13%
RS2	0.5	123 kN, 0.19 MPa, 25%	147 kN, 0.23 MPa, 30%
RS3	0.5	82 kN, 0.13 MPa, 17%	106 kN, 0.17 MPa, 22%
RS4	1.0	123 kN, 0.19 MPa, 25%	147 kN, 0.23 MPa, 30%
RS5	1.5	123 kN, 0.19 MPa, 25%	147 kN, 0.23 MPa, 30%
RS6	1.0	82 kN, 0.13 MPa, 17%	106 kN, 0.17 MPa, 22%

* N_{top} and N_{bot} are the total axial load applied at the top and bottom of the walls, respectively. N_{bot} corresponds to N_{top} plus the self-weight of the wall.

2.2.3 Instrumentation

In this testing campaign, two types of measuring systems were used: (i) classical hard-wired instruments to measure the forces and selected displacements and (ii) an optical measurement system that used digital image correlation (DIC) to measure the 3D displacement field on both sides of the wall.

The hard-wired instrumentation consisted of 14 linear variable differential transformers (LVDTs) denoted as “lv” and arranged as depicted in Figure 2.5. Four LVDTs (lv1-lv4) were used to monitor the loading beam movement during the tests. Two LVDTs (lv1 and lv2) measured the top and bottom horizontal displacement of the loading beam in regards to a reference column (Figure 2.5). Two further LVDTs (lv3 and lv4) at the two extremities of the beam were used to compute the rotation of the loading beam. These four LVDTs (lv1-lv4) were only used during the testing phase. LVDTs lv5-lv7 and lv12-lv14 were placed on the north and south sides of the walls to measure the separation of the leaves. The LVDTs were mounted approximately 400, 800 and 1200 mm above the wall base with a base length of around 25 cm. Additionally, to obtain local deformations of the compressed zones, four LVDTs (lv8-lv11) measured the vertical displacements on the north face of the walls. The forces applied by the three actuators were measured using load cells.

The optical measurements consisted of two stereo-camera systems placed on both sides of the wall that acquired high-resolution grey-scale images. The digital image correlation measurements followed the procedures suggested by the International Digital Image Correlation Society (2018) and included such techniques as preparing the surfaces with speckles, lightening the surfaces and appropriately calibrating the cameras. The average speckle dimension was 2 mm and the speckles were randomly sprayed on the wall faces (Figure 2.7). Additionally, some speckled patches were placed on the foundation, plate and loading beam to track their displacements (Figure 2.7). The cameras were calibrated by taking images before the test using a standard calibration target plate. To compute the 3D displacement field, the software VIC-3D version 8.2.4 (Correlated Solutions, 2018) was used. All horizontal displacements presented in Section 2.3 were derived from the DIC measurements.

(a) Plaster side

(b) Masonry side

Figure 2.7 – Preparing the wall façades for the digital image correlation (DIC) showing detail of the painting and random speckle.

2.3 Experimental Results

2.3.1 Cyclic response and bilinear idealization

The cyclic shear force-horizontal displacement/drift hystereses of the six tested walls are plotted in Figure 2.8. The horizontal displacement was computed as the average value of the horizontal displacements of the speckle patterns on the steel plate (Figure 2.5 and Figure 2.7). Figure 2.8 also depicts the envelope and bilinear curves, together with the hystereses. The envelope curves are derived by connecting data points corresponding to displacements that the wall experiences for the first time throughout the applied loading history (Godio et al., 2019), whereas the bilinear curves come from the effective stiffness and the ultimate drift and force of the envelope curves. The data points recorded after the axial load bearing capacity was reached are highlighted in red in Figure 2.8. The effective stiffness is computed as the secant stiffness at 70% of the peak force V_P; the ultimate drift is the drift at which the shear resistance has dropped by 20%V_P; and the ultimate force is defined such that the area under the bilinear curve is equal to the area under the envelope curve. The mentioned procedure was applied for all walls except RS5, as there was not a 20% drop of force in the negative direction. For this wall, the maximum drift that the wall reached was considered to be the ultimate drift. For RS5, the test was stopped at this point because the sudden occurrence of a diagonal crack and the sudden increase in vertical displacement indicated that wall collapse was imminent.

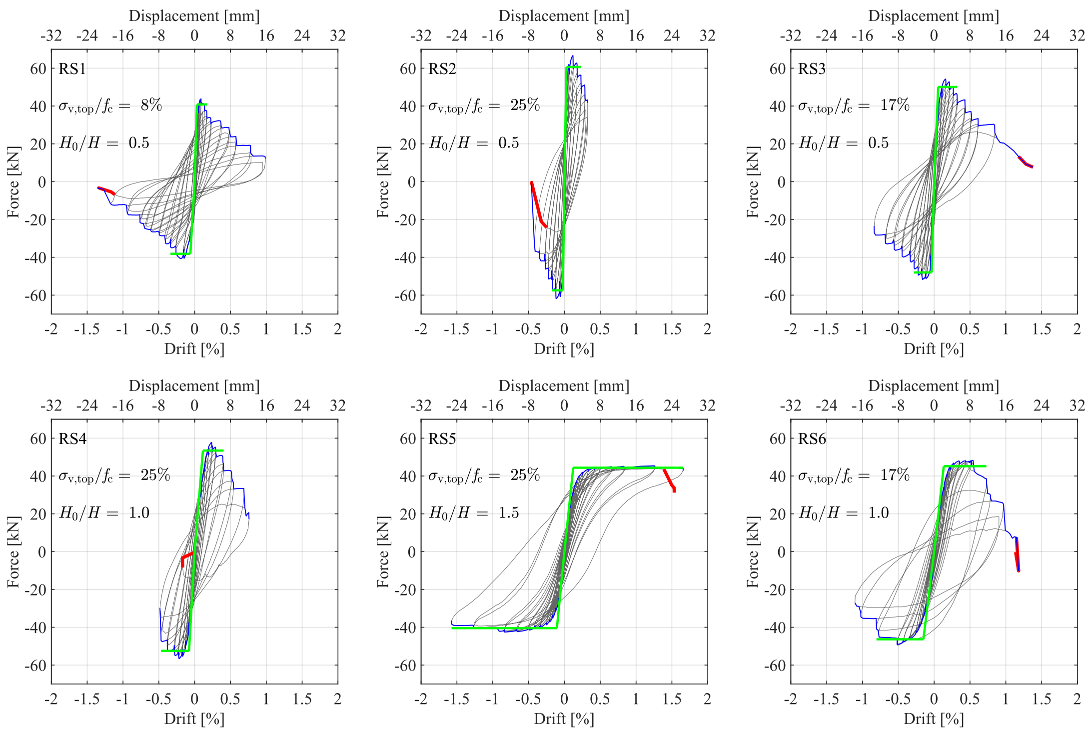

Figure 2.8 – Cyclic shear force-horizontal displacement/drift response. The plots also show the corresponding envelope curve (blue) and its bilinear idealization (green). The red-highlighted portion of the hysteretic response represents the phase at the end of the test when the wall could no longer sustain the axial load.

2.3.2 Failure mode

The evaluation of the progressive damage and the failure mode of the walls was based on a visual inspection during the tests, the analysis of the photographs that were taken and conclusions inferred from the shape of the hystereses of the walls (Figure 2.8). Two types of damage were considered in the evaluation. The first was the in-plane damage, i.e., damage that manifested itself through cracks in the masonry (east) and plaster (west) sides of the wall. The second was the development of out-of-plane deformation caused by an opening between the masonry leaves or by the detachment of the plaster from the masonry.

In-plane damage

Because the crack initiation was more visible on the plastered face (west), the observations presented here are mainly based on the crack pattern of the plastered face. However, at near collapse, the cracks also became apparent on the masonry side. Figure 2.9 and Figure 2.10 show the damage patterns at the last drift level before the axial load failure, i.e., before the wall could no longer carry the applied vertical load.

RS1

The wall RS1 was subjected to a double-bending moment profile and the lowest of the three axial load ratios ($\sigma_{v,top}/f_c$ = 8%). The first visible cracks, which appeared at a small drift demand (0.04%), were a horizontal crack at the interface between the wall and the foundation and a horizontal crack below the top row of stones. A diagonal crack started to form as the drift amplitude increased (drift = 0.15%). The diagonal cracks started at the centre of the wall and propagated towards the corners, suggesting that the behaviour changed from flexure-dominated to shear-dominated. This is supported by the loops of the hysteresis curves, which are narrow at small drift levels, confirming the flexure-dominated response. With increasing drift demands (from approximately 0.15% onwards), the loops widened and the behaviour was increasingly dominated by shear deformations.

RS2, RS3

The walls RS2 and RS3 were, as RS1, subjected to a double-bending moment profile, though with a higher axial load ratio, i.e., 25% and 17%, respectively. These two walls developed a very similar crack pattern, with first visible cracks appearing at the centre of the walls and propagating diagonally towards the corners at a 0.04% and 0.08% drift demand for RS2 and RS3, respectively. The high energy dissipation and high stiffness degradation observed in the post-peak regime of the hysteresis curves point towards a pure shear failure mode.

RS4

The wall RS4 was tested as a cantilever under an axial load ratio of 25%. Its cracking sequence was similar to that of RS1: First, a horizontal crack was observed along the interface between the wall and foundation (drift = 0.09%), and then diagonal shear cracks followed.

RS5

The wall RS5 was the only one tested with a shear span ratio of $H_0/H = 1.5$, and it was subjected to an axial load ratio of 25%. Like for walls RS1 and RS4, the first crack appeared at the interface between the wall and the foundation. For each loading direction, a horizontal crack developed at mid-height of the wall that changed to reach diagonally from the wall edge to the left and right bottom corners. At a drift demand of 1.39%, a sudden diagonal crack appeared, and the previous horizontal cracks closed, which marked the transition from a flexure-dominated to a shear-dominated response. This transition is also reflected in the hysteretic response, which is characterized by a nearly constant peak force over a large drift range. The appearance of the diagonal crack led to a sudden drop in the horizontal force in the positive direction (Figure 2.8). At this point, the vertical displacement also suddenly increased, and the test was therefore stopped.

RS6

The wall RS6 was tested as a cantilever with an intermediate axial load ratio of 17%. The first visible cracks were similar to those observed for RS1, RS4 and RS5 (horizontal cracks at the interface between the wall and foundation). As for RS5, two horizontal cracks appeared at mid-height at the extreme borders of the wall at a drift demand of 0.04%. At the final load steps (after 0.25%), a shear diagonal crack developed in the centre of the wall that extended towards the corners. This is also reflected in the hysteretic response, which began as a nearly elastic nonlinear response that indicated a rocking behaviour. At a drift of 0.25%, the hysteretic loops became fatter, indicating the onset of a shear failure.

Out-of-plane deformation

In this campaign, out-of-plane deformations due to either splitting cracks between the two masonry leaves (Figure 2.11a) and plaster detachment (Figure 2.11b) were observed. The deformations due to splitting cracks opening between the masonry leaves are reported in other experimental campaigns performed on multi-leaf stone masonry walls (Silva et al., 2014; Tomaževič et al., 2012; Milosevic et al., 2015; Wang et al., 2018). The delamination of the wall's wythes or buckling/out-of-plane bulging of the leaves is attributed to a poor connection between the leaves, the absence of through-stones and the outward pressure of infill material on the leaves (Quelhas et al., 2014; Decanini et al., 2004; Bothara and Brzev, 2012; Meyer et al., 2007).

The opening between the masonry leaves was recorded by LVDTs lv5-7 (north face) and LVDTs lv12-14 (south face), see Figure 2.5. Out-of-plane deformations of the east and west faces were also optically recorded. As an illustration, the displacements measured by the LVDTs placed on the north and south cross sections of wall RS2 are plotted in Figure 2.12. The opening between the leaves accumulated over the cycles and increased significantly after the 20% drop in horizontal force in the positive direction.

Table 2.5 summarizes the opening of the leaves at different levels of force in the post-peak regime for all the tested walls. In these tests, as the axial load increased, the opening of the leaves increased. Moreover, in general, the higher the shear span ratio, the larger the opening became. Assuming a no-tension elastic, perfectly plastic material law for a masonry wall, the compressed length at the base of the wall can be expressed as $l_c = 3(l/2 - VH_0/N)$ (Benedetti and Steli, 2008). Therefore, as the shear span ratio increased, the portion of the wall that was under compression decreased, which resulted in a higher compression stress. This might explain the positive correlation between shear span ratio and the opening of the leaves.

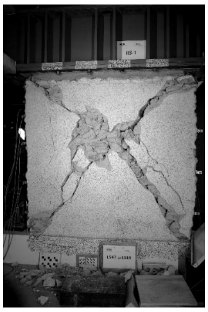

(a) RS1, drift = 0.95% [+]

(b) RS2, drift = 0.32% [+]

(c) RS3, drift = 0.84% [-]

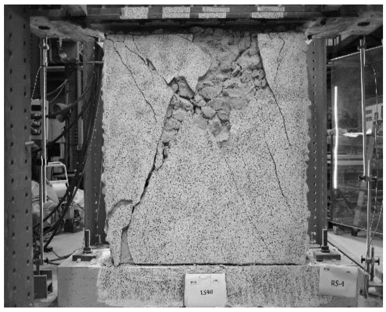

(d) RS4, drift = 0.75% [+]

(e) RS5, drift = 1.53% [+]

(f) RS6, drift = 1.10% [-]

Figure 2.9 – Damage pattern on the plaster side, indicating the drift and sign convention (positive: [←] and negative: [→]).

2.3.3 Initial, elastic and effective stiffness

Using the results of both simple and shear compression tests, the following values can be computed for the wall stiffness: the initial stiffness of the walls from the cyclic response (K_{init}^{exp}) defined as the secant stiffness at 15% V_P (Vanin et al., 2017); the initial (elastic) stiffness of the walls ($K_{init}^{Timoshenko}$) using the Timoshenko-beam model (Equation 2.2 and setting $G/E = 0.33$) (Vanin et al., 2017) and the Young's modulus obtained from the simple compression tests (Vanin et al., 2017); and the effective stiffness K_{eff} previously defined in subsection 2.3.1. According to Figure 2.13a showing the plot of the effective stiffness vs. axial load ratio at the base of the wall, the effective stiffness of the walls generally increased with the axial

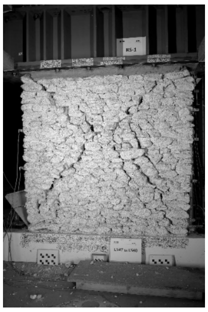

(a) RS1, drift = 0.95% [+]

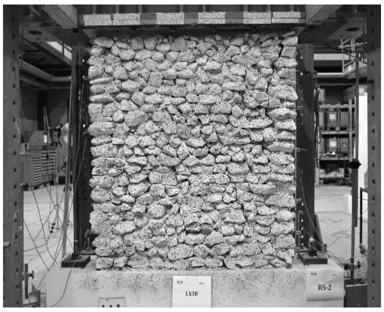

(b) RS2, drift = 0.32% [+]

(c) RS3, drift = 0.84% [-]

(d) RS4, drift = 0.75% [+]

(e) RS5, drift = 1.53% [+]

(f) RS6, drift = 1.10% [-]

Figure 2.10 – Damage pattern on the masonry side, indicating the drift and sign convention (positive: [→] and negative: [←]).

load ratio except for walls RS1 and RS3. In the literature, some experimental campaigns such as Vasconcelos (2005) observed a positive correlation between axial load ratio and the effective stiffness, whereas in others like Magenes et al. (2010), the trend is not marked. Further detailed explanation can be found in Vanin et al. (2017). Figure 2.13b illustrates the ratio of the effective to initial stiffness. The mean of K_{eff}/K_{init}^{exp} is 0.59. This is 18% and 9% higher than 0.50, which is the value recommended by Eurocode 8 - Part 3 (2005), and 0.54, which was obtained from the analysis of the database of shear compression tests performed by Vanin et al. (2017). The ratio of $K_{eff}/K_{init}^{Timoshenko}$ vs. axial load ratio is depicted in Figure 2.13c. The mean of the $K_{eff}/K_{init}^{Timoshenko}$ values is 0.49, which is quite close to 0.50 (Eurocode 8 -

(a) (b)

Figure 2.11 – Examples of (a) splitting cracks in the cross section (RS6, drift = 1.08%); and (b) plaster detachment (RS4, drift = 0.75%).

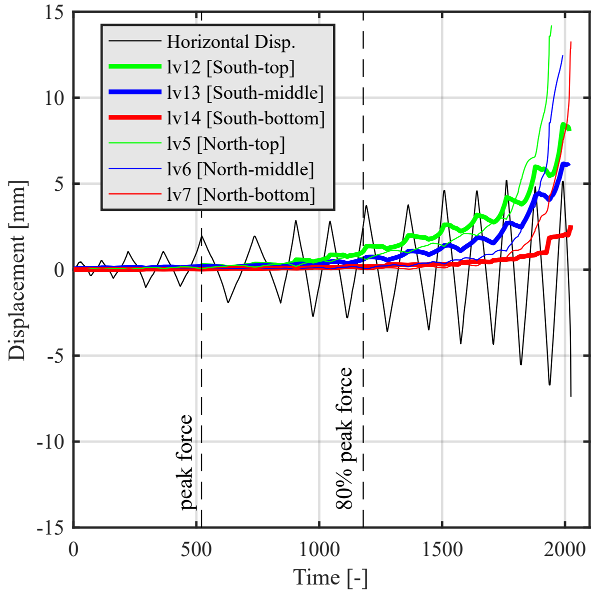

Figure 2.12 – Opening between the leaves of the wall RS2.

Part 3, 2005), although the variance in the results is high (CoV = 54%). The shaded area in Figure 2.13 shows one standard deviation above and below the mean. Comparing Figure 2.13b and Figure 2.13c, one can see that using Young's modulus as determined from the compression tests to calculate the elastic stiffness of the walls resulted in a less robust estimation of effective stiffness because the effect of axial load ratio on the E-modulus was not considered. Moreover, the elastic stiffness obtained using the E-modulus from the compression tests overestimated the actual initial (elastic) stiffness of the walls (i.e., on average $K_{init}^{exp}/K_{init}^{Timoshenko} < 1$, as the mean of $K_{eff}/K_{init}^{exp} = 0.59$ is higher than the mean of $K_{eff}/K_{init}^{Timoshenko} = 0.49$). This finding

Table 2.5 – Opening of the leaves in mm.

Wall name	V_p	$0.80V_p$	$0.75V_p$	$0.70V_p$	$0.65V_p$
RS1	0.0	0.0	0.0	0.0	0.1
RS2	0.2	1.4	2.0	2.6	4.0
RS3	0.1	1.0	1.0	2.4	2.8
RS4	0.4	8.2	*	*	*
RS5	2.3	*	*	*	*
RS6	0.1	0.1	13.8	*	*

Note: *These values were higher than the LVDT measurement range (~20 mm)

is not in accordance with what Vanin et al. (2017) reported.

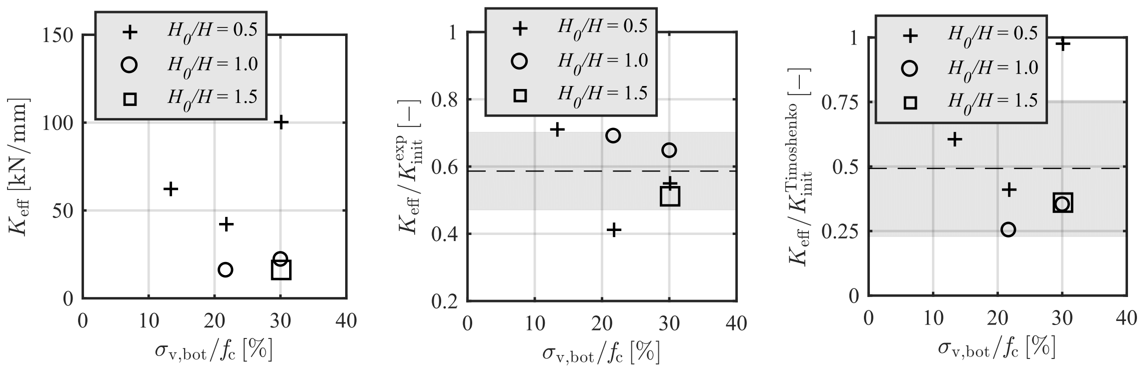

Figure 2.13 – For RS1–6, (a) effective stiffness; (b) effective to initial stiffness ratio (mean of 0.59 and CoV of 20%); and (c) effective to elastic stiffness (mean of 0.49 and CoV of 54%) vs. axial load ratio.

The E-modulus can also be back-calculated from the second phase of the shear compression test, i.e., the application of the horizontal load, using a Timoshenko-beam model (Vanin et al., 2017):

$$E = K\frac{6 \times H(1 + G/E \times H^2/L^2 \times 5 \times (H_0/H - 1/3))}{5 \times L \times t \times G/E} \tag{2.2}$$

The E-modulus is calculated by setting $G/E = 0.33$ (Vanin et al., 2017) and $K = K_{init}^{exp}$. The mean and CoV of the E-modulus are 1039 MPa and 57%, respectively, which is 6% lower than the value computed by Vanin et al. (2017) (1110 MPa) and 20% higher than the average value recommended by the Ministry of Infrastructures and Transportation (MIT) (2009) (870 MPa). To compare the initial E-modulus obtained from the simple compression tests and the one back-calculated from the shear compression tests, the mean of the two methods is plotted in Figure 2.14. The blue and black lines represent the average of the E-modulus value from the simple compression (1191 MPa) and shear compression (1039 MPa) tests, respectively. The obtained Young's modulus estimates were rather close, which suggests that obtaining the initial stiffness by performing three loading/reloading cycles in the simple compression tests results in a robust approximation of the Young's modulus. These conclusions are, of course, limited to the axial load ratio range covered in this test series, i.e., $\sigma_{v,top}/f_c$ between 8–25%. The values of initial and effective stiffness, Young's modulus and the ratio of the effective to initial stiffness of the walls are summarized in Table 2.6.

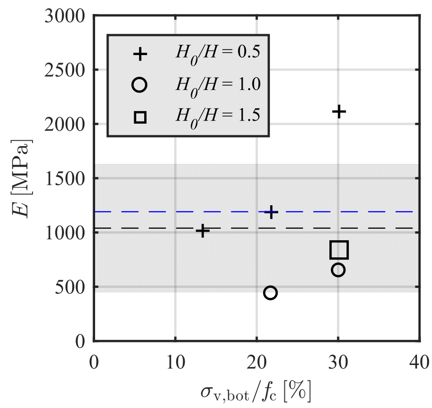

Figure 2.14 – Plot of E-modulus vs. axial load ratio. The blue and black dashed lines are the average of the E-modulus from the simple compression and shear compression tests, respectively. The shaded area shows one standard deviation above and below the mean.

Table 2.6 – Initial and effective stiffness, Young's modulus and the ratio of effective to initial stiffness of the walls.

Wall name	K_{init}^{exp} [kN/mm]	K_{eff} [kN/mm]	E [MPa]	K_{eff}/K_{init}^{exp} [-]
RS1	88	62	1016	0.71
RS2	182	100	2114	0.55
RS3	102	42	1187	0.41
RS4	34	22	647	0.65
RS5	32	16	839	0.51
RS6	22	16	436	0.69

2.3.4 Peak and ultimate shear force

Figure 2.15a compares the peak shear forces (V_p) obtained in the positive and negative loading directions. The similarity in these values confirms the quality of the testing set-up. In Figure 2.15b, the average peak shear force is plotted against the axial load ratio. The peak shear force increases as the axial load ratio increases and decreases as the shear span increases.

These trends are well known in the literature and are captured by standard shear force capacity models for masonry walls (Vanin et al., 2017; Godio et al., 2019; Eurocode 8 - Part 3, 2005; Magenes et al., 2010). Another value that is of interest is the ratio of the average ultimate force (V_u) to the average peak shear force, as shown in Figure 2.15c. The mean of V_u/V_p is almost 0.94, which is close to the value found by Tomaževič (1999) for masonry walls and the values obtained from experimental tests on rubble stone masonry walls by Milosevic et al. (2015) ($V_u/V_p = 0.90$). The results of V_p and V_u/V_p are summarized in Table 2.7.

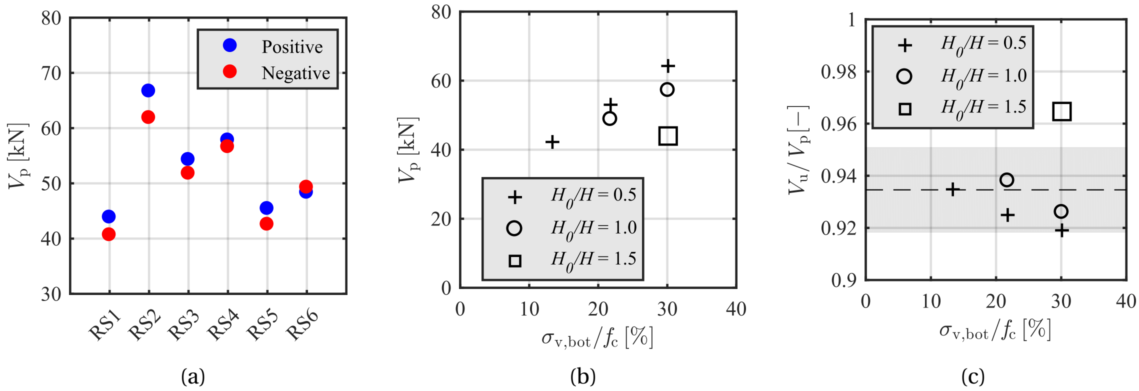

Figure 2.15 – For RS1–6, the (a) peak force for the positive and negative loading direction; (b) average peak force as a function of the axial load ratio at the base of the wall; and (c) the ratio between average ultimate force and average peak force vs. axial load ratio as a function of the axial load ratio at the base of the wall.

Table 2.7 – Peak force and the ratio of ultimate force to peak force.

Wall name	V_P [kN]		V_u/V_P [-]
	Positive	Negative	
RS1	43.8	40.6	0.93
RS2	66.7	61.9	0.92
RS3	54.3	51.8	0.93
RS4	57.8	56.6	0.93
RS5	45.4	42.5	0.96
RS6	48.3	49.3	0.94

Assuming that the Turnšek–Čačovič (Turnšek and Čačovič, 1971) and Coulomb criteria can estimate the force capacity of masonry walls reasonably well, the tensile strength, friction coefficient and cohesion of the masonry can be back-calculated by fitting these models to the experimental data. This was done by fitting the models to the experimental values for the peak strength V_P and ultimate strength V_u.

The Turnšek–Čačovič criterion is expressed as:

$$V_{TC} = \frac{Lt}{b} f_t \sqrt{1 + \sigma_{v,mid} / f_t} \tag{2.3}$$

where f_t is the tensile strength of masonry, $\sigma_{v,mid}$ is the vertical stress at mid-height of the wall and $b = H/L$ (Benedetti and Tomaževič, 1984). By fitting the model to the experimental data (except for RS5 that exhibited a rocking behaviour) and setting $V_{TC} = V_P$ (see Figure 2.16), the tensile strength was estimated to be 0.036 MPa, which is only 8% lower than the value suggested by the Ministry of Infrastructures and Transportation (MIT) (2009). The tensile strength back-calculated from the shear-compression tests was lower than the value obtained from the diagonal compression tests using $\alpha = 0.35$. The difference can be attributed to the difference between the tensile strength of the mortar used for the construction of the RSD wallettes (1.4 MPa) and the RS walls (1.0 MPa). Additionally, by setting $V_{TC} = V_u$, the tensile strength was computed to be 0.031 MPa (see Figure 2.16).

The Coulomb criterion (Eurocode 8 - Part 3, 2005) dictates:

$$V_{MC} = Lt\left(\frac{1.5c + \mu\sigma_{v,bot}}{1 + \frac{3cH_0}{\sigma_{v,bot}L}}\right) \tag{2.4}$$

in which c and μ are the characteristic cohesion and friction coefficients of masonry, respectively. By fitting the Coulomb criterion to all data points except RS5 and setting $V_{MC} = V_P$ (see Figure 2.16), c and μ were calculated to be 0.036 MPa and 0.34, respectively. The cohesion was estimated by $c = 2\mu f_t$, with $\mu = 0.4$ (from Eurocode 8 - Part 3 (2005)) and $f_t = 0.039$ MPa (from the Ministry of Infrastructures and Transportation (MIT) (2009)), to obtain a value of 0.031 MPa, which was close to the estimated cohesion from the test (0.036 MPa, 16% difference). The obtained friction coefficient was 15% less than the value of 0.4 that was proposed by Eurocode 8 - Part 3 (2005) for modern masonry. Furthermore, considering $V_{MC} = V_u$, the cohesion and coefficient of friction were calculated to be 0.035 MPa and 0.30, respectively (see Figure 2.16).

2.3.5 Drift limits

For each of the walls, the drifts were determined at six limit states defined in Vanin et al. (2017), which are δ_{cr}, drift at the onset of cracking; δ_y, drift at yield, defined in subsection 2.3.1; δ_p, drift at peak force; δ_{SD}, drift at Significant Damage limit, defined as $\delta_{SD} = \min(3\delta_{cr}, \delta_p)$; δ_u, ultimate drift, defined in Section 2.3.1; and δ_c^*, drift at 50% drop in force. Additionally, the drift at collapse δ_c is defined and discussed here.

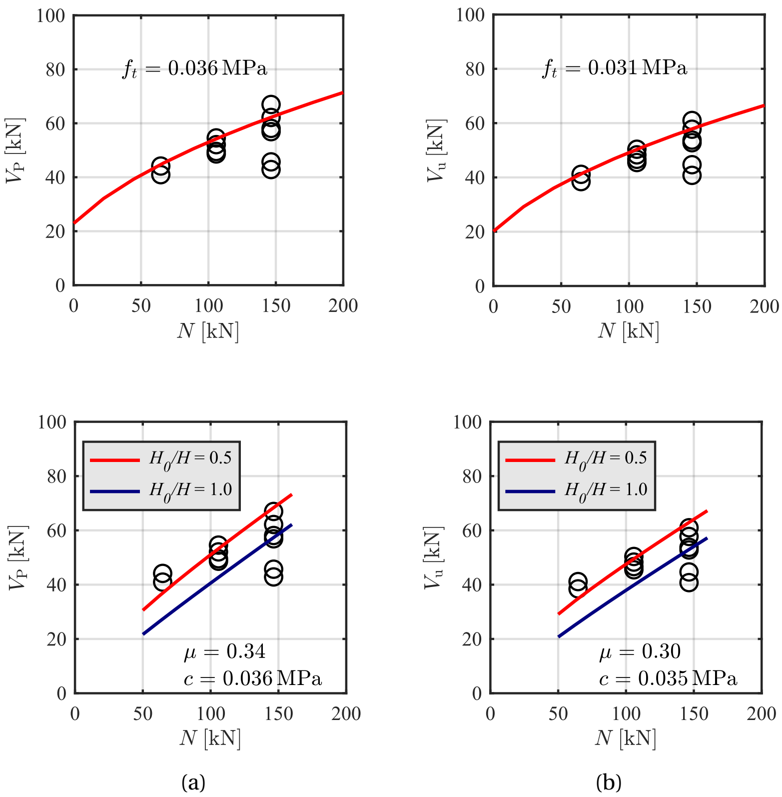

Figure 2.16 – Fitted criteria for predicting (a) peak force and (b) ultimate force. Top row: Turnšek–Čačovič criterion; Bottom row: Coulomb criterion

Drift limits before the axial load failure

In Figure 2.17, the drift values obtained for RS1–6 are plotted against the axial load ratio and compared to the models proposed by Vanin et al. (2017). Because horizontal cracks appeared at an early stage of horizontal loading in all walls except RS2 and RS4, the drift at the onset of cracking (δ_{cr}) increased with the axial load ratio, since a higher axial load ratio delays the decompression of the section. Figure 2.17a shows that the first cracks were observed at about half the drift value reported by Vanin et al. (2017). The following two reasons might explain this difference: First, in the previous experimental campaigns (based on which Vanin et al. (2017) proposed this limit), the cracking was reported via visual inspection at each drift target (when the test was stopped), while images of the cracking were inspected in the current campaign. The location at which the first crack was likely to appear was identified using the displacement and maximum principle strain fields derived from DIC to make sure that no crack was overlooked. Second, in previous experimental campaigns, none of the sides were plastered such that the visual inspection was carried out on unplastered masonry, which makes it much more difficult to spot the cracks. In the current campaign, crack initiation was detected on the plastered side. Table 2.8, which summarizes the drift limits, reports the drifts at the appearance of two types of cracks, horizontal (flexural) and diagonal (shear). In

Figure 2.17a, the smaller of the two values is plotted.

The overall correlation between the drift at yield, at peak force, at ultimate limit state and at a 50% drop in force and the axial load ratio was negative, which was expected and also observed in other test campaigns (Vanin et al., 2017; Godio et al., 2019; Petry and Beyer, 2015a). In fact, a higher axial load ratio leads to an increased wall stiffness that causes both the maximum force to be reached at a lower drift and the force degradation in the post-peak regime to be accelerated, leading to a lower ultimate drift (Petry and Beyer, 2014a). The correlation between the drift at the significant damage limit state and the axial load ratio, however, seems to be zero. Keeping the axial load ratio constant for walls RS3-RS6 and RS2-RS4-RS5 while changing the shear span ratio shows that the ultimate drift increases with an increasing shear span ratio (Figure 2.17), which can be the result of additional flexural cracks. The same trend was observed in other test campaigns, such as tests on brick masonry walls with different boundary conditions by Petry and Beyer (2015a). According to Figure 2.17, it seems that the formula suggested in Vanin et al. (2017) for estimating the drift at a 50% drop in force ($\delta_c^* = 1.15\delta_u$) underestimates this drift limit. The same observation can be made from the experimental results in Godio et al. (2019).

Table 2.8 – Drift values of RS1-RS6 at various limit states.

Wall name	δ_{cr} [%]		δ_y [%]		δ_p [%]		δ_{SD} [%]	δ_u [%]		δ_c^* [%]		δ_c [%]	
	Flexural crack	Shear crack	Pos.	Neg.	Pos.	Neg.	-	Pos.	Neg.	Pos.	Neg.	Pos.	Neg.
RS1	0.04	0.15	0.03	0.06	0.09	0.19	0.09	0.17	0.34	0.59	0.76	0.99	1.18
RS2	-	0.04	0.03	0.02	0.12	0.12	0.12	0.23	0.18	-	-	0.32	0.42
RS3	-	0.08	0.06	0.03	0.16	0.16	0.16	0.32	0.28	0.85	-	1.17	0.84
RS4	0.09	0.11	0.12	0.08	0.24	0.22	0.22	0.41	0.47	0.70	-	0.76	0.48
RS5	0.06	-	0.12	0.10	1.26	0.84	0.19	1.66	1.57	-	-	1.66	1.57
RS6	0.04	0.25	0.13	0.15	0.53	0.52	0.11	0.73	0.81	0.99	-	1.15	1.11

It should be noted that there was an error in the column δ_{SD} in the published article . These values are corrected here.

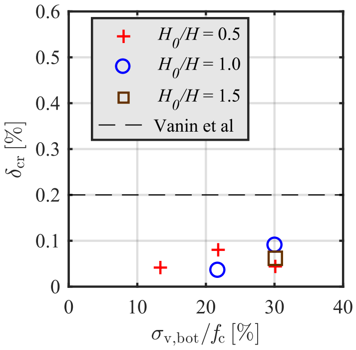

(a) Drift at plaster cracking

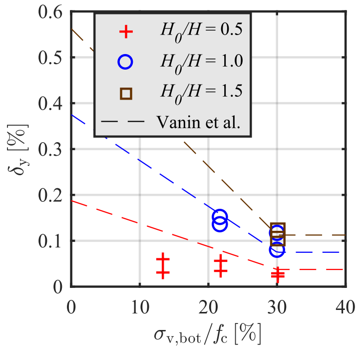

(b) Drift at yield

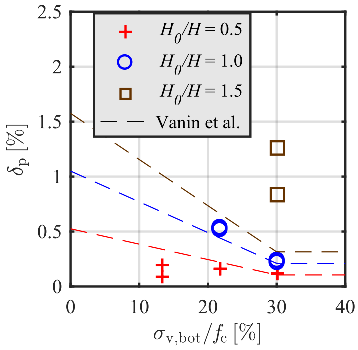

(c) Drift at peak force

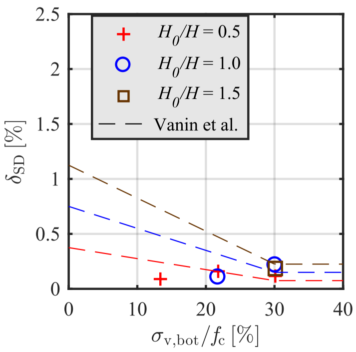

(d) Drift at Significant Damage limit state

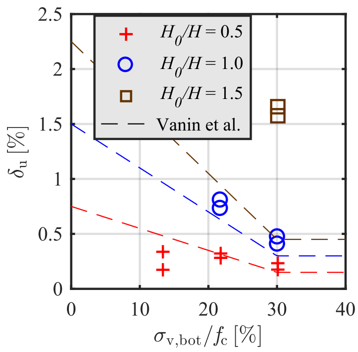

(e) Drift at ultimate limit state

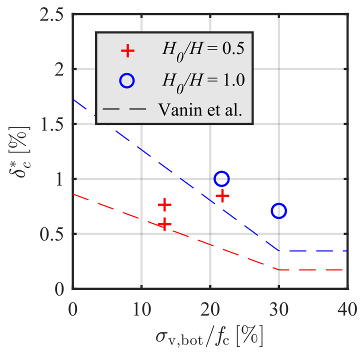

(f) Drift at 50% drop in force

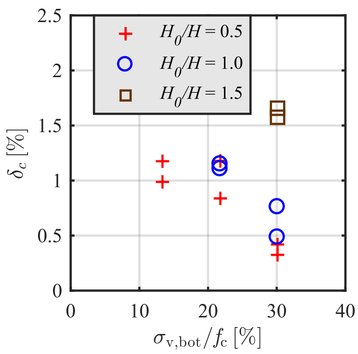

(g) Drift at collapse

Figure 2.17 – Comparison between the drift limits obtained from the tests and those in the models proposed by Vanin et al. (2017).

Drift at the axial load failure

In this test series, the walls were loaded up to the loss of their axial load-bearing capacity. Data about this parameter is scarce for any masonry typology, with walls tested up to failure in only a few examples, including a test series on single-leaf stone masonry walls with dressed rectangular stones by Godio et al. (2019), a test series on three-leaf stone masonry walls by Silva et al. (2014) and a test series on modern hollow clay brick unit masonry by Petry and Beyer (2015a). Due to the absence of such data for stone masonry, Vanin et al. (2017) used the drift at 50% drop in force as a proxy for the drift at collapse. Despite this approximation, such data was only available for 7 of the 67 walls contained in the database, as most of the campaigns reported in the literature were stopped at a 20% drop in force. The axial load failure is herein defined as the point in the test at which a sudden drop of axial force is recorded and the wall can no longer support the axial load to which it was subjected. This point is illustrated in Figure 2.18 and Figure 2.19, where the shear vs. axial force and the vertical displacement vs. drift are plotted, respectively. The drift corresponding to this situation, called drift at collapse δ_c, is defined as the maximum absolute drift that the wall can resist up to this point. In Figure 2.18 and Figure 2.19, the data points recorded before and after the occurrence of axial load failure are depicted as black and red, respectively. The values of δ_c for walls RS1–RS6 are summarized in Table 2.8.

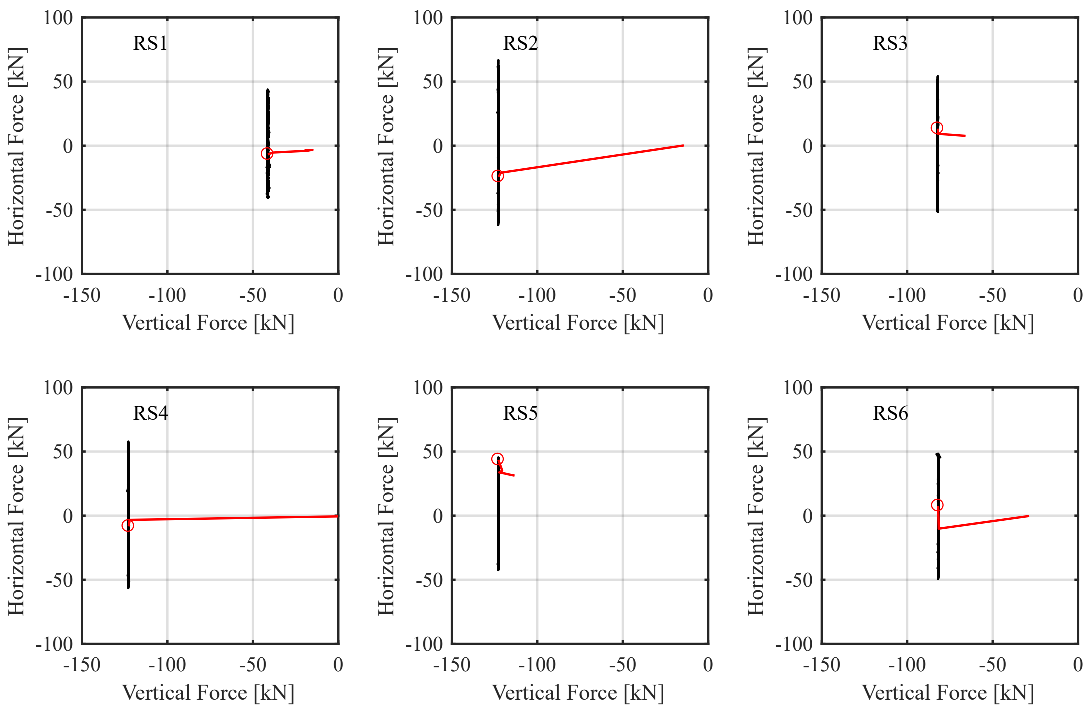

Figure 2.18 – Horizontal force vs. vertical force. The red part of the curve represents the phase at the end of the test when the wall could no longer sustain the axial load. The red circle marks the beginning of this phase.

Very little literature data is available for the drift at axial load failure (δ_c), though much more is available for the ultimate drift (δ_u), making the ratio between the two drifts of particular interest for studies on the collapse risk of buildings. This ratio would provide an indication of the reserve displacement capacity between the horizontal and axial load failure of a pier.

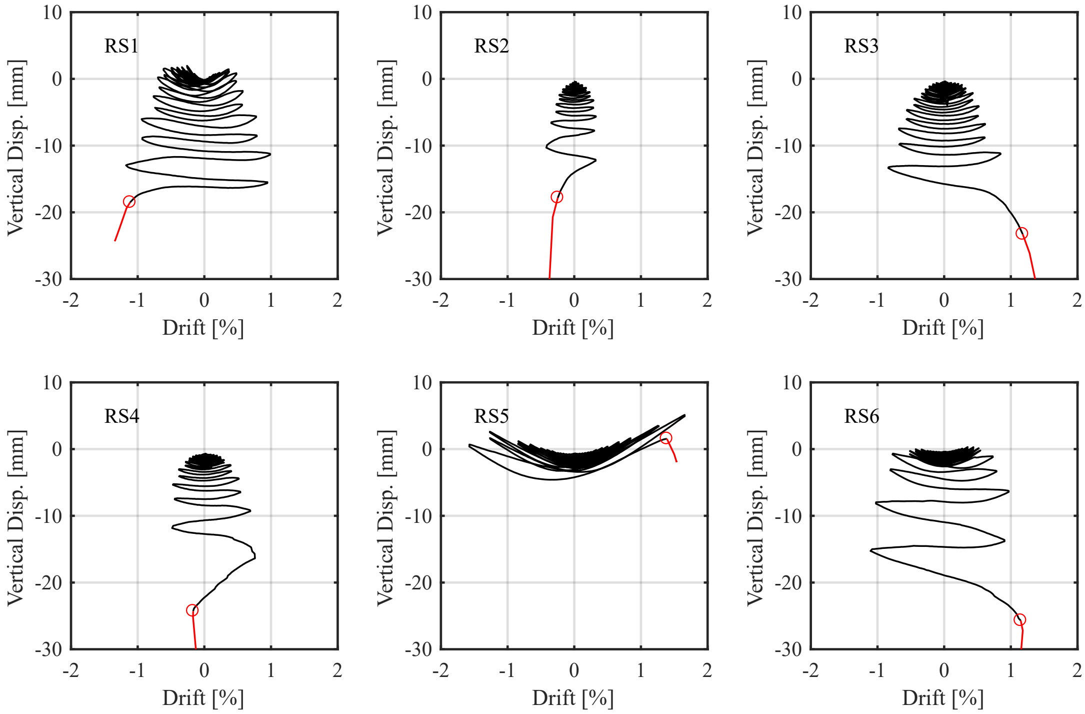

Figure 2.19 – Vertical displacement vs. drift. The red part of the curve represents the phase at the end of the test when the wall could no longer sustain the axial load. The red circle marks the beginning of this phase.

Figure 2.20a plots the ratio δ_c/δ_u against the axial load ratio for the three test series in which testing was continued up to axial load failure. With an increasing axial load ratio, the δ_c/δ_u ratio decreases. Because δ_u also decreases with an increasing axial load ratio, the delta difference between the ultimate drift and the one at axial load failure decreases with an increasing axial load ratio. Figure 2.20a shows that, for a given axial load ratio, these ratios are higher for rubble stone masonry (current tests) than for stone masonry walls with well-dressed stones that have a regular texture (tests by Godio et al. (2019)). While the trend for the axial load ratio is very evident, the scatter of the ratios at a given axial load ratio is considerable. The smallest δ_c/δ_u ratio is 1.0 for rubble stone masonry and 1.2 for stone masonry walls with a regular texture. Very small ratios between 1.0 and 1.5 are obtained for hollow clay brick masonry walls (tests by Petry and Beyer (2015a)). This is attributed to the brittleness of the brick units under compression. Figure 2.20b depicts the δ_c^*/δ_c ratio, showing that this ratio varies between 0.46 and 1.0 and tends to increase with an increasing axial load ratio. The parameter δ_c^* therefore appears to be a biased proxy of the drift at collapse—for high axial load ratios, it estimates the drift at collapse well, whereas for low axial load ratios, it significantly underestimates it. For modern brick masonry walls, the available data suggests that δ_c^* leads to a good approximation of the actual collapse drift.

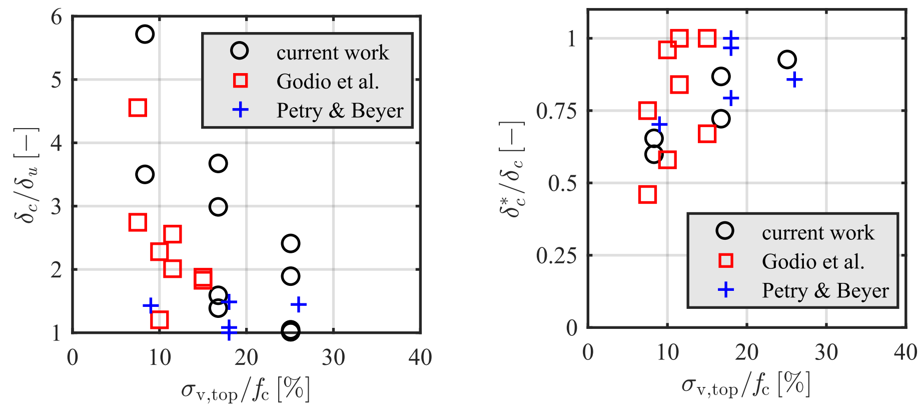

Figure 2.20 – Plot of δ_c/δ_u and δ_c^*/δ_c vs. axial load ratio.

2.4 Conclusions

Six quasi-static shear-compression tests on rubble stone masonry walls with plaster were conducted at École Polytechnique Fédérale de Lausanne (EPFL). The tests were designed to determine the influence of static boundary conditions, herein idealized in terms of the shear span ratio and the axial load ratio, on the in-plane behaviour of rubble stone masonry walls. This is especially relevant to the stiffness, force capacity and drift at different limit states, which are the key parameters characterizing wall behaviour in performance-based seismic assessment methods. The focus was on the drift capacity at the loss of axial load bearing capacity, shortly denoted as axial load failure, for which the available literature data is particularly scarce. The main findings of the paper are summarized as follows:

- The Young's modulus of the masonry walls back-calculated from the shear-compression test using a Timoshenko beam model (1039 MPa) was quite close to the value obtained from the simple compression test (1191 MPa), which supports the practice of deriving the Young's modulus from simple compression tests. The obtained values from both approaches were close to the upper bound of the range (690–1050 MPa) recommended by the Ministry of Infrastructures and Transportation (MIT) (2009).

- The effective stiffness of the walls tended to increase with increasing axial load, which is in agreement with the findings in Vanin et al. (2017). Additionally, the average ratio of effective to initial stiffness (K_{eff}/K_{init}^{exp}) of the walls was 0.59, which is only 9% higher than 0.54 obtained from analysing a database of shear compression tests on stone masonry walls by Vanin et al. (2017). The K_{eff}/K_{init}^{exp} ratio mainly decreased with axial load ratio, though no clear trend could be detected between this ratio and the H_0/H ratio.

- The tests of the present campaign confirmed that both codified models for the force capacity of the walls, i.e. Turnšek–Čačovič and Coulomb, could estimate the peak force on a different range of axial loads and shear spans rather well when the correct tensile strength, cohesion and coefficient of friction of rubble stone masonry were assumed. These properties were back-calculated by fitting the models to the experimental data. A comparison with code values showed that the tensile strength of 0.039 MPa suggested by the Ministry of Infrastructures and Transportation (MIT) (2009) for rubble stone masonry slightly overestimated the tensile strength of the herein-tested walls. Additionally, the coefficient of friction of 0.4 for modern masonry suggested by Eurocode 8 - Part 3 (2005) is slightly higher than the value back-calculated from the experimental results.

- In addition to the in-plane cracking typically observed in walls tested under shear compression, i.e., shear tension and flexural cracks, bulging of the wall leaves was observed. These out-of-plane deformations continuously increased during the test and became significant in the post peak regime. An increase in the axial load and/or the shear span ratio led to a larger opening between the wall leaves. The largest opening was therefore observed for the test unit RS5, which was subjected to the largest axial load ratio (25%) and the largest shear span ratio ($H_0/H = 1.5$).

- The tests confirmed previous findings regarding the influence of the axial load ratio and the shear span ratio on the drifts at various limit states as the drift at yield, at peak force, at ultimate state and at 50% drop in force decreased with an increasing axial load ratio and increased with an increasing shear span. The obtained drift capacities were compared to the empirical drift capacity models proposed by Vanin et al. (2017) for stone masonry walls. The suggested models predict the drift at yield, at peak force and at ultimate limit state rather well, though failed in predicting the drift at the onset of cracking, at the significant damage state, which is defined as a function of the drift at the onset of cracking and at peak force $\delta_{SD} = \min(3\delta_{cr}, \delta_p)$, and at a 50% drop in force. The drift at the onset of cracking was only approximately half the value reported in previous campaigns, on which the drift capacity model in Vanin et al. (2017) is based. This is attributed to two effects: (i) One of the faces of the walls tested here was plastered. Cracks are more visible on the plastered side than on the masonry side and can therefore be detected at much lower drift values. (ii) Additionally, unlike in other test series, DIC results were used herein to identify the likely location of a crack, which was then identified visually from images to ensure that cracks were not overlooked. Both differences probably led to the fact that cracks were identified at lower drift levels than in previous campaigns.

- Next to the general objective of providing more data on the in-plane behaviour of rubble stone masonry walls, this test series was designed to yield information on the deformation capacity at collapse. The tests were therefore continued up to the point when the walls could no longer sustain the applied axial load. A comparison of this data with the very few other series that had been tested up to this point led to the following conclusions: As at the other drift limits, the drift at collapse decreases with an increasing axial load ratio. The drift at a 50% drop in force, which was considered a proxy of the drift at collapse in a previous study, yields a biased estimate for the drift at collapse because the ratio of δ_c^*/δ_c varies with the axial load ratio. For low axial load ratios, δ_c^* was found to be only about half the drift at collapse. The delta in drift $\delta_c - \delta_u$ decreases strongly with axial load ratio, i.e., for walls subjected to high axial load ratios, the collapse occurs soon after horizontal load failure (δ_u), while for low axial load ratios, a considerable margin between the two limit states exists. This margin is much larger for stone masonry than for modern brick masonry, where brittle unit failure occurs.

In this testing campaign, one single specimen was tested per a combination of axial load ratio and shear span ratio. More experimental tests are certainly required to have an estimate of the confidence interval related to the obtained data points. The variability of experimental test results with regard to stiffness, strength and drift capacity of stone masonry elements was evaluated in Vanin et al. (2017). It showed that for typology A, the literature lacks results of repeated quasi-static cyclic test results and this should be addressed in the future. It is also known that laboratory test provides results that can be different from in-situ tests; comparing the results of laboratory tests with in-situ tests systematically would allow the results of this campaign to be put further into a real context.

Acknowledgments

The project is supported by the Swiss National Science Foundation (grant 200021_175903/1 “Equivalent frame models for the in-plane and out-of-plane response of unreinforced masonry buildings”). The authors thank the technicians of the Structural Engineering Laboratory at EPFL and the master students, Loris Silva Brites and Alexandre Norcaro for their help with the testing.

3 Crack detection on laboratory images

This chapter represents the slightly modified post-print version of the article:

Rezaie, A., Achanta, R., Godio, M. and Beyer, K., 2020. “Comparison of crack segmentation using digital image correlation measurements and deep learning”. *Construction and Building Materials*, 261, p.120474.

The formatting and numbering of equations, tables and figures have been adapted to this document. The contributions of the first author are: Methodology, Validation, Formal analysis, Investigation, Data curation, Writing - original draft, Writing - review and editing, Visualization, writing the article. Contributions of the second author: Conceptualization, Methodology, Resources. Contributions of the third author: Investigation, Writing - original draft, Writing - review and editing, Visualization. Contributions of the forth author: supervision of the first author, Conceptualization, Methodology, Investigation, Resources, Writing - original draft, Writing - review and editing, Funding acquisition.

Abstract

Reliable methods for detecting pixels that represent cracks from laboratory images taken for digital image correlation (DIC) are required for two main reasons. Firstly, the segmented crack maps are used as an input for some DIC methods that are based on discontinuous fields. Secondly, detected crack patterns can serve as inputs for predictive empirical models to obtain the level of damage to a body. The aim of this paper is to compare the performance of two approaches for crack segmentation on grayscale images acquired from two experimental campaigns on stone masonry walls. In the first approach, a threshold is applied to the maximum principal strain map calculated using post-processed DIC results. In the second approach, a deep convolutional neural network is used. The two methods are compared in terms of standard segmentation criteria, namely precision, dice coefficient and sensitivity. It is shown that the precision and dice coefficient obtained from the deep learning approach are much higher than those obtained from the threshold method (by almost 47%

and 34%, respectively). However, the sensitivity computed from the deep learning method is slightly (~4%) lower than the threshold method. These results show that the deep learning method can better preserve the geometry of detected crack patterns, and the prediction in terms of pixels belonging to a crack is finally more accurate than the threshold method. The dataset of crack images and corresponding ground-truth masks is publicly available here: https://doi.org/10.5281/zenodo.4307686

Keywords: Crack segmentation; Digital image correlation; Deep learning; Threshold method; Masonry.

3.1 Introduction

Digital image correlation (DIC) is an optical measurement technique widely used in experimental mechanics to compute the deformation of a body (Peters and Ranson, 1982; Sutton et al., 2009). For the local subset DIC, images of a sample are compared at a regular time interval. In this process, a small group of pixels called subset is tracked (Sutton et al., 2009) by comparing the reference image that is taken from the undeformed body with later images of the deformed body taken at intervals over time. To perform this procedure, called matching, a correlation error function that describes the difference between the subset in the reference image and the image taken at a later stage is minimized (refer to Sutton et al. (2009); Zhao et al. (2019) for suggested error functions). However, the correlation process might fail if a crack passes through a subset; in this case, the user must exclude such areas in advance before the matching phase (Helm, 2008). Additionally, multiple cracks crossing the sample can divide its surface into segregated areas, for which initial seed points—the initial pixels considered for the matching—must be defined separately. This can make it a cumbersome process to analyze the hundreds of sets of images usually taken during an experiment (Helm, 2008). To tackle this problem, Helm (2008) proposed using a cutoff on the correlation values obtained for each subset and discarding the subsets with error values higher than this cutoff. However, the threshold value must be defined by the user.

Detecting crack pixels on images could help to automate the generation of the initial seed point in the local subset DIC method for segregated regions and to remove noisy results around the discontinuities (Helm, 2008). Automated crack detection would also be useful for assessing the damage state of structural elements, because a pixel-wise segmentation of crack pixels, i.e., classifying all pixels of the image whether they belong to a crack or not, can be an important input for the damage assessment of a structural element (Dolatshahi and Beyer, 2019; Momeni and Dolatshahi, 2019; Arvin et al., 2019; Farhidzadeh et al., 2013; Athanasiou et al., 2020; Rezaie et al., 2020c; Madani and Dolatshahi, 2020). This is particularly relevant for concrete and masonry elements, for which cracks are the key damage feature.

In the present study, two approaches for crack segmentation are compared using images that were taken during two experimental campaigns conducted at EPFL (Rezaie et al., 2020b; Godio et al., 2019). The two approaches are the following: (i) crack segmentation by applying a threshold to the maximum principal strain map and (ii) crack segmentation using deep learning. To evaluate and compare the performance of each method, standard segmentation criteria in the computer vision domain, namely precision (PC), sensitivity (SE), and dice coefficient (DC) are used. The sensitivity of the threshold method to the subset size, which is an input parameter for performing the local DIC, is explored. Furthermore, the effect of using a pre-trained encoder in the deep learning network is investigated. In what follows, previous studies on crack detection are reviewed in section 3.2. A brief description of the conducted experimental campaigns is introduced in section 3.3. Thereafter, the image dataset and the segmentation metrics are mentioned in section 3.4. The segmentation methods are detailed in section 3.5 and section 3.6; and finally, the performance of the methods is compared in section 3.7.

3.2 Related research studies

3.2.1 Crack segmentation by post-processing of DIC results

In some research, crack detection is integrated directly into the DIC method (Helm, 2008). In the structural engineering community, however, it is addressed in post-processing results derived from DIC measurements, such as strain maps or displacement fields. Destrebecq et al. (2011) tested a reinforced concrete beam under four-point bending. They verified the crack patterns obtained from the DIC method by comparing it to a visual inspection performed during the experiment. The criteria used for this verification was the location and width of cracks. Tung et al. (2008) observed that the cracking of a 45° brick wall under compression loading could be better depicted using the von Mises strain map than horizontal and vertical strain maps. However, this work did not include a quantitative justification for the accuracy of crack detection by applying a threshold on the von Mises strain maps. Ghorbani et al. (2015) stated that visualizing the maximum principal strain (ϵ_1) can detect cracking of confined masonry walls tested under cyclic shear-compression loading. They compared a colored map of the maximum principal strain with the hand-drawn crack patterns at the ultimate state depicted during the experiments. They observed that masonry cracking can be captured by visualizing ϵ_1 maps, though again, a quantitative comparison was not mentioned. Similarly, Korswagen et al. (2020b, 2019) studied crack propagation in masonry walls using post-processed DIC results. Hoult et al. (2016) used the horizontal strain map, defined as the horizontal displacement of adjacent subsets divided by the step size (i.e., the initial distance between subsets), to detect cracking of six reinforced concrete beams tested under four-point bending. Morgan (2017) studied the initiation, propagation and coalescence of cracks using the DIC method by conducting several compression tests on Opalinus shale specimens. In this study, they applied a threshold to the lateral strain ϵ_{xx} to obtain crack maps. By qualitatively comparing crack maps sketched during experiments and those obtained using the results of the DIC method, they concluded that the DIC analysis is capable of detecting more cracks than visual inspection. Cinar et al. (2017) proposed a sequence of image processing algorithms to identify crack patterns, including phase congruency and active contour segmentation on the displacement field obtained from DIC measurements. They tested this method using both synthetic and laboratory data, but the efficiency was not verified for specimens with multiple cracks. Recently, Gehri et al. (2020) proposed a pipeline to compute automatically the crack opening and slipping using the DIC measurements. They used the principal tensile strain to localize cracked area. They qualitatively evaluated the performance of crack detection by overlying the principal tensile strain map over the region of interest.

3.2.2 Crack segmentation using deep learning

Deep learning methods have been successfully applied to detect and segment cracks on natural images, such as asphalt, concrete, masonry and steel surfaces (Yang et al., 2018; Mei et al., 2020; Spencer et al., 2019; Zhang et al., 2019; Gopalakrishnan et al., 2017; Ren et al., 2020; Park et al., 2020; Dorafshan et al., 2018; Brackenbury et al., 2019; Chaiyasarn et al., 2018). Generally, two approaches, namely classification and segmentation, have been used in the literature for crack detection. In the first method, small patches of an image are classified as crack or non-crack. In the second approach, every pixel is classified as a crack or non-crack. Using the first methodology, Zhang et al. (2016) proposed a shallow network to classify patches of road images as crack or non-crack. They observed that extracting hierarchical features using a convolutional network resulted in higher precision, recall, and F1-score (refer to subsection 3.4.2 for the definition) compared to using hand-crafted features and designing an SVM (Support Vector Machine) or Boosting classifier. Cha et al. (2017) classified patches by training a convolutional neural network using 40k images of concrete surfaces (train/validation) with a resolution of 256×256 pixels. They achieved a classification accuracy of around 98%. Wang and Hu (2017) trained a CNN (Convolutional Neural Network) to classify crack vs. non-crack patches using two patch sizes of either 32×32 pixels or 64×64 pixels. With the larger patch size, they observed an increase in the precision, recall and F1-score. To classify image blocks as background, crack or sealed crack on road images, Kaige et al. (2018) trained a CNN utilizing the concept of transfer learning. In a second step, they trained a linear model to find an optimum threshold for each image block to segment the crack pixels. Finally, they used tensor voting (Medioni et al., 2000) to connect broken crack fragments. Gopalakrishnan et al. (2017) extracted features from pavement images using a pre-trained VGG16 (VGG: Visual Geometry Group at the University of Oxford) truncated deep network. They used five classifiers to classify image patches as crack or non-crack, including a single neural network layer, random forest, extremely random trees, support vector machines and logistic regression. It was observed that the single-layer neural network had the highest prediction accuracy, precision, recall, F1-score and Cohen's Kappa score. To detect cracks on metallic surfaces in video frames, Chen and Jahanshahi (2018) proposed a CNN with naive Bayes data fusion.

Using the second methodology, i.e., pixel-level crack detection, Yang et al. (2018) proposed a fully convolutional network to segment crack pixels on different surfaces. The proposed network consisted of a down-sampling part, wherein they used VGG19, and an up-sampling part. They achieved around 98% accuracy, 82% precision, 79% recall and an 80% F1-score. Zou et al. (2019) proposed a hierarchical encoder-decoder architecture called “DeepCrack”, in which a prediction map is created at multiple convolution stages by fusing feature maps from the encoder and decoder path. All fused maps are concatenated and fused to produce a multi-scale output. They stated that DeepCrack outperforms other crack segmentation methods such as CrackForest (Shi et al., 2016) and CrackTree (Zou et al., 2012). Liu et al. (2019) proposed a variant of U-Net to predict crack pixels on concrete surfaces. They reported that U-Net requires only 57 images for training and validation, and it achieved an F1-score of 90%. Ji et al. (2020) used DeepLabv3+ (Chen et al., 2018) to segment crack pixels on asphalt images followed by an algorithm to quantify crack maps in terms of length, mean width, maximum width, area and ratio.

The literature review presented in section 3.2 shows that the previous studies using the threshold method lack quantitative image-based criteria to verify the quality of crack detection. In this study, however, the threshold method is evaluated by quantitative metrics. With regard to the deep learning approach, all the conducted research has focused only on natural images. In this study, natural images refer to images taken from structural elements without the presence of small black dots, termed speckles. However, these approaches have never been tested for images taken in the laboratory for use in DIC (in short referred to as “laboratory images” in this article). One significant difference between natural images and laboratory images is the presence of speckles on the background (see Figure 3.1 and Figure 3.2), which complicates the detection process compared to natural images with a simpler background.

3.3 Description of the case studies

3.3.1 Experimental tests and procedures

As a case study, the data from two experimental campaigns conducted at EPFL, wherein DIC was applied to measure the displacement fields, were used in this work. These two experimental campaigns are briefly described below.

Tests on stone masonry walls of typology A

This testing campaign included six shear-compression tests (specimen label: RS), three compression tests (specimen label: RSC) and three diagonal-compression tests (specimen label: RSD). The specimens for shear-compression tests (RS) were 160 cm high, 160 cm long and 40 cm wide and were plastered on one side. Figure 3.1a and Figure 3.1b show views of the faces with and without plaster as well as views of the two stereo camera systems placed on either side of the wall to measure the 3D displacement fields via DIC. During the tests, the horizontal red actuator applied cyclic horizontal displacements while the vertical red actuators applied a constant vertical load. For more details about the experimental campaign, please refer to Rezaie et al. (2020b).

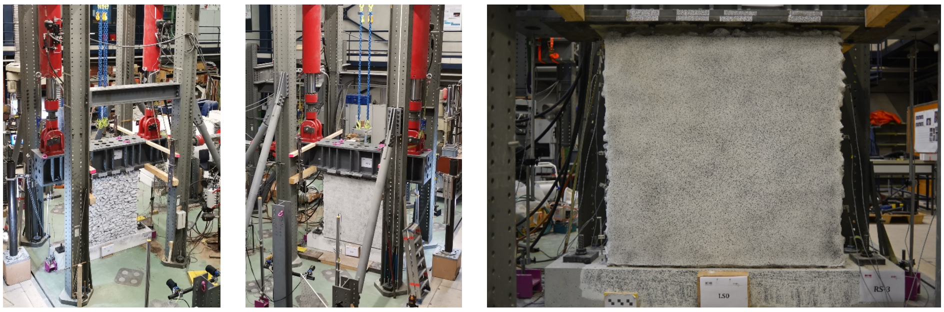

(a) (b) (c)

Figure 3.1 – Test setup for shear-compression tests at EPFL. (a) view of the stone side without plaster, (b) view of the plastered side and (c) a closed view of the plastered side covered with random speckles.

(a) (b)

Figure 3.2 – Tests on wallettes: (a) simple-compression test and (b) diagonal compression test. The images show the plastered side of the wallettes.

In addition to shear-compression tests, three diagonal-compression and three simple-compression tests were performed on wallettes that were 90 cm high, 90 cm long (one of the wallettes tested under simple compression load was 80 cm long) and 40 cm wide. Figure 3.2a and Figure 3.2b show images taken from simple-compression and diagonal-compression tests, respectively. As for the shear-compression tests, displacement fields on either side of the wallettes were measured by two sets of stereo cameras used in conjunction with DIC.

Tests on stone masonry walls of typology E

Godio et al. (2019) conducted six cyclic shear-compression tests on stone masonry walls (specimen labels: SC) with regular typology. The walls were 90 cm high, 90 cm long and 20 cm wide. In addition to shear-compression tests, two simple-compression tests were carried out on specimens labelled RSM, measuring 90 cm high, 78 cm long and 20 cm wide and one diagonal-compression test on a wall measuring 78 cm high, 78 cm long and 20 cm wide. For a detailed explanation about the tests, please refer to Godio et al. (2019). Just as for the tests performed on walls of typology A by Rezaie et al. (2020b), the wall surfaces were speckled and two stereo camera systems were used to measure 3D displacement fields on either side of the walls.

3.3.2 Three-dimensional DIC setup

To use the DIC method, a number of preparatory steps was performed in both campaigns. On the specimens, the regions of interest (ROI) were first painted in white; then the wall surfaces were covered with random speckle patterns with an average dimension of 2 mm. These black speckles were either sprayed using a paint pistol (see Figure 3.1c) or a printer gun (see Figure 3.2). Additionally, stereo camera systems and lighting conditions were set up. Cameras were mounted on a rigid bar and placed far enough from the specimens to view the entire region of interest. They were set up such that the centres of the two cameras pointed towards the same location on the specimens. The average ratio of mm/pixel for all tested specimens (Rezaie et al., 2020b; Godio et al., 2019) was almost 0.4. On each side of the walls, two LED lamps were placed to illuminate the regions of interest. The cameras were calibrated by taking around 80 pairs of images of a calibration board containing circular dots with known dimensions. For a more detailed explanation about the necessary preparation steps to use the DIC method, see previous work on the topic (Sutton et al., 2009; International Digital Image Correlation Society, 2018). During the experiments, pairs of grayscale images were taken from both sides of the walls and wallettes at specified time intervals. For testing large-scale walls, images with dimensions of 4384×6576 pixels were acquired, while for small-scale walls (wallettes) images with dimensions of 2192×3288 pixels were acquired.

To perform the DIC method, the commercial software VIC-3D version 8.2.4 (Correlated Solutions, 2018) was used, which uses a local subset DIC approach that divides the region of interest into subsets. The local subset DIC method is formulated as an optimization problem using a cross-correlation loss function (Sutton et al., 2009; Correlated Solutions, 2018). As an illustration, Figure 3.3 depicts a subset in a reference image (green box) and the corresponding deformed subset (red quadrilateral) in the deformed image. The result of the DIC method is the 3D deformation of the centres of each subset (the green circle shown in Figure 3.3a), for which the correlation problem is solved. The correlation problem is usually solved for overlapping subsets (referred to as the step size). An important parameter affecting the accuracy and spatial resolution is the subset size (Sutton et al., 2009; Ghorbani et al., 2015; Zhou and Goodson, 2001; Lecompte et al., 2006). One way to select a subset size is to take several images at the beginning of a test when a specimen is intact and investigate the standard deviation and bias of some measurements, such as horizontal or vertical displacements (Ghorbani et al., 2015). In this study, the subset size is considered as a variable parameter so that its influence on the segmentation metrics described in subsection 3.4.2 could be investigated.

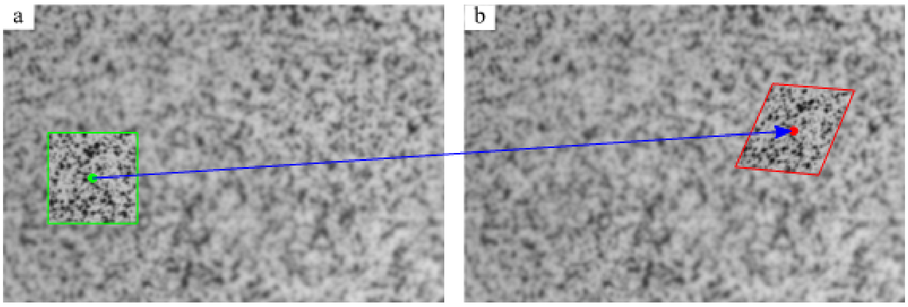

Figure 3.3 – Schematic illustration of DIC (a) reference and (b) deformed image. The selected green subset is deformed into the red quadrilateral.

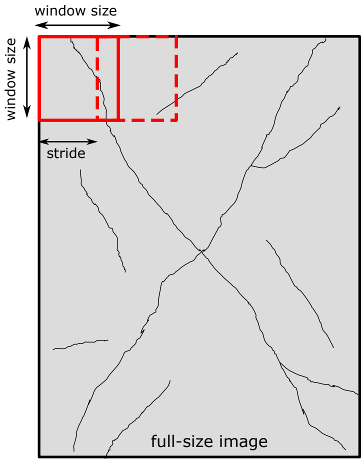

Figure 3.4 – Illustration of the sliding window to obtain equally sized image patches from the full-size image.

3.4 Crack segmentation dataset and metrics

Crack segmentation is performed on a pixel basis, i.e., by classifying each pixel as part of a crack or not. Two approaches of crack segmentation are applied and compared in this study: 1) an approach based on a threshold applied on the principal strain map that is derived from the displacement field measured using DIC, and 2) an approach by deep learning making use of the images taken as input to DIC. subsection 3.4.1 introduces the dataset of images used in the two approaches, while the criteria used in the evaluation and comparison of the approaches are defined in subsection 3.4.2.

3.4.1 Training and test datasets

Small image patches were extracted from the full-size images by sliding a 256×256 pixels window with a stride of 256 pixels along the two directions (Figure 3.4), which will be used as inputs to the network.

(a) (b) (c)

Figure 3.5 – Full-size images used to create test data (dataset B), (a and b) two images of specimen RS4 taken at two load steps, and (c) an image of specimen RS6.

For the training and validation data (dataset A), 17 full-size laboratory images were selected from the specimens RSC2-3, RSD1, RSD2, RSM2, SC1-7, RS1-3. The images taken during the experimental campaigns illustrate the state of the plastered wall surfaces under different loading levels and support conditions (Rezaie et al., 2020b; Godio et al., 2019). The images that were selected as part of the training and validation dataset cover a wide combination of crack widths, speckle patterns, and lighting conditions. In this way, the robustness of the crack segmentation approaches tested in the paper is challenged. From the 17 full-size images, 430 image patches were generated. The crack pixels contained in the patches were manually annotated by use of the open-source software “Pixel Annotation Tool” (Breheret, 2017).

For the test data (dataset B), three full-size images were selected from specimens RS4 and RS6 at different loading levels (see Figure 3.5). To obtain a fair model, no images taken from specimens RS4 and RS6 were included in the training/validation data (dataset A). Using the sliding window with the same window size and stride as for the training/validation data, 100 image patches were generated, and the ground-truth masks (binary images in which crack pixels are annotated, i.e., crack pixels are set to one and the background to zero) were annotated. These test image patches were used to compare the performance of the two segmentation approaches. All images and corresponding ground-truths are made publicly available at https://doi.org/10.5281/zenodo.4307686. Note that the manual labelling of cracks was limited by what was visible—the minimum crack width visible on the images from dataset B was about 0.1 mm. Moreover, due to the presence of speckle patterns on images, perfect manual labeling is often difficult as the speckle patterns and the crack pixels are both black, and for situations where the boundary of a crack is in contact with speckle pixels, the ground-truth might not be without error. To overcome this issue, relaxed segmentation metrics (Mosinska et al., 2018) can be used (i.e., a buffer size of, for example, 3 pixels, can be used to determine true crack pixels).

Because the DIC results could be noisy around the border of the ROI, image patches cor-

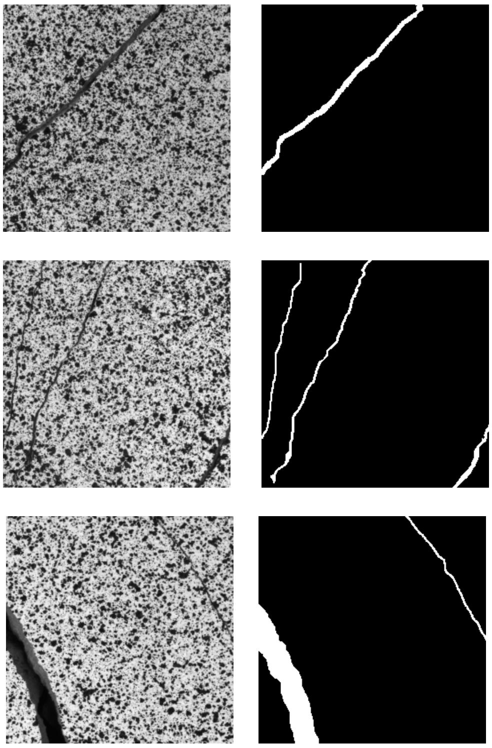

(a) (b)

Figure 3.6 – Examples of the crack image database: (a) images and (b) annotated ground-truth masks.

responding to these areas were discarded even if they had cracks. Further explanation is provided in section 3.5. Figure 3.6 depicts examples of image patches and the corresponding ground-truth masks.

3.4.2 Segmentation metrics

Though there is a broad range of options, one widely used group of semantic segmentation metrics is pixel-wise metrics (Mosinska et al., 2018), which can be divided into two categories: (i) Evaluation of the segmentation by comparing the segmentation results to the ground truth on a pixel by pixel basis (i.e., without skeletonization of the cracks), and (ii) evaluation of the segmentation by skeletonizing the crack pattern. In this study, the former approach was chosen. For this approach, three quantities were computed: the precision (PC), the sensitivity (SE), also known as recall, and the dice coefficient (DC), also known as F1-score, which is the harmonic mean of PC and SE. These are defined as:

$$PC = \frac{TP}{TP + FP} \tag{3.1}$$

$$SE = \frac{TP}{TP+FN} \tag{3.2}$$

$$DC = \frac{2}{PC^{-1}+SE^{-1}} \tag{3.3}$$

where TP, FP and FN are the number of true positive, false positive and false negative pixels, respectively. Dice coefficient measures the similarity between the predicted crack mask and the ground truth. If the predicted mask and the ground truth are identical, DC is equal to 1, while if the predicted crack mask and the ground truth do not intersect, DC is equal to 0. Otherwise, DC is between 0 and 1.

3.5 Crack segmentation by the threshold method

3.5.1 Method implementation

The DIC method gives as output the 3D displacement field at the points for which the correlation problem is solved. This field was extracted from the software VIC-3D, and a python code was developed for post-processing the results. The post-processing includes generating a mesh of triangular elements (constant strain triangle) and calculating the maximum principal strain ϵ_1 at the center of each element. These strain values were then interpolated to obtain the ϵ_1-value for each pixel, and a threshold was applied to transform the obtained strain maps to binary crack masks.

To explore the effect of subset size on the crack segmentation results, four DIC analyses were performed by choosing different subset sizes, i.e., 15×15 pixels, 19×19 pixels, 23×23 pixels and 33×33 pixels. For all analyses, the step size was set to 2×2 pixels, and the ratio mm/pixel was 0.43 (for specimens RS4 and RS6). There is a lower bound on the ideal subset size, though, because when the subset size is too small, the subsets might contain too few speckles, which finally decreases the accuracy of the DIC method (Sutton et al., 2009). It is suggested that each subset should contain at least 3×3 speckle pixels (Sutton et al., 2009). Therefore, in this study, the subset size of 15×15 pixels (6.45×6.45 mm^2) was selected as the minimum subset size. Figure 3.7 shows an example of the obtained ϵ_1-map for a subset size of 19×19 pixels for a selected loading level of specimens RS4 and RS6 (test dataset B).

To extract crack pixels, 25 threshold values were applied to the ϵ_1 maps: 0.5%, 1.5%, 2.5%, 3.5%, ... , 24.5%. For each of these thresholds, the pixels with an ϵ_1 value larger than the threshold were labeled as crack, and not if otherwise.

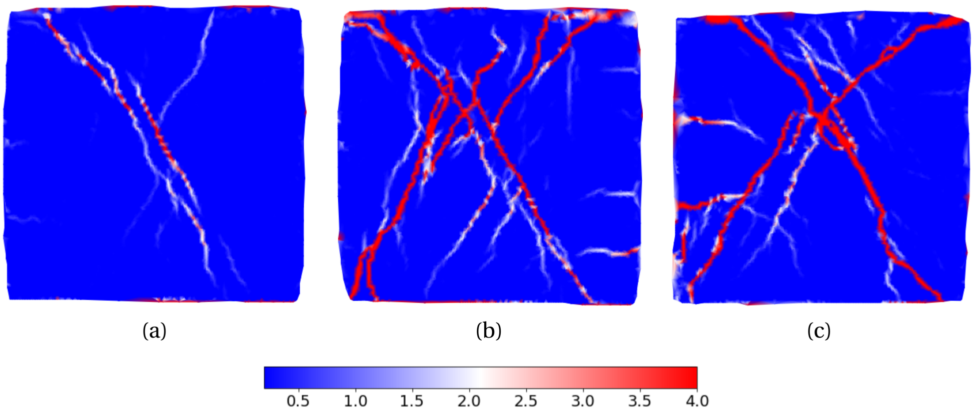

Figure 3.7 – Maximum principal strain maps for specimen RS4 (a and b) and specimen RS6 (c) shown in Figure 3.5; subset size = 19 × 19 pixels.

3.5.2 Results

Figure 3.8 shows the segmented cracks obtained by applying the smallest and largest threshold values to the strain map of Figure 3.7c. In this figure, the boundary of the wall is plotted with a dotted green line. It is evident from the figure that the extracted crack pattern is very sensitive to the applied threshold value. The threshold value of 0.5% (Figure 3.8a) resulted in a highly noisy crack segmentation (see the ground truth mask Figure 3.8c), which could be reduced in a post-processing step using mathematical morphology (Haralick et al., 1987). On the other hand, the crack map obtained by applying the threshold value of 24.5% is far less noisy, but there are still many pixels around the boundary of the ROI that are misclassified as a crack (see the ground truth mask Figure 3.8c). This is because subset pixels are squares, and when the border of the ROI is curved, part of the background falls into the subset, which causes errors in the correlation step of the local subset DIC method (Sun et al., 2015). Indeed, this problem can be avoided by choosing a smaller ROI; however, this comes at the cost of losing information, which is not desirable. Moreover, by applying such a high threshold, some crack pixels are wrongly misclassified as background, and the continuity of several thin cracks is not preserved. Furthermore, in addition to the above-mentioned qualitative reasons, the following analysis will show that even with the optimum threshold value and subset size, the results of the crack segmentation are poor.

The performance of the crack segmentation by application of a threshold to the ϵ_1 map was evaluated quantitatively by analysing 100 images of the test data (dataset B) and computing and plotting the segmentation metrics defined in subsection 3.4.2 as a function of the threshold value. The results are presented in Figure 3.9. It can be seen that for all subset sizes, as the threshold decreases, more pixels are classified as cracks (i.e., high SE in Figure 3.9a). However, the PC of segmentation is quite poor in Figure 3.9b, which also reduces the DC because it is simply a harmonic mean of the SE and PC. By increasing the threshold value, though, the PC and DC are slightly improved while the SE is reduced.

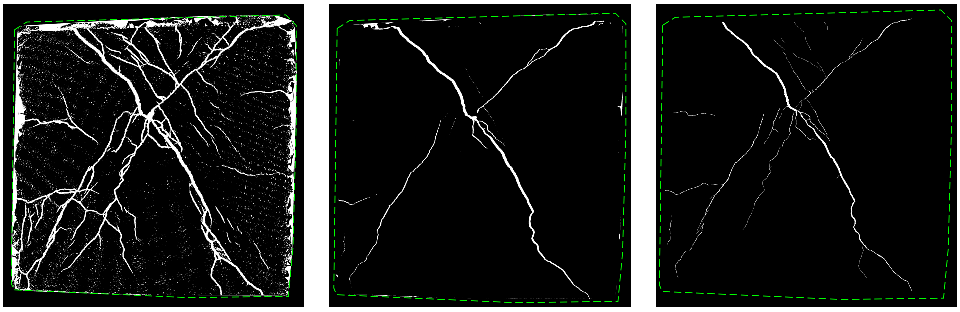

(a) (b) (c)

Figure 3.8 – Segmented crack patterns obtained by applying threshold values of (a) 0.5% and (b) 24.5% on the ϵ_1 map shown in Figure 3.7c; (c) manually annotated crack mask. The green box shows the boundary of the wall.

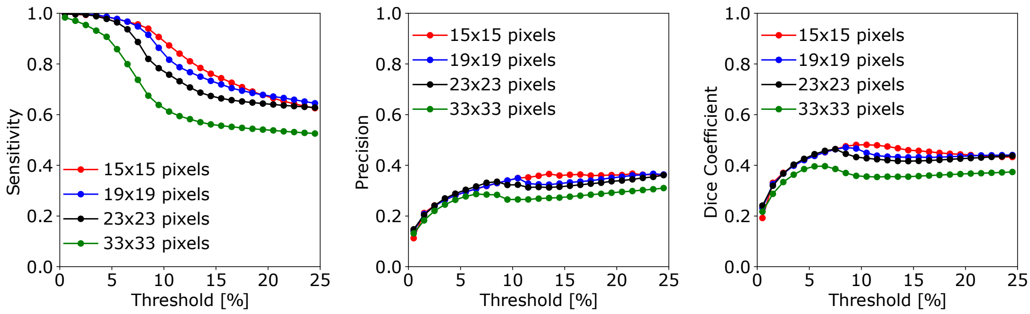

(a) (b) (c)

Figure 3.9 – Sensitivity (a), precision (b) and dice coefficient (c) of the threshold method as a function of the threshold value on the maximum principal strain and the subset size for the test data (dataset B).

Furthermore, the subset size affects the resolution, and therefore the accuracy of the crack segmentation. By increasing the subset size, the spatial resolution of the result decreases along with the SE, PC and DC values. This is most pronounced for the subset size of 33×33 pixels. In general, as the subset size decreases, crack pixels are more accurately classified.

The combination of subset size and threshold value that resulted in the maximum DC is the subset size of 15×15 pixels and the threshold value of 10.5%. Examples of the segmented crack patterns obtained using these values for three crack images and the corresponding ground-truth images are shown in Figure 3.10c. It is clear that the segmented cracks are quite coarse, i.e., wider than the width of the actual cracks (for instance, ex. 1, 2, 5 of Figure 3.10c), which increases FP and decreases PC and DC. Furthermore, for very thin cracks (1–2 pixels) such as ex. 3 in Figure 3.10, the segmented cracks are not continuous.

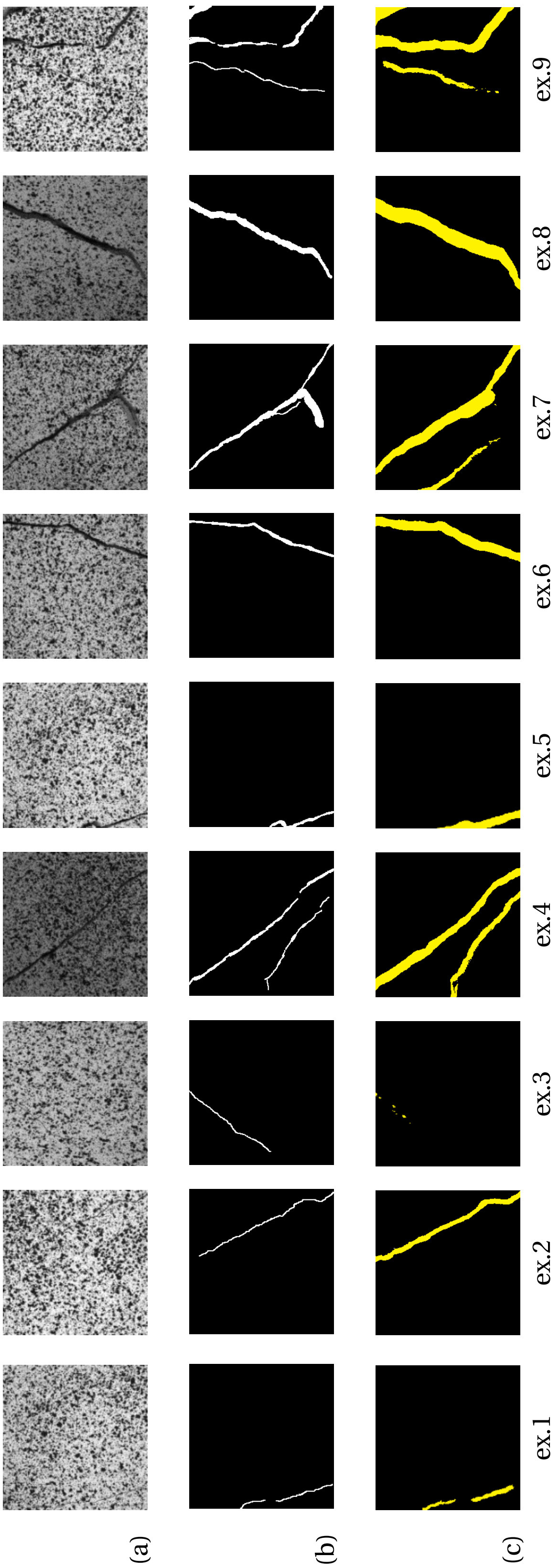

Figure 3.10 – Results of crack segmentation by the threshold method. (a) images, (b) ground truth masks, and (c) segmented crack mask made by applying the threshold value of 10.5% to the maximum principal strain map (post-processing of DIC results).

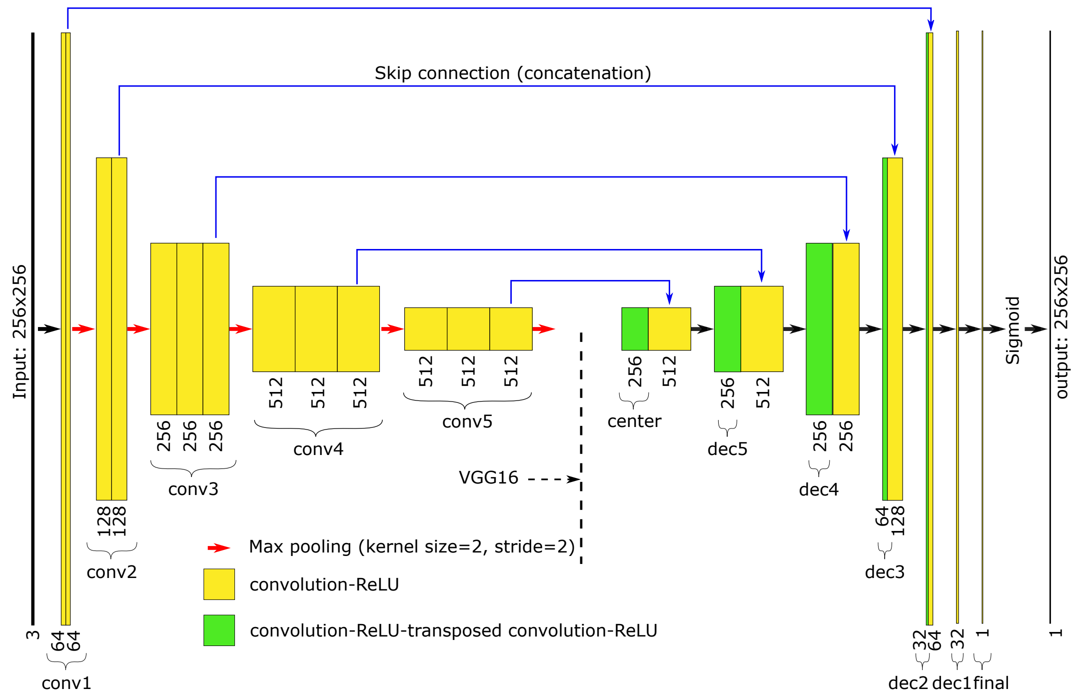

Figure 3.11 – TernausNet architecture (Shvets et al., 2018; Iglovikov and Shvets, 2018).

3.6 Crack segmentation by deep learning

3.6.1 Network architecture

A UNet-like architecture (Ronneberger et al., 2015) called "TernausNet" (Shvets et al., 2018; Iglovikov and Shvets, 2018) was chosen for segmenting crack pixels. UNet-like architectures usually consist of two parts: encoder and decoder paths. In the encoder path, multiple blocks of operations, including stacks of convolutional layers, activation functions and pooling layers, are applied successively to the input of each layer. The in-plane size of the input to each layer reduces due to the convolutional and pooling operations deeper into the network. In the decoder path, the original size of the input is recovered by up-sampling the feature maps obtained in the encoder path. Moreover, to increase the localization accuracy of the prediction, the feature maps in the encoder path are copied into the decoder path via skip connections (Ronneberger et al., 2015; Iglovikov and Shvets, 2018). For this study, the TernausNet architecture (Shvets et al., 2018; Iglovikov and Shvets, 2018) was chosen, which uses VGG16 (Simonyan and Zisserman, 2015) blocks as the encoder (see Figure 3.11). This network was chosen because (i) previous studies have found that U-Net type architectures require few training examples for a satisfactory performance (Ronneberger et al., 2015), which is required for our problem, and (ii) the encoder block is the VGG16, which can be initialized using the pre-trained weights on ImageNet. The detailed network architecture is summarized in Table 3.1, as implemented in PyTorch version 0.4.1. The table includes the number of filters at each layer, stride, padding, activation function and the up-sampling method.

Table 3.1 – Details of operations in TernausNet.

Layer name	Operation	Kernel size	Number of kernels	Stride	Padding
conv1	Convolution + ReLU*	3 x 3	64	1	1
	Convolution + ReLU	3 x 3	64	1	1
conv2	Convolution + ReLU	3 x 3	128	1	1
	Convolution + ReLU	3 x 3	128	1	1
conv3	Convolution + ReLU	3 x 3	256	1	1
	Convolution + ReLU	3 x 3	256	1	1
	Convolution + ReLU	3 x 3	256	1	1
conv4	Convolution + ReLU	3 x 3	512	1	1
	Convolution + ReLU	3 x 3	512	1	1
	Convolution + ReLU	3 x 3	512	1	1
conv5	Convolution + ReLU	3 x 3	512	1	1
	Convolution + ReLU	3 x 3	512	1	1
	Convolution + ReLU	3 x 3	512	1	1
center	Convolution + ReLU	3 x 3	512	1	1
	Transposed Convolution + ReLU	4 x 4	256	2	1
dec5	Convolution + ReLU	3 x 3	512	1	1
	Transposed Convolution + ReLU	4 x 4	256	2	1
dec4	Convolution + ReLU	3 x 3	512	1	1
	Transposed Convolution + ReLU	4 x 4	256	2	1
dec3	Convolution + ReLU	3 x 3	256	1	1
	Transposed Convolution + ReLU	4 x 4	64	2	1
dec2	Convolution + ReLU	3 x 3	128	1	1
	Transposed Convolution + ReLU	4 x 4	32	2	1
dec1	Convolution + ReLU	3 x 3	32	1	1
final	Convolution	1 x 1	1	1	1

*ReLU stands for the “Rectified Linear Unit” activation function defined as max(0, the input of the function).

3.6.2 Training setup and optimization scheme

As the goal was to obtain the highest performance in terms of both SE and PC, the dice loss function (Equation 3.4), which was first proposed by Milletari et al. (2016), was used to train models.

$$\text{Dice loss} = 1 - \frac{\sum_{i=1}^{n} 2\hat{y}_i y_i + \epsilon}{\sum_{i=1}^{n} \hat{y}_i + \sum_{i=1}^{n} y_i + \epsilon} \tag{3.4}$$

where, y_i and $\hat{y}_i$ are the target (0 or 1) and predicted probability for pixel i, respectively, n is the number of pixels in the image, and $\epsilon = 1$.

Out of 430 image patches, 301 (70%) and 129 (30%) images were selected as the training and validation data, respectively. The validation set guided the choice of learning rate and the

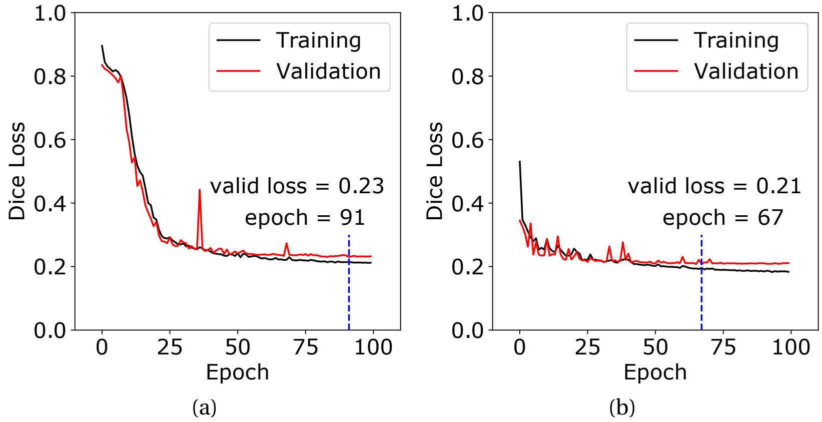

Figure 3.12 – Dice loss vs. epoch over training and validation data. (a) Encoder weights initialized using random initialization, and (b) encoder weights initialized with pre-trained values.

best model (lowest validation loss). The initial learning rate was halved every 20 epochs. To increase the size of the database, the data was randomly augmented. This was performed using the transforms module of Torchvision version 0.2.1 and included: a) random rotation with an angle equal to 90, 180 or 270 degrees; b) horizontal and vertical flip and c) brightness and contrast change at a ratio of 0.2. The models were trained for 100 epochs using the Adam optimizer (Kingma and Ba, 2015) with a batch size equal to one on a single NVIDIA Tesla P100 (12 GB) GPU. Apart from the learning rate, other parameters of the optimizer were set to the default values defined in the PyTorch optimization module. Weights of the encoder path were initialized using either model A or B. In model A, the weights of the encoder path were initialized randomly using the default method in PyTorch. For this case, a grid search led to the initial learning rate of 9e-5. In model B, the encoder path was initialized with parameters pre-trained on the ImageNet database (Russakovsky et al., 2015). For this case, a grid search led to the initial learning rate of 2e-4. Weights of the decoder path, however, were initialized randomly using the default method in PyTorch. All layers of the network were trained with a single learning rate.

The dice loss was evaluated on the training and validation data, and the trends are shown in Figure 3.12 for both considered models (A and B). The plot of loss function vs. epoch shows that both training and validation losses decreased, while in higher epochs, the training loss became slightly lower than the validation loss due to overfitting. Therefore, the best model for each case was selected based on the validation loss. By comparing plots of loss function vs. epoch of both models, it can be observed that the dice loss over validation data converged faster (epoch = 67) to a lower value (0.21) in model B compared to model A (epoch = 91, loss = 0.23).

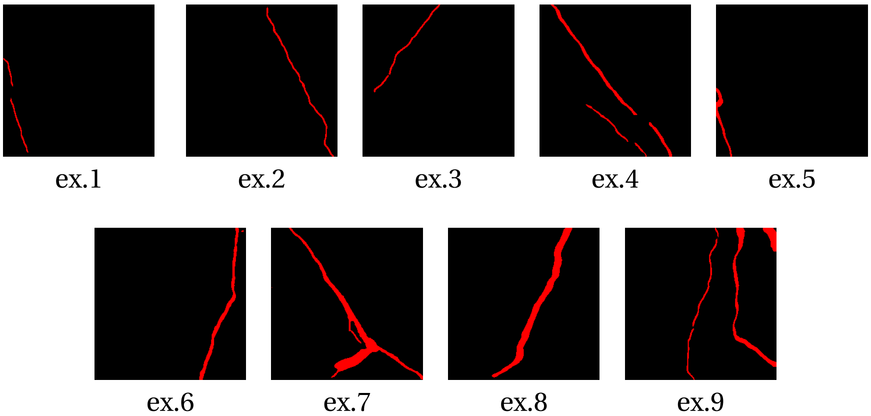

Figure 3.13 – Segmented cracks on examples images in Figure 3.10a by TernausNet (model B).

3.6.3 Results

TernausNet (model B) was then used to predict the crack patterns in images shown in Figure 3.10. Figure 3.13 depicts the predicted crack patterns. The figure shows that the trained TernausNet could detect cracks with a wide width range, from very thin cracks to cracks of several pixels in width. In this set of examples, the continuity of the cracks is also well preserved. In section 3.7, the TernausNet performance is quantitatively compared with the threshold method.

In spite of the satisfactory prediction by TernausNet, there are some images in which the model fails to correctly predict crack pixels. Some examples are shown in Figure 3.14. The yellow boxes in Figure 3.14b and Figure 3.14c highlight crack pixels that are not detected by the model (FN) and pixels that are incorrectly classified as a crack (FP).

3.7 Comparison of the methods

To fairly compare the two methods, i.e., (i) the segmentation by applying a threshold value on the ϵ_1 map and (ii) the deep learning method, the performance of each model on the test data is summarized in Table 3.2. In both cases, the best performing model was used for this comparison. This means that for the segmentation by applying a threshold value on the ϵ_1 map, the model with a subset size of 15×15 pixels and a threshold value of 10.5% was used. For the deep learning method, model B was used, wherein the parameters of the encoder path were initialized using pre-trained values on the ImageNet database. Regarding SE, the application of a threshold on the ϵ_1 maps slightly outperformed the deep learning approach. However, the precision of the detection was quite poor (0.350) compared to that obtained by the deep learning approach (0.819). Similar performance indices were obtained for the DC metric, which was considered the most relevant metric and which served as the criterion for choosing the best parameter combination for each class of model—either the best combination of subset size and threshold value or the loss function to optimize. Note that

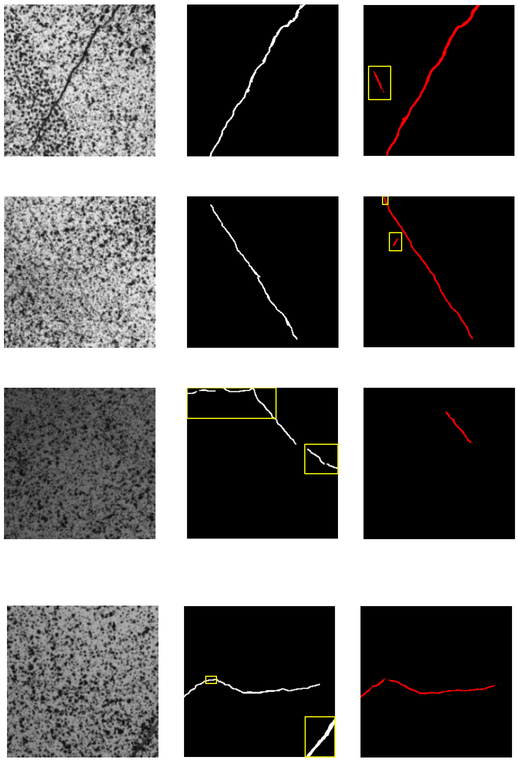

(a) (b) (c)

Figure 3.14 – Illustration of erroneous segmented crack pixels using TernausNet (model B). (a) images, (b) ground-truth masks, and (c) prediction.

the SE of the deep learning approach could be increased by choosing another loss function, such as Tversky loss (Salehi et al., 2017) wherein the weights associated with FP and FN pixels can be tuned (in the dice loss, they are weighted equally) (Salehi et al., 2017).

Although applying a threshold on the ϵ_1 map can detect the majority of crack pixels, many more pixels are also incorrectly classified as cracks (false positive values). Therefore, the geometry of crack patterns is not well preserved in this approach. Conversely, the deep learning approach is a promising alternative method to the classical threshold method, as most of the crack pixels were segmented correctly and the precision of detection for crack/non-crack pixels is much higher than for the threshold method. For this reason, the deep learning method outperformed segmentation by applying a threshold value on the ϵ_1 map. Furthermore, the deep learning approach can be used as a pre-processing step to detect crack pixels before the DIC analysis. This can be useful for automating the initial seed generation in the segregated areas. The crack geometry can also be used as an input for DIC methods that are based on discontinuous rather than continuous displacement fields (Réthoré et al., 2008; Roux et al., 2009).

Table 3.2 – Comparison of the performance of the two segmentation methods on test data.

Segmentation method			SE	PC	DC
Apply a threshold to maximum principal strain map (Subset size = 15x15 pixels, threshold value = 10.5%)			**0.873**	0.350	0.481
Deep learning (TernausNet)	Encoder weights	Random initialization	0.827	0.801	0.810
		Pre-trained weights on the ImageNet database	0.834	**0.819**	**0.821**

3.8 Conclusions

This study compares the performance of two methods—(i) the threshold and (ii) the deep learning method—for detecting crack pixels on laboratory images, i.e., grayscale images that are inputs for the local DIC method. The image database was selected from images taken from two experimental campaigns on stone masonry walls that were plastered on one side (Rezaie et al., 2020b; Godio et al., 2019). The DIC measurements discussed in this paper were obtained from this plastered side.

In the first approach, DIC analyses were performed by setting the subset size to 15×15 pixels, 19×19 pixels, 23×23 pixels, and 33×33 pixels (step size = 2×2 pixels, mm/pixel = 0.43) using VIC-3D software (Correlated Solutions, 2018). Then, from the resulting 3D displacement fields, the maximum principal strains were computed. Different threshold values were chosen (0.5%, 1.5%, 2.5%, 3.5%, ..., 24.5%) to produce a binary crack mask from the maximum principal strain maps. In the second approach, a deep convolutional neural network called TernausNet was adopted to perform pixel-wise crack segmentation. TernausNet is an encoder-decoder architecture that uses VGG16 convolution blocks as the encoder and is initialized either using random initialization (model A) or pre-trained values on the ImageNet (model B).

The performance of the two approaches was examined in terms of sensitivity, precision and dice coefficient. It was shown that the deep learning model B, in which the encoder parameters were initialized using the pre-trained values on the ImageNet database, converged faster and to a lower loss compared to model A, where the encoder weights were initialized using the default PyTorch random initialization method. Additionally, it was found that the threshold method resulted in higher sensitivity (0.873) than the deep learning model B (0.834). However, the precision of the predictions made by the threshold method was quite poor (0.350) compared to the deep learning model B (0.819). Consequently, this led to a low dice coefficient of 0.481 for the threshold method, while the corresponding value for deep learning model B was 0.821. The high dice coefficient showed that the deep learning approach could detect the majority of the visible cracks and that the detection was precise. The higher sensitivity for the threshold method revealed that more cracks could be detected compared to the deep learning method, but as the precision of the detection was quite low, there were many pixels incorrectly labeled as cracks. It was observed that in the threshold method, detected pixels were fragmented for very thin cracks. In other words, the continuity of the crack was not preserved. Moreover, the detected cracks were wider than the actual cracks in this method. Conversely, the deep learning method better preserved the geometry of cracks.

Possible directions for future studies to improve the performance of the deep learning method include implementing an iterative refinement of predictions (Mosinska et al., 2018), increasing the size of the database, and adding loss functions to consider the topology of the crack maps (Mosinska et al., 2018). Post-processing of the predicted crack maps could also be performed to both remove the noisy outputs and connect the gaps between crack segments, which could be done by implementing methods such as tensor voting (Kaige et al., 2018; Medioni et al., 2000).

Acknowledgments

The project is supported by the Swiss National Science Foundation (grant 200021_175903/1 “Equivalent frame models for the in-plane and out-of-plane response of unreinforced masonry buildings”).

4 Crack quantification: Crack width

This chapter represents the pre-print version of the article:

Rezaie, A., Godio, M. and Beyer, K., 2021. "Investigating the cracking of plastered stone masonry walls under shear-compression loading". *to be submitted to Construction and Building Materials.*

The formatting and numbering of equations, tables and figures have been adapted to this document. The contributions of the first author are: methodology, validation, formal analysis, investigation, data curation, writing - review and editing, visualization. The contributions of the second author are: investigation, writing - review and editing. The contributions of the third author are: supervision of the first author, conceptualization, methodology, investigation, resources, writing - review and editing, funding acquisition.

Abstract

Cracks are the most important source of information about the damage that occurs to unreinforced masonry piers under seismic actions. To predict the structural state of unreinforced masonry piers after an earthquake, research models have been developed to quantify important features of crack patterns. One of the most used crack features is the width, but this can be influenced by several parameters such as axial load ratio, shear span ratio, and the loading history, which have not been fully addressed in previous research studies.

In this work, we use experimental data to investigate the evolution of cracking in stone masonry piers during the application of cyclic shear-compression loading. The data consist of grayscale images taken during quasi-static shear-compression tests performed on six plastered rubble-stone masonry walls subjected to constant axial force and cycles of increasing drift demand. Through the combined use of digital image correlation and a pre-trained deep learning model, crack pixels are identified, post-processed, and quantified based on their width. The dependency of the crack width on the axial load ratio, shear span ratio, and loading protocol at the peak force and ultimate drift limit state of the piers is clarified by a displacement

vector field analysis, histogram of the crack widths, and concentration of deformation in the cracks.

We show that, as opposed to flexural cracks, diagonal tension cracks do not fully close when moving from the applied drift demand to the residual drift measured upon removal of the lateral load. Furthermore, we are able to provide the maximum residual crack width at peak force and ultimate drift limit states. This work will improve the decision making abilities of future models used to quantify earthquake-induced damage to stone masonry buildings.

Keywords: Masonry ; Crack width; Digital image correlation; Deep learning; Post-earthquake assessment.

4.1 Introduction

Stone masonry buildings have shown poor performance in previous earthquakes (D'Ayala, Dina F and Paganoni, Sara, 2011). According to FEMA 306 (1998), usability and serviceability of a damaged building can be assessed based on the severity and type of damage. In brittle construction materials, like masonry and concrete, cracks are the primary source of information on the damage severity. They are used to build empirical and physics-based models to classify the failure mode and estimate their residual capacity (Napolitano and Glisic, 2020, 2019; De Vent et al., 2011; Dolatshahi and Beyer, 2019; Madani and Dolatshahi, 2020; Jonathan P. Rivera Emma Lejeune, Bismarck N. Luna, and Andrew S. Whittaker, 2015). Several studies link a qualitative description of the crack pattern and maximum crack width to the maximum displacement ductility that the structural system has undergone (Tomaževič, 2007; Bosiljkov, V and Page, A W and Bokan-Bosiljkov, V and Žarnić, R, 2010; Kržan et al., 2015; Korswagen et al., 2020b).

For assessing the severity of cracking in a structural member, the prime criteria are the crack orientation and maximum crack width (FEMA 306, 1998). In addition, the following other criteria have been used in the literature to quantify the extent of cracking in a structural member: crack length (Jonathan P. Rivera Emma Lejeune, Bismarck N. Luna, and Andrew S. Whittaker, 2015; Rouzbeh et al., 2018; P. Rivera and S. Whittaker, 2019), crack density (P. Rivera and S. Whittaker, 2019; Abbiati et al., 2018a), a dimensionless quantity combining the number of cracks and their width and length (Korswagen et al., 2019, 2020a), fractal and multifractal characteristics of crack patterns (Dolatshahi and Beyer, 2019; Madani and Dolatshahi, 2020; Rezaie et al., 2020c; Ebrahimkhanlou et al., 2016; Farhidzadeh et al., 2013; Momeni and Dolatshahi, 2019; Arvin et al., 2019; Carrillo and Avila, 2017), and crack size (De Vent et al., 2011).

The choice of which crack feature to use as criterion for damage severity depends mainly on the scope and methodology of the research topic. FEMA 306 (1998) recommends classifying the damage level using the crack width, the extent of the cracked area, and the type of crack (oriented diagonally or horizontally, stair-stepped, X-shape). It categorizes damage severity in a structural component as insignificant, slight, moderate, heavy, or extreme (FEMA 306, 1998), and based on this damage grade, proposes modification factors for stiffness, strength, and deformation capacity. Similarly, AeDES (Baggio et al., 2007) determines the damage severity (slight, medium-severe, and very heavy) based on the type of crack, the surface crack position, and crack width. Here, slight damage consists of flexural or diagonal shear cracks of less than 1 mm in width, and medium-severe damage contains flexural cracks of 10—15 mm or diagonal shear cracks of 2–10 mm in width. Additionally, Novelli and D'Ayala (2019) used crack pattern and damage severity to develop a knowledge-based system for the post-earthquake assessment of masonry buildings that would output the failure mode type and its level. Tomaževič (2007) proposed a correlation between EMS-98 damage grades (Grünthal, 1998), limit states, and the crack width information recorded during cyclic shear-compression tests on masonry walls with clay units. Korswagen et al. (2019) proposed a dimensionless quantity called damage level parameter (Ψ) that depends on the number of cracks and their length and width. It is empirically defined as Eq. 4.1:

$$\Psi = 2n_c^{0.15}\hat{c}_w^{0.3}, \tag{4.1}$$

where n_c is the number of cracks in the specimen, and $\hat{c}_w$ is formulated as:

$$\hat{c}_w = \frac{\sum_{i-1}^{n_c} c_{w,i}^2 c_{L,i}}{\sum_{i-1}^{n_c} c_{w,i} c_{L,i}}. \tag{4.2}$$

Here, $c_{w,i}$ and $c_{L,i}$ are the maximum width and the length of crack branch i (Korswagen et al., 2019). This quantity was used to track the intensity of damage, independent of specimen size, during in-plane cyclic tests on solid clay-brick specimens (Korswagen et al., 2019).

Dolatshahi and Beyer (2019) used the notion of fractal dimension to correlate stiffness and strength reduction with the crack patterns observed in shear-compression tests on brick masonry walls conducted by Petry and Beyer (2015a). Rezaie et al. (2020c) showed that the fractal dimension of crack patterns is very sensitive to the settings of the box-counting method used to determine it. They thereby proposed a set of recommendations to select the correct set of parameters for computing the fractal dimension of crack patterns on masonry walls.

Most unreinforced masonry buildings have walls covered with layers of plaster, which are sometimes considered as artistic assets. To understand how the damage in plaster is related to the structural damage, a number of studies can be found in the literature. Calderini et al. (2015) considered two groups of damage states referencing the structural and non-structural (plaster/artistic asset) components. They found a linear trend between the crack width and the drift of the panel at peak force by analyzing the results of two experimental campaigns on stone masonry panels, namely Genoa's panels and Ljubljana's walls. They also found that Genoa's panels never reached the A4 damage limit state (plaster collapse), and, in most of the walls in Ljubljana, the drift at A2 damage state (first visible structural crack on the plaster) was considerably lower than the drift at the FC damage limit state (first structural crack). On average, the ratio of drift at first visible structural crack on the plaster to the drift at first structural crack (on masonry) was around 0.67. However, this observation is significantly lower than the value of 0.91 reported from cyclic test results on stone masonry walls by Godio et al. (2019), wherein the walls were plastered on one side while the other side was left bare. A possible reason for this discrepancy is that both campaigns visually detected cracks on the unplastered side of the wall, and visual inspection is always prone to error. As another alternative, Didier et al. (2018) defined two quantities, namely the normalized crack area (NCA) and normalized crack length (NCL) defined in Eqs. (4.3) and (4.4), respectively, to quantify the accumulation of damage to plastered clay brick walls tested under cyclic shear-compression loading. In their testing campaign, they used a two-dimensional digital image correlation (DIC) method to obtain the in-plane deformation of specimens. The two quantities are defined as follows:

$$\mathrm{NCA} = \frac{\text{damaged area of the plaster}}{\text{total area of the plaster}} = \frac{\text{number of white pixels on cumulative von Mises strain map}}{\text{total number of pixels on cumulative von Mises strain map}}. \tag{4.3}$$

$$\mathrm{NCL} = \frac{\text{sum of length of all cracks}}{\text{length of wall diagonal}} = \frac{\text{sum of crack perimeters}/2}{\text{length of wall diagonal}}. \tag{4.4}$$

They obtained the damaged region by setting a threshold on the von Misses strain map to produce a binary image where white pixels represent damage (crack in their work) (Didier et al., 2018). They found that the normalized crack area is a better damage descriptor, as it more reliably represents the actual damage than the normalized crack length.

Using the normalized cumulative cracked area as a damage measure, Abbiati et al. (2018b) obtained a probabilistic fatigue model to predict plaster cracking. Xie et al. (2020) reviewed existing methods for damage states of infill masonry walls and categorized them into three distinct classes based on: phenomena, force-displacement skeleton curves, and maximum crack widths. They tested nine full-scale plastered masonry infilled reinforced concrete frame specimens under cyclic shear-compression loading and obtained the fragility functions with the mentioned methods. They made two important conclusions: 1) defining damage states based on the maximum crack width yielded the least dispersion in the determination of fragility functions; 2) applying plaster did not have a statistically significant effect on the obtained fragility functions. In other words, the maximum crack width observed on both sides of the specimens was almost equal.

From the perspective of repairability of cracks, it is also desirable to use the crack width as a damage variable to define damage limit states. For cracks with a width of less than 10 mm, Eurocode 8-Part 3 recommends sealing them with mortar or injecting them with cement grout, depending on the thickness of the masonry walls, while epoxy grouting can be used for fine cracks. Otherwise, if the crack width is greater than 10 mm, the damaged area should be reconstructed (Eurocode 8 - Part 3, 2005). Vintzileou et al. (2020) analyzed the evolution of cracking of brick masonry walls by relating the crack width to the drift demand observed on the walls tested by Petry and Beyer (2014a, 2015a). They concluded that the damage is easily repairable up to the point of reaching the force capacity of the wall due to limited crack width (Vintzileou et al., 2020). However, when the ultimate drift capacity (20% drop in force) is reached, it is advised to call this near collapse state (from Eurocode 8 - Part 3 (2005)) and consider the damage as not easily repairable (Vintzileou et al., 2020). This is partly due to the disintegration of masonry (for example, due to X-shaped cracks) and partly to the increase of crack width (up to 9 mm) (Vintzileou et al., 2020).

Throughout the presented literature, the crack width is mainly selected as the signature for describing a crack network. However, several questions related to the cracking of stone masonry walls under shear-compression loading are still not fully addressed: What is the influence of the loading protocol on the crack width distribution? What is the relationship between the maximum crack width at the maximum drift demand and the residual drift? What is the influence of the shear span and axial load ratio on the maximum crack width of damaged stone masonry walls? Answering these questions is important and useful from a variety of perspectives: a) understanding the impact of the above-mentioned parameters on maximum crack width can aid in revising future post-earthquake damage assessment recommendations to include those factors; b) the relationships between crack width at maximum drift demand and residual crack width can be used to validate numerical models that capture cracking, such as the advanced numerical methods developed by Zhang and Beyer (2019); Zhang et al. (2017) and Saloustros et al. (2017, 2015, 2018); c) within the scope of a rapid post-earthquake assessment of damaged masonry buildings using artificial intelligence and image data, the prior incorporation of experimentally verified knowledge can improve predictive models.

In this study, we address these topics using the experimental data obtained during quasi-static cyclic shear-compression loading on six large-scale rubble stone masonry walls. We detect and quantify cracks based on images taken systematically during the loading sequence and processed using DIC. Crack pixels are detected using a deep learning model previously proposed by the authors (Rezaie et al., 2020a). The cracks are then skeletonized and cleaned. Finally, the crack width is automatically computed from the DIC outputs for all cracks using an in-house-developed Python script. We use this developed crack detection and quantification pipeline to investigate the above-mentioned questions in greater depth.

The paper is structured as follows: Section 4.2 explains the experimental data. Section 4.3 elaborates the steps required to detect, skeletonize, clean, and quantify the crack width. Section 4.4 discusses the previously mentioned questions, and Section 4.5 summarizes the main findings of this study.

Table 4.1 – Test matrix showing shear span and axial load ratio for the cyclic shear-compression tests on six full-scale rubble stone (RS) masonry walls conducted by Rezaie et al. (2020b).

Specimen label	σ/f_c	H_0/H
RS1	8%	0.5
RS2	25%	0.5
RS3	17%	0.5
RS4	25%	1.0
RS5	25%	1.5
RS6	17%	1.0

4.2 Description of experimental data

In an earthquake, buildings are subjected to gravity loads and dynamic loads resulting from the ground motion and the dynamic response of the building. Though the ground moves in all three directions, the most damaging components are the two horizontal directions. The forces generated from these ground motions can be mimicked in a conventional experimental test to determine the cyclic performance of load-bearing walls, termed the quasi-static cyclic shear-compression test (Godio et al., 2019; Petry and Beyer, 2015a; Anthoine et al., 1995; Salmanpour et al., 2015). In this test, a constant vertical load and a cyclic horizontal displacement are applied to the specimen. The cyclic horizontal displacement follows a protocol that specifies the increase in displacement amplitude from one cycle to the next.

In an experimental campaign conducted at École Polytechnique Fédérale de Lausanne (EPFL), cyclic shear-compression tests on six full-scale plastered rubble stone masonry walls, labelled RS, were carried out (see Figure 4.1). This testing campaign was primarily designed to enrich the existing database in terms of the response of stone walls to shear-compression loading (Vanin et al., 2017). Of particular interest were the drift limit states of rubble stone masonry walls, which is the most irregular and weakest masonry typology (typology A according to the Italian code (Ministry of Infrastructures and Transportation (MIT), 2009)). Two main quantities were varied between the specimens, the axial load ratio σ/f_c and the shear span ratio H_0/H, as previous experimental and numerical research studies highlighted their effects on the drift and force capacity and effective stiffness of the walls (Vanin et al., 2017; Wilding and Beyer, 2018a,b; Dolatshahi et al., 2018). The axial load ratio is the ratio of the applied vertical stress σ to the compression strength f_c of the masonry, and the shear span ratio is the ratio of the height of zero moment H_0 to the height of the wall H. The test matrix including specimen labels, the axial load ratio, and the shear span ratio are summarized in Table 4.1. For a more detailed explanation, refer to Rezaie et al. (2020b).

In this campaign, stereo-camera systems were used to acquire gray-scale images from walls wherein one side was plastered while the other remained unplastered during the entire loading sequence. Figure 4.1a shows the testing set-up, though only the stereo system placed on the plaster side of the wall is highlighted; the stereo system on the stone side is not visible behind

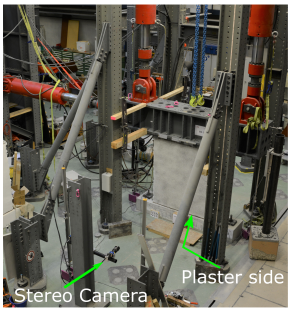

(a)

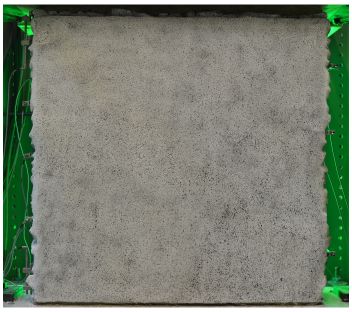

(b)

(c)

Figure 4.1 – View of the (a) test setup; (b) plaster side; (c) masonry (stone) side for the cyclic shear-compression tests on six full-scale rubble stone masonry walls conducted by Rezaie et al. (2020b).

the wall. The wall surfaces were painted white and then sprayed with a black speckle pattern (see Figure 4.1b, c) to enhance the use of DIC to compute the 3D displacement of the visible surfaces.

Gray-scale images were taken as inputs to the DIC method at specified time intervals and were synchronized with the value of the vertical and horizontal forces applied to the specimens. Therefore, there are corresponding gray-scale images for each data point of the horizontal force-displacement response of the walls. As an illustration, Figure 4.2 plots the horizontal force-drift response of specimen RS6 and provides images taken at two states A and B, where the horizontal force is almost zero. These images are 4384 x 6576 pixels in size, where each pixel corresponds to 0.43 mm.

4.3 Detection and quantification of crack pattern

4.3.1 Crack segmentation

The process of using deep learning for crack detection and segmentation from images is a well-studied problem, and there are several articles addressing this using machine learning methods (Rezaie et al., 2020a; Cha et al., 2017; Zou et al., 2019; Pantoja-Rosero et al., 2021; Dais et al., 2021; Liu et al., 2019; Mosinska et al., 2018; Chaiyasarn et al., 2018). To detect surface cracks developed in the plastered side of the walls in this study, we used a deep convolutional neural network trained in our previous study for detecting crack pixels on laboratory images (Rezaie et al., 2020a). The trained encoder-decoder architecture is a variant of U-Net (Ronneberger et al., 2015) and includes a pre-trained VGG16 (Simonyan and Zisserman, 2015) on the ImageNet database (Russakovsky et al., 2015) as an encoder. For a detailed analysis of the performance of the trained network in segmenting crack pixels, refer to Rezaie et al. (2020a). An illustration of a gray-scale image taken from specimen RS5 at the drift value of 1.66% and the corresponding crack mask predicted by the trained deep model is shown in Figure 4.3.

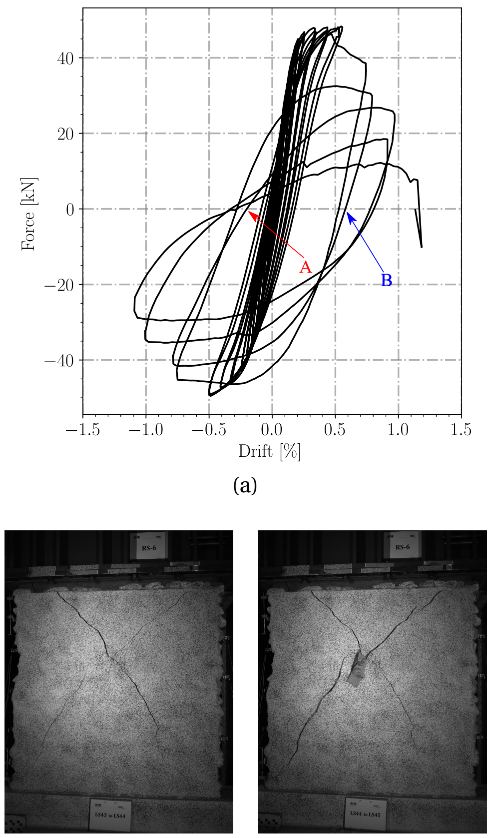

(a)

(b) (c)

Figure 4.2 – (a) Horizontal force-drift response of specimen RS6 for the cyclic shear-compression tests conducted by Rezaie et al. (2020b); (b) the image taken at state A, corresponding to the data point where the horizontal force is almost 0 and the drift value is equal to -0.28%; (c) the image taken at state B, corresponding to the data point where the horizontal force is almost 0 and the drift value is equal to 0.57%. Both images shown here were taken by the stereo system's right camera located on the plaster side of the wall. Note that the brightness of images was adjusted and they were cropped for enhanced visualization.

It can be seen that the prediction made by the deep learning model (Rezaie et al., 2020a) is pixel-wise, meaning that all pixels belonging to a crack are detected and presented as white pixels. Note that the prediction mask in this figure is cleaned to reflect only the area of interest, meaning that falsely detected crack pixels outside of the wall area were removed.

4.3.2 Crack cleaning and skeletonization

Errors are often present in deep-learning predictions used for crack detection; some cracks can be missed, and some pixels that do not belong to a crack can be misclassified as cracks. Here, we apply several post-processing steps to obtain a clean crack pattern and remove noisy results. These steps and the reasons for implementing them are outlined briefly in the following:

(a) (b)

Figure 4.3 – Example of crack segmentation by the trained deep learning model developed by Rezaie et al. (2020a). (a) Gray-scale image of specimen RS5 at the drift value of 1.66% that was inputted to the deep model. The brightness of this image was changed for enhanced visualization. (b) The cleaned output of the deep model, which is a binary image where white pixels represent cracks and black pixels represent non-cracked areas of the wall. Note that in this crack mask, the false-positive crack pixels that were outside the plaster area were removed.

- **Filling holes**: To compute the crack width from the DIC output, we first find the centerline of the cracks (see Section 4.3.3). To avoid branching of the centerlines, holes in the crack maps must be filled. This operation is detailed in Section 4.3.2.
- **Skeletonization**: The centerlines are determined by applying a skeletonization algorithm to the detected crack pattern (see Section 4.3.2).
- **Linking crack skeletons**: To preserve the continuation of crack centerline networks, centerlines close to each other are connected (see Section 4.3.2).
- **Remove short crack branches**: The crack segmentation model falsely classifies some non-crack pixels as cracks (Rezaie et al., 2020a). These false positives appear as a small group of pixels. To remove these misclassified crack pixels, a threshold is applied to the area of the connected skeleton crack pixels (see Section 4.3.2).

All these steps were implemented in a Python code using the open-source image processing libraries scikit-image version 0.16.2 (Van der Walt et al., 2014) and mahotas version 1.4.9 (Coelho, 2012). The implemented pipelines will be shared in an open-source Python package called “PyCrack" (https://github.com/eesd-epfl/PyCrack) aimed at quantifying crack patterns on structural systems using physics-based and machine–learning-based crack features. This package is developed and maintained by the Earthquake Engineering and Structural Dynamics (EESD) group at EPFL.

Filling holes

The crack pixels segmented by the deep model in Rezaie et al. (2020a) sometimes contain small holes that can damage the skeletonization of crack patterns. To fill these gaps in the detected crack maps, a mathematical morphology operation called closing was applied (Haralick et al., 1987) using a square structuring element of 10 x 10 pixels (4.3 x 4.3 mm^2). The size of the structuring element needs to be chosen on case-by-case basis. This filling operation was implemented using a scikit-image function called skimage.morphology.binary_closing, and an example image that has undergone this process is shown in Figure 4.4.

(a) (b) (c)

Figure 4.4 – Illustration of the binary closing operation used to fill gaps in detected crack patterns. (a) An image patch sized 256 x 256 pixels was extracted from the original image; (b) the detected binary image of crack pixels with holes; (c) the result after binary closing was performed using a square structuring element of 10 x 10 pixels.

Skeletonization

Each detected crack branch was reduced to a single-pixel-wide skeleton using the function morphology.skeletonize from the scikit-image library. Figure 4.5 illustrates this operation for an example image.

Linking crack skeletons

After extracting the crack skeletons, some crack branches were fragmented (see Figure 4.6a). To connect these fragmented skeleton branches, the following steps were implemented: (a) Find the distance transform of the inverse image (see Figure 4.6b); (b) Apply a threshold to the distance map; (c) Skeletonize the thresholded image from the previous step (see Figure 4.6c).

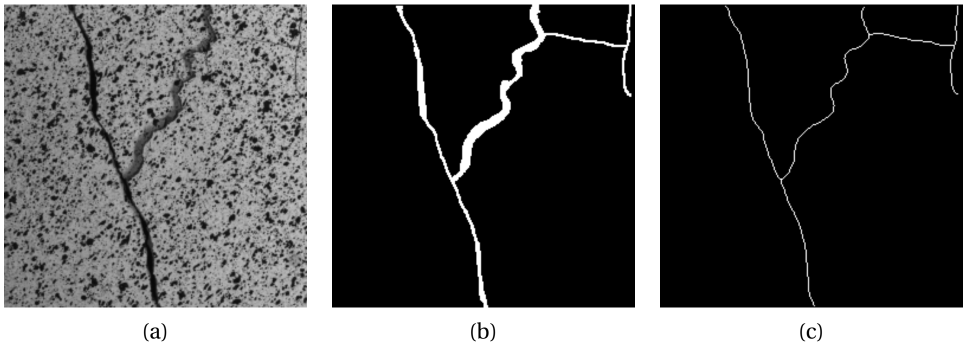

Figure 4.5 – Illustration of crack skeletonization. (a) An image patch of 256 x 256 pixels was extracted from the original image; (b) the detected binary image of crack pixels; (c) the crack skeleton.

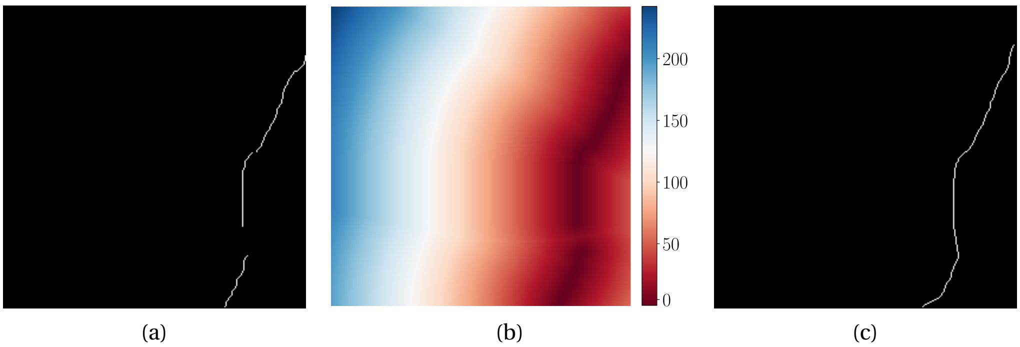

Figure 4.6 – Illustration of linking crack skeletons. (a) An image with fragmented crack skeletons; (b) distance transform of the inverse crack skeleton image; (c) the result after applying a threshold on the distance transform and then thinning.

Remove small crack skeleton

Using the function regionprops from the scikit-imag library, crack skeleton branches with areas smaller than a threshold of 30 pixels (~13 mm) were removed. Figure 4.7 illustrates the detected crack skeleton formed via the reduction of binary crack maps to single-pixel wide objects after applying the aforementioned steps for the example image shown in Figure 4.2b. Note that the crack detection and skeletonization were performed individually at a given time step irrespective of the previous or next time step.

4.3.3 Computation of crack width

The output of the DIC method is a 3-dimensional (3D) displacement field on a grid of points. We developed a Python code to compute crack width from the displacement field extracted from the VIC-3D software. Gehri et al. (2020) have also recently developed a MATLAB-based software to compute crack kinematics from the outputs of the VIC-3D software, though ours

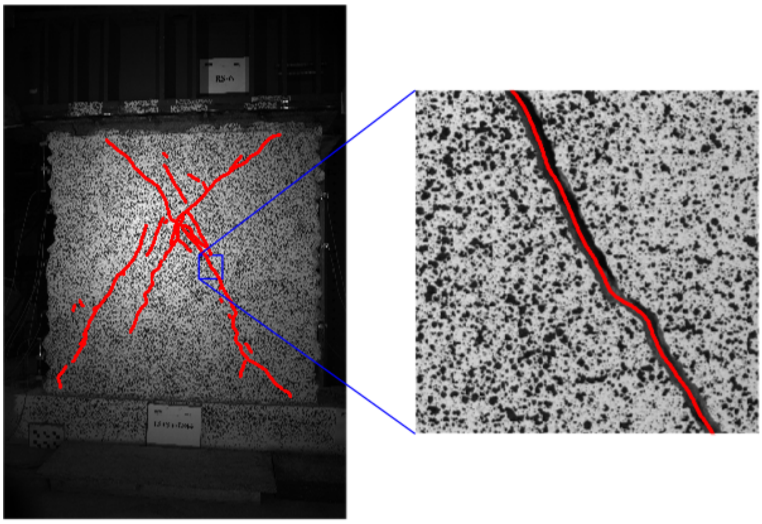

Figure 4.7 – Illustration of the detected crack centerlines for the example image shown in Figure 4.2b. The crack centerlines (skeletons) are highlighted in red.

differs in several aspects, including the detection of cracks, computation of crack orientation and width, and dealing with outliers. The steps implemented in our code are summarized in the following:

1. **Computing crack skeleton pixel orientation**: For each crack skeleton pixel, the orientation with respect to the horizontal axis (axis c in Figure 4.8) was computed. To do this, the center of a square kernel of 21 x 21 pixels, or 9 x 9 mm^2, (shown as k in Figure 4.8) was placed at each crack skeleton pixel, and a linear line was fitted to the crack pixels present in the kernel (see Figure 4.8). The slope of the line was considered to correspond to the local orientation of the crack skeleton pixel. The angle of crack pixels ranges between -90° to 90° and is positive when rotating clockwise and negative when rotating anti-clockwise with respect to the axis c in Figure 4.8.

2. **Reading horizontal and vertical displacement of two sides of the crack surface**: For each crack skeleton pixel, we obtained the horizontal and vertical displacement of two points placed 40 pixels (~17 mm) away from the crack pixel in the direction perpendicular to the orientation of the crack pixel.

3. **Computing crack width**: Using the computed displacement vectors of two points at both sides of the crack surface (points A and B in Figure 4.8) and the orientation of crack pixels in previous steps, we projected the displacement vectors perpendicular (along the axis n in Figure 4.8) and parallel (along the axis t in Figure 4.8) to the crack surface. For each crack pixel, the component perpendicular to the crack surface is the crack width.

4. **Removing outliers**: The displacement field computed by the DIC can produce noisy results, which were removed using two steps:

1) One output of the VIC-3D software is the sigma field (in terms of pixel), which is the confidence bound in the match considered as the larger eigenvalue of the inverse of the Hessian matrix of the image (Sutton et al., 2009). Sigma values larger than 0 indicate noise. A user-defined upper-bound was set to discard the noisy displacement field of points A and B. This upper bound was not constant and varied between analyzed images, selected based on engineering judgment. We checked whether computed crack width is physically meaningful or not.

2) After the first step for outlier removal, there were still several cases with a computed maximum crack width that was too large with no physical meaning. As a second step for removing outliers, we first computed the crack width directly from the crack masks segmented by the deep learning method. Here, the crack width was calculated as the number of crack pixels perpendicular to the crack orientation times the mm/pixel ratio. We then discarded the results with a significant difference between the crack width computed directly from the extracted crack masks and the DIC outputs. The threshold here also varied between images and could be adjusted by the user.

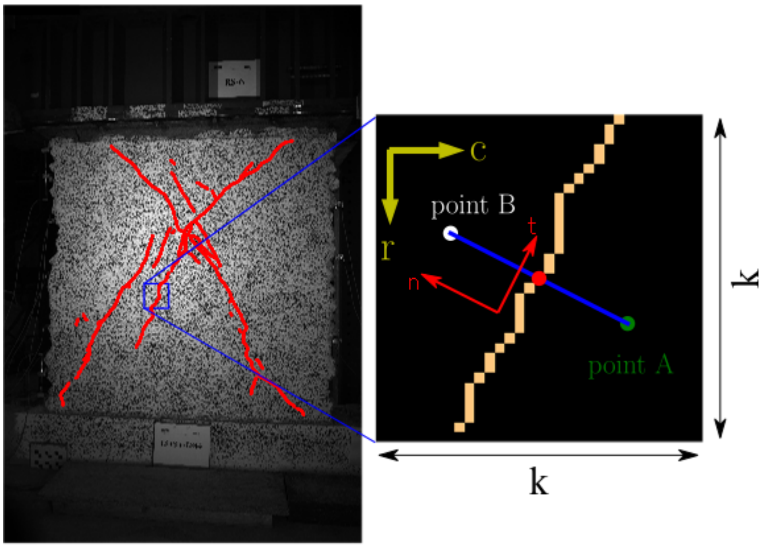

Figure 4.8 – Illustration of the computation of the crack pixel orientation and the coordinates of the points A and B. Here, the crack pixel of interest is highlighted in red, k is the size of the kernel in terms of pixel, and *c* and *r* are the local coordinate system in the kernel.

To verify the adequacy of the chosen kernel size, 21 x 21 pixels (~9 x 9 mm^2), and the distance from the crack pixel, 40 pixels (~17 mm), we compared the crack width computed by our code with the manual measurement of crack width using a crack gauge at certain locations on the plaster. The crack gauge could measure a discrete set of crack widths of 0.1, 0.15, 0.20, 0.25, 0.30, 0.35, 0.40, 0.50, 0.60, 0.80, 1.00, 1.50, 2.00, 2.50 mm. The comparisons are summarized in Table 4.2. Here it can be seen that the crack widths measured by the crack gauge and those obtained by our code are satisfactorily close.

Table 4.2 – Comparison of the crack width at certain locations on the plaster side of the walls measured by a crack gauge during the tests and computed by our code.

Index	Specimen label	Horizontal force [kN]	Drift [%]	Crack width [mm]	
				Crack gauge	DIC
1	RS3	-49.0	-0.20	2.50	2.87
2	RS3	-40.0	-0.31	1.00	1.10
3	RS4	-55.0	-0.15	0.50	0.48
4	RS4	-54.0	-0.15	0.60	0.66

To explore the sensitivity of the kernel size (k) and the distance to the crack pixel on the measured crack width, Figure 4.9 plots the crack width as a function of these two parameters. Regarding the distance to the crack (Figure 4.9a), at up to 40 pixels, computed crack widths for all four examples seem to be constant. However, for distances larger than 40 pixels, the computed crack width of example index 1 starts to increase with the distance. It can also be seen from Figure 4.9b that the measured crack width is not sensitive to the kernel size for the examined range. Overall, this and the comparison between the crack width measured by the crack gauge during the test and computed by the code justify the chosen kernel size of 21 x 21 pixels and the distance to the crack of 40 pixels.

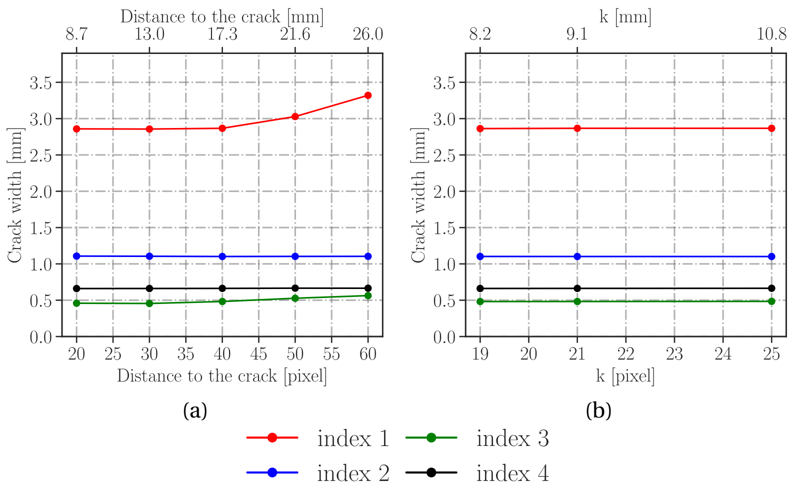

Figure 4.9 – Plot of crack width as a function of (a) distance to the crack pixel; and (b) kernel size (k) for all examples in Table 4.2.

4.4 Relationship between crack width and drift

4.4.1 Crack width at drift demand and residual drift states

Figure 4.10 illustrates the force-drift diagram of the tested walls (Rezaie et al., 2020b) along with the developed damage patterns right before the axial load failure of the walls. In general, the crack patterns developed in this test series can be categorized into two types: (a) shear cracks, which appeared in the middle of the specimens and progressively spread towards the wall corners; (b) horizontal cracks. For a more detailed explanation of each specimen's cracking sequence, refer to (Rezaie et al., 2020b).

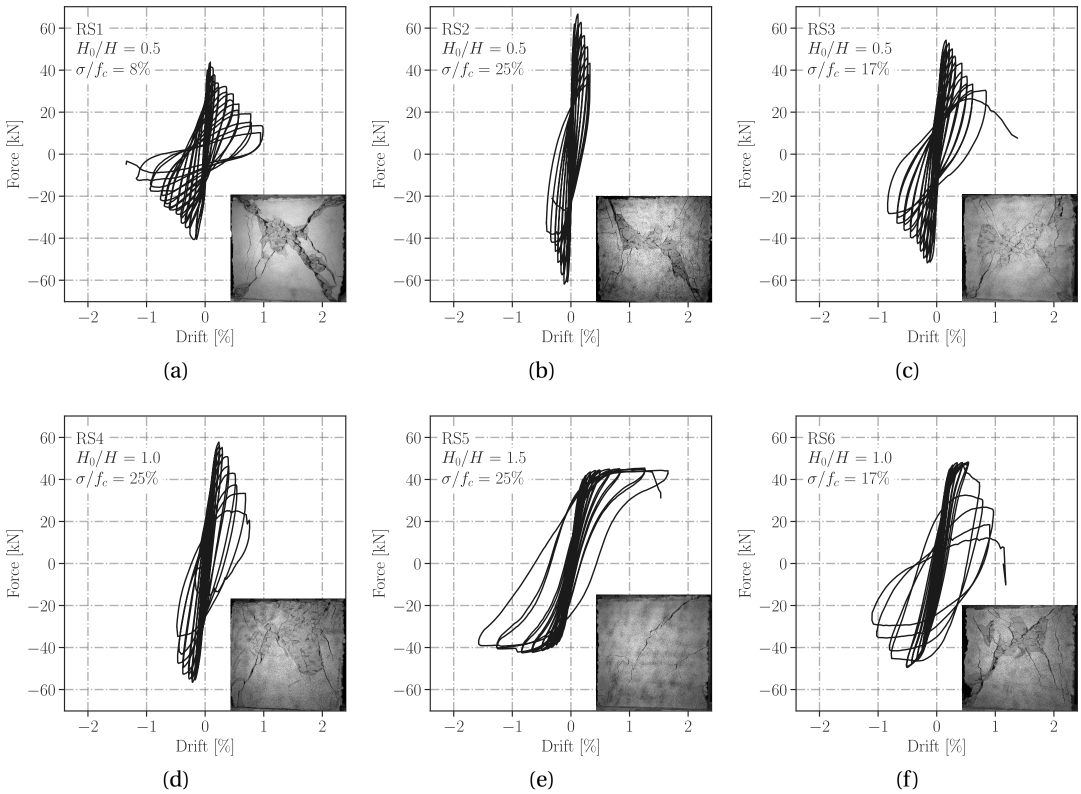

Figure 4.10 – Plot of the force-drift response and the crack pattern obtained before the loss of the axial load bearing capacity (Rezaie et al., 2020b).

Figure 4.11 plots the maximum crack width as a function of the maximum drift demand reached per cycle. The red and blue markers represent, respectively, the maximum crack width at the maximum drift demand per cycle and the residual drift, indicating the unloading from the maximum drift state to the zero-force state. The black, orange, and green dashed lines highlight drifts at peak force, ultimate, and collapse drift limits, respectively. Note that in the last cycles, the plaster detached and the cracking was considerable; since the DIC results were not reliable in those cases, the corresponding maximum crack width values are not reported in Figure 4.11.

From Figure 4.11, two crack types can be distinguished:

1. **Flexural cracks**: These cracks are oriented horizontally and open during loading and close upon load removal. Examples of such openings can be observed in the plot of the opening of horizontal cracks developed at the wall/foundation interface of specimens

RS5 (see Figure 4.11e) and RS6 (Figure 4.11f). These plots show that up to a drift smaller than that at peak force, the maximum crack width tends to zero when the specimen is unloaded.

2. **Shear cracks**: The opening and closing of these shear cracks are different from the opening and closing of flexural cracks. For this type of crack, the maximum crack width at the residual drift (zero horizontal force) is close to the crack width at the peak drift of this cycle, i.e., the crack width does not change significantly when unloading from the peak drift to the residual drift. This is very different from the behavior of the flexural cracks and results in the fat hysteresis loops with near-vertical unloading branches. Examples of such opening-closing behavior can be seen in the plot of the opening of diagonal cracks developed in the middle of specimen RS2 (see Figure 4.11b) and RS3 (Figure 4.11c).

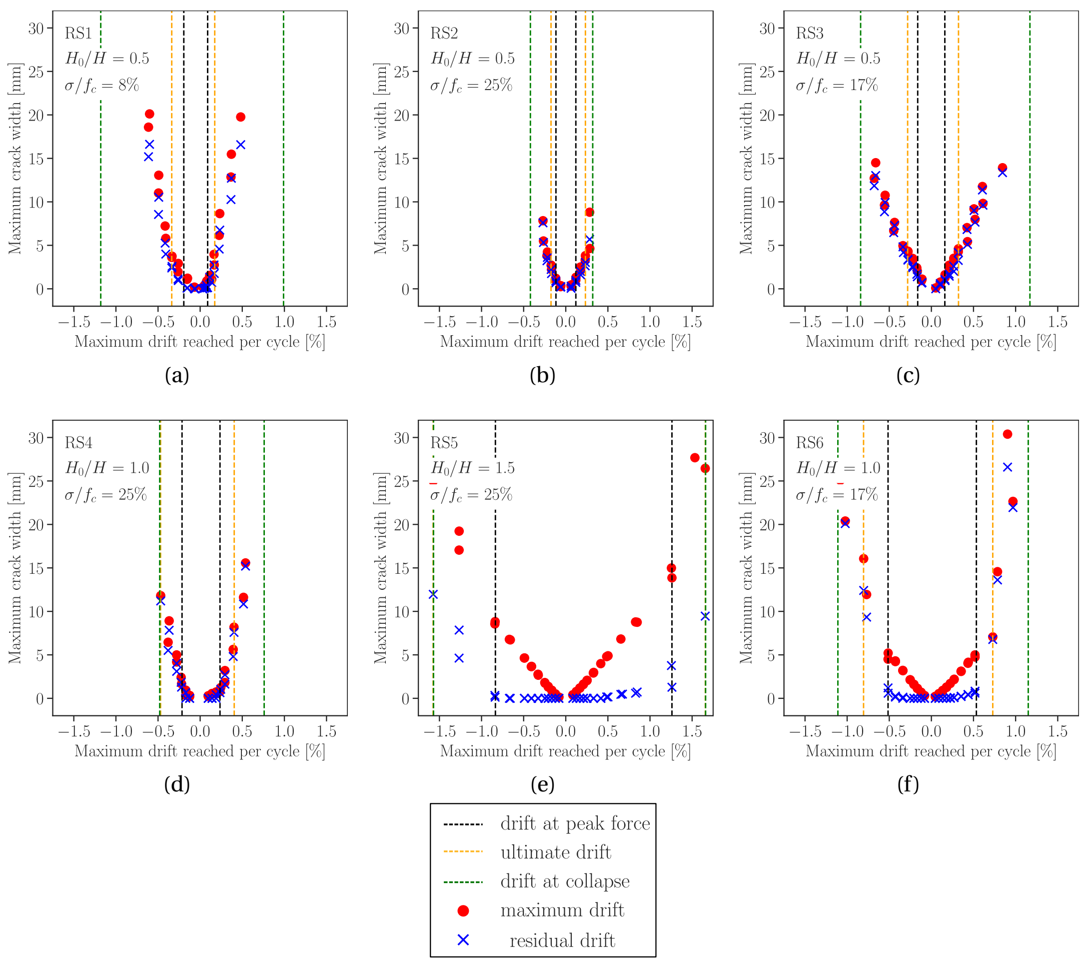

Figure 4.11 – Maximum crack width versus maximum drift reached per cycle of the tested specimens under quasi-static cyclic shear-compression tests performed by Rezaie et al. (2020b).

4.4.2 Residual crack width at peak force and ultimate drift limit state

Table 4.3 summarizes the maximum crack width at the residual drift attained at the peak force and ultimate drift limits. For both drift limits, the average residual width of flexural cracks developing at the wall/foundation interface ranges between 0.4–0.5 mm. This is expected, as the flexural cracks usually close after unloading. However, for the shear cracks, the difference is significant. The average residual diagonal crack width is 1.0 mm at the peak force and 5.5 mm at the ultimate drift limit state.

Table 4.3 – Values of maximum residual crack width after reaching the peak force and ultimate drift limit states in the quasi-static cyclic shear-compression tests performed by Rezaie et al. (2020b).

Specimen label	σ/f_c	H_0/H	Maximum residual crack width [mm] *			
			Peak force		Ultimate drift	
			Flexure	Shear	Flexure	Shear
RS1	8%	0.5	0.1	0.9	0.2	2.1
RS2	25%	0.5	0	0.7	0	2.6
RS3	17%	0.5	0	1.3	0	3.8
RS4	25%	1.0	0	1.0	0	9.4
RS5	25%	1.5	0.7	0	**	**
RS6	17%	1.0	0.6	1.0	0.5	9.6
mean ± standard deviation			0.5 ± 0.3	1.0 ± 0.2	0.4 ± 0.2	5.5 ± 3.3

* The values reported in this table are the average maximum crack opening of the positive and negative residual drifts (i.e., first and third quadrant of the force-drift plot).
** As in the envelope of RS5, the wall collapsed before reaching a 20% drop in force, the crack width values for the ultimate limit state are not reported.

4.4.3 Residual crack width as a function of shear span and axial load ratio

Figure 4.12 plots the residual shear crack width as a function of the shear span and axial load ratio for both the peak force and ultimate drift limit states. In general, there is no clear trend between the axial load ratio and the crack width. A trend can be seen at the ultimate limit state, though, where the value of the maximum residual crack width increases with the shear span ratio. Under the shear span ratio of 0.5 (walls RS1, RS2, and RS3), the average residual diagonal crack width is approximately 2.8 mm, while for a shear span of 1.0 (walls RS4 and RS6), the corresponding value is almost 9.5 mm. This may be because the experimental results showed that walls with a shear span ratio of 1.0 have a higher displacement capacity than walls with a shear span ratio of 0.5 (Rezaie et al., 2020b). It was also observed that in the post-peak regime, in general, the measured deformation tended to concentrate along previously formed diagonal cracks rather than forming new cracks, which manifests as an increase in the width of diagonal cracks. As an illustration, the concentration of deformations along diagonal cracks is shown at two instances for RS4 in Figure 4.13: (a) drift = -0.22%, force = -56.6 kN; and (b) drift = -0.36%, force = -52.7 kN. In this plot, the thickness of cracks is proportional to the crack width.

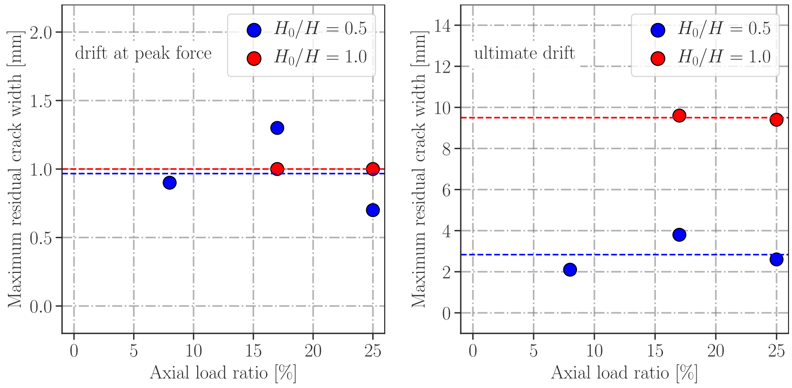

(a) (b)

Figure 4.12 – Residual crack width as a function of axial load and shear span ratio. The dotted lines represent average values.

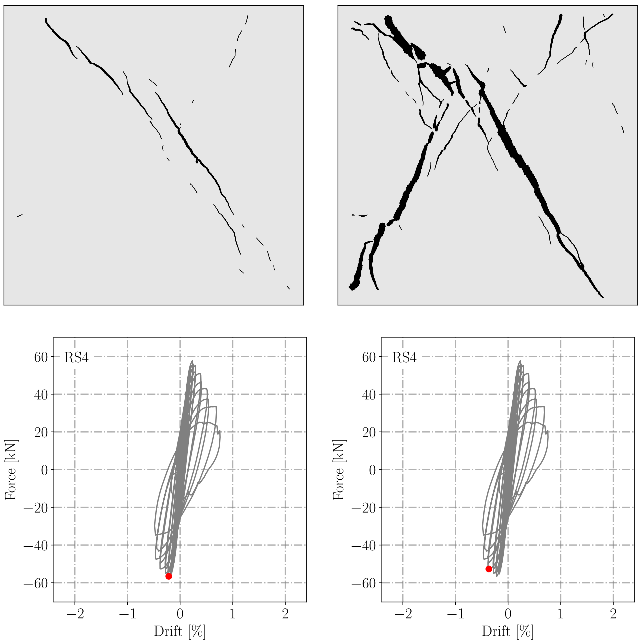

(a) (b)

Figure 4.13 – Illustration of the concentration of deformations along diagonal cracks. (a) Drift = -0.22%, force = -56.6 kN; (b) drift = -0.36%, force = -52.7 kN.

4.4.4 Dependency of crack width on the loading protocol

In the conducted testing campaign (Rezaie et al., 2020b), the horizontal displacement was applied according to a loading protocol that increased drift demand levels with two cycles per drift level. To illustrate the dependency of crack width on the loading protocol, Figure 4.14

plots the crack width at states of maximum force per cycle and residual drift for two selected points (crack index A and B) on the crack skeleton of specimen RS3. These two points were selected on two opposing propagation directions such that they had an angle of orientation of around 45° and -45°. It can be seen that the value of the crack width is slightly higher when the wall is loaded to the same level of drift for the second time. To rationalize this and to better illustrate the kinematics of the wall, displacement vector fields of specimen RS3 are shown in Figure 4.15 for the following combination of (drift, force): a) 0.0%, 21 kN; b) 0.2%, 53.0 kN; c) 0.1%, -1 kN (almost zero); d) -0.2%, -49.0 kN; e) -0.1%, 0.0 kN; f) 0.0%, 25.0 kN; and g) 0.2%, 50.0 kN. These combinations include the following states: i) when the beam is at its original position (drift = 0.0%); ii) when the maximum force is reached in a given cycle, and iii) when the force is almost zero (residual drift).

Figure 4.15a clarifies that the wall was divided into four semi-rigid blocks consisting of top/bottom triangles and left/right quadrilaterals at this state. It appears that when the wall is loaded in the positive or negative direction (see Figure 4.15b, Figure 4.15d, and Figure 4.15g), blocks above the formed diagonal cracks move with the beam while the bottom triangle remains in its original position. This also illustrates that when the beam is at its original position (drift = 0.0%), there is a considerable residual displacement in the left/right quadrilaterals, which is why the crack width is higher in the second cycle. To better illustrate the residual displacement of the two lateral blocks, Figure 4.16 plots the difference between the displacement vector fields shown in Figure 4.15a-f and Figure 4.15b-g. Each color used in this plot represents a vector in the color code shown in Figure 4.16c. The white color represents the zero displacement vector $\vec{0}$.

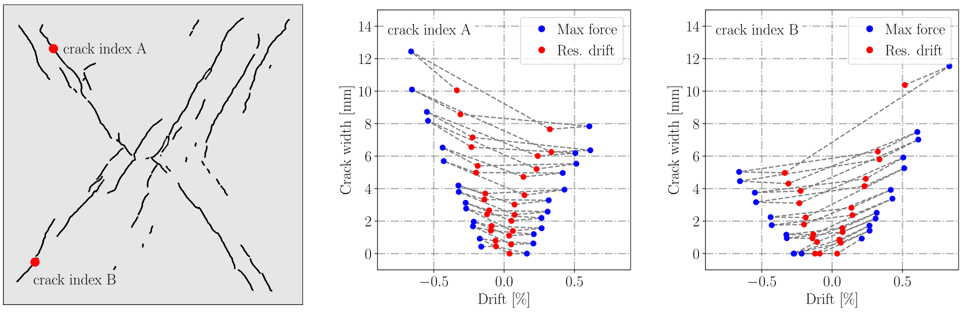

(a) (b) (c)

Figure 4.14 – (a) A sketch of the crack pattern of specimen RS3, and a plot of crack width as a function of drift for crack index (b) A and (c) B.

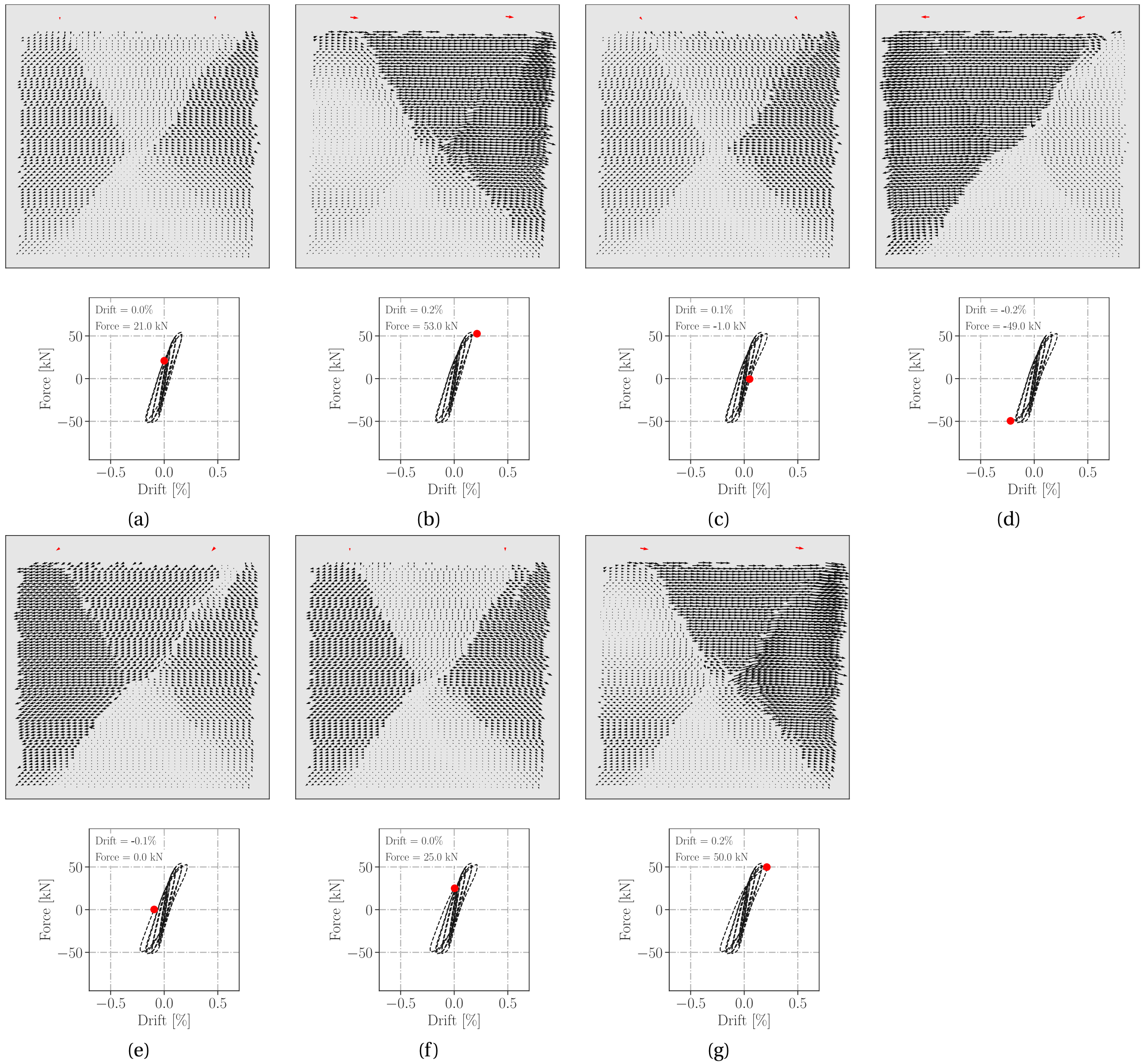

Figure 4.15 – (a–g) Plots of the displacement vector field of specimen RS3 at various force/drift combinations. The reference point is the undeformed state of the wall before the application of vertical force. The red arrows show the displacement vector of the loading beam. Note that the displacement vector plots have been horizontally flipped to align the horizontal loading direction with the positive direction of the drift coordinate axis in the force-drift plots.

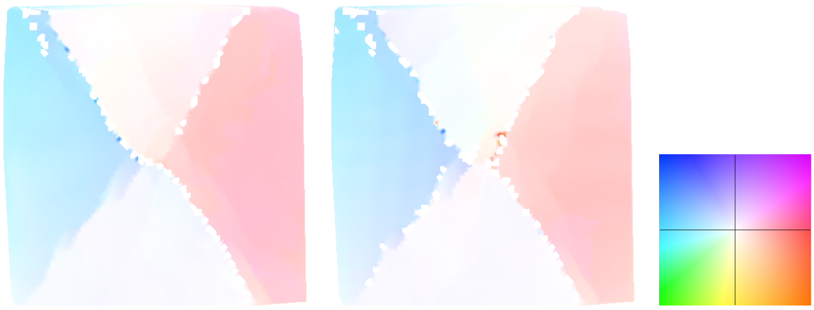

(a) (b) (c)

Figure 4.16 – Plot of the difference between the displacement field shown in (a) Figure 4.15f and Figure 4.15a; and (b) Figure 4.15g and Figure 4.15b. (c) The displacement vector color code.

To investigate how the distribution of residual crack width changes between two consecutive cycles, Figure 4.17 provides the box plot of residual crack width at various residual drift levels and for different walls. In general, there is a shift in the distribution and the maximum value, and the 75th percentile increases in the second cycle.

4.5 Conclusion

Maximum crack width is mainly used in the literature to express the level of damage due to a cyclic horizontal load applied to a masonry pier. In this study, we further investigated: a) the influence of several parameters affecting the maximum crack width, including the shear span, axial load ratio, type of crack, and loading protocol; and b) how the maximum crack width changes from the applied drift demand to the residual drift.

To address these topics, we used data from an experimental campaign employing quasi-static cyclic shear-compression tests on six full-scale rubble stone masonry walls conducted at École Polytechnique Fédérale de Lausanne (EPFL). One side of each wall was covered with plaster while the other one was left bare. Two stereo-camera systems were used to record gray-scale images of the surface of the specimens during the application of the load. These images were used as input for the DIC method to compute the displacement field as well as for the deep model previously developed by the authors (Rezaie et al., 2020a) to detect crack pixels.

A series of Python codes was developed to: a) post-process the crack masks outputted by the deep model, including filling gaps, skeletonization, linking crack skeletons, and removing small cracks; and b) compute the crack width for each crack skeleton pixel from the DIC outputs. To determine the orientation of the crack skeleton pixels, we verified the choice of the kernel size. We also verified the distance to the crack pixel, which is used to obtain the displacements of the points on two sides of the crack fronts, by comparing the crack width computed from the DIC outputs with the values recorded using a crack gauge during the test survey. The codes were used to automatically compute crack width at the instance of residual

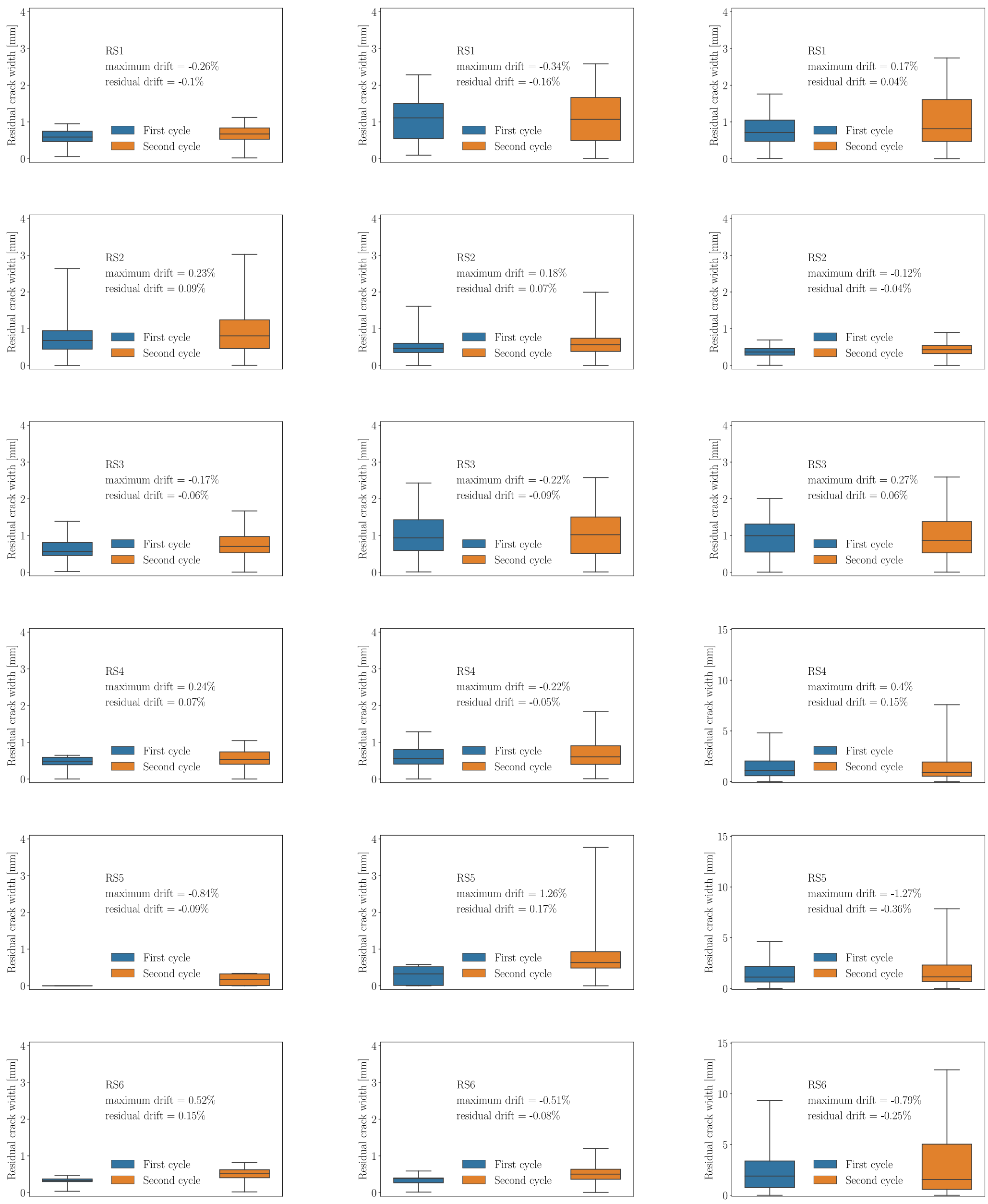

Figure 4.17 – Histogram of the residual crack width at two consecutive cycles for different walls.

drift, maximum force, and maximum drift demand per cycle and to investigate a number of factors on the crack width values.

The following summarizes the main findings:

- Two types of cracks developed in the tested walls: flexural and shear. It was shown that when moving from the applied drift demand to the residual drift, the maximum diagonal shear crack width did not reduce significantly, while the flexural cracks tended to close. This finding has practical implications on post-earthquake assessments: (i) For diagonal shear cracks, the residual crack width measurements after an earthquake can approximate the crack width at the peak displacement demand. Conversely, if experimental campaigns only report crack widths at peak drift, these values can be used to assess limit states after earthquakes. (ii) Some documents (e.g. AeDES (Baggio et al., 2007) and FEMA 306 (1998)) do not indicate whether the reported diagonal crack widths in masonry walls are at peak or residual. Our results suggest that this missing information does not compromise the application of the document.

- No clear trend could be observed between the axial load and shear span ratio and the maximum residual crack width at the peak force limit state. However, at the ultimate drift limit state, the maximum residual crack width obtained in walls with a shear span ratio of 1.0 was significantly higher than walls with a shear span ratio of 0.5. We argued that the higher drift capacity of the cantilevered walls and the concentration of residual cracks along the diagonal cracks are the reasons for obtaining higher residual crack width for walls with a shear span of 1.0.
- The crack width increased in specimens loaded to the same level of drift for the second time, which shows the dependency of crack width on the loading protocol. Plotting the displacement vector fields revealed that the selected specimen (RS3) was divided into four semi-rigid blocks, top/bottom triangles and left/right quadrilaterals. The bottom triangle remained in its original position during the loading sequence, while the top triangle moved with the loading beam. The residual displacement of the left and right quadrilaterals was considered to be the main reason for the increase in crack width in the second round when the same level of drift was reached for the walls with diagonal shear cracks. Additionally, the increase in crack width in the second cycle was shown using box plots of residual crack width at two consecutive cycles. The maximum crack width and the 75th percentile were higher in the second cycle compared to the first.

In this study, the crack detection was conducted individually for each image without considering the previous or the next recorded images. In future works, incorporating time could improve the detection of crack pixels. Additionally, other features such as the fractal dimension, density of cracks, length, complexity dimension, etc. can be used to quantify crack patterns and correlate them with the degradation of force, drift capacity, and stiffness of the wall. This information can be used to improve automated post-earthquake assessments.

Acknowledgments

This project is supported by the Swiss National Science Foundation (grant 200021_175903/1 “Equivalent frame models for the in-plane and out-of-plane response of unreinforced masonry buildings”).

5 Crack quantification: Fractal dimension

This chapter represents the slightly modified post-print version of the article:

Rezaie, A., Mauron, A.J. and Beyer, K., 2020. "Sensitivity analysis of fractal dimensions of crack maps on concrete and masonry walls". *Automation in Construction*, 117, p.103258.

The formatting and numbering of equations, tables and figures have been adapted to this document. The contributions of the first author are: methodology, validation, formal analysis, investigation, data curation, writing - review and editing, visualization. The contributions of the second author are: help of the first author to prepare crack data. The contributions of the third author are: supervision of the first author, conceptualization, methodology, investigation, resources, writing - review and editing, funding acquisition.

Abstract

Assessing building damage after earthquakes requires a visual inspection of the damage, indicated by maps of the cracking pattern on walls, which could be standardized via automated algorithms. To quantitate this damage, fractal dimensions of these crack maps could be computed by the box-counting algorithm to capture the complexity and irregularity of the pattern. When using the box-counting method, however, the computed fractal dimensions depend on several parameters that can render the measurement ambiguous: the box size interval, the scale factor for the box sizes, the choice of breakpoint location, and the grid disposition and orientation. This paper, therefore, uses a literature search and an evaluation of crack map databases to investigate the sensitivity of the measured fractal dimensions of crack maps on reinforced concrete and unreinforced masonry walls to these four parameters. It then formulates recommendations for the choice of these factors. Because the value of the estimated fractal dimension varied by up to 0.5 depending on the assumed parameters, it is therefore important to use the same set of assumptions when comparing the fractal dimensions of crack patterns.

Keywords: Fractal; Box-counting Method; Crack Map; Concrete Walls, Masonry Walls.

5.1 Introduction

The first step in assessing the safety of buildings after earthquakes is a visual evaluation of the damage (FEMA 306, 1998), which will likely be automated in the future through high-resolution cameras mounted on unmanned aerial vehicles (UAVs). This is currently done instead via an expert assessment of the appearance of cracks in structural elements to determine the extent of the damage and to understand the behavior mode of the element and the damage severity (FEMA 306, 1998; BIRM, 2002; FEMA 307, 1998). To successfully apply unmanned imaging techniques to this evaluation, however, the extraction of the damage pattern and the interpretation of the damage should be done automatically. Towards this end, various approaches have been developed to detect cracks on images (Dung and Anh, 2019; Zou et al., 2019; Huyan et al., 2019; Liu et al., 2019; Hoang et al., 2018). To automatically interpret the extracted crack patterns and estimate the effect of the cracks on the properties of the structural elements, it is necessary to quantitatively characterize the crack pattern. When visually evaluating these patterns, physical characteristics of cracks, including the orientation, length, and width, are used (Zhu et al., 2011; Adhikari et al., 2014). When a visual inspection is replaced by image-based inspection, these crack characteristics can be complemented by other measures, such as fractal dimensions, which can only be evaluated using computational tools. A growing body of research in civil engineering involves investigating the applicability of fractal dimensions for characterizing crack patterns (Carpinteri et al., 1997, 2012; Carpinteri and Yang, 1996; Maosen et al., 2006; Yang et al., 2017; Chiaia et al., 1998; Adhikari et al., 2016; Arvin et al., 2019; Athanasiou et al., 2020; Momeni and Dolatshahi, 2019), as using fractal dimensions rather than a classical visual inspection can reduce the subjectivity of a visual assessment, which often depends heavily on the experience and expertise of the inspector (Ebrahimkhanlou et al., 2016; Farhidzadeh et al., 2013).

The notion of a fractal can be traced as far back as studies in the 1800s to early 1900s by Hilbert (1891). However, it was Mandelbrot (1982) in the 1980s who found that mathematical fractals have some common features with natural shapes (Peitgen et al., 2006). The concept of fractal dimensions has been applied in a variety of research domains, including plant science (Corbit and Garbary, 1995; Bouda et al., 2016; Berntson, 1994), neuroscience (Di Ieva, 2016), architecture (Ostwald, 2013), porous structures (Torre et al., 2016; Roy and Perfect, 2014; Dathe et al., 2006), crack maps (Ebrahimkhanlou et al., 2016; Farhidzadeh et al., 2013; Carrillo and Avila, 2017), etc., and is being used as a quantitative approach to describe the complexity, irregularity, and space-filling of objects (Mandelbrot, 1982; Corbit and Garbary, 1995; Bouda et al., 2016; Sandau, 1996; Di Ieva et al., 2007; Mandelbrot, 1967). In general, there is not a universal definition of fractals (Feldman, 2012), and different values of the fractal dimensions can be obtained for a particular set based on the applied concept (Sandau, 1996).

In deterministic fractal geometries that are generated based on a construction process, like in Figure 5.1a, a small portion of the pattern exactly resembles the larger portion (exact self-similarity) (Feldman, 2012). Real-life crack patterns, however, are only statistically or approximately self-similar, like in Figure 5.1b. Although crack maps are not perfect fractals, the notion of fractal dimensions can still be used to describe them. For example, some recent studies relate the fractal dimensions of crack maps on both concrete and masonry walls to some structural properties, like stiffness loss, strength loss, and the peak drift ratios (Ebrahimkhanlou et al., 2016; Farhidzadeh et al., 2013; Carrillo and Avila, 2017; Dolatshahi and Beyer, 2019). To compute each fractal dimension, there are various approaches, including box-counting methods, gliding box algorithm, fractal Brownian motion, area measurement methods, wavelet methods, and so on (Lopes and Betrouni, 2009; Allain and Cloitre, 1991). All of these methods have some advantages and drawbacks, which may restrict their applicability to certain types of problems (Lopes and Betrouni, 2009). In addition to the classical fractal dimension, which shows the space-filling and complexity characteristic of patterns, further types of fractal dimensions have been put forward to describe other aspects of patterns on images. Among these are the lacunarity, showing the distribution of gaps in patterns (Mandelbrot, 1982; Plotnick et al., 1993), and the succolarity, representing the connectivity of the pattern (Mandelbrot, 1982; de Melo and Conci, 2013), though these dimensions have not yet been used for characterizing crack patterns of structural elements and will not be discussed further in this paper.

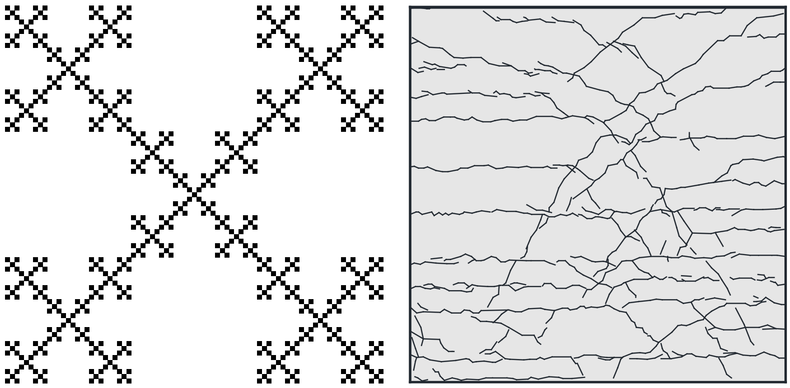

(a) (b)

Figure 5.1 – Exact vs. statistical fractal. (a) Box fractal (image adopted from (Feldman, 2012)) and (b) a typical crack map on a concrete wall surface (Almeida et al., 2016).

To evaluate the fractal dimension of crack patterns of structural elements (Ebrahimkhanlou et al., 2016; Farhidzadeh et al., 2013; Carrillo and Avila, 2017; Dolatshahi and Beyer, 2019), existing studies have used the box-counting method, which—due to its ease of calculation—is the most common (Falconer, 2004). When applying this method, several choices need to be made (Di Ieva et al., 2007) related to the grid position and orientation with regard to the crack pattern, the box sizes used, and the box size interval over which a straight line is fitted to the resulting log-log graph, which relates the number of boxes that contain a pattern pixel and the size of the boxes. It has been demonstrated that slight changes in the considered methodological factors might lead to different fractal dimension estimations (Bouda et al., 2016; Berntson, 1994; Ostwald, 2013; Ristanović et al., 2014; So et al., 2017; Foroutan-pour et al., 1999; Da Silva et al., 2006; Roy et al., 2007; Buczkowski et al., 1998; Harrar and Hamami, 2009;

Hou et al., 1990). The objectives of this paper are (i) to investigate how sensitive the fractal dimensions of crack patterns are to these choices and (ii) to formulate some recommendations for these parameters. For this purpose, we review both the parameter choices in existing crack-pattern studies and recommendations for these parameters that have been made for patterns other than crack maps. For this purpose, we analyze crack patterns from reinforced concrete and unreinforced masonry walls. The paper begins with the definition of the fractal dimension and an explanation of the box-counting method. Afterward, we tested the sensitivity of the fractal dimensions of crack patterns to the various parameters of the box-counting method. Finally, we investigated a database of crack maps of brick masonry and concrete walls tested at EPFL (Petry and Beyer, 2015a, 2014b) to determine the extent of the influence of each parameter and provide suggestions for the standardization of these parameters.

5.2 Key definitions

5.2.1 Fractal dimension

The goal of this paper is to determine the parameters required for calculating the fractal dimension (short: dimension) of a crack map, which is considered the “set” in our fractal studies. There are various methods for determining the dimension of a set, though the common point in all methods is that dimensions measure the set at various scales and investigate how these measurements change as the scale tends to zero (Falconer, 2004). For fractal geometries and approximately self-similar patterns such as crack patterns, this dimension is a fractional number between 1 and 2, which can be computed using the box-counting method explained in the following section.

5.2.2 The Box-counting method

A box-counting algorithm is a way of computing the fractal dimension of both exactly and approximately self-similar patterns (Di Ieva, 2016; Feldman, 2012). For approximate (statistical) self-similar patterns, the fractal dimension is obtained over a given range of scales (Mandelbrot, 1967; Feldman, 2012). In the field of image processing, to investigate the dimension of binary patterns, i.e., black and white images, the pattern is covered by a set of grids with box sizes of r, and the number of boxes $N(r)$ that contain at least one black pixel is counted. The relation between r and $N(r)$ is defined as follows (Feldman, 2012):

$$N(r) = k(\frac{1}{r})^{FD} \tag{5.1}$$

where k is a constant, and FD is the fractal dimension. In practice, to compute the fractal dimension of a binary image, such as skeletonized crack patterns, these steps need to be followed:

1. **Creating a grid**: To create a grid, an arbitrary point (a) is assumed as the point where the grid is created, which is denoted as the origin of the grid (Ostwald, 2013; Karperien, 2007). In the following, it will be shown that the origin of the grid position and the orientation of the grid with regard to the crack pattern can influence the estimated fractal dimension.

2. **Placing the pattern on the grid**: In the second step, the bounding box, which is the smallest enclosing box that includes the pattern on the image (Karperien, 2007; Kaye, 2008), illustrated by the red box in Figure 5.2, is defined. The minimum and maximum sizes of the wall and bounding box are w_{min}, w_{max} and b_{min}, b_{max}, respectively. Then, a fixed point of the bounding box, the bottom left corner in this example, is placed on the origin of the Cartesian coordinate system O. For illustration, these procedures are depicted in Figure 5.2.

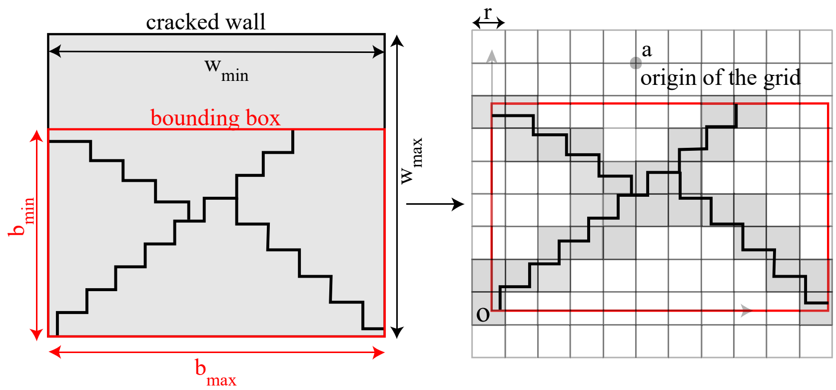

Figure 5.2 – Placing a bounding box on a grid with a box size of r.

3. **Finding the slope**: Grids of different sizes, for example, $r = 1, 2, 4, 8, \ldots, 2^n$ (scale factor of 2), are created according to step (1), and the number of boxes intersecting the object $N(r)$ is counted. To estimate the fractal dimension, $\log N(r)$ is plotted against $\log r$ and a line is fitted, typically using the least-squares method, to the points over the range where the points lie approximately on a straight line. The absolute value of the slope of the line is the estimation of fractal dimension, FD. Figure 5.3 illustrates the diagrams of $\log N(r)$ versus $\log r$ for two different cases. In Figure 5.3a, the pattern can be delineated by reporting just one fractal dimension (FD_1) since there is only one scale interval ($r_1 < R_1 < r_2$) wherein the plot is linear. However, the pattern in Figure 5.3b is more complex, and two dimensions must be reported (FD_1 and FD_2) (Peitgen et al., 2006; Kaye, 2008), because there are two intervals $r_1 < R_1 < r_2$ and $r_3 < R_2 < r_4$ wherein points fall on a straight line. As will be outlined later, one challenge is to determine over which range of scales the plot is approximately linear. In other words, the upper and lower limits of each interval, i.e. r_1, r_2, r_3, r_4, are referred to as cutoffs and must be determined. It has been shown that the choice of scale factor and the cutoffs influence the fractal dimensions of crack maps.

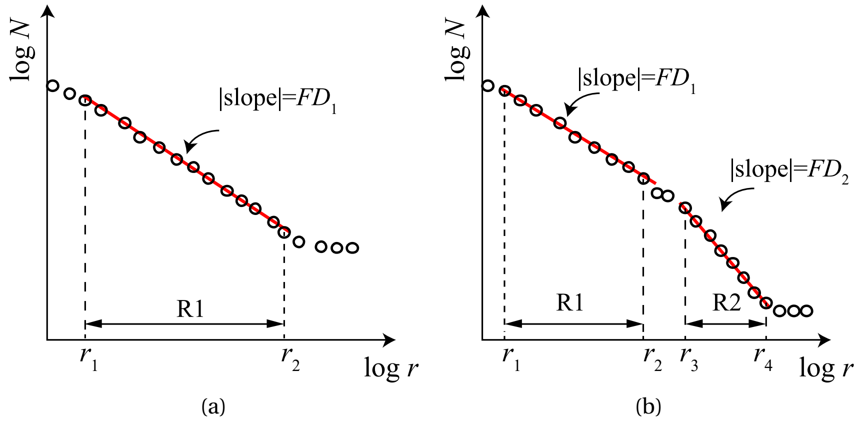

Figure 5.3 – Plot of $\log N(r)$ versus $\log r$. (a) Pattern with one FD and (b) pattern with two FDs.

With a deterministic monofractal, i.e., generated by a series of repetitive operations, a diagram like Figure 5.3a is obtained, and the absolute slope will be the estimation of the fractal dimension that can also be calculated analytically. However, as alluded to earlier, the box-counting method can also be applied to patterns that are not deterministic fractals (Di Ieva, 2016). For crack maps, the fractal dimension is obtained for the interval $r_3 < R_2 < r_4$ in Figure 5.3b, which is referred to as the fractal regime (Dolatshahi and Beyer, 2019), are suitable for characterizing the complexity of crack patterns. The fractal dimension obtained for the interval $r_1 < R_1 < r_2$ in Figure 5.3a and Figure 5.3b tends toward 1 if the crack pattern consists only of lines and not of patches (e.g. due to crushing of the material). Thus, it cannot describe the space-filling property of the crack patterns. In summary, Figure 5.4 shows different dimensions associated with different scale intervals (Farhidzadeh et al., 2013; Dolatshahi and Beyer, 2019). In this figure, regions one and two are denoted as the Euclidean regime (where the fractal dimension is one at small scales) and fractal regime, respectively. R_E is the scale at which the behavior of the pattern changes from Euclidean to fractal and is associated with the spacing between the objects in an image (Carpinteri et al., 2008). R_F is the maximum size of the bounding box for which only one box is needed to intersect the pattern. Thus, the fractal dimension becomes zero in region three (Farhidzadeh et al., 2013; Dolatshahi and Beyer, 2019).

By following these steps, it is possible to compute different FDs for the same image because some factors, like the position of the grid origin, the orientation of the grid, scale intervals, and scale factor, influence the results (Bouda et al., 2016; Berntson, 1994; Ostwald, 2013; Ristanović et al., 2014; So et al., 2017; Foroutan-pour et al., 1999; Da Silva et al., 2006; Roy et al., 2007; Buczkowski et al., 1998; Harrar and Hamami, 2009; Hou et al., 1990). Moreover, other factors, like the thickness of the crack segments, can have a bearing on the estimated fractal dimension (Gonzato et al., 2000). We will, therefore, show that it is necessary to report the estimate of a fractal dimension that is computed by the box-counting method together with the following information: 1) whether crack patterns were skeletonized or not; 2) grid position and orientation; 3) set of box sizes (or scale factor), and 4) box size interval. Parametric studies

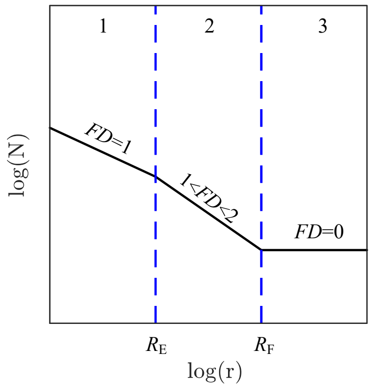

Figure 5.4 – Observed behavior of crack maps according to various scale intervals (adopted from Farhidzadeh et al. (2013); Dolatshahi and Beyer (2019)). Region 2 is a fractal regime, and regions 1 and 3 are non-fractal regimes. The range between R_E and R_F is the interval over which a fractal dimension can be defined.

on crack patterns of masonry and concrete walls provide recommendations for each factor to adjust the box-counting algorithm for obtaining the fractal dimension of crack patterns.

5.2.3 Set of example crack maps

The crack maps used as examples in this study have been obtained from three sets of experiments conducted at EPFL (Figure 5.5) (Almeida et al., 2016; Petry and Beyer, 2015a, 2014b). All three sets are quasi-static cyclic tests on walls:

- Tests on large-scale brick masonry walls (PUP Series): Tests on six brick masonry walls (PUP1-6) with dimensions of 2010 mm×2250 mm were carried out by applying different axial load ratios and shear spans, resulting in flexural, shear, and hybrid failure of the walls (Petry and Beyer, 2015a).

- Tests on small-scale brick masonry walls (PUM Series): Tests on five brick masonry walls (PUM1-5) with dimensions of 1005 mm×1113 mm were conducted to examine the influence of scaling masonry specimens on stiffness, strength, and failure mechanisms (Petry and Beyer, 2014b).

- Tests on thin reinforced concrete walls (TW Series): Five thin reinforced concrete walls (TW) were tested to investigate the in-plane and out-of-plane behavior. Test units TW1-TW4 and TW2-TW3-TW5 measured 2620 mm×2000 mm and 2580 mm×2000 mm, respectively. The spacing of the horizontal reinforcement was 200 mm and 130 mm, respectively (Almeida et al., 2016).

Based on images taken during the tests (Figure 5.6), skeletonized binary crack patterns were drawn in AutoCAD at a scale of 1 pixel = 1 mm. In this study, 83 and 45 crack maps of

(a) (b) (c)

Figure 5.5 – (a) Test setup, (b) masonry walls (Petry and Beyer, 2015a, 2014b), and (c) concrete walls (Almeida et al., 2016).

masonry and concrete walls, respectively, obtained at the maximum drift levels and zero forces were utilized. All of the images and results have been documented and are available online (https://eesd.epfl.ch/data_sets).

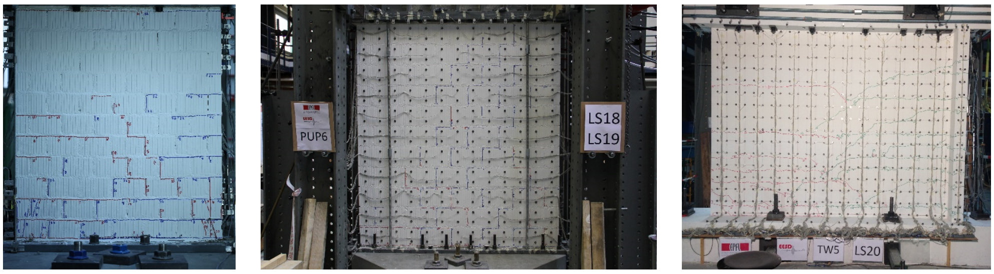

(a) (b) (c)

Figure 5.6 – Images that served as the basis for the crack maps. (a), (b) masonry walls (Petry and Beyer, 2015a, 2014b) and (c) concrete walls (Almeida et al., 2016).

5.3 Fractal dimension sensitivity to various parameters

5.3.1 Grid position and orientation

Studying the various approaches regarding how to choose the grid position can be of critical importance; the origin of the grid position and orientation of the grid are effective factors for determining FD because they affect the number of boxes intersecting the pattern (Bouda et al., 2016; Ristanović et al., 2014; Foroutan-pour et al., 1999; Da Silva et al., 2006; Roy et al., 2007; Gonzato et al., 2000; Pruess, 1995). Some researchers (e.g. Roy et al. (2007)) stated that to satisfy the boundary condition defined by Hausdorff (1919), the minimum number of boxes intersecting the object should be determined for each box size. To do so, every possible position and orientation of the pattern must be examined at each scale, and the position in which the number of boxes is the smallest must be considered. In FracLac (Karperien, 2007), a plugin for ImageJ (Rasband, 1997) that is used for fractal analysis (Di Ieva, 2016), however, a finite number of grid positions is randomly considered, and the value of FD at each grid position and orientation is computed. Gonzato et al. (2000) suggested taking at least 20 random positions and reporting the average FD as the estimation of the fractal dimension. More recently, optimization techniques have also been used to find the rotation and location of the grid where the number of boxes intersecting the pattern reaches a minimum (Bouda et al., 2016). According to Falconer (2004), there are two approaches for counting $N(r)$ for practical applications while the grid elements are rectangular: i) the number of boxes intersecting the pattern, and ii) the minimum number of boxes that cover the pattern. In the former method, there is no need to find the minimum number of boxes. In the latter, however, at each scale (r), the position and orientation of the grid at which the number of boxes intersecting the pattern is minimized must be determined.

To show the effect of grid orientation and position of the origin of the grid, an image on which there is a diagonal line is examined in Figure 5.7. In the initial configuration (Figure 5.7a, eight boxes are intersected. By changing the position of the origin of the grid in Figure 5.7b and rotating the grid in Figure 5.7c, the number of intersected boxes changes to seven. Therefore, these two factors influence the number of intersected boxes.

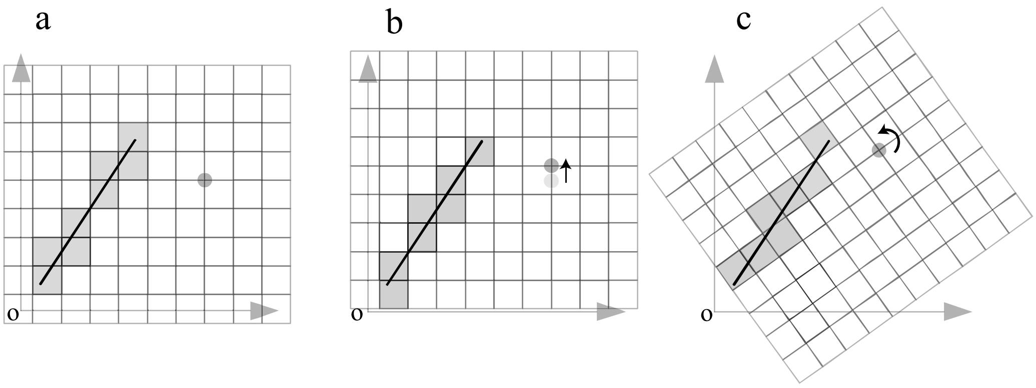

Figure 5.7 – Illustration of the influence of the origin of the grid position and the orientation of the grid. (a) Initial position, $N = 8$; (b) changing the position of the grid, $N = 7$; and (c) changing the orientation of the grid, $N = 7$.

For crack maps, as the size of the bounding box is not necessarily a multiple of the scale, the position of the origin of the grid can also influence the FD. To investigate this effect, the origin of the grid has been considered as the bottom right corner, bottom left corner, top right corner, and top left corner of the bounding box, and the orientation of the grid is assumed to be parallel to the sides of the wall. Figure 5.8 shows the difference between the maximum and minimum of the computed FDs for the crack patterns contained in the concrete and masonry databases that have a fractal behavior. Among the available crack maps, 61/83 for masonry walls and 30/45 for concrete walls show fractal behavior, i.e., the slope of the interval

$r_3 < R_2 < r_4$ in Figure 5.3b is greater than 1.0. It can be observed that the choice of the origin of the grid location can change the fractal dimension up to 0.5. Figure 5.8 shows that the effect was stronger for masonry walls than for concrete walls.

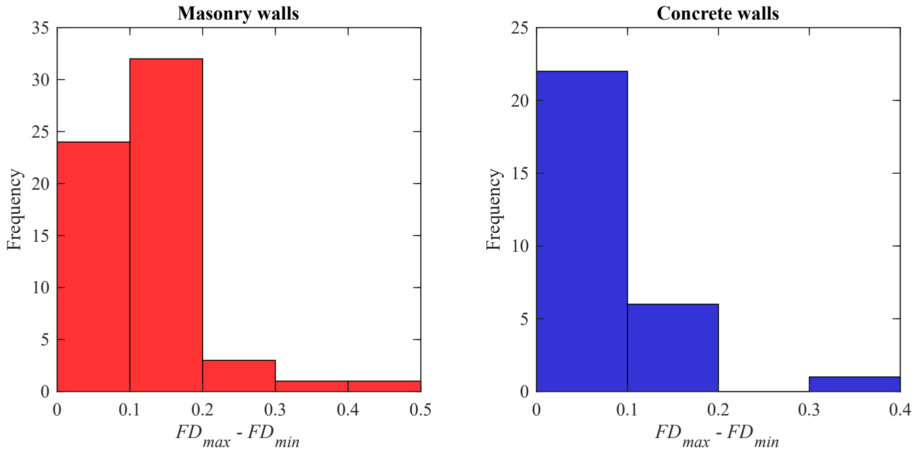

(a) (b)

Figure 5.8 – Influence of the grid position (without rotation) on the obtained FD. (a) Masonry walls, wherein 61/83 showed fractality (Petry and Beyer, 2015a, 2014b), and (b) concrete walls, wherein 30/45 showed fractality (Almeida et al., 2016).

Besides taking the four corners, choosing a random point inside the bounding box as the origin of the grid is possible, and based on the obtained results in the previous analysis, it is expected to change the FD. To tackle this issue, one solution is that researchers must report at least the origin of the grid position and grid orientation—its influence is addressed at the end of this section—in any studies establishing correlations between estimated fractal dimensions and some physical properties. Another solution involves calculating the mean value of the fractal dimension by considering multiple random positions (Karperien, 2007). Figure 5.9 illustrates the change in the mean value of FDs due to considering 1, 5, 10, 15, 20, 25, and 30 random positions inside the bounding box (the mean is normalized by the value obtained at 30 random positions). It is observed that for both databases, the mean values of fractal dimensions steady at around 25 random positions. The final possible solution is to find the minimum number of boxes intersecting the cracks, which requires exhaustive search or optimization procedures. Unfortunately, in most of the papers conducting the fractal analysis of crack patterns on walls, the origin of the grid position has not been mentioned, making their results not reproducible.

To explore the impact of grid rotation on the estimation of fractal dimension, the bounding boxes encompassing the crack patterns were rotated with respect to the horizontal axis with angles ranging from 0 to 180 degree (with the step of 10 degree). From Figure 5.10, it can be concluded that whereas the maximum range in the masonry database is greater than in the concrete database, this factor is more influential for the concrete crack maps since the computed range is around 0.4 for more than half of the database. This can be due to the higher randomness in the crack spacing of concrete walls compared to the masonry walls where the

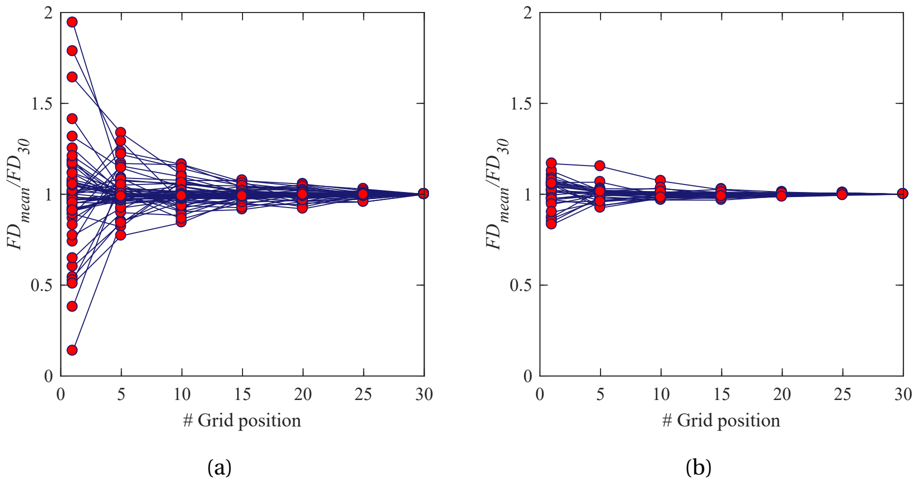

Figure 5.9 – Mean FDs calculated using a number of random grid positions as specified on the X-axis. (a) Masonry walls, wherein 61/83 showed fractality (Petry and Beyer, 2015a, 2014b), and (b) concrete walls, wherein 30/45 showed fractality (Almeida et al., 2016).

crack spacing of multiples of one brick height dominate.

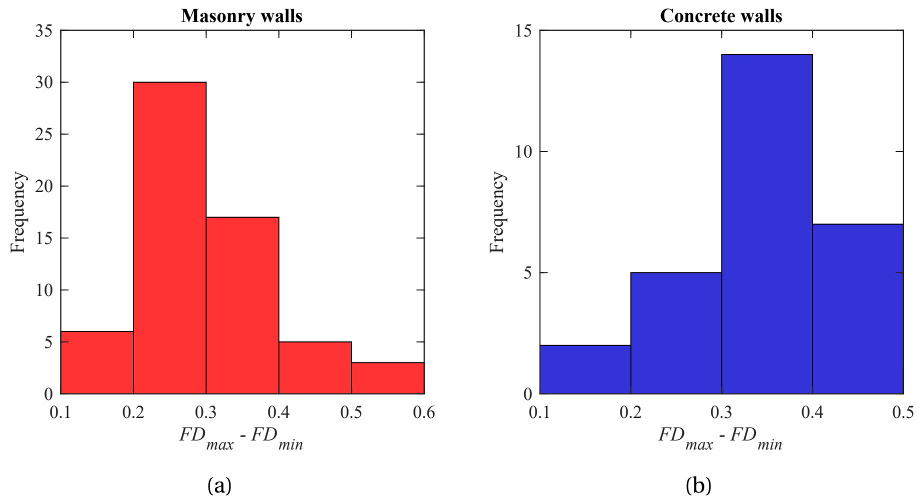

Figure 5.10 – Influence of the grid rotation on FD. (a) Masonry walls, wherein 61/83 showed fractality (Petry and Beyer, 2015a, 2014b), and (b) concrete walls, wherein 30/45 showed fractality (Almeida et al., 2016).

5.3.2 Scale factor for box sizes

Several studies have been conducted to find the influence of the various sampling strategies (e.g. Ostwald (2013); Buczkowski et al. (1998)) on the computation of the estimated fractal dimension by the box-counting method. It was determined that white areas around the pattern affect the results (Ostwald, 2013). In general, any white spaces added to the pattern during the covering procedure might lower the accuracy of the box-counting method (Feldman, 2012). Additionally, a sequence of discrete box sizes, typically multiples of a basic box size, must be chosen (Ostwald, 2013), and enough box sizes must be considered to fit the straight line, as shown in Figure 5.3 (Buczkowski et al., 1998). Often, a scale factor of 2 is chosen, and the powers of 2 ($r = 1, 2, 4, 8, \ldots, 2^n$) are taken as the set of sampling sizes (Peitgen et al., 2006). This approach has also been used in previous studies addressing the fractal dimensions of crack patterns (Ebrahimkhanlou et al., 2016; Farhidzadeh et al., 2013; Dolatshahi and Beyer, 2019). However, it is not always the best sampling strategy, especially if the given image has dimensions that are not powers of 2 (So et al., 2017).

The relative size of the bounding box and the size of the elements of the pattern can assist in the choice of an appropriate scale factor. For example, Figure 5.11b,c demonstrates the impact of the scale factor for the box sizes on the estimated value of the fractal dimension of the box fractal (Figure 5.11a), whose exact fractal dimension is 1.4647. The smallest elements in this binary image are 3×3 filled squares with the dimension of 81×81 pixels. According to the Figure 5.11b, the FD is close to the exact fractal dimension when the scale ratio is three and the set of box sizes $r = 1, 3^1, 3^2, 3^3, 3^4$. However, if a scale factor of 2 is used and the set of box sizes is $r = 1, 2^1, 2^2, 2^3, 2^4, 2^5, 2^6$, the obtained FD is lower than the true fractal dimension (Figure 5.11c). As demonstrated in Figure 5.13, this difference in the scale factor can affect the results (up to 0.5 difference in the estimation of FD); in the example, the difference in computed FD is, however, relatively small (2.9%).

Along with the scale factor, there have been some suggestions for how to include the appropriate number of points to fit the linear line to reduce errors (Ostwald, 2013; Meisel and Johnson, 1997). To test this, a wide range of scale factors, including $1.1, 1.2, 1.3, 1.4142\,(\sim \sqrt{2})\ldots 2$, has been assumed to evaluate the effect of scale factor on the estimation of fractal dimensions (Ostwald, 2013). Among these scale factors, the square root of 2 is advised by some authors (Ostwald, 2013; Gonzato et al., 2000). In another more recent attempt, So et al. (2017) developed a new sampling method in which the number of boxes intercepted by the black pixels could be a non-integer number as opposed to the conventional box-counting algorithm. By considering non-integer box numbers, the estimation of fractal dimensions was more precise for fractal geometries.

For non-mathematically fractal structures such as crack maps, however, there is no benchmark with which to compare the results of the computed FD. In these cases, by implication, it is advisable to assume a scale factor that provides more points that deviate only minimally from the line for the linear fitting, since insufficient sampling sizes and narrow intervals might lead to anomalous results (So et al., 2017; Gonzato et al., 2000). Figure 5.12 compares the results obtained by assuming two different scale factors for one of the crack maps in the masonry database. It is evident that with the scale factor 2, there are only two points in the fractal region that can be used to fit the line, which is not suitable, whereas the scale factor $\sqrt{2}$ gives three points to fit the line. Figure 5.13 shows the distribution of the range of FDs for different

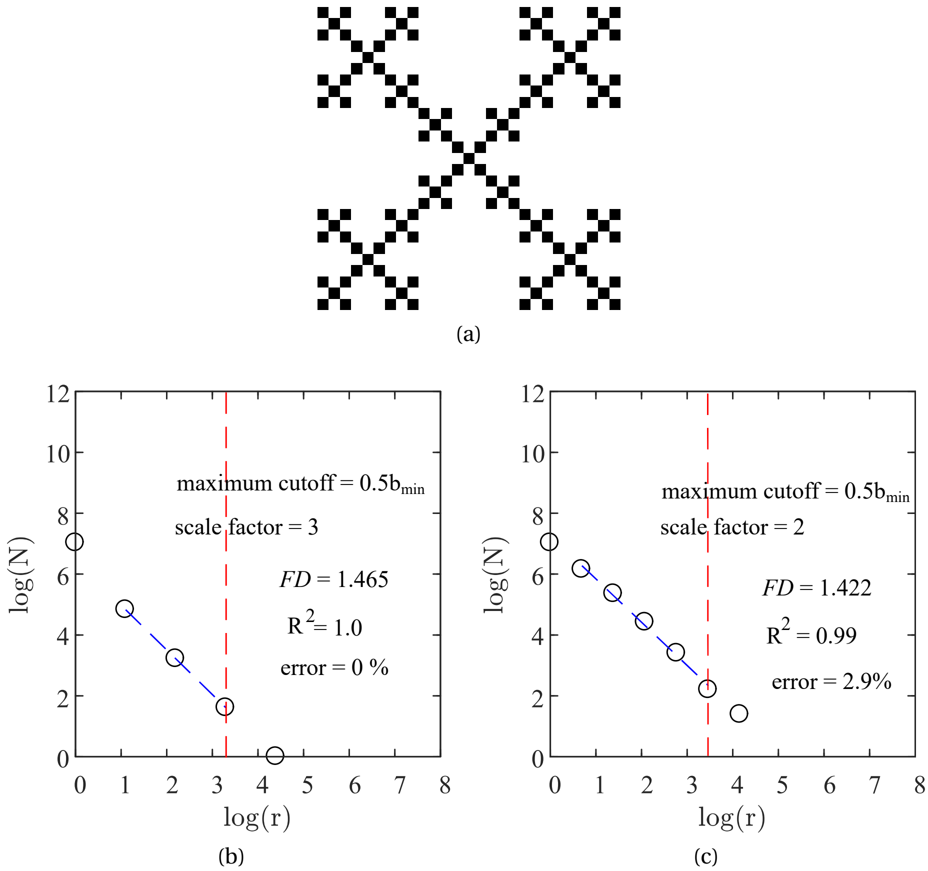

Figure 5.11 – Influence of the scale factor on estimating the fractal dimension of the (a) "box fractal" (image adopted from Feldman (2012).

scale factors, including 1.1, $\sqrt{2}$, 1.6, and 2. It is evident that for both masonry and concrete crack patterns, changing the scale factor could change the FD up to 0.5, which shows the high sensitivity of FD to this factor.

5.3.3 Box size interval

Calculating the fractal dimension of crack maps can be affected by the box size interval, which is the interval over which a self-similarity of the crack pattern is assumed, i.e., the range of scales over which $\log N(r) - \log r$ graphs, such as those shown in Figure 5.3, are assumed as linear. Complex patterns often cannot be described by reporting just one dimension for the whole range of scales. Therefore, for each range of scales that follows a linear trend, the corresponding dimension must be determined as shown in Figure 5.4. For crack maps of unreinforced masonry and reinforced concrete walls, we have observed patterns that can be described either by one or by two fractal dimensions (Figure 5.3a or Figure 5.3b). In general, when there are a few unconnected cracks like Figure 5.17, the results will be like Figure 5.3a; alternately, as the cracks grow and spread over the whole wall, the graph will be similar to

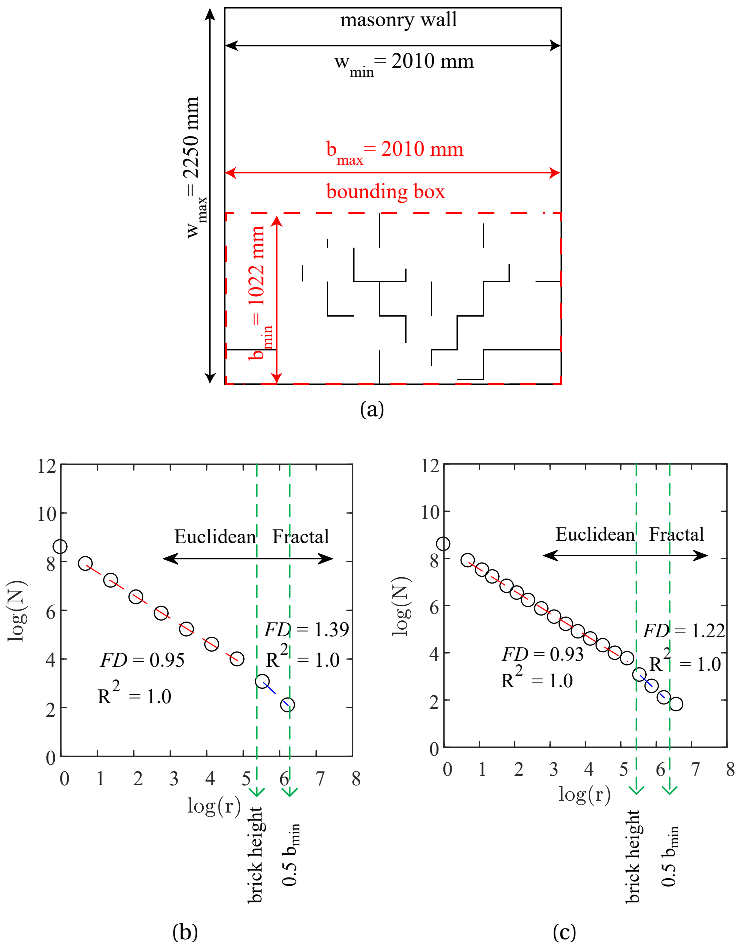

Figure 5.12 – Comparison of the scale factors (b) 2 and (c) $\sqrt{2}$ on the FD of a crack map (a) of the masonry wall PUP6 at a drift level of 0.10%. As can be seen from the blue-fitted line, the scale factor of 2 only provides two points to fit the line, whereas a scale factor of square root 2 provides three.

Figure 5.3b. In the following, some suggestions are made for choosing the global minimum cutoff r_1 in Figure 5.3, the global maximum cutoff r_2 in Figure 5.3a and r_4 in Figure 5.3b, and the location of breakpoint r_2 or r_3 in Figure 5.3b when determining the fractal dimensions of crack maps. In practice, the scales r_2 and r_3 can also be assumed to be equal. Further details about this assumption are explained in subsection 5.3.4.

For the value of the global maximum cutoff, some studies have used 25% of the shorter side of the bounding box (b_{min}) (Ostwald, 2013; Koch, 1993; Cooper and Oskrochi, 2008). Harrar and Hamami (2009) used twice this global maximum cutoff (0.5 b_{min}) to calculate the fractal dimension of gray-scale images. Roy et al. (2007) also considered 0.5 b_{min} when computing fractal dimensions of fracture systems. For the global minimum cutoff, Foroutan-pour et al. (1999) proposed a range of one to five pixels. They expressed that the best minimum size is the point, after which there is a deviation from the fitted straight line and verified their suggestions

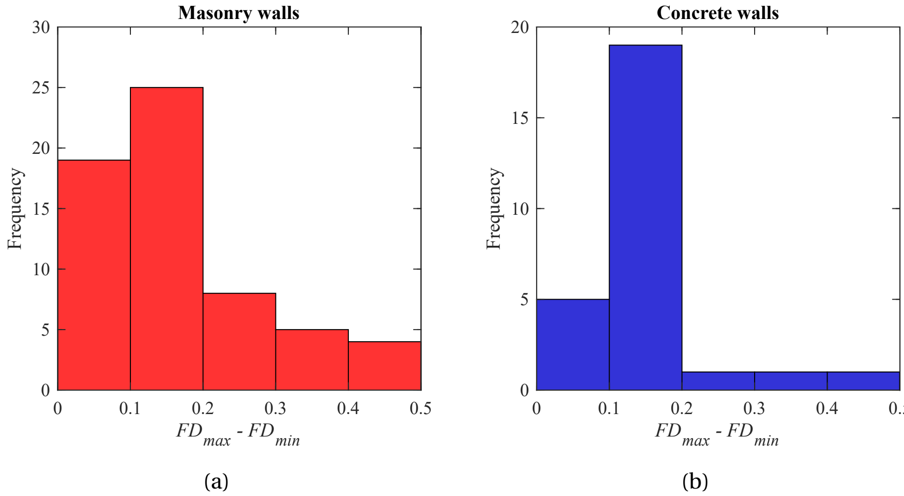

Figure 5.13 – Influence of the scale factor on FD. (a) Masonry walls, wherein 61/83 showed fractality (Petry and Beyer, 2015a, 2014b), and (b) concrete walls, wherein 30/45 showed fractality (Almeida et al., 2016). The high differences between the FD_{max} and FD_{min} show the sensitivity of estimating FD to the choice of the scale factor

by analyzing some well-known fractal geometries. Koch (1993) proposed that 0.03 b_{min} should be considered as the global minimum cutoff (Ostwald, 2013). Roy et al. (2007) suggested plotting the standard deviation of the slope of the fitted line versus box sizes, wherein the minimum cutoff would be where the graph constantly remains at zero.

Specifically for crack maps, Farhidzadeh et al. (2013) assumed the maximum cutoff based on the maximum crack length, and for the minimum cutoff, they considered the point where the fractal changes to the Euclidean regime. Dolatshahi and Beyer (2019) used the wall size as the global maximum for finding the structural fractal dimension of crack patterns on masonry walls because the cyclic loads caused the cracks to spread over the whole wall. Carrillo and Avila (2017) used the software Benoit (https://www.trusoft-international.com/) to compute the fractal dimensions of cracks on concrete walls. In most of the studies in this field, the effect of the global maximum cutoff, which is determined by the size of the bounding box, was not investigated. Table 5.1 summarizes different maximum and minimum cutoffs that have been used in different articles.

5.3.4 Breakpoint location

For some patterns, such as the crack maps depicted in Figure 5.14, there is an apparent slope change in the log-log plots (Figure 5.3b), meaning two fractal dimensions must be reported to characterize the complexity. As long as the value of the coefficient of determination is high, it is feasible to assume one breakpoint location, i.e., $r_2 = r_3$ in Figure 5.3b. To determine the fractal dimension of crack patterns, the location of the breakpoint and the global minimum

Table 5.1 – Maximum and minimum cutoffs proposed for non-mathematical fractal patterns in literature.

Reference	Minimum cutoff	Maximum cutoff
Ostwald (2013); Cooper and Oskrochi (2008)	$0.03b_{min}$	$0.25b_{min}$
Roy et al. (2007)	Using the derivative of the standard deviation of FD	$0.5b_{min}$
Karperien (2007)	Variable	0.2-$0.5b_{min}$
Foroutan-pour et al. (1999)	One to five pixels	$0.25b_{min}$
Farhidzadeh et al. (2013)	Change of fractal to Euclidean	Maximum size of the object (crack)
Dolatshahi and Beyer (2019)	One pixel	Wall size

and maximum cutoffs must be defined. It is shown that the breakpoint of crack maps is related to the crack spacing (also reported in previous studies like (Dolatshahi and Beyer, 2019)). In brick masonry walls, the crack spacing is very regular because it is determined by the brick size (Dolatshahi and Beyer, 2019). In concrete walls, it is somewhat less regular. For this reason, the breakpoint location for masonry and concrete crack maps is investigated separately.

When crack patterns in the masonry database showed apparent fractality over a range of scales, two different plots representative of a portion of the database were obtained, as depicted in Figure 5.14. In both types of crack maps, the fractal dimension is 1 in the first part of the graph, meaning that the pattern does not show fractality in this range. In the second part, however, the pattern shows fractal behavior, and FD is a fractional number between 1 and 2. The location of the breakpoint relates to the vertical/horizontal distances between cracks (Dolatshahi and Beyer, 2019). For brick masonry walls, it was postulated (Dolatshahi and Beyer, 2019) that the breakpoint location is roughly equal to the smaller dimension of the bricks (Dolatshahi and Beyer, 2019). In fact, as bricks have a uniform size and cracks mainly follow joints, the crack spacing in these walls is approximately uniform (Dolatshahi and Beyer, 2019). In Figure 5.14, the black, blue, and red dashed lines highlight the location of the breakpoint, 0.5 b_{min}, and b_{min}, respectively. In some crack patterns, all points after the breakpoint fall on the same line, as shown in Figure 5.14a. However, an arrow at the last point in a graph in Figure 5.14b indicates it does not follow the fitted line and should therefore not be considered. It should be pointed out that all analyses in this section have been conducted with the following assumptions: the origin of the grid is the left bottom corner of the bounding box, the orientation of the grid is considered to be parallel to the wall sides, and the scale factor is presumed to be $\sqrt{2}$, i.e., $r = 1, \sqrt{2}, \sqrt{2}^2, ..., \sqrt{2}^n$.

To demonstrate the difference that the global maximum cutoff can make on the calculations, Figure 5.15a compares the histograms of FD computed under two assumptions for the global maximum cutoff: 0.5 b_{min} and b_{min}. This analysis was conducted only for the crack patterns that have a fractal regime in their plot, like Figure 5.3b; there are 83 crack maps in the masonry

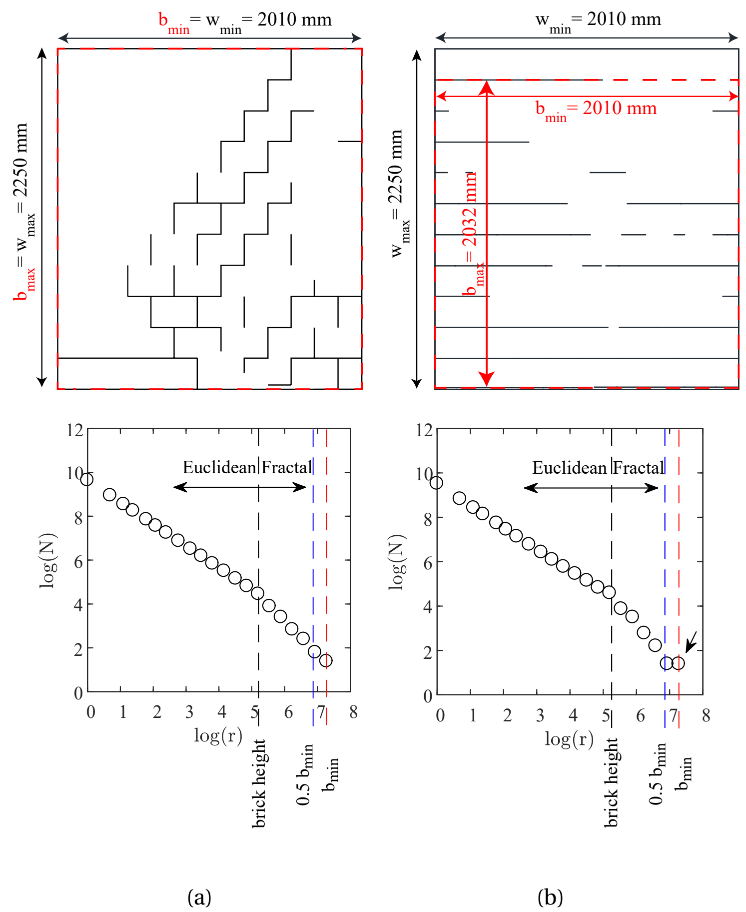

Figure 5.14 – Box size interval and the breakpoint location for walls in the masonry database (Petry and Beyer, 2015a, 2014b). (a) Crack map of the brick masonry wall PUP6 at a drift level of 0.15%, and (b) crack map of the brick masonry wall PUP3 at a drift level of 0.30%.

database, of which 61 show statistical fractality. The other 22 crack maps contain too few cracks for a fractal dimension to be defined (see discussion at the end of this section). It is evident that in both cases, the value of the coefficient of determination is high (Figure 5.15b), although the results can be quite different Figure 5.15a). Indeed, the differences between the maximum and minimum *FD*s are around 0.2 (Figure 5.15c). Moreover, the mean of the distribution, as demonstrated in Figure 5.16, is 1.00, which means that the choice of the current breakpoint location and the choice to consider the global minimum to be greater than one pixel—i.e., excluding the first point where $r = 1$—are appropriate assumptions.

As mentioned previously, Figure 5.15 represents only 61/83 crack patterns within the masonry database. If the crack maps contain only a few cracks, no fractal behavior can be observed, and these patterns were therefore not included in the analysis of Figure 5.15. Two examples of the 22 images of crack maps not showing fractality and their corresponding $\log N(r) - \log r$ plot are shown in Figure 5.17. In these plots, there is only one linear trend in the graph (like Figure 5.3a) related to the Euclidean dimension, which is not capable of representing the complexity of the

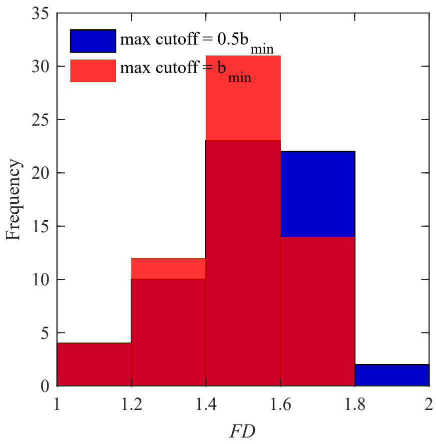

(a)

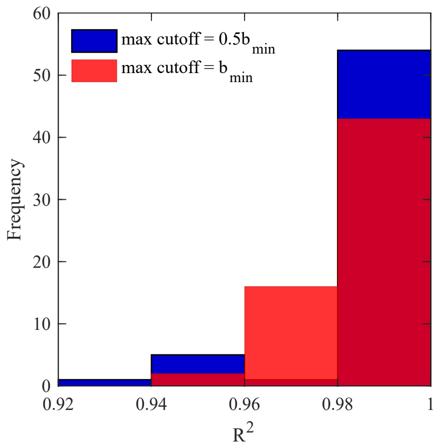

(b)

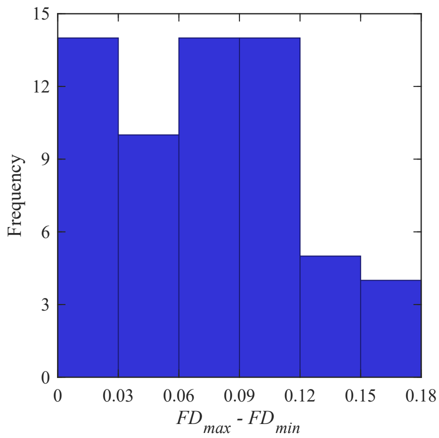

(c)

Figure 5.15 – For brick masonry walls, the influence of global maximum cutoff on (a) FD of masonry database and (b) the coefficient of determination. (c) The distribution of the difference between FD computed with a maximum cutoff of 0.5 b_{min} and FD computed with a maximum cutoff of b_{min}.

crack patterns. In these cases, other fractal dimensions, like an extended fractal dimension that captures the visual complexity of a pattern, could be more useful (Sandau, 1996; Sandau and Kurz, 1997).

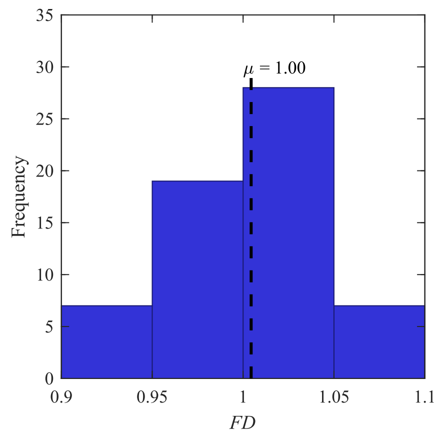

Figure 5.16 – Histogram showing the distribution of FD in the Euclidean regime for walls in the masonry database (Petry and Beyer, 2015a, 2014b).(This result obtained by setting the global minimum to $r = 1$ and the breakpoint location to the height of the brick.)

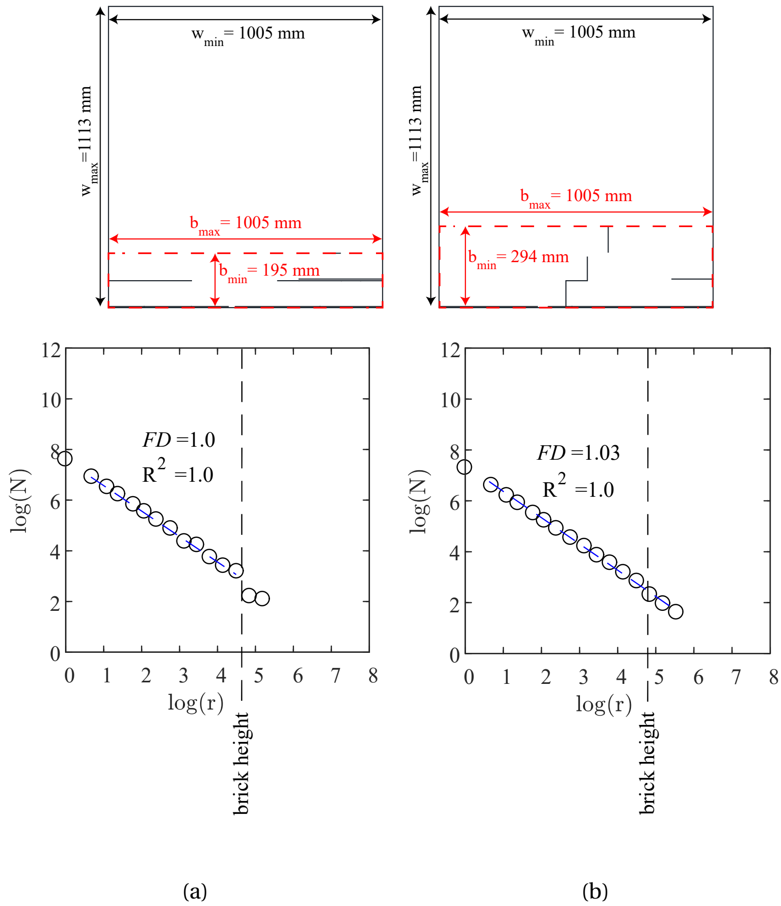

Figure 5.17 – Examples of crack maps lacking fractality (Petry and Beyer, 2014b). (a) Crack map of the masonry wall PUM4 at the drift level of 0.20%. (b) Crack map of the masonry wall PUM5 at the drift level of 0.15%.

To account for the less-regular crack patterns in concrete walls, the effects of cutoffs on their calculated fractal dimension are now addressed. Like crack maps in brick masonry walls, the global maximum cutoff for crack patterns showing fractal behavior in concrete walls can either be 0.5 b_{min} or b_{min} (Figure 5.18). Thus, the maximum cutoff can be determined according to the number of points that fit the straight line and the value of the coefficient of determination. Moreover, Figure 5.18 represents only a group of crack maps in the concrete database due to unconnected cracks that lack fractal behavior in several of the walls. Out of 45 crack patterns in the concrete database, 30 maps show statistical fractal behavior.

Because the crack spacing is not as uniform in concrete walls as in brick masonry walls, determining the breakpoint location is more difficult for concrete. As mentioned previously, the breakpoint location pertains to the crack distance. In concrete walls, the crack spacing is often controlled by the spacing of the horizontal reinforcement. For this reason, the smallest crack spacing typically occurs in the boundary elements where the spacing of the horizontal reinforcement is smaller than in the web, i.e., in between the boundary elements. Investigating the plots obtained for the crack maps showing fractality, the point where the regime changes is mostly associated with the spacing of transverse reinforcements. This can be verified by investigating the histograms that show the frequency of the crack distances (vertically). It can be observed that most of the crack distances are lower than 200 mm and 130 mm—the values corresponding to the spacing of the transverse reinforcements—for the crack maps in Figure 5.18a and Figure 5.18b, respectively.

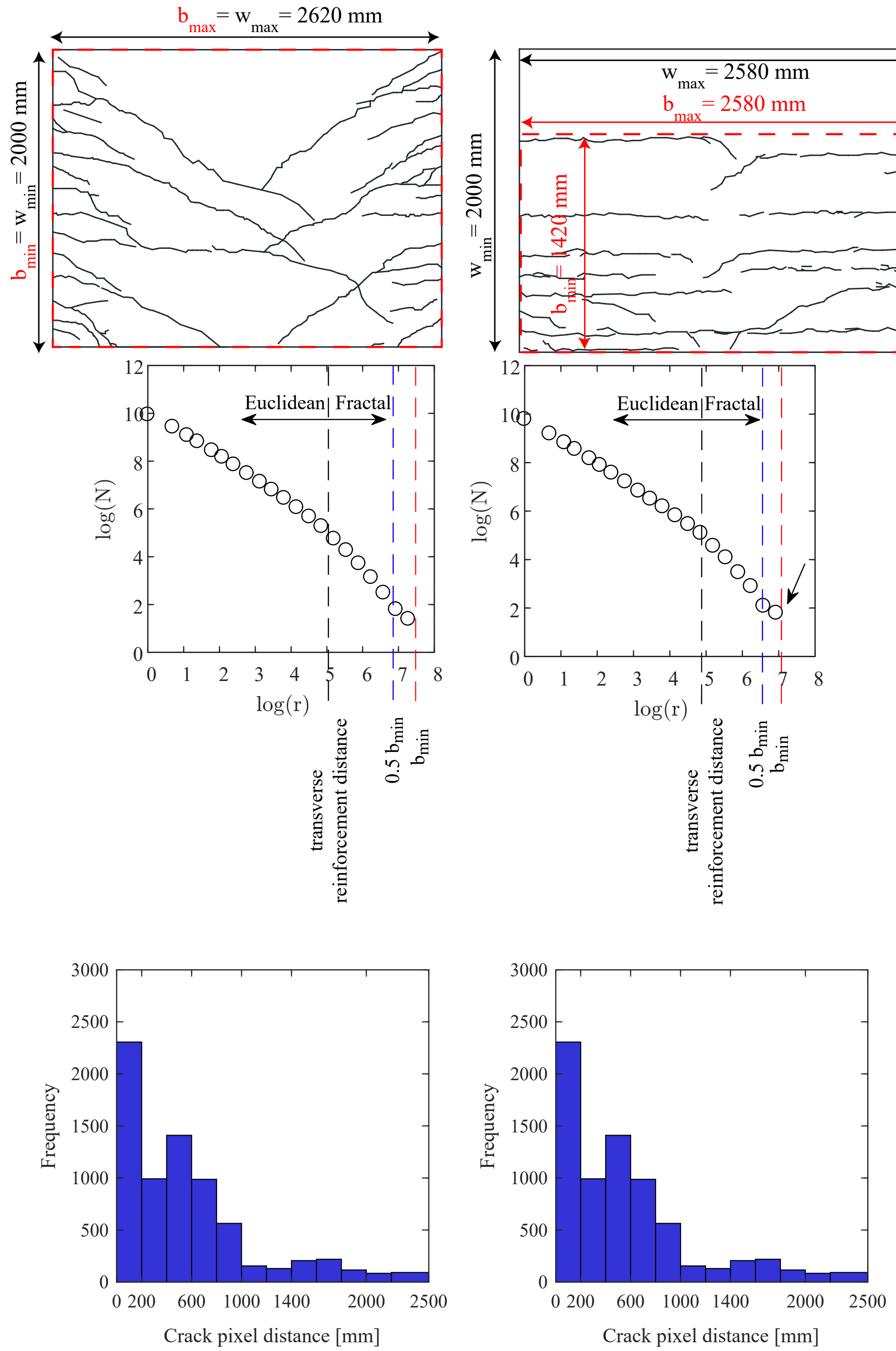

(a) (b)

Figure 5.18 – Box size interval and breakpoint location for the walls in the concrete database (Almeida et al., 2016). (a) Crack map of the concrete wall TW1 at a drift level of 0.25%. (b) Crack map of the concrete wall TW5 at a drift level of 0.12%.

From Figure 5.19c, it can be deduced that, for most cases, the estimated fractal dimensions of concrete crack patterns are not hugely affected by the choice of the maximum cutoff. In the masonry database, the ranges (Figure 5.15c) were more variable and, on average greater than those of concrete crack maps, meaning that the estimated fractal dimension of the masonry crack patterns is more sensitive to the global maximum cutoff. As depicted in Figure 5.20, the mean value of the Euclidean FD is 1.04, which is quite close to 1.

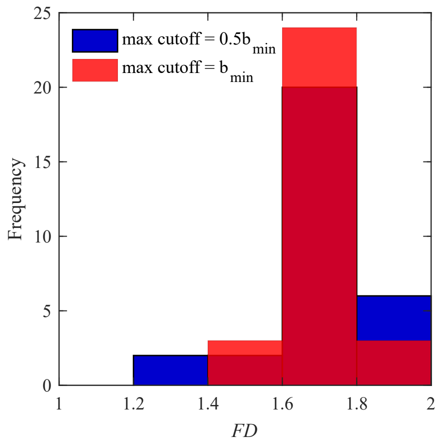

(a)

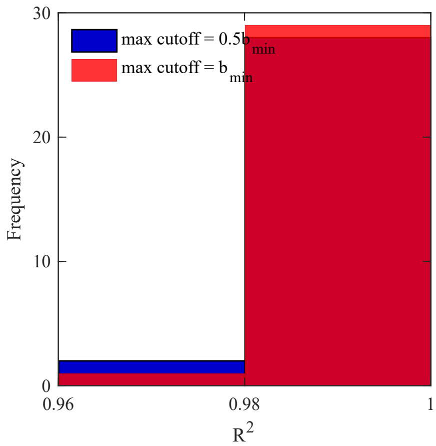

(b)

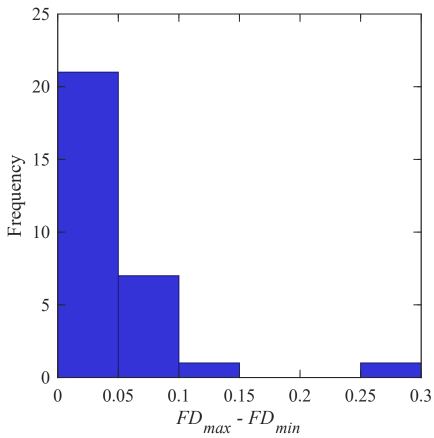

(c)

Figure 5.19 – For concrete walls, the influence of global maximum cutoff on (a) the FD of walls in the concrete database (Almeida et al., 2016) and (b) the coefficient of determination. (c) The distribution of the difference between FD computed with a maximum cutoff of 0.5 b_{min} and FD computed with a maximum cutoff of b_{min}.

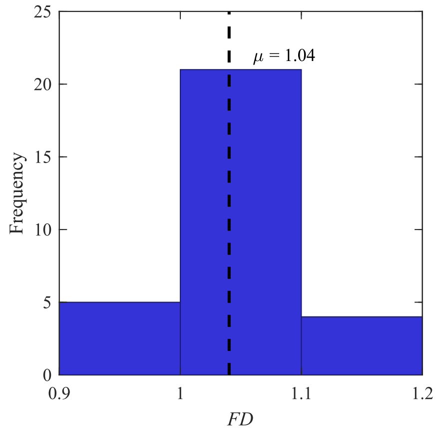

Figure 5.20 – Histogram showing the distribution of FD in the Euclidean regime for walls in the concrete database (Almeida et al., 2016).

5.4 Conclusions

In this study, the box-counting method that is generally used to estimate the fractal dimension of both deterministic and non-deterministic fractals is reviewed. Various parameters affecting the results, including sampling sizes, maximum and minimum cutoffs, grid position and orientation, and breakpoint location are investigated. For each of these factors, suggestions provided by previous studies, which have been obtained mostly by exploring mathematical fractal geometries, are indicated. Furthermore, some new recommendations for exploring the fractality of crack maps are introduced by analyzing two databases containing 45 and 83 crack maps from concrete and masonry wall surfaces, respectively, that were tested at EPFL (Petry and Beyer, 2015a, 2014b; Almeida et al., 2016). The results from these investigations are summarized in the following.

- **Box size interval**: The box size interval is the interval over which a self-similarity of the crack pattern is assumed, i.e., the range of scales over which $\log N(r) - \log r$ graphs are assumed as linear. To determine the maximum size of the interval, the results when taking $0.5b_{min}$ and b_{min} as the maximum limit were compared. Based on the obtained high values for the coefficient of determination, it was shown that both values can be used as the global maximum cutoff. It should be pointed out that for a group of crack maps, however, one must consider $0.5b_{min}$, since the points after this limit might not fall on the same line as others.

- **Breakpoint location**: For some crack maps, there is an apparent slope change in the log-log plots, meaning two fractal dimensions must be reported to characterize the complexity. Because only the part of the $\log N(r)$ versus $\log r$ plot indicating fractal behavior is of concern, one must define the location where the behavior of the crack maps changes from Euclidean regime to fractal regime. This point pertains to the crack spacing. The crack spacing in brick masonry walls is almost uniform because the cracks mainly pass through the joints, so the brick height can be considered as the breakpoint location. For concrete crack maps, the distance of the transverse reinforcement is suggested as the breakpoint location. It is important to point out that in both crack map databases, a portion of the patterns does not show any fractal behavior ($FD = 1$), so other dimensions like extended-box counting could be used for evaluating the visual complexity of these patterns (Sandau, 1996; Sandau and Kurz, 1997).

- **Sampling strategy**: The sampling strategy refers to the sequence of discrete box sizes r, for which N is evaluated. Typically multiples of a basic box size are chosen, and the ratio of two consecutive box sizes is referred to as scale factor. The considered scale factor for the box sizes should provide enough points, at least three, that can be used to fit the line. For the examined crack map databases, the scale factor of $\sqrt{2}$ was the best, as was also suggested by previous studies concerning fractal geometries (Ostwald, 2013; Gonzato et al., 2000). The box sizes should, therefore, be $1, \sqrt{2}^1, \sqrt{2}^2, \sqrt{2}^3, \ldots, \sqrt{2}^n$.

- **Grid disposition and orientation**: The origin of the grid position and orientation of the grid with regard to the wall edges affect the computed FD. Based on the considerable differences that can be measured by changing the variables involved in the box-counting method, the origin of the grid position and the orientation of the grid must be reported for each analysis to make the results comparable. Moreover, it is possible to either choose different grid positions and orientations and take the mean value of the computed fractal dimensions or to find the optimum grid configuration, which is considered as the grid position that leads to the lowest FD (Bouda et al., 2016; Karperien, 2007; Gonzato et al., 2000).

In summary, non-deterministic fractal patterns, like crack maps, do not have a benchmark with which to compare the results of the estimated fractal dimensions. Therefore, it is of the upmost concern that any parameters used in the analysis are clearly defined. In this study, general suggestions are provided to aid in the choice of the scale factor, grid position and orientation, breakpoint location, and the cutoffs. For the crack maps of brick masonry and concrete walls that were investigated here, it was shown that the fractal dimension computed by means of the box-counting method is particularly sensitive to assumptions with regard to the grid orientation and the scale factor. However, further studies addressing databases containing more crack patterns are needed to deeply investigate the influence of each parameter on the fractal dimension of crack patterns. This study also showed that crack maps have only fractality if the crack map contains a certain number of cracks. If the crack maps contain too few cracks, by applying the box-counting method and plotting $\log N(r)$ vs. $\log r$ there will be only one slope to report as the fractal dimension, which is constant (equal to unity); thus, other fractal dimensions, like an extended fractal dimension that captures the visual complexity of a pattern, could be more useful and should be explored in future works.

Acknowledgments

The project is supported by the Swiss National Science Foundation (grant 200021_175903/1 "Equivalent frame models for the in-plane and out-of-plane response of unreinforced masonry buildings").

6 Predictive machine learning models

This chapter represents the pre-print version of the article:

Rezaie, A., Godio, M., Achanta R. and Beyer, K., 2021. “Machine-learning Predictions of Stiffness, Strength, and Drift Capacity Degradation of Damaged Rubble Stone Masonry Piers Using Surface Crack Features”. *to be submitted to Automation in Construction.*

The formatting and numbering of equations, tables and figures have been adapted to this document. The contributions of the first author are: methodology, validation, formal analysis, investigation, data curation, writing - review and editing, visualization. The contributions of the second and third authors are: investigation, writing - review and editing. The contributions of the forth author are: supervision of the first author, conceptualization, methodology, investigation, resources, writing - review and editing, funding acquisition.

Abstract

Under seismic actions, stone masonry buildings are prone to damage, including the cracking of mortar joints and units. To assess the severity of damaged masonry buildings and their failure modes, engineers connect these problems to surface crack features, such as crack width and the extent of cracking. We aim to further these assessments in this study, wherein we propose using simple machine learning models to predict: 1) three ratios encoding the degradation of stiffness, strength, and displacement capacity of damaged rubble stone masonry piers as a function of crack features, axial load, and shear span ratio; and 2) the pre-peak vs. post-peak regime based on crack features. The three crack features used in this study are maximum crack width, length density, and complexity dimension.

When predicting the stiffness, force, and drift ratios, the prediction error is significantly reduced when the axial load and shear span ratio are included in the feature vector. Furthermore, when predicting the pre-peak vs. post-peak regime, simple machine learning models such as the k-nearest neighbor and the logistic regression result in remarkable accuracy.

The obtained results have significant implications on the automated post-earthquake assessment of masonry buildings using image data. It is shown that by selecting proper crack features and incorporating information about the kinematic and static boundary conditions, even simple machine learning models can predict accurately the damage level caused to a rubble masonry pier. The pipeline developed in this paper is general enough and is applicable to other masonry typologies and elements upon new evaluation of crack features and image data.

Keywords: Damage assessment; Crack pattern; Masonry building; Machine learning; Post-earthquake assessment.

6.1 Introduction

The extent of structural damage caused by seismic activity can be estimated based on the damage that is visible (FEMA 306, 1998). This can be seen in stone masonry structures, which have performed poorly in previous earthquakes (D'Ayala and Paganoni, 2011), as the damage manifests first in cracks before the structure might partially or fully collapse. However, to classify the damage to a building's structural or non-structural components, we must first realize that damage is subjective and depends entirely on demands that we define (De Vent et al., 2011).

Lagomarsino and Cattari (2015) defined performance levels with respect to the three classes of safety and conservation requirements: use and human life, building conservation, and artistic assets. The authors correlated these performance levels with damage grades defined in the European Macroseismic Scale (EMS-98) (Grünthal, 1998), and Table 6.1 presents sketches of the damaged masonry buildings used to make these correlations and their corresponding performance limits. The damage grades proposed in EMS-98 (Grünthal, 1998) are mainly used for assessing the seismic vulnerability and loss assessment of masonry buildings (Lestuzzi et al., 2016; Michel et al., 2017; Reuland et al., 2019b,a; Diana et al., 2019). To classify the damage level of a masonry building based on EMS-98, there are three naming conventions used in the literature (Lagomarsino and Cattari, 2015; Grünthal, 1998; Novelli and D'Ayala, 2019), which are also summarized in Table 6.1. Additionally, the qualitative description of each damage grade is presented in Table 6.2. Also summarized in Table 6.1 and Table 6.2, Tomaževič (2007) suggested a relationship between EMS-98 damage grades, limit states, and the damage observed during experimental tests on masonry and assessed the usability of a damaged masonry building based on the assigned damage grade. From Table 6.2, it can be seen that the original criteria for each damage grade in EMS-98 (Grünthal, 1998) are purely qualitative, though Tomaževič (2007) attempted to remedy this through included quantitative measures, such as crack width and information about the reparability of the damage. Bosiljkov et al. (2010) related the residual crack width, drift, and damage level to the possible rehabilitation strategy for unreinforced brick masonry walls, as depicted in Figure 6.1. It can be seen, however, that no quantitative values describe the residual crack pattern.

FEMA 306 (1998) proposes modification factors to reduce stiffness, strength, and deformation capacity of a damaged masonry element as a function of the damage grade. Petry and Beyer (2015c) found that these values differed for brick masonry walls failing in shear. Additionally, by analyzing cyclic shear-compression tests on brick masonry walls (Petry and Beyer, 2014a, 2015a), the authors proposed five limit states depending on the failure mode (Petry and Beyer, 2015c) and related the proposed limit states and the performance levels proposed by Bosiljkov et al. (2003) to the damage levels indicated in FEMA 306 (1998) (Table 6.3). Again, when describing local damage patterns for each limit state, no quantitative criteria were used (Petry and Beyer, 2015c) (see Table 6.3) because the main purpose of proposing these limit states was to inform about local damage and its connection to the global response of brick masonry walls (Petry and Beyer, 2015c). This information was used to derive and validate analytical models of the response of masonry walls under shear-compression loading (Wilding and Beyer, 2017, 2018a,b; Petry and Beyer, 2015b).

Table 6.1 – Definition of damage grades and performance levels based on Lagomarsino and Cattari (2015); Grünthal (1998); Novelli and D'Ayala (2019); Tomaževič (2007)

EMS-98 sketches	Damage grade/level			Performance level			
	EMS-98 (Grünthal, 1998)	Lagomarsino and Cattari (2015)	Novelli and D'Ayala (2019)	Lagomarsino and Cattari (2015)		Tomaževič (2007)	
				Use and human life	Building conservation	Limit states	Usability of building
	Grade 1: negligible to slight damage (no structural damage, slight non-structural damage)	DS1*: slight	ND: no damage	Operational	No damage	-	Safe and usable
	Grade 2: moderate damage (slight structural damage, moderate non-structural damage)	DS2: moderate	LD: light damage	Immediate occupancy	Damage limitation	Crack (damage) limit state, where the first cracks occur in the walls causing evident changes in stiffness of the structural system. The crack limit on the resistance curve is sometimes associated with the serviceability of the limit state of the structure	
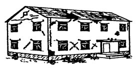	Grade 3: substantial to heavy damage (moderate structural damage, heavy non-structural damage)	DS3: heavy	SD: significant damage	Life safety	Significant but restorable damage	Maximum resistance**	Safe and usable/ Safe but no longer usable
	Grade 4: very heavy damage (heavy structural damage, very heavy non-structural damage)	DS4: very heavy	NC: near collapse	-	Near collapse	Desing ultimate limit state, where the resistance of the system degrades below the acceptable level	Safe but no longer usable
	Grade 5: destruction (very heavy structural damage)	DS5: collapse	C: collapse	-	-	Limit of collapse, defined by the partial or total collapse of the structure	-

Notes:
* DS stands for Damage State.
** In Tomaževič (2007), it is indicated that the Grade 3 damage might develop after the attained maximum resistance.

Table 6.2 – Description of damage for each damage grade (Grünthal, 1998)

Damage grade (Grünthal, 1998)	Criteria		
	EMS-98	Tomaževič (2007) - based on cyclic tests on plain masonry walls (hollow clay units) with shear behavior	Tomaževič (2007) - based on shake table tests on masonry buildings (clay block/calcium silicate/stone)
1	- Hairline cracks in very few walls - Fall of small pieces of plaster only - Fall of loose stones from upper parts of buildings in very few cases	- No structural damage	-
2	- Cracks in many walls - Fall of fairly large pieces of plaster - Partial collapse of chimneys	- Formation of the first hardly visible diagonally oriented cracks in the middle part of the wall - Slight damage	- First structural damage, which may cause noticeable decay of the first natural vibration frequency of the building
3	- Large and extensive cracks in most wall - Roof tiles detach - Chimneys fracture at the roof line - Failure of individual non-structural elements (partitions, gable walls)	- Increased number of cracks with limited width (less than 0.2 mm wide), oriented diagonally in both diagonal directions - Moderate, repairable damage, which may be defined as acceptable damage at serviceability limit state	- Increased number of cracks, typical for the governing behavior mechanism of the structural system (diagonal cracks in the case of shear, horizontal tension cracks in the case of a flexural mechanism) - As in the case of individual walls, this type of crack pattern is typically observed at, or very soon after, the attained maximum lateral resistance of the building - Moderate, repairable damage
4	- Serious failure of walls - Partial structural failure of roofs and floors	- Increased number of diagonally oriented cracks that are more than 1 mm but less than 10 mm wide - Crushing of individual masonry units - Heavy damage, which is in most cases repairable, but sometimes repair is not economical	- Heavy damage to the walls, defined by crushing at the corners of the building, falling out of parts of the walls, and (or) crushing of individual masonry units - Damage is in most cases repairable, but sometimes the repair is not economical
5	- Total or near total collapse	- Increased crack width (more than 10 mm) - Crushing of units along both wall diagonals - Severe strength degradation and final collapse	- Increased damage to the walls - Damage to horizontal structural elements, such as slabs and bond beams; crushing of concrete, and rupture of buckling of reinforcing bars (if reinforced) - Final collapse

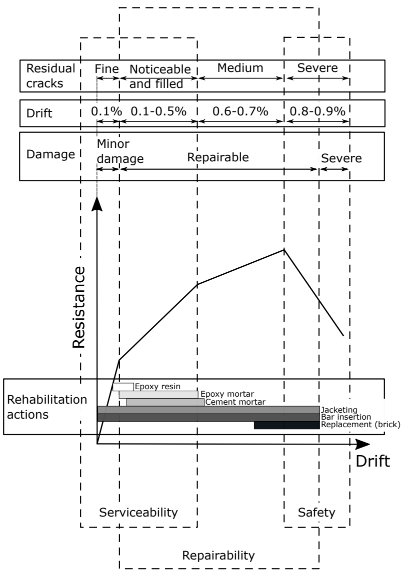

Figure 6.1 – Relationship between residual cracks, drift, damage, and the possible rehabilitation actions for brick masonry walls (taken from Bosiljkov et al. (2010)).

Old unreinforced masonry in general and stone masonry buildings in particular are prone to damage, which has been reported for earthquakes with moment magnitudes as low as 3–3.5 when the epicentral distances were small (Korswagen et al., 2019; Didier et al., 2017). Two examples are the damage caused to unreinforced masonry buildings in the city of Basel, Switzerland and in the province of Groningnen in the Netherlands due to earthquake-induced activities related to the geothermal system project (Mignan et al., 2017, 2015) and gas produc-

Table 6.3 – Limit states proposed by Petry and Beyer (2015c) for brick URM walls.

Limit states	Local damage pattern	Influence on global response	Performance levels	Damage levels
For walls with shear behavior				
LS-S1	First appearance of diagonal stair-step cracks in mortar joints	Preceded by a first reduction of stiffness	Immediate occupancy	Insignificant
LS-S2	First appearance of vertical and inclined cracks through bricks along the diagonals	Negligible influence on force-displacement response	–	Insignificant
LS-S3	Deformations start concentrating in one diagonal crack	Peak load is typically attained shortly afterwards	Life safety	Moderate
LS-S4	Shearing off of the corners of the bricks	Significant loss of the lateral resistance	Collapse prevention	Heavy/extreme
LS-S5	Crushing of bricks along the diagonal crack	Axial load failure	–	–
For walls with flexural behavior				
LS-F1	First appearance of a crack in a bed joint	First reduction of stiffness	First crack	Insignificant
LS-F2	Visible separation of the unloaded zone from the compressed zone	Negligible influence on force-displacement response	–	Moderate
LS-F3	Appearance of vertical splitting cracks in compressed corner	Peak load is typically attained shortly afterwards	Life safety	Heavy
LS-F4	Loss of part of the toe region due to crushing	Significant loss of the lateral resistance	Collapse prevention	Extreme
LS-F5	Crushing of entire compression zone	Axial load failure	–	–

Table 6.4 – Damage levels used in Korswagen et al. (2019) to classify damage.

Damage grade	Damage level	Description	Parameter of damage	Approx. crack width (mm)
DS0	DL0	-	$\Psi < 1$	Imperceptible cracks
Aesthetic damage DS1 (Grade 1)	Negligible (DL1)	- Hairline cracks	$1 < \Psi < 1.4$	Up to 0.1 mm
	Very slight (DL2)	- Fine cracks, which can easily be treated during normal decoration - Perhaps isolated slight fracturing in a building - Cracks in external brickwork visible on close inspection	$1.5 < \Psi < 2.4$	Up to 1 mm
	Slight (DL3)	- Cracks easily filled - Redecoration probably required - Several slight fractures showing inside of building - Cracks are visible externally, and some repainting may be required externally to ensure water tightness	$2.5 < \Psi < 3.4$	Up to 5 mm
DS2 (Grade 2)	-	-	$\Psi > 3.5$	5–15 mm

tion (Dost et al., 2018), respectively. These events were the starting point of many research studies on the progress and accumulation of light damage to unreinforced masonry buildings (Korswagen et al., 2020b, 2019, 2020a; Didier et al., 2017; Sarhosis et al., 2019; Abbiati et al., 2018b; Didier et al., 2018; Korswagen and Rots, 2020) and on developing fragility functions for non-structural damage (Crowley et al., 2019). In the literature, damage grade 1 (EMS-98) is interpreted as non-structural/minor damage such as cosmetic cracks in plaster or plaster fall-off (Korswagen et al., 2019; Didier et al., 2018). Damage to non-structural components might not jeopardize the safety of a building, but it can cause huge financial costs (Didier et al., 2018; Beyer et al., 2017). Inspired by Giardina et al. (2013), Korswagen et al. (2019) used the criteria mentioned in Table 6.4 to classify damage using their proposed damage level parameter (Ψ), which is a function of the length, the number, and width of cracks. Furthermore, there have been several studies attempting to understand how plaster damage (non-structural element) relates to structural damage. For example, Kržan et al. (2015) proposed two classes of damage state for artistic assets and structural elements, as indicated in Table 6.5. For further information about the relationship between artistic damage and structural damage, refer to Calderini et al. (2015); Godio et al. (2019); Valluzzi et al. (2020).

What these studies have in common is the establishment of a connection between earthquake-

Table 6.5 – Structural and non-structural (plaster) damage state defined in Kržan et al. (2015); Calderini et al. (2015).

Component	Damage state	Description
Walls/Structural elements (SE)	Damage limitation (FC)	This corresponds to the displacement (or the drift) at which the first structural crack is attained.
	Significant damage (SD)	This corresponds to the displacement (or the drift) at which the maximum resistance is reached.
	Near collapse (NC)	This corresponds to the maximum displacement or drift.
Plaster/Artistic assets (AA)	A1	First detachment of plaster
	A2	First visible structural crack on the plaster
	A3	Plaster largely detached but still repairable
	A4	Collapse of the plaster

induced damage on the one hand and seismic assessment, loss estimation, and post-earthquake assessment of unreinforced masonry buildings on the other hand. We noticed two drawbacks related to the description of damage in the early literature: 1) it is mainly qualitative; 2) in some studies, it is not clear whether the descriptions of damage from experimental data, such as crack width, were measured when the wall was loaded or after unloading. The lack of sophisticated instrumentation capable of documenting the sequence of damage evolution in an experimental test is one of the reasons why previous research studies and national codes or guidelines did not provide a comprehensive quantitative measure of damage. Fortunately, the use of optical measurement devices in an experimental test enables researchers to record damage during the loading sequence and has gained popularity in recent years, for examples see, Korswagen et al. (2020b); Petry and Beyer (2015a); Mojsilović and Salmanpour (2016); Korswagen et al. (2019); Godio et al. (2019); Rezaie et al. (2020b); Ghorbani et al. (2015); Nabouch et al. (2019). As a result, in an experimental test like a shear-compression test, information about damage features can be extracted and correlated with the degradation in force, stiffness, and displacement capacity of a specimen.

Even though FEMA 306 (1998) provides reduction factors for unreinforced masonry components, these values cannot be adopted for stone masonry structural components, as they were fitted using experimental tests on brick masonry. In this study, we aim to estimate the decay of stiffness, strength, and displacement capacity of rubble stone masonry piers using surface crack features by machine learning models. We use the data gathered from an experimental campaign previously conducted by the authors on plastered rubble stone masonry walls. The output of this study can be used as an input to an equivalent frame modeling approach (Lagomarsino et al., 2013; Vanin et al., 2020) to numerically model a damaged stone masonry building after an earthquake. Furthermore, we use simple machine learning models based on the crack features to estimate whether the wall is in the pre- or post-peak regime. Or, in other words, we estimate whether or not the wall has surpassed its maximum force capacity. This is an important information for post-earthquake assessment because the load-path dependency of the behavior of the wall is much more evident in the post-peak phase than in the pre-peak phase (Rezaie et al., 2021a; Godio et al., 2019; Wilding et al., 2017).

In what follows, section 6.2 describes the experimental data, section 6.3 explains the extraction of crack features, section 6.4 discusses the exploratory data analysis, section 6.5 discusses the classification of pre-peak and post-peak, and finally, section 6.6 explains the estimation of the properties of damaged walls.

6.2 Description of data

Six large-scale plastered rubble stone masonry piers were tested under quasi-static cyclic shear-compression loading as part of an experimental campaign (Rezaie et al., 2020b) conducted at École Polytechnique Fédérale de Lausanne (EPFL). Images of specimens were taken by two stereo-camera systems at predetermined time intervals during the application of the horizontal load. We only used images from the plastered side of the specimens in this study. These images were fed into both a digital image correlation (DIC) method to compute the displacement field and a deep convolutional neural network trained by the authors in a previous work to detect crack pixels (Rezaie et al., 2020a)(see Figure 6.2). An in-house Python script was written to skeletonize and clean crack patterns, to compute crack width from the DIC measurements (Rezaie et al., 2021a), and to extract the crack features, which were used in this study. Extracted crack features are explained in the following section.

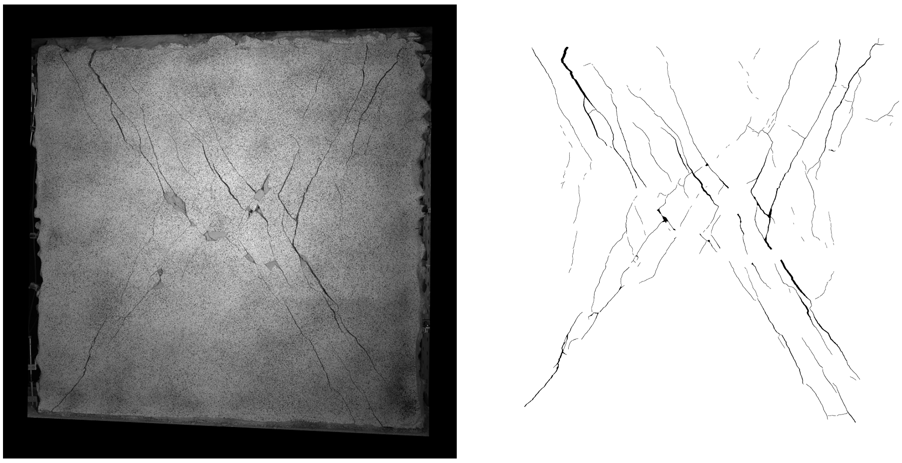

(a) (b)

Figure 6.2 – (a) An image taken from the specimen RS3 at the instance where force = -36.3 kN and displacement = -8.7 mm and (b) the detected crack pattern by the deep model (Rezaie et al., 2020a).

6.3 Crack feature extraction

We address two types of tasks in this study: a) classification and b) regression. In the context of a classical machine learning approach, both of these tasks first require us, as the designers of the classifier/regressor, to extract a set of useful features. Thereafter, we can build predictive models to output the desired target. This section defines a set of features encoding crack skeleton networks consisting of the maximum width, length density, and complexity dimension. The definition of each feature and the method used to compute it are described below.

6.3.1 Maximum width

In our experimental campaign, we used DIC to extract the crack width distribution for crack branches. We used maximum crack width among all branches as one of the crack features.

6.3.2 Length density

The feature length density is defined as the sum of the total length of skeleton crack branches divided by the area of the wall:

$$\text{length density} = \frac{\sum_{i \in \Omega} l_i}{A} \tag{6.1}$$

6.3.3 Complexity dimension

The space-filling characteristics of crack patterns as described by fractal dimension have been shown to correlate with the level of the damage (Carrillo and Avila, 2017; Ebrahimkhanlou et al., 2016; Farhidzadeh et al., 2013; Ebrahimkhanlou et al., 2015; Arvin et al., 2019; Athanasiou et al., 2020; Madani and Dolatshahi, 2020; Momeni and Dolatshahi, 2019; Dolatshahi and Beyer, 2019). The fractal dimension of a crack pattern is usually computed by a method called “box-counting" (Farhidzadeh et al., 2013; Rezaie et al., 2020c; Dolatshahi and Beyer, 2019; Carrillo and Avila, 2017). However, this method has several drawbacks, one being that there are a number of parameters that can affect the estimated fractal dimension, including the position of the grid, the orientation of the grid, and the location of the cutoff (Rezaie et al., 2020c). A detailed study regarding the sensitivity of the fractal dimension of crack patterns has been conducted by Rezaie et al. (2020c). Apart from that, Sandau (1996) and Sandau and Kurz (1997) showed that methods using linear regression to compute the fractal dimension, such as the box-counting method, do not fulfill the maximum property criteria. In the context of crack patterns, we explain below the drawback of encoding crack maps by the box-counting method.

To illustrate the major issue here, suppose that there are two images, A and B, containing binary skeleton crack maps; the number of crack pixels in image A is less than in image B. From the mechanical perspective, it is plausible to assume that the damage level presented in image B is higher than the damage level presented in image A. Therefore, we expect that the fractal dimension of the crack map on image B is higher than the crack map on image A, as the fractal dimension intends to describe the space-filling characteristics of crack patterns. However, this might not necessarily happen due to the regression analysis used in the box-counting method (Sandau, 1996; Sandau and Kurz, 1997), which could make the fractal dimension of image B even be lower than image A. To tackle this problem, Sandau Sandau (1996) proposed a dimension called “x-dim" (herein referred to as complexity dimension) that encodes the visual complexity of patterns and fulfills the quasi-maximum property. Therefore, we use the complexity dimension to characterize the spatial distribution of crack patterns. We apply this method to the skeletonized crack pattern, wherein the crack width of all crack segments is unity.

To calculate the complexity dimension, a window of the size of $w \times w$ must first be chosen (see Figure 6.3), where it is advised that w is a multiple of 2, i.e. $\{2, 4, 8, ...\}$ (Sandau, 1996; Sandau and Kurz, 1997). This window is discretized into grids of equal sizes $g \times g$ (see Figure 6.3), which can also be selected as a multiple of 2. Then, we slide this window over the entire image with a stride of size s (set to $w/4$ in this study), indicating the number of pixels that the window moves from one location to another, and compute the number of grids that intersect with the crack pattern, N. In Figure 6.3, the grids intersecting the crack skeleton are highlighted in gray. Therefore, for each position of the window on the image, we have the corresponding N. The complexity dimension is written as:

$$\text{complexity dimension} = \frac{\log_2 N_{max}}{\log_2 w - \log_2 g} \tag{6.2}$$

where N_{max} is the maximum number of intersections over all positions. The complexity dimension ranges between 0 to 2.

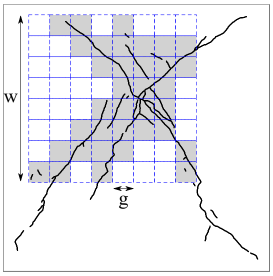

Figure 6.3 – Illustration of the window and grid size used to compute the complexity dimension. To do this, this window is moved over the entire image to find N_{max}.

It should be noted that the considerations for the grid orientation mentioned in Rezaie et al. (2020c) must be accounted for when computing the complexity dimension. The grid orientation in this work was chosen to be parallel to the orientation of the image coordinate system.

To demonstrate the similarity between the complexity dimension and the fractal dimension computed by the box-counting method, we determined the complexity dimension for a few specific crack patterns when the window size is equal to the wall size and the wall is square with a dimension multiple of 2. If a crack pattern intersects only one grid, $N_{max} = 1$, the complexity dimension is zero. If the crack pattern is space-filling, at the limit $N_{max} = (w/g)^2$, the complexity dimension is two. A single horizontal crack crossing the entire wall or a diagonal crack from one corner to the opposite one would lead to a complexity dimension of 1.0. We extracted the complexity dimension of crack patterns at various scales, i.e., multiple grid and window sizes. The window size was selected from the set $\{1024, 2048, 4096\}$ pixels, which roughly equal the size of a quarter, half, and full wall, respectively, and the grid size was chosen from the set $\{32, 64, 128, 256\}$ pixels, resulting in the extraction of $3 \times 4 = 12$ new features. Figure 6.4 illustrates how complexity dimension increases with residual drift.

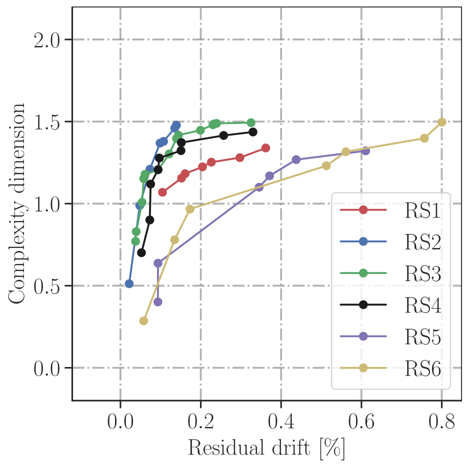

Figure 6.4 – Illustration of the trend between complexity dimension of crack patterns and residual drift. To compute the complexity dimension in this figure, we set $w = 4096$ pixels and $g = 32$ pixels.

6.4 Exploratory data analysis (EDA)

To create the input for the machine learning models, crack features were extracted from images taken at residual displacement instances (zero horizontal force) of the cyclic curves. The created dataset contains 108 samples and 14 features (only crack features). To check the correlation between these features, the absolute Pearson correlation matrix is plotted in Figure 6.5. It is evident that the complexity dimension features are highly correlated. Therefore, we removed the redundant complexity features and keep only one of them, i.e., the complexity dimension computed by setting $w = 4096$ pixels, and $g = 32$ pixels, resulting in a dataset with only three features.

Figure 6.6 illustrates violin plots of the three features in this dataset, color-coded based on class labels. It can be seen that there is an overlap between the distribution of pre- and post-peak class for each feature. One way to rank these features in terms of separability of the two classes is to compute the Fisher Discriminant Ratio (FDR), which quantifies the separation between two distributions. Here, it is defined as (Bishop, 2006):

$$FDR = \frac{(\mu_{\text{pre-peak}} - \mu_{\text{post-peak}})^2}{\sigma^2_{\text{pre-peak}} + \sigma^2_{\text{post-peak}}}, \tag{6.3}$$

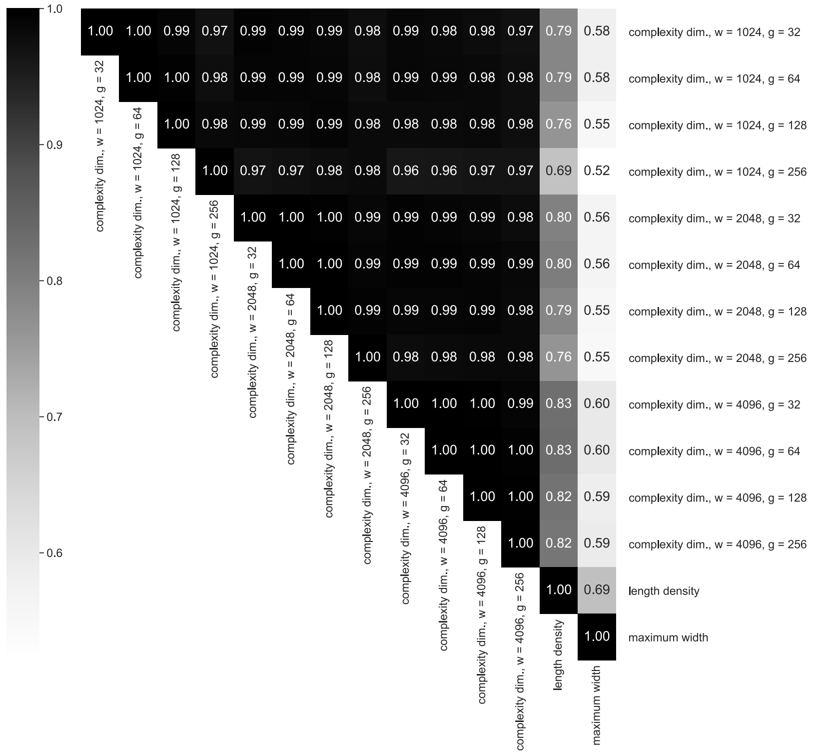

Figure 6.5 – Plot of the absolute of the Pearson correlation coefficient matrix.

where μ and σ are the mean and standard deviation of the distribution. As the distance between the means of two distributions grows, so does the FDR. The FDR also increases when the distance between the means is constant due to the decrease in the standard deviation of the distribution. The FDR values for the maximum width, length density, and complexity dimension features are 1.0, 2.0, and 4.1, respectively. This suggests that if we want to use only a threshold with one feature to classify the pre-peak vs. post-peak regime, the complexity dimension is a better feature compared to others.

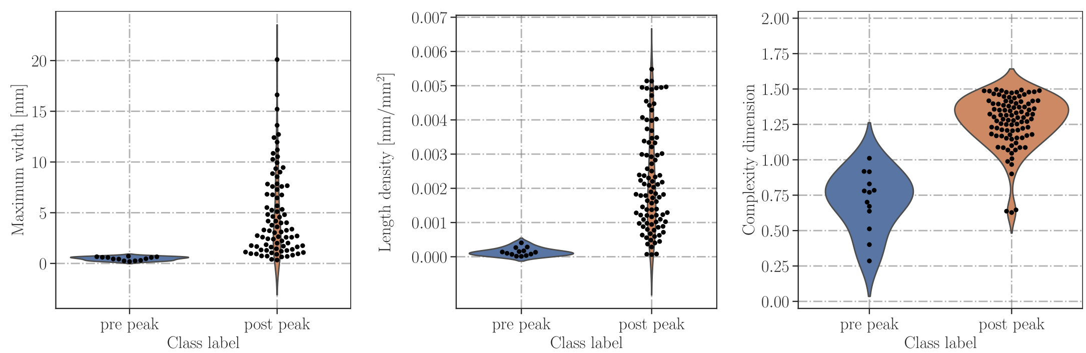

Figure 6.6 – Violin plots of maximum width, length density, and complexity dimension for the pre-peak and post-peak classes.

6.5 Classification: pre-peak vs. post-peak

As outlined above, predicting whether the wall has reached its maximum force capacity is essential in the post-earthquake assessment. In this section, we use the features extracted from a crack image to classify the image as “pre-peak" or “post-peak". This task can be solved using different machine learning models, and we herein examine two possible approaches.

6.5.1 K-nearest neighbors (KNN)

A simple, yet powerful classifier is the k-nearest neighbors (KNN), wherein a query point will have the same class as the majority class of its k-nearest data points in the training set. The term “nearest" is subjected to the definition of the distance. In this study, we used the Euclidean distance as defined below. As the distance is affected by the scale of each feature, we normalized each feature to have a zero mean and unit variance. Different K-values (1, 3 and 5) are tested in the construction of the machine learning models.

$$d(\mathbf{x}_i, \mathbf{x}_j) = \sqrt{\sum_{d=1}^{D} (\mathbf{x}_i^d - \mathbf{x}_j^d)^2}, \tag{6.4}$$

where $d(.)$ is the Euclidean distance function and D is the dimension of the feature vector.

6.5.2 Logistic regression

In the logistic regression method, the probability of belonging to a class given the feature vector $\mathbf{x} \in R^{D\times 1}$ is written as:

$$\begin{aligned} P(Y = \text{post-peak}|\mathbf{x}) &= \frac{1}{1+\exp(-\tilde{\mathbf{w}}^\top \tilde{\mathbf{x}})}, \\ P(Y = \text{pre-peak}|\mathbf{x}) &= 1 - P(Y = \text{post-peak}|\mathbf{x}), \end{aligned} \tag{6.5}$$

where $\mathbf{w} \in R^{D\times 1}$ is the column vector of weights and $\tilde{\mathbf{x}} = [\mathbf{x}^\top 1]^\top$ and $\tilde{\mathbf{w}} = [\mathbf{w}^\top w_0]^\top$, where w_0 is the bias term.

6.5.3 Results

To estimate the performance of each model on unseen data, we performed stratified 5-fold cross validation, meaning that the data was first split into 5 parts. Then, each model was trained on four of the parts and tested on the remaining part for all four combination of 5 parts. Additionally, the ratio of data points for each class was preserved in the training/validation split. The metric “accuracy", used to assess the performance of each model, is defined as:

$$\text{Accuracy} = \frac{TP+TN}{TP+TN+FP+FN}, \tag{6.6}$$

where TP = true positive, FP = false positive, TN = true negative, and FN = false negative.

Table 6.6 summarizes the mean and standard deviation (std) of the accuracy for each model obtained by 5-fold cross validation. Although the models used are simple, the obtained accuracy mean is high with a small standard deviation. Between the two applied methods, KNN with K = 3 has the highest average accuracy.

Table 6.6 – The accuracy of two machine learning models for classifying pre-peak vs. post-peak regime.

Model	**Accuracy**	
	mean	std
KNN (K = 3)	0.93	0.06
Logistic regression	0.91	0.06

6.6 Regression: force, drift, and stiffness ratios

In the previous section, we predicted whether a wall was in the pre-peak or post-peak regime. If a wall has been determined to have exceeded its maximum force capacity (in the post-peak regime), then it is important to answer the following questions:

- What is the lateral stiffness degradation?
- What is the residual force capacity of the damaged wall?
- What is the residual displacement (drift) capacity of the damaged wall?

To address these questions, in the following, we first introduce three ratios to represent the stiffness degradation, residual force, and displacement capacity of the walls. Then, we develop several regression models to predict these quantities using the post-peak data.

6.6.1 Definition of stiffness ratio (SR), force ratio (FR), and drift ratio (DR)

The three quantities representing the damage level of the walls are introduced as follows:

1. Loss of horizontal stiffness: To quantify the stiffness loss, we introduce the term “stiffness ratio” (SR) as:
$$SR = \frac{K}{K_{init}}, \tag{6.7}$$

where K is the tangential stiffness at the instance of residual displacement (when the horizontal force is zero) and K_{init} is the initial stiffness defined as the slope of the line connecting the origin to the data point where the force is equal to 15% of the force capacity. The initial stiffness values are reported in Rezaie et al. (2020b). The tangential stiffness at each residual displacement instance was set to the slope of a linear line fitted to the data points with absolute values of the horizontal force that were less than 15% of the maximum absolute force at the current cycle.

2. Loss of force capacity: The loss of force capacity is quantified as the “force ratio" (FR):

$$FR = \frac{F}{F_{max}}, \tag{6.8}$$

where F is the maximum force that the wall experiences at the current load cycle, and F_{max} is the force capacity of the wall.

3. Residual drift capacity: The “drift ratio" (DR) is defined to capture the residual drift capacity of a damaged wall and is written as:

$$DR = \frac{|\delta_{ult}| - |\delta_{res}|}{|\delta_{ult}|}, \qquad s.t.\ |\delta_{res}| < |\delta_{ult}| \tag{6.9}$$

where $|\delta_{res}|$ is the absolute residual drift at the current cycle and $|\delta_{ult}|$ is the absolute ultimate drift capacity of the wall.

Figure 6.7 depicts the scatter plots of $SR/FR/DR$ vs. the different features. The size and color of the markers indicate, respectively, the shear span ratio, which is the ratio between the height of the zero moment profile and the height of the wall, and the axial load ratio, which is the ratio between the applied axial stress and the compression strength of the wall. It can be seen that there is a negative trend between the $SR/FR/DR$ and each feature: the complexity dimension, length density, and maximum width. Additionally, cracked walls with the same complexity dimension, length density, or maximum width have different $SR/FR/DR$ depending on the axial load and shear span ratios, which shows the dependency on these factors.

6.6.2 Linear regression

The linear model is written as:

$$\hat{y}_n = \tilde{\mathbf{w}}^\top \tilde{\mathbf{x}}_n, \tag{6.10}$$

where $\hat{y}_n$ is the prediction for the data sample n.

The loss function that we used to train such a model was the mean squared error loss (MSE),

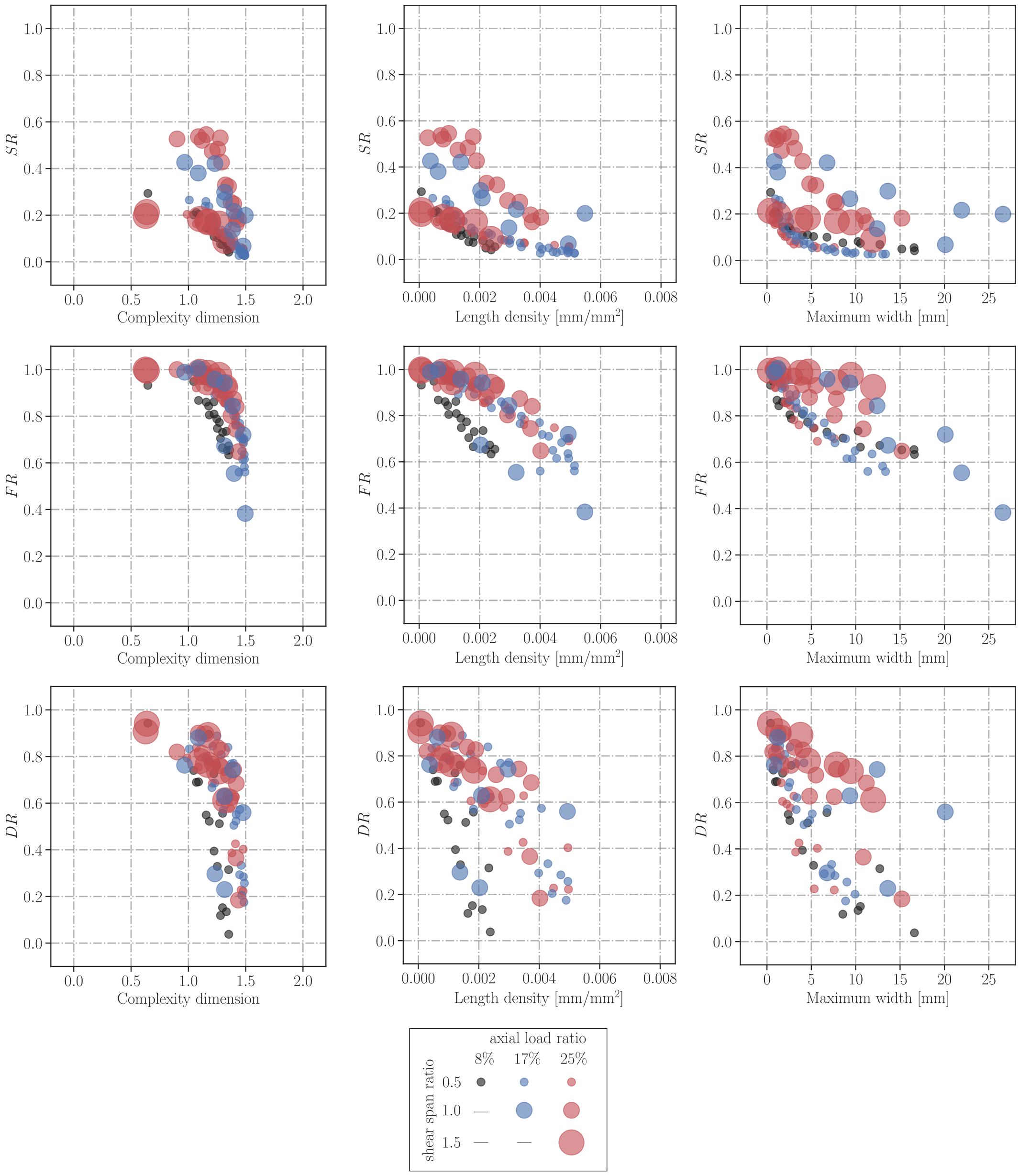

Figure 6.7 – Scatter plot of $SR/FR/DR$ vs. crack features. In the plots of DR vs. crack features, data points with $|\delta_{res}|$ values larger than $|\delta_{ult}|$ are not shown.

computed as:

$$\mathsf{MSE}(\tilde{\mathbf{w}}) = \frac{1}{N}\sum_{n=1}^{N}[y_n - \hat{y}_n]^2, \tag{6.11}$$

where y_n is the target value of the data sample n.

6.6.3 Ridge regression with polynomial features

A standard strategy for including the non-linearity in a linear regression pipeline is to augment the feature vector using degree-P polynomial features. However, by increasing the representational power of the linear model using polynomial features, the risk of over-fitting increases, and as a result, the generalization of the model decreases. Therefore, it is advised to add a term to the MSE function that penalizes large weights. Training a linear model by adding the l_2-regularization is known as Ridge regression, which is formulated as:

$$\begin{aligned} \mathbf{x}_n \in R^{D\times 1} \mapsto \o(\mathbf{x}_n) \in R^{P\times 1}, \quad P > D \\ \hat{y}_n = w_0 + \mathbf{w}^\top \o(\mathbf{x}_n), \\ \text{Ridge Loss}(\mathbf{w}) = \frac{1}{N}\sum_{n=1}^{N}[y_n - \hat{y}_n]^2 + \lambda \|\mathbf{w}\|_2^2, \end{aligned} \tag{6.12}$$

where $\o(\mathbf{x}_n)$ is the function that maps $\mathbf{x}_n$ to the polynomial feature space, and λ is the regularization strength.

6.6.4 Results

Model selection and hyper-parameter optimization

To select the best model and optimize the hyper-parameters, such as P and λ, we implemented the following 5-fold cross validation strategy:

1. Define dataset S as the collection of data from specimens RS1, RS2, RS3, RS4, and RS6. Because the behavior of specimen RS5 differed from that of the other specimens—this wall was mainly rocking during the loading sequence—the data from this specimen was not included in this section.
2. Select the validation set from one specimen, RSi, in which $i \in \{1,2,3,4,6\}$.
3. Train the model using the data from all remaining specimens as RSj, where $j \neq i$
4. Repeat steps 2 and 3, until data from each specimen, RS1, RS2, RS3, RS4, and RS6, is used once as the validation set.

Prediction of SR, FR and DR

Tables 6.7, 6.8, and 6.9 summarize the selected hyper-parameters and the performance of trained models. In these tables, we report the mean and standard deviation (std) of the root mean squared error (RMSE) in 5-fold cross validation.

For a rapid post-earthquake assessment, we may not have information about the axial load and shear span ratio, meaning that the only available information is the visible surface damage, such as cracks. Therefore, it is of interest to investigate how well our models can predict the damage level using only crack features and compare this with when we know the shear span and axial load ratios. Thus, we trained each model using two sets of features: a) only crack features and b) crack features plus shear span and axial load ratio.

Regarding SR, the best model was Ridge regression with augmented features using the polynomial degree of 3, $\lambda = 10$ and accounting for both crack features and axial load and shear span ratio; this model had the lowest average RMSE of 0.061 with the error bound of $[0.021, 0.101]$. It can be seen that incorporating the shear span and axial load ratio reduces the lowest average RMSE by more than 50% when compared to the case where we only used crack features.

Regarding FR, the best model was Ridge regression with augmented features using the polynomial degree of 2 and $\lambda = 100$. Similar to the prediction of SR, adding the axial load and shear span ratio decreased the average RMSE to 0.054 with the error bound of $[0.019, 0.089]$. The average RMSE decreased by nearly 20% when those features were added, which is less than the 50% reduction we reported for predicting SR.

Regarding DR, the best model was Ridge regression with augmented features using the polynomial degree of 2 and $\lambda = 1$, with an average RMSE of 0.137 with the error bound of $[0.064, 0.210]$. In this case, adding the axial load and shear span ratio decreased the average RMSE by almost 8%.

It can be seen that adding non-linearity using proposed feature augmentation decreases the average RMSE for predicting SR, FR, and DR by 10%, 5%, and 21%, respectively.

Table 6.7 – The performance of trained regression models to predict SR.

Features	**Model**	**Degree of poly.**	λ	**RMSE [5-fold]**	
				mean	**std**
Crack features	Linear	-	-	0.126	0.084
	Ridge	2	100	0.122	0.082
Crack features & axial load ratio & shear span ratio	Linear	-	-	0.068	0.041
	Ridge	3	10	0.061	0.040

Table 6.8 – The performance of trained regression models to predict FR.

Features	**Model**	**Degree of poly.**	λ	**RMSE [5-fold]**	
				mean	**std**
Crack features	Linear	-	-	0.070	0.046
	Ridge	2	100	0.070	0.040
Crack features & axial load ratio & shear span ratio	Linear	-	-	0.057	0.032
	Ridge	2	100	0.054	0.035

Shown in Figure 6.8 are the plots of target $SR/FR/DR$ vs. predicted $SR/FR/DR$ performed using the best selected models and hyper-parameters and after re-training models using all data. It can be observed in the plots of target/predicted SR and FR that the data points fall roughly on the ideal red dotted line. However, in the plot of target DR vs. predicted DR, the data points are more dispersed.

Table 6.9 – The performance of trained regression models to predict DR.

Features	Model	Degree of poly.	λ	RMSE [5-fold]	
				mean	std
Crack features	Linear	-	-	0.194	0.117
	Ridge	2	0.1	0.149	0.076
Crack features & axial load ratio & shear span ratio	Linear	-	-	0.173	0.104
	Ridge	2	1	0.137	0.073

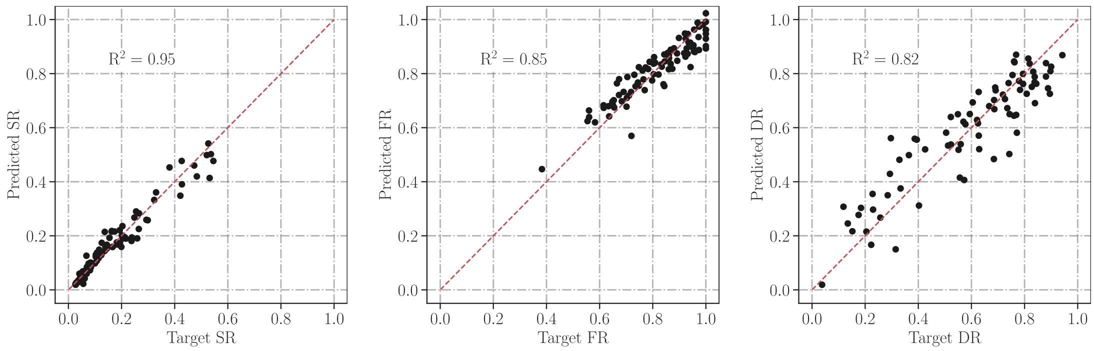

(a) (b) (c)

Figure 6.8 – Plot of predicted vs. target values of (a) SR, (b) FR, and (c) DR. R^2 is the coefficient of determination that is computed as $1 - \frac{\sum_i (y_i - \bar{y})^2}{\sum_i (y_i - \hat{y}_i)^2}$, where $\bar{y}$ is the mean of the target vector.

To compare these regression tasks and to evaluate which of these ratios can be better predicted using the proposed modeling approach and features, we scaled SR, FR, and DR to the range $[0, 1]$ and computed the average 5-fold RMSE using the selected model and hyper-parameters. The average RMSE values when predicting SR, FR, and DR are 11.3%, 8.8%, and 15%, respectively. Therefore, the proposed pipeline more accurately predicts, in order, FR, SR, and DR. The DR prediction may be less accurate due to the auxiliary definition of the ultimate drift, i.e., the drift at a 20% drop in force, which does not necessarily correspond to a physical phenomenon.

6.7 Conclusion

To be able to numerically model a damaged stone masonry building after an earthquake, we need to first quantify the observable damage and build predictive models to map damage features to mechanical properties of damaged structural elements. With this, we can update the properties of piers and spandrels in an equivalent frame modeling approach.

In this study, we use the data recorded during six shear-compression tests on plastered rubble stone masonry piers. The data included images of walls at different levels of damage/load, with the damage in this study narrowed to surface cracks. We computed three features from the crack patterns, which were the maximum crack width, crack length density, and complexity dimension. We then built predictive machine learning models to estimate three ratios representing the decrease of the force/drift capacity and lateral stiffness of rubble stone masonry piers.

Our results showed that simple machine learning models can predict the reduction in stiffness, force, and drift capacity with an average RMSE of 0.061, 0.054, and 0.137, respectively. We also developed machine learning models to predict whether the wall is in the pre-peak or the post-peak regime. Again, a simple KNN model was the most accurate at 93%, which highlights the appropriate selection of crack features. Using the FDR, we observed that the complexity dimension was the feature most able to separate the pre-peak and post-peak distributions.

It is important to note that the trained machine learning models are based on the dataset from a single experimental campaign. As a result, to extrapolate the implemented pipeline, careful consideration must be given to the dependence of maximum crack width on wall size; as a result, when more data for walls of various sizes is available, this crack feature should be normalized to the specimens' height, length, or diagonal.

There are several ways to potentially improve the current proposed pipeline: a) quantify only those cracks that have a significant influence on the overall wall behavior, such as those where most of the deformations concentrate; b) detect and quantify cracking on the masonry side of the walls and differentiate between the cracking in the mortar, the stone/mortar interface, and the units; and c) train more performative and generalizable machine learning models by increasing the size of the dataset from further experimental tests or numerical simulations that can capture masonry cracking, such as the models developed by Saloustros et al. (2017, 2018) and Zhang et al. (2017); Zhang and Beyer (2019). Additionally, increasing the dataset size will allow us to use more sophisticated machine learning models, feature conditioning, and feature extraction methods, or to implement an end-to-end deep learning model to predict the degradation of stiffness, strength, and displacement capacity while classifying the pre-peak vs. post-peak regime directly from images of crack patterns.

Acknowledgments

This project is supported by the Swiss National Science Foundation (grant 200021_175903/1 "Equivalent frame models for the in-plane and out-of-plane response of unreinforced masonry buildings").

7 Conclusions and future work

7.1 Conclusions

Stone masonry buildings are highly vulnerable to seismic activities. Even minor earthquakes can cause significant damage. Currently, in the framework of rapid post-earthquake assessment, experienced inspectors visit the site and determine the level of safety of damaged buildings. However, this approach is costly, subjective, and inefficient. With the daily advance of artificial intelligence, drone technology, computer vision, and computational modeling of masonry buildings, an objective, robust and physics-based approach can replace the current visual inspection method.

There have been numerous works in the literature on the detection of damage from image data. However, there is a lack of work on how the appearance of damage is correlated with the physical properties of a damaged masonry element. To achieve such a goal, the damage feature selection becomes essential. Additionally, how damage features change as a function of kinematic and static boundary conditions is critical to design physics-informed predictive machine learning models.

This research aims at filling this gap by investigating the cracking of unreinforced masonry walls subjected to cyclic shear-compression loading Godio et al. (2019); Petry and Beyer (2015a). The majority of the presented work, in particular, is based on the data obtained from an experimental campaign on plastered rubble stone masonry walls conducted as a part of the Ph.D. work. In what follows, the main conclusions derived from the conducted work are explained. These findings fall into five main categories: a) experimental observations of the most important parameters, i.e., stiffness, strength, and drift capacity, defining the behavior of a rubble stone masonry pier in performance-based seismic assessment approaches; b) observed damage patterns and failure modes; c) crack detection; d) crack quantification; and e) predictive models to estimate the degradation of stiffness, strength and displacement capacity of rubble stone masonry piers and to differentiate the pre-peak from the post-peak regime.

7.1.1 Stiffness, strength and drift capacity of rubble stone masonry piers

- The effective stiffness of the tested piers had a positive correlation with the axial load ratio. This confirmed previous findings from tests on brick and stone masonry (e.g. Vanin et al. (2017); Petry and Beyer (2014a)).

- The force capacity of the walls could be estimated accurately using both Turnsek–Cacovic and Coulomb criteria with calibrated parameters.

- By increasing the shear span ratio and decreasing the axial load ratio, the drift at yield, peak force, ultimate state, and collapse increased. This confirmed previous findings from tests on brick and stone masonry (e.g. Vanin et al. (2017); Petry and Beyer (2014a)).

- The obtained drifts at yield, peak force, and ultimate state were fairly consistent with the empirical formulas proposed by Vanin et al. (2017).

- The drift at 50% drop in force, which was used as a proxy of the drift at collapse in Vanin et al. (2017), leads to estimates that are biased by the axial load ratio. It significantly underestimated the drift at collapse for axial load ratios smaller than 20% because the ratio of the drift at 50% drop in force to the drift at collapse increased with increasing axial load ratio.

7.1.2 Damage pattern and failure modes

- The walls were subjected to in-plane loading only but the developed damage comprised in-plane damage as well as out-of-plane deformations of the leaves and plaster layers. The in-plane damage appeared as flexural and shear cracks, while the out-of-plane damage appeared either as plaster layer detachment or as vertical splitting cracks between the two leaves of the walls, which were followed by out-of-plane displacements of the two leaves. Compression failure was triggered by the out-of-plane buckling of the leaves. The splitting cracks played therefore an important role in the collapse mechanism. It was found that the out-of-plane displacements became larger with increasing shear span ratio. This was attributed to the fact that the buckling length of the compression zone was larger: If the shear span ratio is $H_0/H = 0.5$ the location of the compression zone changes from one end of the wall to the other at mid-height of the wall. If the shear span ratio is $H_0/H = 1.0$ or larger, the compression zone stays over the entire height of the wall on one end of the wall.

- All tested specimens started cracking at small drift levels between 0.04%–0.09%. The obtained drifts at the onset of cracking were less than half of the value (0.2%) reported by Vanin et al. (2017), which was computed from the analysis of a database of 123 shear-compression tests on stone masonry walls. This is due to two factors: a) In the conducted experimental campaign, one side of the tested walls was plastered, and because cracks are more visible on the plastered side than on the masonry side, the obtained drift values were lower. b) I was able to better identify the initiation of cracking during the loading sequence by acquiring images at specific time intervals and using digital image correlation in this testing campaign. However, in other testing campaigns, the cracking initiation was checked when the test was stopped at the maximum applied drift demand.

7.1.3 Crack detection on DIC images

- To detect crack pixels on grayscale images used as input for the DIC method, two methods were implemented and compared: a) the threshold method; and b) the deep learning approach. In the threshold method, a set of thresholds was applied to the maximum principal strain maps computed from the displacement fields outputted by the DIC. A U-Net-like architecture with VGG16 blocks as encoder was trained in the deep learning approach. The VGG16 encoder blocks were initialized in two ways: a) randomly; b) with pre-trained parameters on the ImageNet dataset.

- The two methods were compared in terms of sensitivity, precision, and dice score. The deep learning approach resulted in a higher dice score and precision than the threshold method, while the threshold method had a higher sensitivity score. In other words, the threshold method detected more crack pixels, but the detection was not precise, and there were many false positives.

- Despite the fact that the content of our images differed significantly from that of the ImageNet dataset, initializing the encoder weights with pre-trained parameters on the ImageNet dataset resulted in faster convergence and lower dice loss than random initialization.

7.1.4 Crack pattern quantification

We used different features to quantify crack patterns, including maximum crack width, crack length density, fractal dimension, and complexity dimension. We studied the methodological and physical parameters that affect two of these crack features, the maximum crack width, and the fractal dimension. Below is a summary of the findings.

- **Parameters affecting the maximum crack width**: The maximum crack width, which is the most commonly used damage criterion in the literature, was studied for its sensitivity to the axial load ratio, the shear span ratio, and the loading cycles. There was no discernible relationship between the maximum residual crack width at the peak force and ultimate limit states and the axial load ratio. While the maximum residual crack width increased with shear span ratio at at ultimate limit state. In terms of the influence of loading cycles, it was shown that the maximum and 75th percentile of the crack width distribution increased in the second cycle at the same level of drift demand.

Furthermore, when moving from the applied drift demand to the zero force state, the maximum crack width of diagonal shear cracks changed only slightly. Flexural cracks, on the other hand, almost closed when the specimens were unloaded.

- **Sensitivity of fractal dimension**: We showed that the fractal dimension of crack patterns, a fractional number between 1 and 2, is quite sensitive to the parameter settings of the box-counting method–the widely used method to compute fractal dimension. These parameters are the sampling strategy, the grid position and orientation, the break-point location, and the box size interval. Depending on the setting of these parameters, the fractal dimension can change up to 0.5. Therefore, it is crucial to report all these parameters to have a reproducible estimation of fractal dimension.

7.1.5 Predictive machine learning models

- The crack length density, complexity dimension, and maximum crack width were used to build machine learning models to predict pre-peak vs. post-peak classes and estimate the degradation of stiffness, strength, and drift capacity.

- It was found that the complexity dimension is a better feature in terms of fisher discriminant ratio to classify pre-peak vs. post-peak when using only one crack feature. Additionally, both KNN and logistic regression achieved high accuracy of 93% and 91%, respectively.

- Three degradation ratios were defined to quantify the degradation of stiffness, strength, and drift capacity: stiffness ratio, strength ratio, and drift ratio. These degradation ratios were estimated using two machine learning models, linear regression and ridge regression with polynomial augmented features, using extracted crack features plus the axial load and shear span ratio. When predicting stiffness ratio, force ratio, and drift ratio, adding the shear span and axial load ratio to the crack feature vector reduced the average root mean squared error by 50%, 20%, and 8%, respectively. Furthermore, using the selected hyper-parameters, i.e., the degree of the polynomial and the regularization strength, we retrained the models to estimate the three ratios. The coefficient of determination when fitting for stiffness ratio, force ratio, and drift ratio was 0.95, 0.85, and 0.82, respectively. The results show that simple machine learning models can predict defined ratios reasonably well.

7.2 Limitations

This study was the first step in the EESD vision of an automated post-earthquake assessment of stone masonry buildings using physics, computer vision, and artificial intelligence. There are several assumptions and limitations regarding the applicability of the proposed pipeline that are highlighted below:

- It was assumed that masonry and plaster cracking occur simultaneously. This may not always be the case, depending on the properties of the masonry, plaster, bonds between plaster and masonry, and the masonry typology.

- Seismic actions cause both in-plane and out-of-plane damage. Only in-plane damage (cracking) was considered in this study. Out-of-plane forces can cause damage that affects the in-plane behavior.

- The proposed predictive models to estimate the reduction in stiffness, strength and displacement capacity were functions of crack features. These crack features were the result of applying symmetric cyclic horizontal displacements and a constant axial load and shear span ratio. Therefore, cracking patterns tended to be symmetric. However, in an earthquake, the axial load in external walls of a masonry building varies with the lateral load direction. As a result, in one loading direction, flexural cracks and in the opposite direction shear cracks can develop in a pier resulting in an asymmetric cracking pattern.

- In this study, all detected cracks were assumed to have an equal effect on stiffness, strength, and displacement capacity reduction.

- The proposed predictive models were fitted on the data from only six experimental tests.

7.3 Future work

The topics that can be founded based on the current work and can address the limitations mentioned above are listed below.

7.3.1 Drift limit states of stone masonry piers

The number of quasi-static cyclic shear-compression tests performed on rubble stone masonry piers remains limited, and the fitted empirical models in the literature such as the one proposed by Vanin et al. (2017) to estimate drift limit states are based on very little data. In particular, the six specimens in our experimental campaign are the only two-leaf rubble stone masonry walls that were tested up to the axial load failure. The data on the drift at axial load failure is crucial for the collapse risk analysis of stone masonry buildings. Additionally, the dependency of the drift capacity of the rubble stone masonry walls on the wall size needs further investigations, as it has been some numerical investigations showing the dependency of the drift capacity on the wall size. Furthermore, conducting experiments on walls of different sizes sheds more light on the dependency of the crack width distribution on the wall size at various limit states. These factors highlight the necessity to conduct further experimental tests on rubble stone masonry walls.

7.3.2 Damage detection and quantification

In this study, we only used surface cracks as the main indicator of the damage. However, other signs of damage, such as plaster detachment/collapse or unit crushing, can be detected using DIC measurements or a deep learning method. Crushed area detection and quantification can lead to a more accurate estimation of force/displacement/stiffness degradation.

Additionally, the detection of cracks was performed at a given image frame without considering the previous or the subsequent frames. Therefore, a possibility to enhance the performance of the crack detection is to include the information from the previous and next frames. This idea can be implemented using bidirectional recurrent neural networks. Another method to boost the crack detection pipeline is to use a hybrid DIC/deep learning approach to complement each other.

The developed crack detection and quantification pipeline have applications for the detection of cracks in the wild:

- In an experimental campaign in which a DIC method is used, hundreds of crack images can be cheaply acquired. This data can then be used to pre-train a deep CNN to detect crack pixels on DIC images. This deep CNN can then be fine-tuned to segment crack pixels on the natural images. This pre-training step can be beneficial when the number of crack images in the wild to train a deep CNN is limited.
- The experimental crack data can be used to extract a priori on the crack geometry distribution, for example, a prior distribution about the curvature of crack skeletons. This prior information can then be used to discard crack-like objects, such as wires present in the wild to discard falsely detected crack pixels.

The literature regarding the correlation between the cracking of plaster and masonry is still very limited. It is therefore of interest to investigate the relationship between the drift at plaster cracking and the drift at cracking of masonry using thermal imaging.

7.3.3 Predictive machine learning models

- A larger dataset of crack patterns can be created using numerical platforms that deal with cracking. The larger dataset can then be used to build a machine learning model with greater generalizability.
- The estimation of the degradation of the stiffness, strength, and displacement capacity from crack patterns can be conducted end-to-end by training a CNN, which could potentially improve the results.

A Appendix: Data paper

This chapter represents the pre-print version of the article:

Rezaie, A., Godio, M. and Beyer, K. (2021). "Tests on plastered rubble stone masonry walls subjected to in-plane cyclic loading". *to be submitted to Earthquake Spectra.*

Abstract

Six rubble stone masonry walls made up of irregular blocks and with one face plastered were tested in shear-compression up to collapse. The walls were tested under quasi-static cyclic conditions by varying the applied axial load and shear span ratio. Displacements and forces were measured with classical hard-wired instruments. In addition, optical measurements from two stereo-camera systems monitored the 3D displacement field on both sides of the wall throughout all phases of the tests. The data acquired during the tests are made publicly available through a permanent repository (https://doi.org/10.5281/zenodo.5052675). Included in the repository are the data obtained from the post-processing of the optical measurements using digital image correlation. This paper describes the data and metadata contained in the dataset. To guide analysts interested in the use of this data, there is a Renku project (https://renkulab.io/projects/eesd.epfl/plastered-rubble-stone-masonry-walls) for visualizing and reproducing the test results.

A.1 Introduction

This paper presents the data related to an experimental campaign carried out at École Polytechnique Fédérale de Lausanne (EPFL), Switzerland, on six rubble stone masonry walls. One side of the walls was plastered while the other side remained as visible stone masonry. The walls were tested in shear compression up to failure, indicated by the loss of vertical load bearing capacity. The walls differed with regard to the applied axial load and shear span ratio.

Rezaie et al. (2020b) reports details about the test units, test setup and test protocol along with observations on the main experimental outcomes regarding the structural behaviour of the walls. These observations include the failure mechanisms, stiffness, strength and drift limits derived from the tests and the comparison of these limits with literature provisions. The present paper describes the data organisation and metadata of the experimental campaign. These data are made publicly available through a Zenodo repository (https://doi.org/10.5281/zenodo.5052675).

Due to improvements in camera performance, computational endorsement and correlation algorithms available in commercial software packages, the use of full-field optical measurements, especially digital image correlation (DIC), is becoming more widespread. However, there are currently only a few examples in the literature that use these measurements for studying the local deformation of masonry structural elements. The six modern brick masonry walls tested under shear-compression by Petry and Beyer (2014b) were monitored by a grid of four LEDs positioned on each brick, allowing the average strain of the bricks to be derived and the crack width of the joints to be extrapolated. Salmanpour et al. (2015) used a single camera system in conjunction with DIC software to reconstruct the in-plane deformation of modern brick masonry walls under shear-compression loading. A related technical discussion on the feasibility of using DIC for measuring the masonry deformation is reported in Mojsilović and Salmanpour (2016). Guerrero et al. (2014) applied DIC to evaluate crack maps of masonry infilled frames and to compare the observed failure mechanisms with those predicted by a model proposed in the literature. Ghorbani et al. (2015) derived strain and crack maps of in–plane-loaded confined brick masonry walls using a stereo–camera-based DIC technique. Rezaie et al. (2020a) compared the use of the threshold method and a deep learning model for segmenting crack pixels on DIC images, observing that the deep learning model is superior to the threshold method in terms of preserving cracking geometry. With the trained deep learning model, they investigated the crack kinematic of rubble masonry walls and built machine learning models to estimate the reduction in strength, drift capacity and stiffness as a function of surface crack features (Rezaie et al., 2021a,b). Calderini et al. (2015) monitored the behaviour of plastered stone masonry walls under diagonal compression tests through an optical acquisition system, which was able to capture the evolution of plaster deformation. The same authors analysed the interaction between masonry and plaster on walls subjected to shear-compression tests using infrared thermographic techniques. Bolhassani et al. (2017) employed a stereo-camera system coupled with DIC to monitor the behaviour of a partially grouted reinforced masonry wall tested under shear-compression to derive the strains at different wall locations. Nabouch et al. (2019) used a single–camera-based DIC method to estimate the crack width of in–plane-loaded rammed earth walls and derive subsequent drift limit states for the walls. Shetty et al. (2019) also applied optical measurements coupled with DIC on masonry structural elements, wherein the DIC was used to benchmark the efficacy of acoustic emissions in measuring the damage of masonry under uniaxial compression. Further applications of the in-field monitoring of the displacement history of existing masonry structures are found in Acikgoz et al. (2018) and Dhanasekar et al. (2019).

The above-mentioned works show the usefulness of optical measurements for deriving local deformations and identifying cracks in masonry and plaster. For the latter, reference parameters for the structural behaviour of the wall and for related artistic assets can be obtained through these techniques (Kržan et al., 2015). It is therefore envisioned that the data from these tests will support a variety of future investigations, including the validation of models for the structural analysis of masonry at different scales and subsequent parametric studies. Areas of particular interest for future data users include the assessment of artistic assets related to the structural elements, such as frescoes and paintings.

The paper begins with a brief introduction to the construction and plastering of the walls used in this study, followed by a summary of the experimental test programme; for major details about the campaign, please refer to the related publication (Rezaie et al., 2020b). The paper continues with a description of both the material test data and the shear-compression test data, and it ends with describing the structure of shared data folder.

A.2 Wall construction and plastering

A.2.1 Walls for shear-compression tests

Six rubble stone masonry walls were tested under shear-compression loading as part of the experimental campaign. These walls had a length, height and thickness of 1600 mm, 1600 mm and 400 mm, respectively (see Figure A.1). They were built in two leaves with irregular limestone blocks of up to approximately 30 cm, and the gap between the leaves was filled with pebbles and stone chips (see Figure A.2). A lime-based mortar—aggregate/binder ratio of 3/1 with one portion of water—was used to fill the head and bed joints, where the binder was the commercially available 'OTTERBEIN natural hydraulic lime (NHL5)'. On every wall, the masonry was left visible on one side while the other side was plastered. Two consecutive layers of commercially available 'GeoCalce Intonaco' plaster were applied as illustrated in Figure A.3, with the inner layer measuring about 4–6 cm thick and outer layer measuring 1 cm. The binder to sand weight ratio of 2/1 with 12 l of water was used in the first plaster layer. For the second layer, 25 kg of the binder was mixed with 5.1 l of water. Note that 1–2 cm at the top and bottom of the wall was left without plaster to ensure that the load was applied to the masonry and not to the plaster.

A.2.2 Wallettes for material tests

To determine the material properties of the masonry and obtain representative values for the average masonry properties, three simple-compression and three diagonal-compression tests were carried out. For these tests, wallettes were cut from two long walls constructed with the same typology and material as the walls tested under shear-compression loading. Figure A.4a shows the construction of a long wall and the saw cutting (see Figure A.4b). Once cut, every wallette was plastered on one side, while the masonry was left visible on the other side.

Figure A.1 – Constructed rubble stone masonry walls.

Figure A.2 – Range of stone sizes used to build the walls.

Figure A.3 – Application of plaster layers.

A.3 Shear-compression tests

A.3.1 Testing program

Figure A.5 provides a sketch and photos of the setup used for the shear-compression tests. These tests were conducted in two phases:

(a)

(b)

Figure A.4 – (a) Construction of walls for material tests; (b) cutting the walls into wallettes.

- In the first phase, i.e. LS00_to_LS01 in Table A.1, we increased the forces F_{vn} and F_{vs} in the north and south vertical actuator to apply a centric axial load N:

$$N = \frac{ALR}{100} f_c L t, \tag{A.1}$$

where ALR is the axial load ratio, defined as $\sigma_{v,top}/f_c \times 100$, f_c is the compression strength of the masonry, L is the length of the wall and t is its thickness. The vertical load was applied in three cycles of increasing forces, $N/3$, $2N/3$ and N (see Table A.1).

- In the second phase, we applied cyclic horizontal displacements of increasing drift demand through the horizontal actuator. During this phase, we operated the two vertical actuators in force-controlled mode to ensure a constant axial load and a constant shear span according to the equations:

$$F_{vn} = -\frac{N}{2} + \frac{F_h}{d_{act}}(H_1 - H_0), \tag{A.2}$$

$$F_{vs} = -\frac{N}{2} - \frac{F_h}{d_{act}}(H_1 - H_0), \tag{A.3}$$

where F_h is the force exerted by the horizontal actuator (actuator 1 in Figure A.5a), d_{act} represents the distance between the centre lines of the two vertical actuators and is equal to 2400 mm in this test, H_1 is the distance between the middle axis of the horizontal actuator and the top of the foundation and H is the height of the wall. The load steps and the corresponding nominal drift demand values are mentioned in Table A.1. To restrain the out-of-plane displacement of the loading beam, eight timber beams were placed near the ends of the loading beam. To allow horizontal displacement of the beam, Teflon sheets covered in grease were attached to the cross section of these timber beams where they were in contact with the loading beam.

Table A.1 – Loading protocol for shear-compression tests.

Load step	Initial drift [%]	Final drift [%]	Vertical load [kN]	Note
LS00_to_LS01	- - -	- - -	N/3 2N/3 N	Phase 1: cyclic application of vertical load
LS01_to_LS02	0.000	0.025	N	Phase 2: cyclic application of horizontal displacement
LS02_to_LS03	0.025	-0.025		
LS03_to_LS04	-0.025	0.025		
LS04_to_LS05	0.025	-0.025		
LS05_to_LS06	-0.025	0.050		
LS06_to_LS07	0.050	-0.050		
LS07_to_LS08	-0.050	0.050		
LS08_to_LS09	0.050	-0.050		
LS09_to_LS10	-0.050	0.100		
LS10_to_LS11	0.100	-0.100		
LS11_to_LS12	-0.100	0.100		
LS12_to_LS13	0.100	-0.100		
LS13_to_LS14	-0.100	0.150		
LS14_to_LS15	0.150	-0.150		
LS15_to_LS16	-0.150	0.150		
LS16_to_LS17	0.150	-0.150		
LS17_to_LS18	-0.150	0.200		
LS18_to_LS19	0.200	-0.200		
LS19_to_LS20	-0.200	0.200		
LS20_to_LS21	0.200	-0.200		
LS21_to_LS22	-0.200	0.250		
LS22_to_LS23	0.250	-0.250		
LS23_to_LS24	-0.250	0.250		
LS24_to_LS25	0.250	-0.250		
LS25_to_LS26	-0.250	0.300		
LS26_to_LS27	0.300	-0.300		
LS27_to_LS28	-0.300	0.300		
LS28_to_LS29	0.300	-0.300		
LS29_to_LS30	-0.300	0.400		
LS30_to_LS31	0.400	-0.400		
LS31_to_LS32	-0.400	0.400		
LS32_to_LS33	0.400	-0.400		
LS33_to_LS34	-0.400	0.500		
LS34_to_LS35	0.500	-0.500		
LS35_to_LS36	-0.500	0.500		
LS36_to_LS37	0.500	-0.500		
LS37_to_LS38	-0.500	0.600		
LS38_to_LS39	0.600	-0.600		
LS39_to_LS40	-0.600	0.600		
LS40_to_LS41	0.600	-0.600		
LS41_to_LS42	-0.600	0.800		
LS42_to_LS43	0.800	-0.800		
LS43_to_LS44	-0.800	0.800		
LS44_to_LS45	0.800	-0.800		
LS45_to_LS46	-0.800	1.000		
LS46_to_LS47	1.000	-1.000		
LS47_to_LS48	-1.000	1.000		
LS48_to_LS49	1.000	-1.000		
LS49_to_LS50	-1.000	1.500		
LS50_to_LS51	1.500	-1.500		
LS51_to_LS52	-1.500	1.500		
LS52_to_LS53	1.500	-1.500		
LS53_to_LS54	-1.500	2.000		
LS54_to_LS55	2.000	-2.000		
LS55_to_LS56	-2.000	2.000		
LS56_to_LS57	2.000	-2.000		
LS57_to_LS58	-2.000	2.500		
LS58_to_LS59	2.500	-2.500		
LS59_to_LS60	-2.500	2.500		
LS60_to_LS61	2.500	-2.500		

Table A.2 provides details of the test matrix. The axial load N and the shear-span ratio (H_0/H) were varied between the specimens. Units were labelled as RS<number>, where RS stands for

Rubble Stone. It should be noted that the actuator forces were set to zero after connecting the loading beam.

Table A.2 – Shear-compression test matrix.

Specimen label	H_0/H	N [kN]	ALR [%]
RS1	0.5	41	8
RS2	0.5	123	25
RS3	0.5	82	17
RS4	1.0	123	25
RS5	1.5	123	25
RS6	1.0	82	17

A.3.2 Instrumentation

In this testing campaign, a speckle pattern for tracking displacements was applied by spraying onto the wall surfaces, and speckled paper patches were attached to the beam flange and the steel plate, as shown in Figure A.5c. Two sets of stereo-camera systems were placed on either side of the specimens to capture images while the loads were applied. These images were inputted to a local DIC method, a commercial software called VIC-3D (Correlated Solutions, 2018), to compute the 3D deformations of the walls, and we extracted the computed displacement fields. The DIC method tracked the displacement of the speckled patches, and the average horizontal displacement of four patches attached to the steel plate was used to compute the drift. For a more detailed explanation about the setting of the DIC setup, refer to Rezaie et al. (2020b).

The vertical distance between the lv1 and lv2 (see Figure A.5a) was around 540 mm, and the horizontal distance between the lv3 and lv4 (see Figure A.5a) was around 2870 mm. The base length and the vertical distance between the LVDTs and the top of the foundation (shown as “y” in Figure A.5a) are mentioned in Table A.3.

A.3.3 Results

Table A.4 summarizes the following parameters obtained from the shear compression tests: a) K_{init}, the initial stiffness of the wall defined as the secant stiffness at 15% of maximum force (computed only for the positive direction of the load); b) K_{eff}, the effective stiffness defined as the secant stiffness at 70% of the peak force (computed from the envelope curve of the positive direction of the load); c) V_p, the force capacity of the wall; d) V_u, ultimate force obtained by bilinear idealization the envelope curve (Rezaie et al., 2020b); e) δ_y, the drift at yield; f) δ_p, the drift at peak force; g) δ_u, the ultimate drift defined as the drift at 20% drop in maximum force; and h) δ_c, the drift at axial load failure of the wall.

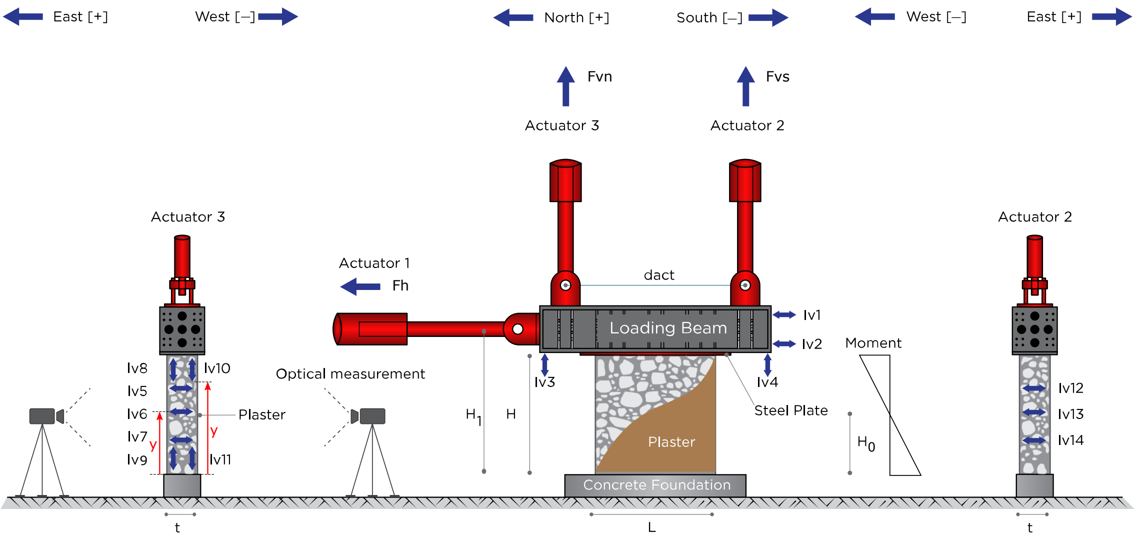

(a)

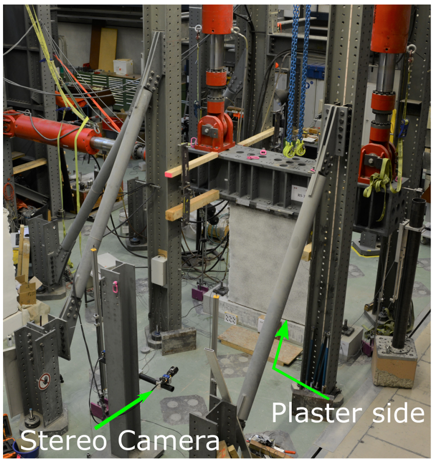

(b)

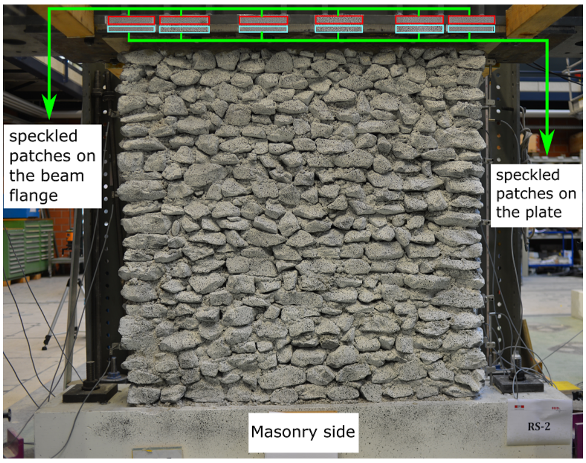

(c)

Figure A.5 – Test setup for shear-compression tests: (a) sketch of the test setup and photos of the (b) plastered side and (c) the bare masonry side.

A.4 Material tests

To determine the mechanical properties of the masonry and its constituent materials, two groups of tests were performed: a) uni-axial compression and diagonal compression tests on masonry wallettes and b) compression and three-point bending tests on mortar samples. No tests were performed on stone samples.

Table A.3 – Position and base length of the lv5–lv14.

Specimen label	LVDT label	lv5	lv6	lv7	lv8	lv9	lv10	lv11	lv12	lv13	lv14
RS1	y (mm)	1230	945	540	1435	45	1240	60	1050	670	280
	base length (mm)	330	330	330	125	150	335	190	325	320	350
RS2	y (mm)	1095	815	455	1385	100	1400	55	1310	940	260
	base length (mm)	285	310	280	180	170	140	160	240	300	260
RS3	y (mm)	1245	770	545	1400	90	1430	40	1245	900	405
	base length (mm)	200	200	200	170	140	120	185	230	270	245
RS4	y (mm)	1095	725	390	1395	70	1395	75	1190	910	435
	base length (mm)	223	245	235	185	160	185	125	230	290	210
RS5	y (mm)	1165	880	360	1400	120	1370	50	1285	860	445
	base length (mm)	220	240	235	155	180	120	140	230	230	230
RS6	y (mm)	1097	785	571	1399	68	1330	88	1260	883	442
	base length (mm)	225	235	240	157	194	201	131	235	235	235

Table A.4 – Shear-compression test results.

Specimen label	K_{init} [kN/mm]	K_{eff} [kN/mm]	V_p [kN]		V_u [kN]		δ_y [%]		δ_p [%]		δ_u [%]		δ_c [%]	
			pos	neg	pos	neg	pos	neg	pos	neg	pos	neg	pos	neg
RS1	88	62	43.8	40.6	40.8	38.1	0.03	0.06	0.09	0.19	0.17	0.34	0.99	1.18
RS2	182	100	66.7	61.9	60.7	57.5	0.03	0.02	0.12	0.12	0.23	0.18	0.32	0.42
RS3	102	42	54.3	51.8	50.1	48.0	0.06	0.03	0.16	0.16	0.32	0.28	1.17	0.84
RS4	34	22	57.8	56.6	53.4	52.5	0.12	0.08	0.24	0.22	0.41	0.47	0.76	0.48
RS5	32	16	45.4	42.5	44.4	40.4	0.12	0.10	1.26	0.84	1.66	1.57	1.66	1.57
RS6	22	16	48.3	49.3	45.2	46.4	0.13	0.15	0.53	0.52	0.73	0.81	1.15	1.11

A.4.1 Masonry properties

Uni-axial compression tests

To obtain the Young's modulus E and the compression strength f_c of masonry, three wallettes (specimens labelled RSC<number>) were tested under uni-axial compression. Setup and instrumentation for these simple compression tests are shown in Figure A.6.

The walls were tested under compression in the direction perpendicular to the bed joints by means of a 10 MN universal testing machine, which was operated in displacement-controlled mode. The bottom beam was attached to the actuator's head, while the top beam remained fixed. Steel plates oriented in the out-of-plane direction were loosely screwed (not tightened) to the beams, while aluminium plates were placed between the steel plates and the beam, ensuring that the plates could slide along the loading beams. Additionally, the rotations of the top and the bottom beams were restrained. Two sets of stereo-camera systems were placed on either side of the wallettes to record the 3D deformation of the leaves.

In the conducted experiments, three loading/unloading cycles were applied before reaching the peak force. The Young's modulus was calculated as the average of the slope of linear lines fitted to each of the three stress-strain cycles (Rezaie et al., 2020b). The strain was computed from DIC outputs, by placing virtual extensometers at 1/3 and 2/3 of the wallette's height–

these virtual extensometers were placed on the masonry side of the wallettes. The dimensions of the tested wallettes plus the obtained E and f_c are reported in Table A.5.

Table A.5 – Geometry and properties of the wallettes tested under simple compression.

Specimen label	Height x length x thickness [mm^3]	E [MPa]	f_c [MPa]
RSC1	900 x 900 x 400	1604	0.66
RSC2	900 x 900 x 400	1177	0.63
RSC3	900 x 800 x 400	792	1.00

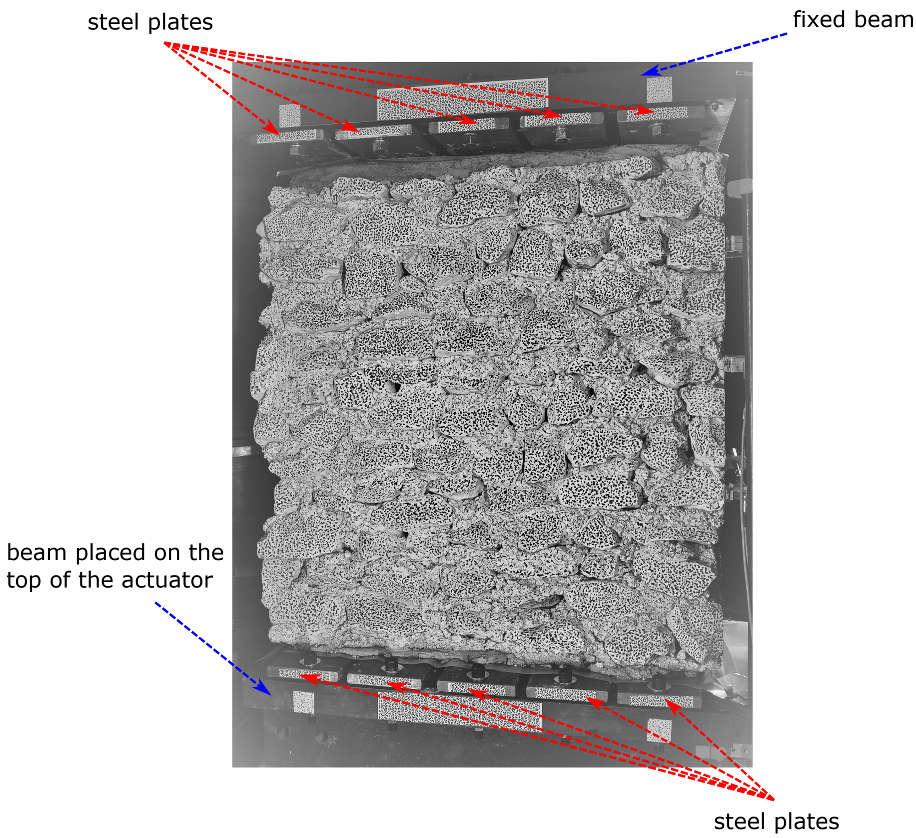

Figure A.6 – Illustration of the compression test on RSC1.

Diagonal compression tests

To obtain the tensile strength of masonry, three wallettes labelled RSD<number> were tested under diagonal compression using the test setup presented in Figure A.7. The tensile strength of the tested wallettes was computed as $f_t = \alpha P_{max}/A$, where α is a coefficient for correcting the stress state, P_{max} is the maximum vertical load and $A = 0.5(L+H)t$ (Rezaie et al., 2020b). As was done for the other tests, two sets of stereo-camera systems were used to monitor the 3D deformations. The dimensions of the tested wallettes plus the obtained f_t using different values of α are reported in Table A.6. For a detailed analysis of the diagonal compression test, please refer to Segura et al. (2021) and Calderini et al. (2010).

Figure A.7 – Illustration of the diagonal compression test on RSD1.

Table A.6 – Geometry and properties of the wallettes tested under diagonal compression.

Specimen label	Height x length x thickness [mm^3]	f_t [MPa]		
		α = 0.707 (ASTM, 2002; RILEM, 1991)	α = 0.5 (Frocht, 1931)	α = 0.35 (Brignola et al., 2008)
RSD1	900 x 900 x 400	0.088	0.063	0.044
RSD2	900 x 900 x 400	0.085	0.060	0.042
RSD3	900 x 900 x 400	0.142	0.100	0.070

A.4.2 Mortar properties

Four-point bending tests and compression tests on mortar samples were carried out. All properties of tested mortar/plaster samples including compression strength and Young's modulus are reported in Rezaie et al. (2020b).

A.5 Test data

The shared data folder on Zenodo is structured as follows:

- Shear_compression_tests: This directory contains six folders called "RS1", "RS2", "RS3", "RS4","RS5" and "RS6". The files and folders in each of these folders have the same structure. Therefore, as an example, we list below files/folders contained in the folder "RS1".

– RS1: This folder contains two folders named "DIC_images" and "DIC_output" and two .csv files named "RS1_cyclic_data.csv" and "RS1_envelope_data.csv".

– In the folder "DIC_images", we shared down-scaled (1/8) images taken at three distinct points of each half-cycle: at the point when the maximum force was reached, at the point when the maximum drift was reached and at the residual drift (i.e. when the horizontal forces was zero). We shared down-scaled images instead of full-size images due to the large file sizes.

  The folder "DIC_output" contains .csv files output from the VIC-3D version 8 software (Correlated Solutions, 2018). These .csv files contain position and displacement fields of a grid of points on the speckled regions. The data points extracted from the plaster and stone surfaces have grid spacing of 20 mm x 20 mm. Again, we only shared the data at instances of maximum force per cycle, maximum drift per cycle and residual drift. To access to the full image and DIC data, contact the head of the EESD lab (https://www.epfl.ch/labs/eesd/).

– The file "RS1_cyclic_data.csv" includes data from the first stage of loading, i.e. cyclic application of the vertical load (LS00_to_LS01), and the second stage of loading, i.e. the cyclic application of the horizontal displacement. The data in RS1_cyclic_data.csv is tabular with the following columns:

  * load_step_names: The label of each load step with the naming convention of "wall name_LS#_to_LS#".
  * image_names: Part of the DIC image names. The naming convention is "LS#_to_LS#_wall name_#".
  * Fh [kN]: The horizontal force (in kN) measured by the horizontal actuator (see Figure A.5).
  * u [mm]: The horizontal displacement of the plate (in mm) obtained from DIC measurements on the stone side. It is computed as the average horizontal displacement of speckled patches on the plate.
  * Fv_total [kN]: The total applied vertical force (in kN), i.e. sum of Fv_s and Fv_n.
  * Fv_s [kN]: The vertical force (in kN) recorded by the south actuator (see Figure A.5).
  * Fv_n [kN]: The vertical force (in kN) recorded by the north actuator (see Figure A.5).
  * lv(1 to 14) [mm]: The measured deformation by lv(1 to 14) in terms of mm. (see Figure A.5).

– The file "RS1_envelope_data.csv" includes derived envelope data. The data is tabular with the following columns:

    * Fh_pos [kN]: The horizontal force (in kN) of the envelope curve on the positive side.
    * u_pos [mm]: The horizontal displacement (in mm) of the envelope curve on the positive side.
    * Fh_neg [kN]: The horizontal force (in kN) of the envelope curve on the negative side.
    * u_neg [mm]: The horizontal displacement (in mm) of the envelope curve on the negative side.
  – Structure_from_motion: To better visualize the texture and morphology of constructed walls and wallettes, two 3D models, one from the large-scale walls (RS1) and one from the wallettes (RSC1) are shared in this folder. These models were constructed using the software Autodesk ReCap Photo. They were down-sampled and extracted as .obj files. Instructions for opening these .obj files are given in the "ReadMe.txt" file in the Structure_from_motion directory.

To visualize the shared data, a Renku project can be found at: https://renkulab.io/projects/eesd.epfl/plastered-rubble-stone-masonry-walls. Renku is a tool designed by the Swiss Data Science center (SDSC) for collaborative open science projects. This project contains a Jupyter notebook plotting the shared shear-compression data.

A.6 Summary

An experimental campaign on plastered rubble stone masonry walls was conducted at École Polytechnique Fédérale de Lausanne (EPFL), Switzerland. This campaign included shear-compression tests on large scale walls, simple-compression and diagonal-compression tests on masonry wallettes and mortar tests. The data set is unique in terms of the richness of optical measurement data that was collected during the experimental campaign. This paper describes construction steps, instrumentation and the structure of shared data folder. The data is publicly available and shared on Zenodo (https://doi.org/10.5281/zenodo.5052675). Furthermore, there is a Renku project for representing the data, allowing readers to easily obtain insights about the data by browsing the developed Jupyter notebook (https://renkulab.io/projects/eesd.epfl/plastered-rubble-stone-masonry-walls). This Renku project was created and is maintained by the EESD group (https://www.epfl.ch/labs/eesd/).

For detailed explanations about conducted experiments and derived conclusions, refer to our related publications Rezaie et al. (2020a,b, 2021a,b).

Acknowledgements

The project is supported by the Swiss National Science Foundation (grant 200021_175903/1 "Equivalent frame models for the in-plane and out-of-plane response of unreinforced masonry buildings"). The authors thank the technicians of the Structural Engineering Laboratory at EPFL and the master students Loris Silva Brites and Alexandre Norcaro for their help with the testing.

Bibliography

Abbiati, G., Broccardo, M., Didier, M., Beyer, K., and Stojadinovic, B. (2018a). A Probabilistic Damage Model for Predicting Plaster Cracks on Unreinforced Masonry Walls. In *16th European Conference on Earthquake Engineering (ECEE 2018)*.

Abbiati, G., Broccardo, M., Gabbi, A., Mojsilović, N., Petrović, M., and Stojadinović, B. (2018b). Calibration of a Probabilistic Fatigue Model for Predicting Plaster Cracks on Unreinforced Masonry Walls Caused by Induced Seismic Hazard. In *Integrating Science, Engineering, & Policy: 11th National Conference on Earthquake Engineering 2018 (11NCEE)*, volume 4, pages 2438–2448. Curran Associates.

Acikgoz, S., DeJong, M. J., and Soga, K. (2018). Sensing dynamic displacements in masonry rail bridges using 2D digital image correlation. *Structural Control and Health Monitoring*, 25(8):1–24.

Adhikari, R. S., Moselhi, O., and Bagchi, A. (2014). Image-based retrieval of concrete crack properties for bridge inspection. *Automation in Construction*, 39:180–194.

Adhikari, S. R., Moselhi, O., Bagchi, A., and Rahmatian, A. (2016). Tracking of Defects in Reinforced Concrete Bridges Using Digital Images. *Journal of Computing in Civil Engineering*, 30(5):4016004.

Allain, C. and Cloitre, M. (1991). Characterizing the lacunarity of random and deterministic fractal sets. *PHYSICAL REVIEW A*, 44(6):3552–3558.

Almeida, J., Prodan, O., Rosso, A., and Beyer, K. (2016). Tests on Thin Reinforced Concrete Walls Subjected to In-Plane and Out-of-Plane Cyclic Loading. *Earthquake Spectra*, 33(1):323–345.

Anagnostopoulos, S., Moretti, M., Panoutsopoulou, M., Panagiotopoulou, D., and Thoma, T. (2004). Post earthquake damage and usability assessment of buildings: further development and applications. *Final report.*

Anthoine, A., Magonette, G., and Magenes, G. (1995). Shear-compression testing and analysis of brick masonry walls. In *Proceedings of the 10th European conference on earthquake engineering*, volume 3, pages 1657–1662.

Applied Technology Council (2005). Field manual: Postearthquake safety evaluation of buildings atc-20-1.

Arvin, E., Apostolos, A., D., H. T., Oguzhan, B., and Salvatore, S. (2019). Fractal and Multifractal Analysis of Crack Patterns in Prestressed Concrete Girders. *Journal of Bridge Engineering*, 24(7):4019059.

ASTM (2002). ASTM E 519-02 standard test method for diagonal tension (shear) in masonry assemblages. ASTM International, West Conshohocken, PA.

Athanasiou, A., Ebrahimkhanlou, A., Zaborac, J., Hrynyk, T., and Salamone, S. (2020). A machine learning approach based on multifractal features for crack assessment of reinforced concrete shells. *Computer-Aided Civil and Infrastructure Engineering*, 35(6):565–578.

Baggio, C., Bernardini, A., Colozza, R., Corazza, L., Della Bella, M., Di Pasquale, G., Dolce, M., Goretti, A., Martinelli, A., and Orsini, G. (2007). Field manual for post-earthquake damage and safety assessment and short term countermeasures (AeDES). *European Commission—Joint Research Centre—Institute for the Protection and Security of the Citizen, EUR*, 22868.

Benedetti, A. and Steli, E. (2008). Analytical models for shear–displacement curves of unreinforced and FRP reinforced masonry panels. *Construction and Building Materials*, 22(3):175–185.

Benedetti, D. and Tomaževič, M. (1984). *Sulla verifica sismica di costruzioni in muratura*.

Berntson, G. M. (1994). Root Systems and Fractals: How Reliable are Calculations of Fractal Dimensions? *Annals of Botany*, 73(3):281–284.

Beyer, K., Penna, A., Vanin, F., Senaldi, I., Godio, M., Guerrini, G., and Tomassetti, U. (2017). Seismic retrofit of cultural heritage buildings – when less is more. In *Proceedings of the 4th Conference on Smart Monitoring, Assessment and Rehabilitation of Civil Structures*.

BIRM (2002). Hartle RA. Bridge Inspector's Reference Manual. US Department of Transportation, Federal Highway Administration.

Bishop, C. M. (2006). *Pattern Recognition and Machine Learning (Information Science and Statistics)*. Springer-Verlag, Berlin, Heidelberg.

Bolhassani, M., Hamid, A. A., Rajaram, S., Vanniamparambil, P. A., Bartoli, I., and Kontsos, A. (2017). Failure analysis and damage detection of partially grouted masonry walls by enhancing deformation measurement using DIC. *Engineering Structures*, 134:262–275.

Borri, A., Castori, G., and Corradi, M. (2015a). Determination of Shear Strength of Masonry Panels Through Different Tests. *International Journal of Architectural Heritage*, 9(8):913–927.

Borri, A., Castori, G., Corradi, M., and Sisti, R. (2014). Masonry wall panels with GFRP and steel-cord strengthening subjected to cyclic shear: An experimental study. *Construction and Building Materials*, 56:63–73.

Borri, A., Castori, G., Corradi, M., and Speranzini, E. (2011). Shear behavior of unreinforced and reinforced masonry panels subjected to in situ diagonal compression tests. *Construction and Building Materials*, 25(12):4403–4414.

Borri, A., Corradi, M., Castori, G., and De Maria, A. (2015b). A method for the analysis and classification of historic masonry. *Bulletin of Earthquake Engineering*, 13(9):2647–2665.

Boschi, S., Galano, L., and Vignoli, A. (2019). Mechanical characterisation of Tuscany masonry typologies by in situ tests. *Bulletin of Earthquake Engineering*, 17(1):413–438.

Bosiljkov, V., Page, A., Bokan-Bosiljkov, V., and Žarnić, R. (2003). Performance based studies of in-plane loaded unreinforced masonry walls. British Masonry Society.

Bosiljkov, V., Page, A., Bokan-Bosiljkov, V., and Žarnić, R. (2010). Evaluation of the seismic performance of brick masonry walls. *Structural Control and Health Monitoring: The Official Journal of the International Association for Structural Control and Monitoring and of the European Association for the Control of Structures*, 17(1):100–118.

Bosiljkov, V and Page, A W and Bokan-Bosiljkov, V and Žarnić, R (2010). Evaluation of the seismic performance of brick masonry walls. *Structural Control and Health Monitoring*, 17(1):100–118.

Bothara, J. and Brzev, S. (2012). *A tutorial: Improving the seismic performance of stone masonry buildings*. Earthquake Engineering Research Institut.

Bouda, M., Caplan, J. S., and Saiers, J. E. (2016). Box-Counting Dimension Revisited: Presenting an Efficient Method of Minimizing Quantization Error and an Assessment of the Self-Similarity of Structural Root Systems. *Frontiers in Plant Science*, 7:149.

Brackenbury, D., Brilakis, I., and DeJong, M. (2019). Automated defect detection for masonry arch bridges. In *International Conference on Smart Infrastructure and Construction 2019 (ICSIC) Driving data-informed decision-making*, pages 3–9. ICE Publishing.

Breheret, A. (2017). Pixel Annotation Tool.

Brignola, A., Frumento, S., Lagomarsino, S., and Podestà, S. (2008). Identification of Shear Parameters of Masonry Panels Through the In-Situ Diagonal Compression Test. *International Journal of Architectural Heritage*, 3(1):52–73.

Buczkowski, S., Kyriacos, S., Nekka, F., and Cartilier, L. (1998). The modified box-counting method: Analysis of some characteristic parameters. *Pattern Recognition*, 31(4):411–418.

Calderini, C., Abbati, S. D., Cotič, P., Kržan, M., and Bosiljkov, V. (2015). In-plane shear tests on masonry panels with plaster: correlation of structural damage and damage on artistic assets. *Bulletin of Earthquake Engineering*, 13(1):237–256.

Calderini, C., Cattari, S., and Lagomarsino, S. (2010). The use of the diagonal compression test to identify the shear mechanical parameters of masonry. *Construction and Building Materials*, 24(5):677–685.

Carocci, C. F. (2012). Small centres damaged by 2009 L'Aquila earthquake: on site analyses of historical masonry aggregates. *Bulletin of Earthquake Engineering*, 10(1):45–71.

Carpinteri, A., Chiaia, B., and Nemati, K. M. (1997). Complex fracture energy dissipation in concrete under different loading conditions. *Mechanics of Materials*, 26(2):93–108.

Carpinteri, A., Corrado, M., and Lacidogna, G. (2012). Three different approaches for damage domain characterization in disordered materials: Fractal energy density, b-value statistics, renormalization group theory. *Mechanics of Materials*, 53(Supplement C):15–28.

Carpinteri, A., Lacidogna, G., Niccolini, G., and Puzzi, S. (2008). Morphological Fractal Dimension Versus Power-law Exponent in the Scaling of Damaged Media. *International Journal of Damage Mechanics*, 18(3):259–282.

Carpinteri, A. and Yang, G. P. (1996). Fractal dimension evolution of microcrack net in disordered materials. *Theoretical and Applied Fracture Mechanics*, 25(1):73–81.

Carrillo, J. and Avila, W. (2017). Assessment of seismic damage of thin and lightly reinforced concrete walls using fractal dimension of cracking. *Earthquake Engineering & Structural Dynamics*, 46(4):661–675.

Cha, Y.-J., Choi, W., and Büyüköztürk, O. (2017). Deep learning-based crack damage detection using convolutional neural networks. *Computer-Aided Civil and Infrastructure Engineering*, 32(5):361–378.

Chaiyasarn, K., Khan, W., Ali, L., Sharma, M., Brackenbury, D., and Dejong, M. (2018). Crack Detection in Masonry Structures using Convolutional Neural Networks and Support Vector Machines. In Teizer, J., editor, *Proceedings of the 35th International Symposium on Automation and Robotics in Construction (ISARC)*, pages 118–125, Taipei, Taiwan. International Association for Automation and Robotics in Construction (IAARC).

Chen, F. and Jahanshahi, M. R. (2018). NB-CNN: Deep Learning-Based Crack Detection Using Convolutional Neural Network and Naïve Bayes Data Fusion. *IEEE Transactions on Industrial Electronics*, 65(5):4392–4400.

Chen, L.-C., Zhu, Y., Papandreou, G., Schroff, F., and Adam, H. (2018). Encoder-decoder with atrous separable convolution for semantic image segmentation. In *Proceedings of the European conference on computer vision (ECCV)*, pages 801–818. Springer International Publishing.

Chiaia, B., van Mier, J. G. M., and Vervuurt, A. (1998). Crack Growth Mechanisms in Four Different Concretes: Microscopic Observations and Fractal Analysis. *Cement and Concrete Research*, 28(1):103–114.

Cinar, A. F., Barhli, S. M., Hollis, D., Flansbjer, M., Tomlinson, R. A., Marrow, T. J., and Mostafavi, M. (2017). An autonomous surface discontinuity detection and quantification method by digital image correlation and phase congruency. *Optics and Lasers in Engineering*, 96:94–106.

Coelho, L. P. (2012). Mahotas: Open source software for scriptable computer vision. *arXiv preprint arXiv:1211.4907*.

Cooper, J. and Oskrochi, R. (2008). Fractal Analysis of Street Vistas: A Potential Tool for Assessing Levels of Visual Variety in Everyday Street Scenes. *Environment and Planning B: Planning and Design*, 35(2):349–363.

Corbit, J. D. and Garbary, D. J. (1995). Fractal Dimension as a Quantitative Measure of Complexity in Plant Development. *Proceedings: Biological Sciences*, 262(1363):1–6.

Corradi, M. (2018). A database of the structural behavior of masonry in shear. *Bulletin of Earthquake Engineering*, pages 3905–3930.

Corradi, M., Borri, A., Castori, G., and Sisti, R. (2014). Shear strengthening of wall panels through jacketing with cement mortar reinforced by GFRP grids. *Composites Part B: Engineering*, 64:33–42.

Corradi, M., Borri, A., Castori, G., and Sisti, R. (2016). The Reticulatus method for shear strengthening of fair-faced masonry. *Bulletin of Earthquake Engineering*, 14(12):3547–3571.

Corradi, M., Borri, A., and Vignoli, A. (2002). Strengthening techniques tested on masonry structures struck by the Umbria–Marche earthquake of 1997–1998. *Construction and Building Materials*, 16(4):229–239.

Corradi, M., Borri, A., and Vignoli, A. (2003). Experimental study on the determination of strength of masonry walls. *Construction and Building Materials*, 17(5):325–337.

Corradi, M., Tedeschi, C., Binda, L., and Borri, A. (2008). Experimental evaluation of shear and compression strength of masonry wall before and after reinforcement: Deep repointing. *Construction and Building Materials*, 22(4):463–472.

Correlated Solutions (2018). *VIC-3D Software Manual*.

Crowley, H., Pinho, R., van Elk, J., and Uilenreef, J. (2019). Probabilistic damage assessment of buildings due to induced seismicity. *Bulletin of Earthquake Engineering*, 17(8):4495–4516.

Da Silva, D., Boudon, F., Godin, C., Puech, O., Smith, C., and Sinoquet, H. (2006). *A Critical Appraisal of the Box Counting Method to Assess the Fractal Dimension of Tree Crowns*, pages 751–760. Springer Berlin Heidelberg, Berlin, Heidelberg.

Dais, D., İhsan Engin Bal, Smyrou, E., and Sarhosis, V. (2021). Automatic crack classification and segmentation on masonry surfaces using convolutional neural networks and transfer learning. *Automation in Construction*, 125:103606.

Dathe, A., Tarquis, A. M., and Perrier, E. (2006). Multifractal analysis of the pore- and solid-phases in binary two-dimensional images of natural porous structures. *Geoderma*, 134(3):318–326.

D'Ayala, Dina F and Paganoni, Sara (2011). Assessment and analysis of damage in L'Aquila historic city centre after 6th April 2009. *Bulletin of Earthquake Engineering*, 9(1):81–104.

de Melo, R. H. C. and Conci, A. (2013). How Succolarity could be used as another fractal measure in image analysis. *Telecommunication Systems*, 52(3):1643–1655.

De Vent, I. A. E., Rots, J. G., and van Hees, R. (2011). *Structural damage in masonry: Developing diagnostic decision support.* PhD thesis, TU Delft, Delft.

Decanini, L., De Sortis, A., Goretti, A., Langenbach, R., Mollaioli, F., and Rasulo, A. (2004). Performance of masonry buildings during the 2002 Molise, Italy, earthquake. *Earthquake Spectra*, 20(S1):S191–S220.

Destrebecq, J. F., Toussaint, E., and Ferrier, E. (2011). Analysis of Cracks and Deformations in a Full Scale Reinforced Concrete Beam Using a Digital Image Correlation Technique. *Experimental Mechanics*, 51(6):879–890.

Dhanasekar, M., Prasad, P., Dorji, J., and Zahra, T. (2019). Serviceability Assessment of Masonry Arch Bridges Using Digital Image Correlation. *Journal of Bridge Engineering*, 24(2):1–16.

Di Ieva, A. (2016). *The Fractal Geometry of the Brain.* Springer; ISBN:978-1-4939-3995-4.

Di Ieva, A., Grizzi, F., Ceva-Grimaldi, G., Russo, C., Gaetani, P., Aimar, E., Levi, D., Pisano, P., Tancioni, F., Nicola, G., Tschabitscher, M., Dioguardi, N., and Baena, R. R. y. (2007). Fractal dimension as a quantitator of the microvasculature of normal and adenomatous pituitary tissue. *Journal of Anatomy*, 211(5):673–680.

Diana, L., Thiriot, J., Reuland, Y., and Lestuzzi, P. (2019). Application of association rules to determine building typological classes for seismic damage predictions at regional scale: the case study of basel. *Frontiers in Built Environment*, 5:51.

Didier, M., Abbiati, G., Broccardo, M., Beyer, K., Danciu, L., Petrović, M., Mojsilović, N., and Stojadinović, B. (2017). Quantification of non-structural damage in unreinforced masonry walls induced by geothermal reservoir exploration using quasi-static cycling tests. In *13th Canadian Masonry Symposium*.

Didier, M., Abbiati, G., Hefti, F., Broccardo, M., and Stojadinovic, B. (2018). Damage quantification in plastered unreinforced masonry walls using digital image correlation. In *10th Australasian Masonry Conference*, pages 14–18.

Dolatshahi, K. M. and Beyer, K. (2019). Stiffness and Strength Estimation of Damaged Unreinforced Masonry Walls Using Crack Pattern. *Journal of Earthquake Engineering*, 0(0):1–20.

Dolatshahi, K. M., Nikoukalam, M. T., and Beyer, K. (2018). Numerical study on factors that influence the in-plane drift capacity of unreinforced masonry walls. *Earthquake Engineering & Structural Dynamics*, 47(6):1440–1459.

Dorafshan, S., Thomas, R. J., and Maguire, M. (2018). Comparison of deep convolutional neural networks and edge detectors for image-based crack detection in concrete. *Construction and Building Materials*, 186:1031–1045.

Dost, B., Edwards, B., and Bommer, J. J. (2018). The relationship between m and ml: A review and application to induced seismicity in the groningen gas field, the netherlandsthe relationship between m and ml: A review and application to induced seismicity in the groningen gas field, the netherlands. *Seismological Research Letters*, 89(3):1062–1074.

Dung, C. V. and Anh, L. D. (2019). Autonomous concrete crack detection using deep fully convolutional neural network. *Automation in Construction*, 99:52–58.

D'Ayala, D. F. and Paganoni, S. (2011). Assessment and analysis of damage in l'aquila historic city centre after 6th april 2009. *Bulletin of Earthquake Engineering*, 9(1):81–104.

Ebrahimkhanlou, A., Farhidzadeh, A., and Salamone, S. (2015). Multifractal analysis of two-dimensional images for damage assessment of reinforced concrete structures. In *Proc.SPIE*, volume 9435.

Ebrahimkhanlou, A., Farhidzadeh, A., and Salamone, S. (2016). Multifractal analysis of crack patterns in reinforced concrete shear walls. *Structural Health Monitoring*, 15(1):81–92.

EN 1015-Part 1 (1999). Methods of test for masonry-Part 1 Determination of compressive strength.

EN 1015-Part 11 (2000). Methods of test for mortar for masonry-Part 11 Determination of flexural and compressive strength of hardened mortar.

Eurocode 8 - Part 3 (2005). Design of structures for earthquake resistance-Part 3: Assessment and retrofitting of buildings, EN 1998-3. Technical report, Brussels: European Committee for Standardization.

Falconer, K. (2004). *Fractal geometry: mathematical foundations and applications.* John Wiley & Sons; ISBN:0470871350, Chichester.

Farhidzadeh, A., Dehghan-Niri, E., Moustafa, A., Salamone, S., and Whittaker, A. (2013). Damage Assessment of Reinforced Concrete Structures Using Fractal Analysis of Residual Crack Patterns. *Experimental Mechanics*, 53(9):1607–1619.

Feldman, D. P. (2012). *Chaos and fractals: an elementary introduction.* Oxford University Press; ISBN:0199566437, Oxford.

FEMA 306 (1998). Federal Emergency Management Agency, Evaluation of earthquake damaged concrete and masonry buildings .

FEMA 307 (1998). Evaluation of earthquake damaged concrete and masonry wall buildings, technical resources. Washington (DC): The Patnership for Response and Recovery.

Foroutan-pour, K., Dutilleul, P., and Smith, D. L. (1999). Advances in the implementation of the box-counting method of fractal dimension estimation. *Applied Mathematics and Computation*, 105(2):195–210.

Frocht, M. M. (1931). Recent advances in photoelasticity and an investigation of the stress distribution in square blocks subjected to diagonal compression. *Trans. ASME*, 53:135–153.

Gehri, N., Mata-Falcón, J., and Kaufmann, W. (2020). Automated crack detection and measurement based on digital image correlation. *Construction and Building Materials*, 256:119383.

Ghorbani, R., Matta, F., and Sutton, M. A. (2015). Full-Field Deformation Measurement and Crack Mapping on Confined Masonry Walls Using Digital Image Correlation. *Experimental Mechanics*, 55(1):227–243.

Giardina, G., Rots, J., and Hendriks, M. (2013). *Modelling of settlement induced building damage*. PhD thesis, Delft University of Technology, TU Delft.

Godio, M., Vanin, F., Zhang, S., and Beyer, K. (2019). Quasi-static shear-compression tests on stone masonry walls with plaster: Influence of load history and axial load ratio. *Engineering Structures*, 192(April):264–278.

Gonzato, G., Mulargia, F., and Ciccotti, M. (2000). Measuring the fractal dimensions of ideal and actual objects: implications for application in geology and geophysics. *Geophysical Journal International*, 142(1):108–116.

Gopalakrishnan, K., Khaitan, S. K., Choudhary, A., and Agrawal, A. (2017). Deep Convolutional Neural Networks with transfer learning for computer vision-based data-driven pavement distress detection. *Construction and Building Materials*, 157:322–330.

Grünthal, G. (1998). European macroseismic scale 1998. Technical report, European Seismological Commission (ESC).

Guerrero, N., Martínez, M., Picón, R., Marante, M. E., Hild, F., Roux, S., and Flórez-López, J. (2014). Experimental analysis of masonry infilled frames using digital image correlation. *Materials and Structures/Materiaux et Constructions*, 47(5):873–884.

Haralick, R. M., Sternberg, S. R., and Zhuang, X. (1987). Image Analysis Using Mathematical Morphology. *IEEE Transactions on Pattern Analysis and Machine Intelligence*, PAMI-9(4):532–550.

Harrar, K. and Hamami, L. (2009). *Implementation of the box-counting method in radiographic images*, pages 299–311. Springer US, Boston, MA.

Hausdorff, F. (1919). Dimension und äußeres Maß. *Mathematische Annalen*, 79(1):157–179.

Helm, J. D. (2008). Digital Image Correlation for Specimens with Multiple Growing Cracks. *Experimental Mechanics*, 48(6):753–762.

Hendry, A. W. and Khalaf, F. M. (2001). *Masonry wall construction.* Spon Press, London.

Hilbert, D. (1891). Ueber die stetige Abbildung einer Line auf ein Flächenstück. *Mathematische Annalen*, 38(3):459–460.

Hoang, N.-d., Nguyen, Q.-l., Tran, V.-D., Nhat-Duc, H., Nguyen, Q.-l., and Tran, V.-D. (2018). Automatic recognition of asphalt pavement cracks using metaheuristic optimized edge detection algorithms and convolution neural network. *Automation in Construction*, 94(July):203–213.

Hou, X.-J., Gilmore, R., Mindlin, G. B., and Solari, H. G. (1990). An efficient algorithm for fast $O(N \ln(N))$ box counting. *Physics Letters A*, 151(1):43–46.

Hoult, N. A., Dutton, M., Hoag, A., and Take, W. A. (2016). Measuring Crack Movement in Reinforced Concrete Using Digital Image Correlation: Overview and Application to Shear Slip Measurements. *Proceedings of the IEEE*, 104(8):1561–1574.

Huyan, J., Li, W., Tighe, S., Zhai, J., Xu, Z., and Chen, Y. (2019). Detection of sealed and unsealed cracks with complex backgrounds using deep convolutional neural network. *Automation in Construction*, 107:102946.

Iglovikov, V. and Shvets, A. (2018). TernausNet: U-Net with VGG11 Encoder Pre-Trained on ImageNet for Image Segmentation.

International Digital Image Correlation Society (2018). *A Good Practices Guide for Digital Image Correlation.*

Ji, A., Xue, X., Wang, Y., Luo, X., and Xue, W. (2020). An integrated approach to automatic pixel-level crack detection and quantification of asphalt pavement. *Automation in Construction*, 114:103176.

Jonathan P. Rivera Emma Lejeune, Bismarck N. Luna, and Andrew S. Whittaker, G. J. (2015). Automated detection and measurement of cracks in reinforced concrete components. *ACI Structural Journal*, 112(3).

Kaige, Z., D., C. H., and Boyu, Z. (2018). Unified Approach to Pavement Crack and Sealed Crack Detection Using Preclassification Based on Transfer Learning. *Journal of Computing in Civil Engineering*, 32(2):4018001.

Karperien, A. (2007). FracLac for ImageJ-FracLac Advanced User's Manual.

Kaye, B. H. (2008). *A random walk through fractal dimensions.* John Wiley & Sons; ISBN:3527615989.

Kingma, D. P. and Ba, J. (2015). Adam: A Method for Stochastic Optimization. In *3rd International Conference on Learning Representations, {ICLR} 2015, San Diego, CA, USA, May 7-9, 2015, Conference Track Proceedings*.

Koch, H. P. (1993). The concept of fractals in the pharmaceutical sciences. *Die Pharmazie*, 48(9):643–659.

Korswagen, P. A., Longo, M., Meulman, E., and Rots, J. G. (2019). Crack initiation and propagation in unreinforced masonry specimens subjected to repeated in-plane loading during light damage. *Bulletin of Earthquake Engineering*, 17(8):4651–4687.

Korswagen, P. A., Longo, M., and Rots, J. G. (2020a). Calcium silicate against clay brick masonry: an experimental comparison of the in-plane behaviour during light damage. *Bulletin of Earthquake Engineering*, 18(6):2759–2781.

Korswagen, P. A., Longo, M., and Rots, J. G. (2020b). High-resolution monitoring of the initial development of cracks in experimental masonry shear walls and their reproduction in finite element models. *Engineering Structures*, 211:110365.

Korswagen, P. A. and Rots, J. G. (2020). Monitoring and Quantifying Crack-Based Light Damage in Masonry Walls with Digital Image Correlation. In *Proceedings of 1st International Conference on Structural Damage Modelling and Assessment*, pages 3–17. Springer.

Kržan, M., Gostič, S., Cattari, S., and Bosiljkov, V. (2015). Acquiring reference parameters of masonry for the structural performance analysis of historical buildings. *Bulletin of Earthquake Engineering*, 13(1):203–236.

Lagomarsino, S. and Cattari, S. (2015). Perpetuate guidelines for seismic performance-based assessment of cultural heritage masonry structures. *Bulletin of Earthquake Engineering*, 13(1):13–47.

Lagomarsino, S., Penna, A., Galasco, A., and Cattari, S. (2013). TREMURI program: An equivalent frame model for the nonlinear seismic analysis of masonry buildings. *Engineering Structures*, 56:1787–1799.

Lecompte, D., Smits, A., Bossuyt, S., Sol, H., Vantomme, J., Van Hemelrijck, D., and Habraken, A. M. (2006). Quality assessment of speckle patterns for digital image correlation. *Optics and Lasers in Engineering*, 44(11):1132–1145.

Lestuzzi, P., Podestà, S., Luchini, C., Garofano, A., Kazantzidou-Firtinidou, D., Bozzano, C., Bischof, P., Haffter, A., and Rouiller, J.-D. (2016). Seismic vulnerability assessment at urban scale for two typical swiss cities using risk-ue methodology. *Natural Hazards*, 84(1):249–269.

Liu, Z., Cao, Y., Wang, Y., and Wang, W. (2019). Computer vision-based concrete crack detection using U-net fully convolutional networks. *Automation in Construction*, 104:129–139.

Lopes, R. and Betrouni, N. (2009). Fractal and multifractal analysis: A review. *Medical Image Analysis*, 13(4):634–649.

Madani, H. M. and Dolatshahi, K. M. (2020). Strength and stiffness estimation of damaged reinforced concrete shear walls using crack patterns. *Structural Control and Health Monitoring*, 27(4):e2494.

Magenes, G., Galasco, A., Penna, A., and Da Paré, M. (2010). In-plane cyclic shear tests of undressed double leaf stone masonry panels. In *Proceedings of the 14th European conference on earthquake engineering. Ohrid.*

Mandelbrot, B. (1967). How long is the coast of Britain? Statistical self-similarity and fractional dimension. *science*, 156(3775):636–638.

Mandelbrot, B. B. (1982). *The Fractal Geometry of Nature.* Freeman; ISBN:0-7167-1186-9, New York.

Maosen, C., Qingwen, R., and Pizhong, Q. (2006). Nondestructive Assessment of Reinforced Concrete Structures Based on Fractal Damage Characteristic Factors. *Journal of Engineering Mechanics*, 132(9):924–931.

Medioni, G., Tang, C.-K., and Lee, M.-S. (2000). Tensor voting: Theory and applications. In *Proceedings of RFIA*, volume 2000.

Mei, Q., Gül, M., and Azim, M. R. (2020). Densely connected deep neural network considering connectivity of pixels for automatic crack detection. *Automation in Construction*, 110:103018.

Meisel, L. V. and Johnson, M. A. (1997). Convergence of numerical box-counting and correlation integral multifractal analysis techniques. *Pattern Recognition*, 30(9):1565–1570.

Meyer, P., Ochsendorf, J., Germaine, J., and Kausel, E. (2007). The impact of high-frequency/low-energy seismic waves on unreinforced masonry. *Earthquake Spectra*, 23(1):77–94.

Michel, C., Hannewald, P., Lestuzzi, P., Fäh, D., and Husen, S. (2017). Probabilistic mechanics-based loss scenarios for school buildings in basel (switzerland). *Bulletin of Earthquake Engineering*, 15(4):1471–1496.

Mignan, A., Broccardo, M., Wiemer, S., and Giardini, D. (2017). Induced seismicity closed-form traffic light system for actuarial decision-making during deep fluid injections. *Scientific reports*, 7(1):1–10.

Mignan, A., Landtwing, D., Kästli, P., Mena, B., and Wiemer, S. (2015). Induced seismicity risk analysis of the 2006 basel, switzerland, enhanced geothermal system project: Influence of uncertainties on risk mitigation. *Geothermics*, 53:133–146.

Milletari, F., Navab, N., and Ahmadi, S.-A. (2016). V-Net: Fully Convolutional Neural Networks for Volumetric Medical Image Segmentation. *2016 Fourth International Conference on 3D Vision (3DV)*, pages 565–571.

Milosevic, J., Gago, A. S., Lopes, M., and Bento, R. (2013). Experimental assessment of shear strength parameters on rubble stone masonry specimens. *Construction and Building Materials*, 47:1372–1380.

Milosevic, J., Lopes, M., Gago, A. S., and Bento, R. (2015). In-plane seismic response of rubble stone masonry specimens by means of static cyclic tests. *Construction and Building Materials*, 82:9–19.

Ministry of Infrastructures and Transportation (MIT) (2009). Circ. N. 617 of 2/2/2009: Istruzioni per l'applicazione delle nuove norme tecniche per le costruzioni di cui al Decreto Ministeriale 14 Gennaio 2008. Italy.

Mojsilović, N. and Salmanpour, A. H. (2016). Masonry walls subjected to in-plane cyclic loading: application of digital image correlation for deformation field measurement. *International Journal of Masonry Research and Innovation*, 1(2):165–187.

Momeni, H. and Dolatshahi, K. M. (2019). Predictive equations for drift ratio and damage assessment of RC shear walls using surface crack patterns. *Engineering Structures*, 190:410–421.

Morgan, S. P. (2017). Using Digital Image Correlation to Detect Cracking in Opalinus Shale. In *Fracture, Fatigue, Failure and Damage Evolution, Volume 8*, pages 125–131. Springer.

Moropoulou, A., Bakolas, A., and Anagnostopoulou, S. (2005). Composite materials in ancient structures. *Cement and Concrete Composites*, 27(2):295–300.

Mosinska, A., Marquez-Neila, P., Koziński, M., and Fua, P. (2018). Beyond the pixel-wise loss for topology-aware delineation. In *Proceedings of the IEEE Conference on Computer Vision and Pattern Recognition*, pages 3136–3145.

Nabouch, R. E., Bui, Q.-B., Plé, O., and Perrotin, P. (2019). Rammed earth under horizontal loadings: Proposition of limit states. *Construction and Building Materials*, 220:238–244.

Napolitano, R. and Glisic, B. (2019). Methodology for diagnosing crack patterns in masonry structures using photogrammetry and distinct element modeling. *Engineering Structures*, 181:519–528.

Napolitano, R. and Glisic, B. (2020). Hybrid physics-based modeling and data-driven method for diagnostics of masonry structures. *Computer-Aided Civil and Infrastructure Engineering*, 35(5):483–494.

Novelli, V. I. and D'Ayala, D. (2019). Use of the Knowledge-Based System LOG-IDEAH to Assess Failure Modes of Masonry Buildings, Damaged by L'Aquila Earthquake in 2009 .

Ostwald, M. J. (2013). The Fractal Analysis of Architecture: Calibrating the Box-Counting Method Using Scaling Coefficient and Grid Disposition Variables. *Environment and Planning B: Planning and Design*, 40(4):644–663.

P. Rivera, J. and S. Whittaker, A. (2019). Damage and Peak Shear Strength of Low-Aspect-Ratio Reinforced Concrete Shear Walls. *Journal of Structural Engineering*, 145(11):4019141.

Pantoja-Rosero, B., Oner, D., Kozinski, M., Achanta, R., P., F., Perez-Cruz, F., and Beyer, K. (2021). Continuity-preserving Crack Detection with Deep Learning. *Submitted to Automation in Construction*.

Park, S. E., Eem, S.-H., and Jeon, H. (2020). Concrete crack detection and quantification using deep learning and structured light. *Construction and Building Materials*, 252:119096.

Peitgen, H.-O., Jürgens, H., and Saupe, D. (2006). *Chaos and fractals: new frontiers of science*. Springer Science & Business Media; ISBN:0387218238, New York, NY, USA.

Peters, W. H. and Ranson, W. F. (1982). Digital Imaging Techniques In Experimental Stress Analysis. *Optical Engineering*, 21(3):427–431.

Petry, S. and Beyer, K. (2014a). Influence of boundary conditions and size effect on the drift capacity of URM walls. *Engineering Structures*, 65:76–88.

Petry, S. and Beyer, K. (2014b). Scaling unreinforced masonry for reduced-scale seismic testing. *Bulletin of Earthquake Engineering*, 12(6):2557–2581.

Petry, S. and Beyer, K. (2015a). Cyclic test data of six unreinforced masonry walls with different boundary conditions. *Earthquake Spectra*, 31(4):2459–2484.

Petry, S. and Beyer, K. (2015b). Force–displacement response of in-plane-loaded urm walls with a dominating flexural mode. *Earthquake Engineering & Structural Dynamics*, 44(14):2551–2573.

Petry, S. and Beyer, K. (2015c). Limit states of modern unreinforced clay brick masonry walls subjected to in-plane loading. *Bulletin of earthquake engineering*, 13(4):1073–1095.

Plotnick, R. E., Gardner, R. H., and O'Neill, R. V. (1993). Lacunarity indices as measures of landscape texture. *Landscape Ecology*, 8(3):201–211.

Pruess, S. A. (1995). *Some Remarks on the Numerical Estimation of Fractal Dimension*, pages 65–75. Springer US, Boston, MA.

Quelhas, B., Cantini, L., and Guedes, J. M. (2014). *Structural Rehabilitation of Old Buildings*, volume 2.

Rasband, W. S. (1997). ImageJ.

Ren, Y., Huang, J., Hong, Z., Lu, W., Yin, J., Zou, L., and Shen, X. (2020). Image-based concrete crack detection in tunnels using deep fully convolutional networks. *Construction and Building Materials*, 234:117367.

Réthoré, J., Hild, F., and Roux, S. (2008). Extended digital image correlation with crack shape optimization. *International Journal for Numerical Methods in Engineering*, 73(2):248–272.

Reuland, Y., Lestuzzi, P., and Smith, I. F. (2019a). An engineering approach to model-class selection for measurement-supported post-earthquake assessment. *Engineering Structures*, 197:109408.

Reuland, Y., Lestuzzi, P., and Smith, I. F. (2019b). Measurement-based support for post-earthquake assessment of buildings. *Structure and Infrastructure Engineering*, 15(5):647–662.

Rezaie, A., Achanta, R., Godio, M., and Beyer, K. (2020a). Comparison of crack segmentation using digital image correlation measurements and deep learning. *Construction and Building Materials*, 261:120474.

Rezaie, A., Godio, M., and Beyer, K. (2020b). Experimental investigation of strength, stiffness and drift capacity of rubble stone masonry walls. *Construction and Building Materials*, 251:118972.

Rezaie, A., Godio, M., and Beyer, K. (2021a). Investigating the cracking of plastered stone masonry walls under shear-compression loading. *Submitted to Construction and Building Materials*.

Rezaie, A., Godio, M., and Beyer, K. (2021b). Prediction of stiffness, residual force and drift capacity of damaged rubble stone masonry piers by machine learning using surface crack features. *Under preparation*.

Rezaie, A., Mauron, A., and Beyer, K. (2020c). Sensitivity analysis of fractal dimensions of crack maps on concrete and masonry walls. *Automation in Construction*, 117.

RILEM (1991). Diagonal tensile strength tests of small wall specimens. Technical Report TC76-LUM, RILEM Publications SARL, Brussels, Belgium.

Ristanović, D., Stefanović, B. D., and Puškaš, N. (2014). Fractal analysis of dendrite morphology using modified box-counting method. *Neuroscience Research*, 84:64–67.

Ronneberger, O., Fischer, P., and Brox, T. (2015). U-net: Convolutional networks for biomedical image segmentation. In *International Conference on Medical image computing and computer-assisted intervention*, pages 234–241. Springer.

Roux, S., Réthoré, J., and Hild, F. (2009). Digital image correlation and fracture: an advanced technique for estimating stress intensity factors of 2D and 3D cracks. *Journal of Physics D: Applied Physics*, 42(21):214004.

Rouzbeh, D., R., M. G., and Nathan, K. J. (2018). Structural Load Estimation Using Machine Vision and Surface Crack Patterns for Shear-Critical RC Beams and Slabs. *Journal of Computing in Civil Engineering*, 32(4):4018024.

Rovero, L., Alecci, V., Mechelli, J., Tonietti, U., and De Stefano, M. (2016). Masonry walls with irregular texture of l'aquila (italy) seismic area: validation of a method for the evaluation of masonry quality. *Materials and Structures*, 49(6):2297–2314.

Roy, A. and Perfect, E. (2014). Lacunarity Analyses of Multifractal and Natural Grayscale Patterns. *Fractals*, 22(03):1440003.

Roy, A., Perfect, E., Dunne, W. M., and McKay, L. D. (2007). Fractal characterization of fracture networks: An improved box-counting technique. *Journal of Geophysical Research: Solid Earth*, 112(B12).

Russakovsky, O., Deng, J., Su, H., Krause, J., Satheesh, S., Ma, S., Huang, Z., Karpathy, A., Khosla, A., Bernstein, M., Berg, A. C., and Fei-Fei, L. (2015). ImageNet Large Scale Visual Recognition Challenge. *International Journal of Computer Vision*, 115(3):211–252.

Salehi, S. S. M., Erdogmus, D., and Gholipour, A. (2017). Tversky loss function for image segmentation using 3D fully convolutional deep networks. In *International Workshop on Machine Learning in Medical Imaging*, pages 379–387. Springer.

Salmanpour, A. H., Mojsilović, N., and Schwartz, J. (2015). Displacement capacity of contemporary unreinforced masonry walls: an experimental study. *Engineering Structures*, 89:1–16.

Saloustros, S., Cervera, M., and Pelà, L. (2018). Tracking multi-directional intersecting cracks in numerical modelling of masonry shear walls under cyclic loading. *Meccanica*, 53(7):1757–1776.

Saloustros, S., Pelà, L., and Cervera, M. (2015). A crack-tracking technique for localized cohesive–frictional damage. *Engineering Fracture Mechanics*, 150:96–114.

Saloustros, S., Pelà, L., Cervera, M., and Roca, P. (2017). Finite element modelling of internal and multiple localized cracks. *Computational Mechanics*, 59(2):299–316.

Sandau, K. (1996). A note on fractal sets and the measurement of fractal dimension. *Physica A: Statistical Mechanics and its Applications*, 233(1):1–18.

Sandau, K. and Kurz, H. (1997). Measuring fractal dimension and complexity — an alternative approach with an application. *Journal of Microscopy*, 186(2):164–176.

Sarhosis, V., Dais, D., Smyrou, E., and Bal, i. E. (2019). Evaluation of modelling strategies for estimating cumulative damage on Groningen masonry buildings due to recursive induced earthquakes. *Bulletin of Earthquake Engineering*, 17(8):4689–4710.

Segura, J., Pelà, L., Saloustros, S., and Roca, P. (2021). Experimental and numerical insights on the diagonal compression test for the shear characterisation of masonry. *Construction and Building Materials*, 287:122964.

Shetty, N., Livitsanos, G., Van Roy, N., Aggelis, D. G., Van Hemelrijck, D., Wevers, M., and Verstrynge, E. (2019). Quantification of progressive structural integrity loss in masonry with Acoustic Emission-based damage classification. *Construction and Building Materials*, 194:192–204.

Shi, Y., Cui, L., Qi, Z., Meng, F., and Chen, Z. (2016). Automatic Road Crack Detection Using Random Structured Forests. *IEEE Transactions on Intelligent Transportation Systems*, 17(12):3434–3445.

Shvets, A. A., Rakhlin, A., Kalinin, A. A., and Iglovikov, V. I. (2018). Automatic Instrument Segmentation in Robot-Assisted Surgery using Deep Learning. *2018 17th IEEE International Conference on Machine Learning and Applications (ICMLA)*.

Siegesmund, S. and Snethlage, R. (2011). *Stone in architecture: properties, durability*. Springer.

Silva, B., Dalla Benetta, M., da Porto, F., and Modena, C. (2014). Experimental assessment of in-plane behaviour of three-leaf stone masonry walls. *Construction and Building Materials*, 53:149–161.

Simonyan, K. and Zisserman, A. (2015). Very Deep Convolutional Networks for Large-Scale Image Recognition. In *International Conference on Learning Representations*.

So, G.-B., So, H.-R., and Jin, G.-G. (2017). Enhancement of the Box-Counting Algorithm for fractal dimension estimation. *Pattern Recognition Letters*, 98(Supplement C):53–58.

Spencer, B. F., Hoskere, V., and Narazaki, Y. (2019). Advances in Computer Vision-Based Civil Infrastructure Inspection and Monitoring. *Engineering*, 5(2):199–222.

Sun, C., Zhou, Y., Chen, J., and Miao, H. (2015). Measurement of Deformation Close to Contact Interface Using Digital Image Correlation and Image Segmentation. *Experimental Mechanics*, 55(8):1525–1536.

Sutton, M. A., Orteu, J. J., and Schreier, H. (2009). *Image correlation for shape, motion and deformation measurements: basic concepts, theory and applications*. Springer Science & Business Media.

Tomaževič, M. (1999). *Earthquake-resistant design of masonry buildings*, volume 1. World Scientific.

Tomaževič, M. (2007). Damage as a measure for earthquake-resistant design of masonry structures: Slovenian experience. *Canadian Journal of Civil Engineering*, 34(11):1403–1412.

Tomaževič, M., Gams, M., and Berset, T. (2012). Seismic strengthening of stone masonry walls with polymer coating. In *Proc., 15th World Conference on Earthquake Engineering (15 WCEE), Lisbon, Portugal*, pages 24–28.

Torre, I. G., Losada, J. C., and Tarquis, A. M. (2016). Multiscaling properties of soil images. *Biosystems Engineering*.

Tung, S.-H., Shih, M.-H., and Sung, W.-P. (2008). Development of digital image correlation method to analyse crack variations of masonry wall. *Sadhana*, 33(6):767–779.

Turnšek, V. and Čačovič, F. (1971). Some experimental results on the strength of brick masonry walls. In *Proc. of the 2nd International Brick Masonry Conference*, pages 149–156.

Uranjek, M., Bosiljkov, V., Žarnić, R., and Bokan-Bosiljkov, V. (2012). In situ tests and seismic assessment of a stone-masonry building. *Materials and Structures*, 45(6):861–879.

Valluzzi, M. R., Calò, S., and Giacometti, G. (2020). Correlation of vulnerability and damage between artistic assets and structural elements: The DataBAES archive for the conservation planning of CH masonry buildings in seismic areas. *Sustainability*, 12(2):653.

Van der Walt, S., Schönberger, J. L., Nunez-Iglesias, J., Boulogne, F., Warner, J. D., Yager, N., Gouillart, E., and Yu, T. (2014). scikit-image: image processing in python. *PeerJ*, 2:e453.

Vanin, F. (2019). Equivalent frame models for in-plane and out-of-plane response of unreinforced masonry buildings. page 173.

Vanin, F., Penna, A., and Beyer, K. (2020). A three-dimensional macroelement for modelling the in-plane and out-of-plane response of masonry walls. *Earthquake Engineering & Structural Dynamics*, 49(14):1365–1387.

Vanin, F., Zaganelli, D., Penna, A., and Beyer, K. (2017). Estimates for the stiffness, strength and drift capacity of stone masonry walls based on 123 quasi-static cyclic tests reported in the literature. *Bulletin of Earthquake Engineering*, 15(12):5435–5479.

Vasconcelos, G. (2005). *Experimental investigations on the mechanics of stone masonry: characterization of granites and behavior of ancient masonry shear walls.* PhD thesis, University of Minho, Portugal.

Vasconcelos, G. and Lourenço, B. (2009). In-Plane Experimental Behavior of Stone Masonry Walls under Cyclic Loading. *Journal of Structural Engineering*, 135(10):1269–1277.

Vintzileou, E., Tselios, I., and Karagiannaki, D. (2020). Quantification of damage to masonry structures under seismic conditions. In *Brick and Block Masonry-From Historical to Sustainable Masonry: Proceedings of the 17th International Brick/Block Masonry Conference (17thIB2MaC 2020), July 5-8, 2020, Kraków, Poland*, page 451. CRC Press.

Wang, M., Liu, K., Lu, H., Shrestha, H., Guragain, R., Pan, W., and Yang, X. (2018). In-plane cyclic tests of seismic retrofits of rubble-stone masonry walls. *Bulletin of Earthquake Engineering*, 16(5):1941–1959.

Wang, X. and Hu, Z. (2017). Grid-based pavement crack analysis using deep learning. In *2017 4th International Conference on Transportation Information and Safety (ICTIS)*, pages 917–924.

Wilding, B., Dolatshahi, K., and Beyer, K. (2017). Influence of load history on the force-displacement response of in-plane loaded unreinforced masonry walls. *Engineering Structures*, 152.

Wilding, B. V. and Beyer, K. (2017). Force–displacement response of in-plane loaded unreinforced brick masonry walls: the critical diagonal crack model. *Bulletin of Earthquake Engineering*, 15(5):2201–2244.

Wilding, B. V. and Beyer, K. (2018a). Analytical and empirical models for predicting the drift capacity of modern unreinforced masonry walls. *Earthquake Engineering & Structural Dynamics*, 47(10):2012–2031.

Wilding, B. V. and Beyer, K. (2018b). The effective stiffness of modern unreinforced masonry walls. *Earthquake Engineering & Structural Dynamics*, 47(8):1683–1705.

Xie, X., Zhang, L., and Qu, Z. (2020). A Critical Review of Methods for Determining the Damage States for the In-plane Fragility of Masonry Infill Walls. *Journal of Earthquake Engineering*, pages 1–22.

Yang, W.-r., He, X.-j., and Dai, L. (2017). Damage behaviour of concrete beams reinforced with GFRP bars. *Composite Structures*, 161(Supplement C):173–186.

Yang, X., Li, H., Yu, Y., Luo, X., Huang, T., and Yang, X. (2018). Automatic Pixel-Level Crack Detection and Measurement Using Fully Convolutional Network. *Computer-Aided Civil and Infrastructure Engineering*, 33(12):1090–1109.

Zhang, L., Yang, F., Zhang, Y. D., and Zhu, Y. J. (2016). Road crack detection using deep convolutional neural network. In *2016 IEEE International Conference on Image Processing (ICIP)*, pages 3708–3712.

Zhang, S. and Beyer, K. (2019). Numerical investigation of the role of masonry typology on shear strength. *Engineering Structures*, 192:86–102.

Zhang, S., Hofmann, M., and Beyer, K. (2018). A 2D typology generator for historical masonry elements. *Construction and Building Materials*, 184:440–453.

Zhang, S., Taheri Mousavi, S. M., Richart, N., Molinari, J.-F., and Beyer, K. (2017). Micromechanical finite element modeling of diagonal compression test for historical stone masonry structure. *International Journal of Solids and Structures*, 112:122–132.

Zhang, X., Rajan, D., and Story, B. (2019). Concrete crack detection using context-aware deep semantic segmentation network. *Computer-Aided Civil and Infrastructure Engineering*, 34(11):951–971.

Zhao, J., Sang, Y., and Duan, F. (2019). The state of the art of two-dimensional digital image correlation computational method. *Engineering Reports*, 1(2):e12038.

Zhou, P. and Goodson, K. E. (2001). Subpixel displacement and deformation gradient measurement using digital image/speckle correlation. *Optical Engineering*, 40(8):1613–1620.

Zhu, Z., German, S., and Brilakis, I. (2011). Visual retrieval of concrete crack properties for automated post-earthquake structural safety evaluation. *Automation in Construction*, 20(7):874–883.

Zou, Q., Cao, Y., Li, Q., Mao, Q., and Wang, S. (2012). CrackTree: Automatic crack detection from pavement images. *Pattern Recognition Letters*, 33(3):227–238.

Zou, Q., Zhang, Z., Li, Q., Qi, X., Wang, Q., Wang, S., and Member, S. (2019). DeepCrack : Learning Hierarchical Convolutional Features for Crack Detection. *IEEE Transactions on Image Processing*, 28(3):1498–1512.

Amir Rezaie

E-mail: amir.rezaie@epfl.ch | arezaie@student.ethz.ch
Linkedin : https://www.linkedin.com/in/amir-rezaie-5389b5160
Github: https://github.com/amirrezaie1415
Google scholar: https://scholar.google.com/citations?user=xAlJoP4AAAAJ&hl=en
ORCID ID: https://orcid.org/0000-0001-7050-5088

Education

2017–2021 **PhD in Structural Engineering**.
École Polytechnique Fédérale de Lausanne (EPFL), Lausanne, Switzerland.
Title: Damage Assessment of Stone Masonry Piers Using Imaged Surface Cracks
PhD supervisor: Prof. Katrin Beyer
Defense date: 28/07/2021

2021–2022 **CAS ETH in Computer Science - Visual Computing**.
ETH Zürich, Zürich, Switzerland.

2020 **Mirco Master in Data Science**.
University of California San Diego, California, USA.
(online)

2015–2017 **Master of Science in Structural Engineering**.
University of Tehran, Tehran, Iran.
Title: Vibration Control of Structures Using Wave Barriers
GPA: 18.86/20
Graduation date: 07/2017

2011–2015 **Bachelor of Science in Civil Engineering**.
University of Tehran, Tehran, Iran.
GPA: 18.86/20
Graduation date: 08/2015

Projects

Laboratory Experience

Experimental tests on rubble stone masonry walls.
Description:
* Testing 6 large-scale stone masonry walls under quasi-static cyclic shear-compression loads.
* Testing 6 masonry panels under compression and diagonal-compression loads.
Link to our publication: https://doi.org/10.1016/j.conbuildmat.2020.118972

Machine Learning and Computer Vision Related Projects

Line-based structure from motion.
Description:
Implementation of the paper "Structure from Motion with Line Segments Under Relaxed Endpoint Constraints" as the project of the course 3D Vision-ETHZ (http://www.cvg.ethz.ch/teaching/3dvision/).
Link to source codes: https://github.com/bgpantojar/amuya_sfm_lines

Crack segmentation.
Description:
Implementation of a deep convolutional neural network to segment crack pixels in images of walls.
Link to our publication: https://doi.org/10.1016/j.conbuildmat.2020.120474

Varroa mites bounding box detection, *Final project of the course Image analysis and pattern recognition [EE-451, EPFL]* , https://edu.epfl.ch/coursebook/en/image-analysis-and-pattern-recognition-EE-451.
Description:
Implementation of a deep convolutional neural network to detect varroa mites in images of beehive.
Our group was ranked first in the leaderboard [https://eval.ai/web/challenges/challenge-page/321/leaderboard/971].

Comparison of pair of MNIST digits, *Project of the course Deep learning [EE-559, EPFL]* , https://edu.epfl.ch/coursebook/en/deep-learning-EE-559.
Description:
This project aimed at developing a deep neural network to compare pairs of MNIST digits and to predict for each pair if the first digit is lesser or equal to the second.
You may see the implemented codes and report in the link below:
https://github.com/amirrezaie1415/Deep-learning-course-projects-EPFL/tree/main/Proj1.

Implementation of a Mini Deep Learning Framework in Python, *Project of the course Deep learning [EE-559, EPFL]* , https://edu.epfl.ch/coursebook/en/deep-learning-EE-559.
Description:
In this project, a new deep learning framework was developed capable of building fully-connected neural networks in Python language using Tensor operations of the PyTorch library.
You may see the implemented codes and report in the link below:
https://github.com/amirrezaie1415/Deep-learning-course-projects-EPFL/tree/main/Proj2.

Higgs Boson; To be, or Not to Be, *Project of the course Machine Learning [CS-433, EPFL]* , https://edu.epfl.ch/coursebook/en/machine-learning-CS-433.
Description:
Implementation of machine learning methods to detect the presence of Higgs Boson particles.
You may see the implemented codes and report in the link below:
https://github.com/amirrezaie1415/Machine-Learning-EPFL_project_1. Our group, with the participant ID our_team, was ranked 20th out of 269 groups in the leaderboard https://www.aicrowd.com/challenges/epfl-machine-learning-higgs/leaderboards?challenge_round_id=78.

Supervision Experience

2020 Semester project (EPFL) | Mr. Remy Dornier | Title: Development of an Image Analysis Algorithm for Crack Detection in Walls

2018 Master thesis (EPFL) | Mr. Antoine Mauron | Title: Predicting the Change in Natural Period of Building due to Damage

Teaching Experience

2018 Mathématiques 1 and Mathématiques 2, Le cours de mise à niveau (MAN) Ecole Polytechnique Fédérale de Lausanne (EPFL), Lausanne, Switzerland

2016 Loading, Professor Seyed Mehdi Zahrai, School of Civil Engineering, University of Tehran, Tehran, Iran

2014 Highway Engineering, Professor Massoud Palassi School of Civil Engineering, University of Tehran, Tehran, Iran

2012–2013 Computer Programming, Professor Shahram Vahdani School of Civil Engineering, University of Tehran, Tehran, Iran

Honors and Awards

2017 **FOE Award-1st Rank**.
Achieving the highest GPA (Master degree) among master students in the Civil Engineering department.

2015–2017 **Iran's National Elites Foundation (INEF) Fellowship**.
INEF is a national organization supports Iranian talents.

2015 **EPFL Excellence Fellowship**.
Selected to receive EPFL Excellence Fellowship for civil engineering master program.

2015 **FOE Award-1st Rank**.
Achieving the highest GPA (Bachelor degree) among bachelor students in the Civil Engineering department.

2014 **FOE Award-1st Rank**.
Achieving the Faculty of Engineering (FOE) award, which is granted to the top 3 one year academic GPA.

2013 **FOE Award-2nd Rank**.
Achieving the Faculty of Engineering (FOE) award, which is granted to the top 3 one year academic GPA.

2012 **FOE Award-3rd Rank**.
Achieving the Faculty of Engineering (FOE) award, which is granted to the top 3 one year academic GPA.

Research Output List

Peer-reviewed publications in international scientific journals.

- **Rezaie Amir**, Godio M, Achanta R, Beyer K. Machine-learning for damage assessment of rubble stone masonry piers based on crack patterns. Submitted to Automation in Construction (July 2021).

- **Rezaie Amir**, Godio M, Beyer K. Investigating the Cracking of Plastered Stone Masonry Walls under Shear-compression Loading. Submitted to Construction and Building Materials (July 2021).

- **Rezaie Amir**, Achanta R, Godio M, Beyer K. Comparison of Crack Segmentation Using Digital Image Correlation Measurements and Deep Learning. Construction and Building Materials. **2020** Nov 20;261:120474.

- **Rezaie Amir**, Mauron AJ, Beyer K. Sensitivity analysis of fractal dimensions of crack maps on concrete and masonry walls. Automation in Construction. **2020** Sep 1;117:103258.

- **Rezaie Amir**, Godio M, Beyer K. Experimental investigation of strength, stiffness and drift capacity of rubble stone masonry walls. Construction and Building Materials. **2020** Aug 10;251:118972.

- Dolatshahi KM, **Rezaie Amir**, Rafiee-Dehkharghani R. Topology optimization of wave barriers for mitigation of vertical component of seismic ground motions. Journal of Earthquake Engineering. **2020** Jan 2;24(1):84-108.

- **Rezaie Amir**, Rafiee-Dehkharghani R, Dolatshahi KM, Mirghaderi SR. Soil-buried wave barriers for vibration control of structures subjected to vertically incident shear waves. Soil Dynamics and Earthquake Engineering. **2018** Jun 1;109:312-23.

Peer-reviewed conference papers.

- **Rezaie Amir**, Mauron A, Dolatshahi KM , Beyer K. Fractal and complexity analysis of crack patterns of masonry walls. 16th European Conference on Earthquake Engineering, **2018**, Thessaloniki, Greece.

Certificates – Online Learning

2020 **Natural Language Processing with Classification and Vector Spaces**.
Issuing Organization: Deeplearning.ai
Credential URL: `https://coursera.org/share/265433ad06dd8c81574596162dd88425`

2020 **Natural Language Processing with Probabilistic Models**.
Issuing Organization: Deeplearning.ai
Credential URL: `https://coursera.org/share/a4639ef49cf3d30cd0b1e2367e0124e2`

2020 **Natural Language Processing with Sequence Models**.
Issuing Organization: Deeplearning.ai
Credential URL: `https://coursera.org/share/1339c3653ef4111b7ee64e2d5a90a6da`

2020 **Sequence Models**.
Issuing Organization: Deeplearning.ai
Credential URL: `https://coursera.org/share/b25a13ee5107796977de11b72248340c`

2018 **Statistical Thinking for Data Science and Analytics**.
Issuing Organization: ColumbiaX [edx]
Credential URL: `https://courses.edx.org/certificates/5305b62fde70470386417cc8466ff88a`

2018 **Introduction to Python for Data Science**.
Issuing Organization: Microsoft [edx]
Credential URL: `https://courses.edx.org/certificates/ffa270c1ddbd439186d7db002ca36f60`

Skills

Programming.
Python: 6 years of experience
MATLAB: 4 years of experience
R: limited experience
C++: limited experience

Languages.
Persian: Native
English: Professional working proficiency
French: Limited working proficiency
German: Elementary proficiency